Cell Death and Differentiation (2015) 22, 898–911

www.nature.com/cdd

# Radiotherapy-induced plasticity of prostate cancer mobilizes stem-like non-adherent, Erk signaling-dependent cells

L Kyjacova[1], S Hubackova[1], K Krejcikova[1], R Strauss[2], H Hanzlikova[1], R Dzijak[1], T Imrichova[1,2], J Simova[3], M Reinis[3], J Bartek*[,1,2] and Z Hodny*[,1]

**Fractionated ionizing radiation combined with surgery or hormone therapy represents the first-choice treatment for medium to high-risk localized prostate carcinoma. One of the main reasons for the failure of radiotherapy in prostate cancer is radioresistance and further dissemination of surviving cells. In this study, exposure of four metastasis-derived human prostate cancer cell lines (DU145, PC-3, LNCaP and 22RV1) to clinically relevant daily fractions of ionizing radiation (35 doses of 2 Gy) resulted in generation of two radiation-surviving populations: adherent senescent-like cells expressing common senescence-associated markers and non-adherent anoikis-resistant stem cell-like cells with active Notch signaling and expression of stem cell markers CD133, Oct-4, Sox2 and Nanog. While a subset of the radiation-surviving adherent cells resumed proliferation shortly after completion of the irradiation regimen, the non-adherent cells started to proliferate only on their reattachment several weeks after the radiation-induced loss of adhesion. Like the parental non-irradiated cells, radiation-surviving re-adherent DU145 cells were tumorigenic in immunocompromised mice. The radiation-induced loss of adhesion was dependent on expression of Snail, as siRNA/shRNA-mediated knockdown of Snail prevented cell detachment. On the other hand, survival of the non-adherent cells required active Erk signaling, as chemical inhibition of Erk1/2 by a MEK-selective inhibitor or Erk1/2 knockdown resulted in anoikis-mediated death in the non-adherent cell fraction. Notably, whereas combined inhibition of Erk and PI3K–Akt signaling triggered cell death in the non-adherent cell fraction and blocked proliferation of the adherent population of the prostate cancer cells, such combined treatment had only marginal if any impact on growth of control normal human diploid cells. These results contribute to better understanding of radiation-induced stress response and heterogeneity of human metastatic prostate cancer cells, document treatment-induced plasticity and phenotypically distinct cell subsets, and suggest the way to exploit their differential sensitivity to radiosensitizing drugs in overcoming radioresistance.**
*Cell Death and Differentiation* (2015) **22,** 898–911; doi:10.1038/cdd.2014.97; published online 11 July 2014

Prostate carcinoma (CaP) is the most frequent type of cancer in men, and the sixth cause of cancer-associated death in men worldwide.[1] Despite the advances in diagnosis and therapy of CaP, the mortality has remained almost unchanged for the last decades. Currently, the most successful treatment for localized CaP is prostatectomy with postoperative fractionated radiotherapy, significantly improving metastasis-free and overall survival, where the median of a 15-year survival is around 47% of patients.[2,3] The rest of the patients develop a metastatic disease that is incurable due to the resistance of CaP to androgen ablation, radiotherapy and chemotherapy. Therefore, understanding the mechanisms of radioresistance and chemoresistance of primary and metastatic CaP, respectively, is fundamental for future efforts to develop more efficient therapeutic strategies.

The mechanism of radioresistance of CaP is not entirely clear. Downregulation of some proteins, such as DAB2IP in metastatic prostate cancer, results in radioresistance and was

[1]Department of Genome Integrity, Institute of Molecular Genetics, v.v.i., Academy of Sciences of the Czech Republic, Prague, Czech Republic; [2]Genome Integrity Unit, Danish Cancer Society Research Center, Copenhagen, Denmark and [3]Department of Tumour Immunology, Institute of Molecular Genetics, v.v.i., Academy of Sciences of the Czech Republic, Prague, Czech Republic

*Corresponding authors: J Bartek and Z Hodny, Department of Genome Integrity, Institute of Molecular Genetics ASCR, v.v.i., Academy of Sciences of the Czech Republic, Videnska 1083 CZ 142 20, Prague 4, Czech Republic. Tel: +(420) 24106 3151; Fax: +(420) 24106 2289; E-mail: jb@cancer.dk or hodny@img.cas.cz

**Abbreviations:** Akt (PKB), protein kinase B; 53BP1, p53 binding protein 1; AKTi, Akt inhibitor; APC, allophycocyanin; Bcl-XL, BCL-2-like 1, long isoform; Bim (EL), Bcl-2 interacting mediator of cell death, extra large form; BrdU, 5-bromo-2'-deoxyuridine; CaP, prostate carcinoma; DAPI, 4',6-diamidino-2-phenylindole; DLL1, delta-like 1; DLL4, delta-like 4; DNA, deoxyribonucleic acid; Dox, doxycycline; Doxo, doxorubicine; ECM, extracellular matrix; EdU, 5-ethynyl-2'-deoxyuridine; EGF, epidermal growth factor; EMT, epithelial-to-mesenchymal transition; ERK1 (MAPK3), mitogen-activated protein kinase 3; ERK2 (MAPK1), mitogen-activated protein kinase 1; ERKi, Erk inhibitor; FACS, fluorescence-activated cell sorting; FAK, focal adhesion kinase; FGF, fibroblast growth factors; fIR, fractionated irradiation; fRT, fractionated radiotherapy; GAPDH, glyceraldehyde 3-phosphate dehydrogenase; Gy, gray; H2AX, H2A histone family, member X; Hes1, hairy and enhancer-of-split 1; Hey1, hairy/enhancer-of-split related with YRPW motif 1; HTS, high throughput sampler; IL, interleukin; IR, irradiation; ITGA2, integrin, alpha 2; LAMC2, laminin, gamma 2; LAMA3, laminin, alpha 3; MACS, magnetic-activated cell sorting; MET, mesenchymal-epithelial transition; MMP-7, matrix metallopeptidase 7; NFkappaB, nuclear factor kappa B; Oct-4, octamer-binding transcription factor-4; PI3K, phosphoinositide-3-kinase; PMA, phorbol 12-myristate 13-acetate; PML, promyelocytic leukemia protein; PML NBs, promyelocytic leukemia nuclear bodies; qRT–PCR, quantitative real time polymerase chain reaction; RNA, ribonucleic acid; RPL37a, ribosomal protein L37a; S.D., standard deviation; SA-$\beta$-gal, senescence-associated beta-galactosidase; siNT, Non-targeting siRNA; STAT, signal transducers and activators of transcription; CTCs, circulating tumor cells; Twist1, Twist-related protein 1

Received 14.12.13; revised 07.5.14; accepted 03.6.14; Edited by G Melino; published online 11.7.14

proposed as a predictive marker of aggressive CaP. The radioresistance in DAB2IP-deficient CaP cells reflects faster repair of DNA double-strand breaks, combined with decreased expression of proapoptotic caspases and enhanced levels of anti-apoptotic proteins Bcl-2 and STAT3.[4] IL-6/STAT3 signaling plays an important role in radioresistance of CaP cells[5,6] and malignant properties in general.[7] Inhibition of the PI3K–Akt pathway, together with the MAPK–Erk pathway, sensitizes CaP cells to IR, likely due to suppression of AP-1[8] and NFkappaB[9] transcription factors. Radiation-surviving CaP cells exhibit enhanced migration, higher levels of androgen and EGF receptors and activation of their downstream pathways, Ras–MAPK, PI3K–Akt and Jak–STAT.[5] Thus the inhibition of IL-6 signaling, which is highly activated in metastatic CaP cells,[10,11] results in radiosensitization,[6] inhibition of cell growth, invasion[12–15] and angiogenesis.[16]

The clinical significance of this topic, and the intriguing yet fragmented insights into the cellular and molecular basis of CaP radioresistance, including its reportedly 'heritable' nature,[5] and the lack of a model of metastatic human CaP that would recapitulate the clinically relevant scenario of long-term fractionated radiotherapy, led us to perform the present study. To our knowledge, this is the first study of a series of human metastatic CaP cell lines in terms of their response to long-term fractionated irradiation (fIR, 35 cycles of 2 Gy, mimicking the clinical regimen), in a multifaceted biological and molecular analysis of the resulting CaP cell populations of both adherent and non-adherent nature. The present data set documents several novel findings including biological heterogeneity of the radiation-surviving cell subpopulations, their phenotypic plasticity, stem-like cell and tumorigenic properties. Furthermore, our results reveal differential sensitivity of the two major subpopulations of the radiation-surviving CaP cells to inhibition of complementary signaling cascades, suggesting a strategy for overall elimination of both subsets of metastatic human radiation-surviving CaP cells by combined targeting of their respective pro-survival signaling pathways.

## Results

**Fractionated ionizing radiation of CaP cells induces two prevalent phenotypes: senescent adherent cells and anoikis-resistant non-adherent cells.** To elucidate radioresistance of metastatic CaP cells, we first followed the clinically used radiotherapy regimen[2,3] and exposed four human CaP cell lines of metastatic origin (DU145, PC-3, LNCaP and 22RV1) to cumulative doses of 70 Gy (2 Gy applied every 24 h for 35 days). Characteristic phenotypic changes observed during the fIR course are schematically depicted in Figure 1a and shown in Figure 1b. As early as after the third dose of fIR, a continuing loss of adhesion was observed in all four cell lines, such non-adherent cells were able to reattach within 10–21 days after the last irradiation time point (re-adherent cell*s*). However, on 35 doses of irradiation, a small subset of the initial cell population remained vitally attached (adherent cells). Similar loss of cell adhesion and subsequent re-adhesion was reproduced with irradiation regimens consisting of either ten consecutive doses of 2 Gy or one dose of 10 Gy. Therefore, in some experiments, these shortened irradiation regimens were used.

Next, we characterized the radiation-surviving adherent fraction. Cell proliferation in this fraction was largely unaffected until the 10th dose of radiation, as detected by EdU incorporation in DU145 (39.1% ± 11.7 labeled, compared with 29.5% ± 5.5 control cells) and PC-3 (36.0% ± 10.6 labeled, compared with 22.5% ± 5.9 control cells), while the proliferation became slower between doses 11–15 (Supplementary Figure 1a). Among these adherent DU145 and PC-3 cells, some developed senescence-like morphology. The senescence was progressively developing during the course of irradiation (active DNA damage signaling was assayed as phosphorylation of Chk2 and p53, elevated expression of the p53 target cdk inhibitor $p21^{waf1/cip1}$; Supplementary Figure 2a and foci positive for 53BP1 and phosphorylated histone H2AX; Supplementary Figure 2c) with characteristic cell enlargement, spreading and vacuolization (Figure 1b), nuclear aberrations, abundant chromatin bridges (Supplementary Figures 1b and c), positivity for senescence-associated $\beta$-galactosidase (SA-$\beta$-gal) (Supplementary Figure 1d), and an increase of PML NBs (Supplementary Figure 2b). Notably, senescent DU145 cells pulsed with BrdU showed asynchronous labeling of nuclei (Supplementary Figure 1c) indicating ongoing DNA endoreduplication in adherent survivors. Some cells resumed proliferation ~2 weeks after the end of irradiation (Figures 1b and c and Figure 4).

As indicated above, small subsets of surviving non-adherent cells were resistant to anoikis, and resumed adherent growth (Figures 1b and c; Supplementary Figure 1e). Once initiated, such re-adhesion was a sudden process lasting several days and encompassed the majority of non-adherent cells, many of them utilizing the already attached cells as adhesion substrate (Figure 1c; Supplementary Figures 1f and 2d). Formation of rosette-like membrane blebbing accompanied reattachment (Supplementary Figure 2d), as did sphere-forming growth (Figure 1c). The tumorigenicity of the re-adherent DU145 cells in immunodeficient mice was preserved (Supplementary Figure 2e). The same effect of fIR was reproduced in the human breast cancer cell line MCF-7 (Supplementary Figures 1e, f and g) indicating the phenomenon is not restricted to CaP cells only.

Altogether, fIR of tumor cells led to development of two phenotypically distinct: adherent and non-adherent radiation-surviving cell populations, both capable of renewed proliferation after termination of the radiation stress.

**Ionizing radiation induces expression of Snail and loss of cellular adhesion.** As the loss of adhesion and resistance to anoikis indicated phenotypic changes, we compared both the non-adherent and adherent radiation-surviving CaP cells for factors involved in epithelial–mesenchymal transition (EMT). We analyzed mRNA levels for EMT-inducers Snail, Slug, Twist1, Twist2, Zeb1 and Zeb2 during fIR in all four populations: parental = non-irradiated, irradiated adherent, non-adherent and re-adherent. The transcription factors whose mRNA levels were altered, that is, Snail, Slug, Twist1 and Zeb2 are shown (Figure 2a; Supplementary Figure 3a).

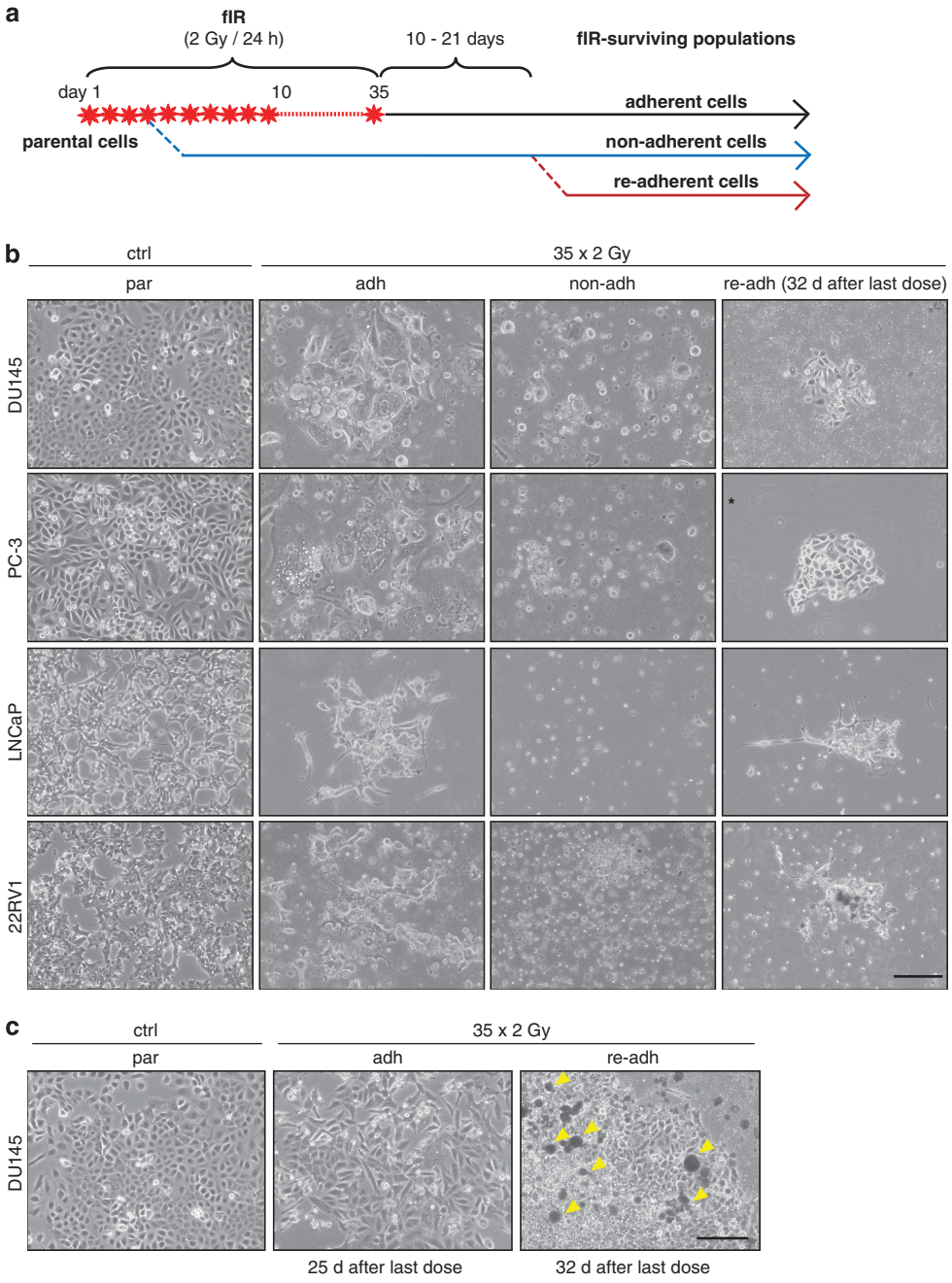


**Figure 1** Generation of adherent and non-adherent radiation-surviving populations in human prostate carcinoma cells by fIR. (**a**) Schematic representation of the irradiation protocol using 2 Gy every 24 h resulting in the generation of radiation-surviving populations (adherent, non-adherent and re-adherent) in human prostate cancer cell lines DU145, PC-3, LNCaP and 22RV1 (See Material and Methods for details). (**b**) Phase contrast microscopic images of non-irradiated parental cells (par) and fIR-surviving DU145, PC-3, LNCaP and 22RV1 cell populations after 35 $\times$ 2 Gy fIR (adh and non-adh) or 32 days after last dose of fIR (re-adh). Representative phase contrast images of one from three independent experiments are shown. The image with asterisk represents the re-adherent colony of PC-3 cells obtained after 10 days of fIR. Scale bar, 100 $\mu$m. (**c**) Phase contrast images of control (parental) and irradiated adherent and re-adherent DU145 single-cell colonies captured at indicated time points after 35 $\times$ 2 Gy of fIR. Note, the 'black' cells (arrowheads) are non-adherent cells starting to attach to the layer of adherent cells. Scale bar, 100 $\mu$m. adh, adherent; non-adh, non-adherent; par, parental; readh, re-adherent

The most consistent changes were observed for Snail, known to regulate stress resistance, stem cell-like commitment and EMT in various cancer types.[17] Snail was induced by all three irradiation regimens in the non-adherent cells in both DU145 and PC-3 cells compared with parental and irradiated adherent cells at mRNA (Figure 2a, Supplementary Figure 3b) and protein (Figures 2b and c) levels (for basal expression of Twist1 in DU145 and PC-3, see Supplementary Figure 3c). Analogous Snail induction was observed in MCF-7 exposed to 10 $\times$ 2 Gy (Figures 2a and b). To test whether the loss of cell adhesion depends on Snail or Twist1, siRNA-mediated knockdown of either factor

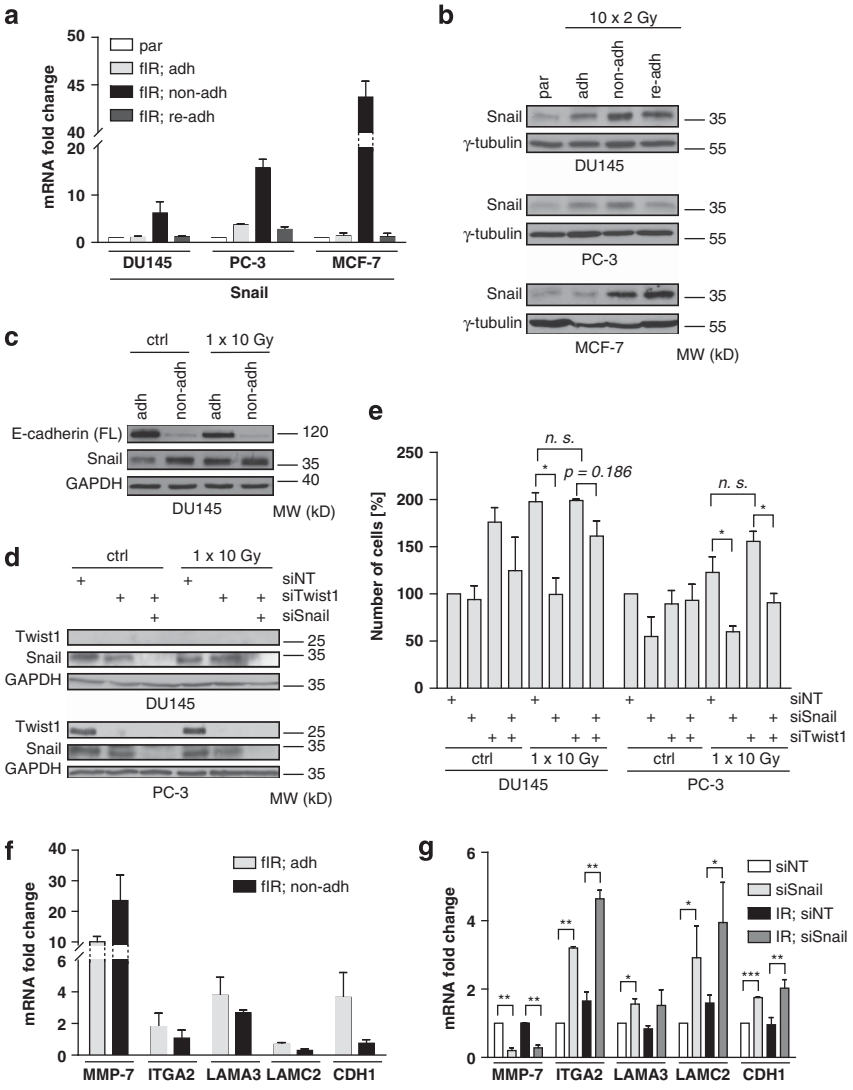


**Figure 2** Snail expression in fIR-surviving human cancer cells. Real time qRT–PCR quantification of Snail mRNA levels (**a**) and Snail immunoblotting detection (**b**) in DU145, PC-3 and MCF-7 control (parental) or irradiated ($10 \times 2$ Gy) adherent, non-adherent and re-adherent cell populations. RPL37a (DU145 and PC-3) and GAPDH (MCF-7) were used as reference genes in (**a**); gamma-tubulin was used as a loading control in **b**. (**c**) E-cadherin and Snail immunoblotting detection in adherent and non-adherent control and irradiated ($1 \times 10$ Gy) DU145 cells. GAPDH was used as a loading control. (**d**) Efficiency of siRNA-mediated knockdown of Snail (siSnail) and Twist1 (siTwist1) estimated by immunoblotting detection of Snail and Twist1 in control or irradiated ($1 \times 10$ Gy) DU145 and PC-3 cells. GAPDH was used as a loading control. (**e**) Effect of siRNA knockdown of Snail (siSnail) and Twist1 (siTwist1) on loss of adhesion expressed as relative number of detached cells assessed by FACS in control or irradiated ($1 \times 10$ Gy) non-adherent DU145 and PC-3 cells. Non-targeting siRNA (siNT) was used as a negative control. Cells were irradiated 24 h after transfection and FACS-analyzed 48 h after IR. Non-irradiated cells transfected with non-targeting siRNA were set as 100% in both cell lines. (**f**) Real time qRT–PCR quantification of mRNA levels of Snail-regulated genes MMP-7, ITGA2, LAMA3, LAMC2 and CDH1 (E-cadherin) in radiation-surviving adherent and non-adherent DU145 cells after irradiation ($10 \times 2$ Gy). $\beta$-actin was used as a reference gene. (**g**) Effect of siRNA knockdown of Snail (siSnail) on Snail-activated (MMP-7) or -repressed genes (ITGA2, LAMA3, LAMC2 and CDH1) estimated by real time qRT–PCR in control and irradiated ($1 \times 10$ Gy) DU145 cells. $\beta$-actin was used as a reference gene. Panels concerning real time qRT–PCR represent data from at least two (**f**, **g**) or three (**a**) independent experiments executed in triplicates. (**e**) Represents three independent experiments. Data in **a**, **e**, **f**, **g** represent means $\pm$ S.D. $^{*}P<0.05$; $^{**}P<0.01$; $^{***}P<0.001$

was performed in DU145 and PC-3 cells before a single dose of irradiation (10 Gy; Figure 2d). Knockdown of Snail, but not of Twist1, reverted the enhanced loss of adhesion in irradiated cells, while having no effect on control cells (Figure 2e). A similar suppressive impact of Snail down-regulation on loss of adhesion was obtained using a tetracycline-inducible Snail shRNA system in DU145 cells exposed to $10 \times 2$ Gy fIR (Figures 3d and e).

Furthermore, genes known to be positively regulated by Snail, such as MMP-7,[18] or negatively, for example, integrin alpha2 (ITGA2[19]), laminin alpha3 (LAMA3), laminin gamma2 (LAMC2[20]) and E-cadherin (CDH1[21,22]) were consistently altered in irradiated non-adherent DU145 cells (Figure 2f), indicating Snail activity. Indeed, knockdown of Snail led to decreased MMP-7 and increased ITGA2, LAMA3, LAMC2 and E-cadherin (Figure 2g). Furthermore, ITGA2 was elevated in the non-adherent DU145 cells with doxycycline-inducible Snail shRNA, consistent with Snail-mediated repression of this gene (Supplementary Figure 3f). Importantly, the major epithelial adhesion molecule E-cadherin was

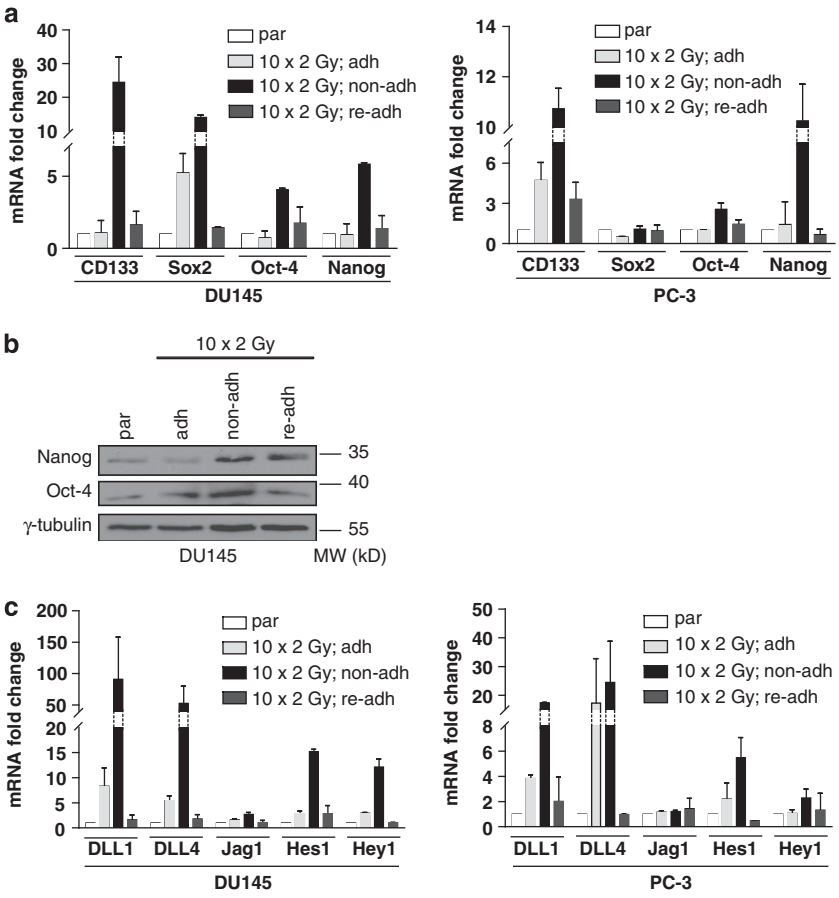


**Figure 3** Non-adherent cells express stem cell-like markers. (**a**) Real time qRT–PCR detection of CD133, Sox2, Oct-4 and Nanog in control (parental) and irradiated ($10 \times 2$ Gy) radiation-surviving DU145 (left) and PC-3 (right) adherent, non-adherent and re-adherent cell populations. RPL37a was used as a reference gene. (**b**) Immunoblotting detection of Nanog and Oct-4 in control (parental) and irradiated ($10 \times 2$ Gy) adherent, non-adherent and re-adherent DU145 cells. Gamma-tubulin was used as a loading control. (**c**) Real time qRT–PCR quantification of Notch signaling ligands DLL1, DLL4, Jag1 and Notch signaling target genes Hes1 and Hey1 by real time qRT–PCR in control (parental) and irradiated ($10 \times 2$ Gy) DU145 (left) and PC-3 (right) radiation-surviving adherent, non-adherent and re-adherent cell populations. RPL37a was used as a reference gene. Data in all graphs represent means ± S.D. from two independent experiments performed in triplicates

markedly decreased in non-adherent fractions of both irradiated and control cells (Figure 2c), confirming that EMT events accompanied the loss of cellular adhesion.

Overall, non-adherent CaP cells lose adhesive properties via EMT, and this process is amplified on radiation stress through elevated expression of Snail.

**Fractionated irradiation-induced expression of stem cell markers in the non-adherent cells.** The anoikis-resistant survival of non-adherent CaP cells might be associated with acquisition of stem cell properties induced during ionizing radiation. Indeed, compared with all other fractions of control and irradiated cells, the non-adherent DU145 and PC-3 cells showed higher mRNA levels of stem cell-associated genes CD133, Sox2, Oct-4 and Nanog (Figure 3a, Supplementary Figure 3g). Shortly after cell re-adhesion, these transcripts returned almost to the pre-irradiation levels observed in the parental cells, indicating a transiently mobilized stem-like cell stage during the non-adherent phase. The elevation of Nanog and Oct-4 protein levels was confirmed (Figure 3b). Notably, an increased activity of Notch signaling, characteristic for progenitor cells[23,24] was detected as elevated mRNA of the NOTCH pathway-regulated genes Hes1[25] and Hey1[26] in the non-adherent irradiated fractions of both DU145 and PC-3 cells (Figure 3c). The induction of Hes1 and Hey1 transcription factors was accompanied by elevated NOTCH ligands DLL1 and DLL4 in irradiated cells (Figure 3c; Supplementary Figure 3h). The transcripts of DLL1, DLL4, Hes1 and Hey1 in irradiated cells reverted nearly to parental cell levels after cell re-adhesion (Figure 3c).

Altogether, the non-adherent irradiated cells differ from the adherent irradiated cells by expression of stem-like cell markers and progenitor cell-associated Notch signaling, in a transient manner that reverted on cell re-adhesion.

**Irradiated non-adherent cells do not proliferate.** To assess proliferation of the radiation-surviving non-adherent cells, we labeled cells with the cell proliferation dye. Whereas the non-irradiated non-adherent cells re-adhered rapidly, during 24 h, and on re-adhesion diluted the dye almost completely within 28 days consistent with ongoing cell proliferation, the non-adherent irradiated cells retained almost the same eFluor670 fluorescence intensity for the 28-day period (Supplementary Figures 4a and b), indicating

lack of cell proliferation. This was confirmed by very low level of EdU incorporation after a 3-hour pulse of EdU among the non-adherent cells (less than 2% EdU-positive cells at day 3 after the end of fIR), suggesting very low replicative activity (Figure 4). However, considering the non-adherent irradiated cells restarted proliferation shortly after re-adhesion, the non-adherent fIR survivors represented a pool of transiently non-proliferating cells capable of proliferation after reestablishment of the adherent phenotype.

**Inhibition of Erk1/2 suppresses Snail expression and impairs survival of non-adherent cells.** Snail levels are regulated by the Erk1/2 and PI3K/Akt pathways.[27,28] Indeed, both Akt and Erk1/2 activities were highest between the second and third dose of IR (Figure 5a), coinciding with the highest levels of Snail and preceding the loss of cell adhesion. The ensuing loss of cell adhesion correlated with loss of active Akt and partial loss of Erk1/2 activity (Figure 5b). Consistent with a previous report,[27] inhibition of Erk1/2 with the MEK-Erk inhibitor U0126 (ERKi) suppressed the levels of Snail in the adherent fraction (Figure 5c), while treatment of the non-adherent cells with the ERKi resulted in anoikis, and also prevented cell detachment after a single dose of IR (Figure 5d; Supplementary Figure 5a). Consistently, activation of the Erk1/2 pathway by a mixture of FGF and EGF (Supplementary Figure 5b) resulted in increased total numbers of detached cells (the sum of live and dead cells; Supplementary Figure 5c) and more surviving non-adherent cells among both the control and irradiated DU145 cells (Figure 5e). Excluding potential nonspecific effects of the ERKi, siRNA-mediated knockdown of Erk1 and/or Erk2 (Supplementary Figure 5e) impaired the loss of adhesion (Supplementary Figure 5d) and survival (Figure 5f) among non-adherent control as well as irradiated DU145 cells, thereby supporting the role of Erk1/2 signaling in the emerging anoikis-resistant cell survival after irradiation.

Anoikis is Bim-mediated apoptosis,[29] and the level (and activity) of proapoptotic Bim is regulated by Erk1/2.[29–31] Consistent with resistance to anoikis, the level of Bim in irradiated non-adherent DU145 cells was substantially lower than in the irradiated adherent cells (Supplementary Figure 5f). Inhibition of Erk1/2 led to increased levels of Bim both in control and irradiated cells (Figure 5g). Furthermore, activation of Erk1/2 by PMA had the opposite effect (not shown) implicating Erk-dependent ubiquitylation and degradation of Bim.[32] In contrast, the anti-apoptotic factor Bcl-XL was increased in non-adherent cells after irradiation (Supplementary Figure 5f). Inhibition of Erk1/2 led to a decrease of Bcl-XL (Figure 5g) indicating Bcl-XL is controlled by Erk1/2. Ectopic expression of Bcl-XL in DU145 cells (Figure 5h) resulted in significantly increased survival of the non-adherent cells after fIR, whereas inhibition of Erk1/2 suppressed survival among the Bcl-XL-overexpressing cells (Figure 5i), supporting the role of the Erk1/2-Bcl-XL axis in radiation-induced anoikis resistance.

In conclusion, loss of cell adhesion, Snail expression, levels of the apoptotic modulators Bim and Bcl-XL, as well as anoikis resistance of the radiation-surviving non-adherent cells is controlled by Erk1/2 activity.

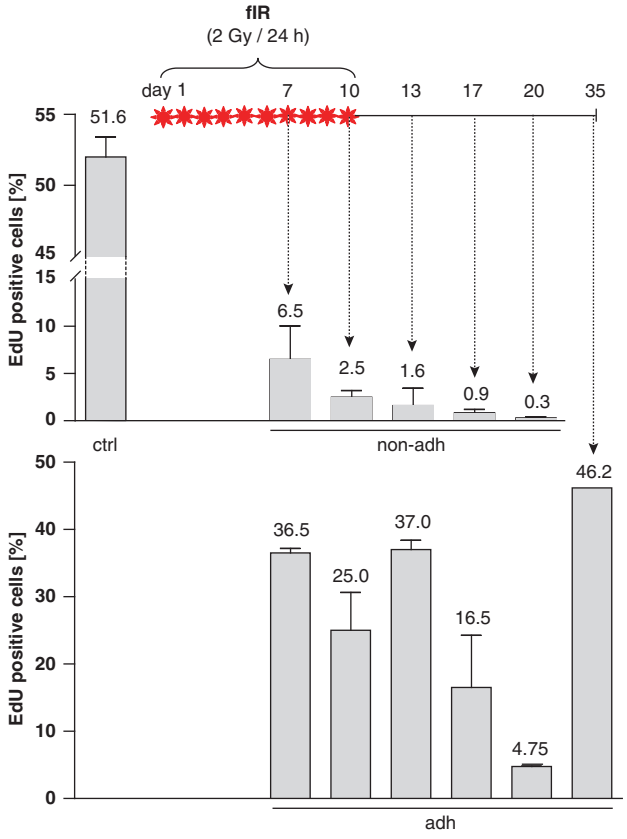


**Figure 4** Proliferation of fIR-surviving adherent and non-adherent DU145 cells. Flow cytometry analysis of EdU incorporation using Click-iT EdU proliferation assay in irradiated (10 × 2 Gy) non-adherent and adherent DU145 cells, during and after fIR, expressed as EdU-positive cells (from viable fraction in percentage, numbers above bars) of total cells analyzed. Non-irradiated adherent cells were used as a control (ctrl). Data (except adherent cells collected at day 35) represent means ± S.D. from two independent experiments

**Simultaneous inhibition of Erk1/2 and Akt pathways has an additive radiosensitizing effect.** Enhanced Erk and PI3K–Akt signaling contribute to chemo- and radioresistance of CaP.[5,8,33] Therefore, we exposed DU145 cells to 10 daily fractions of 2 Gy in the presence or absence of chemical inhibitors of Erk1/2, Akt or their combination (Supplementary Figure 6b) and followed survival and proliferation of non-adherent and adherent cells, respectively. Inhibition of Erk1/2 alone eliminated any live non-adherent cells, while Akt inhibition alone impacted survival of the non-adherent cells only modestly (Figure 6a) correlating with low Akt activity in this fraction (Figure 5a). The combined inhibitors suppressed survival of IR-exposed non-adherent cells and, importantly, showed a greater anti-proliferative effect than treatment with either inhibitor alone on the IR-resistant adherent CaP cells (Figures 6a and c; Supplementary Figure 6a). Furthermore, the observed anti-proliferative effect of the combined inhibitors was greater among the irradiated, compared with non-irradiated CaP cells (Figures 6b and c). In contrast to CaP cells, normal human diploid BJ fibroblasts treated with the radiosensitizing

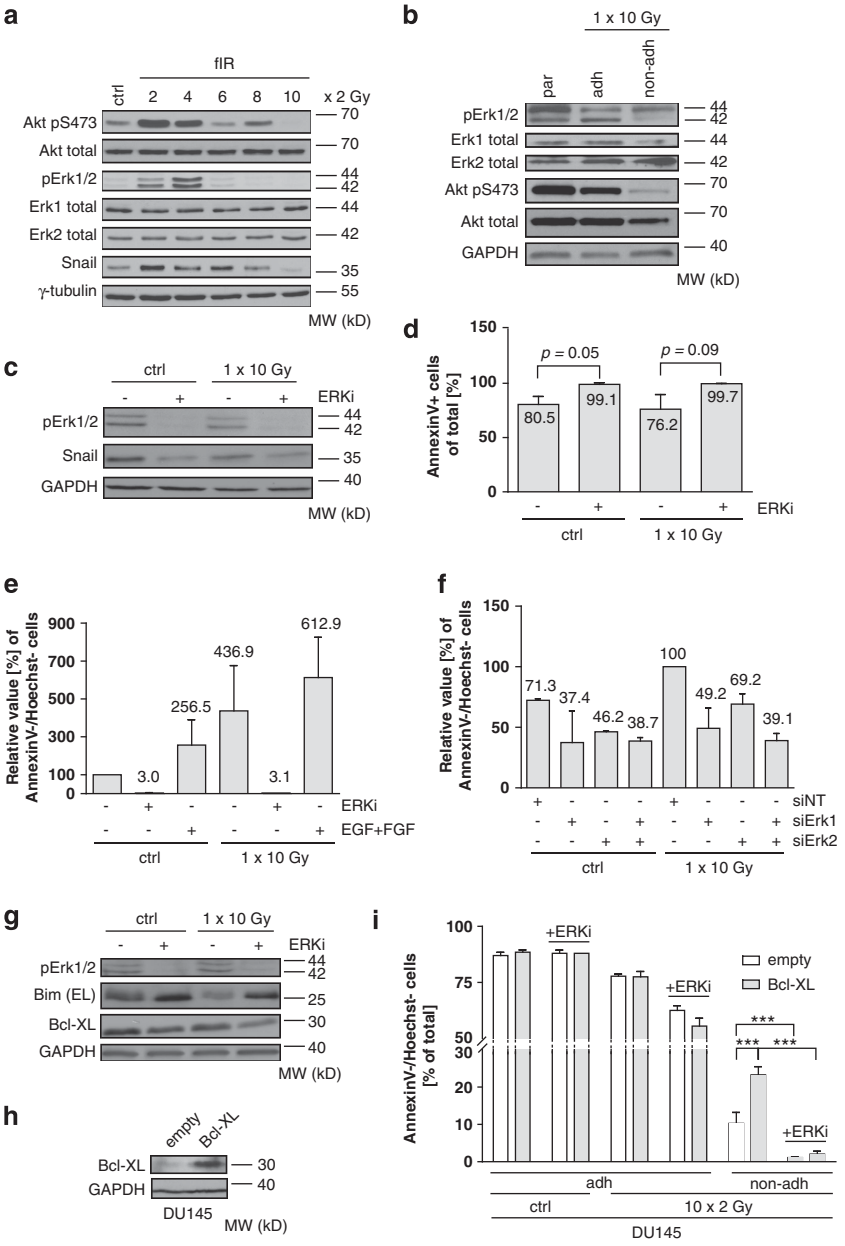


**Figure 5** Effect of Erk1/2 inhibition on viability of fIR-surviving non-adherent DU145 cells. (**a**) Immunobloting detection of total Akt, phosphoserine 473 of Akt, total Erk1 and Erk2, phosphothreonine 204/phosphotyrosine 204 of Erk (pErk1/2) and Snail in control and irradiated ($2-10\times2$ Gy) DU145 cells. Gamma-tubulin was used as a loading control. (**b**) Immunoblotting detection of total Erk1 and Erk2, phosphothreonine 204/phosphotyrosine 204 of Erk1/2 (pErk1/2), total Akt and phosphoserine 473 of Akt in control (parental) and irradiated ($1\times10$ Gy) adherent and non-adherent DU145 cells. GAPDH was used as a loading control. (**c**) Immunoblotting estimation of inhibition of Erk1/2 activity by Erk inhibitor U0126 (ERKi) detected as phosphothreonine 204/phosphotyrosine 204 of Erk (pErk1/2) and its effect on Snail expression in control and irradiated ($1\times10$ Gy) DU145 cells. GAPDH was used as a loading control. (**d**) Effect of Erk1/2 inhibition by ERKi on cell survival in control or irradiated ($1\times10$ Gy) non-adherent DU145 cells assessed by flow cytometry 48 hours after IR. Bars represent relative amount (in percentage, numbers above bars) of apoptotic cells (AnnexinV$^+$/Hoechst$^+$ plus AnnexinV$^+$/Hoechst$^-$) in total non-adherent fraction. (**e**) Effect of Erk1/2 activation (mixture of 10 ng/ml EGF and 50 ng/ml FGF) or chemical inhibition (ERKi) on cell survival assessed by flow cytometry in control or irradiated ($1\times10$ Gy) non-adherent DU145 cells analyzed 48 h after IR by flow cytometry. Bars represent relative amount (in percentage, numbers above bars) of viable AnnexinV$^-$/Hoechst$^-$ cells in non-adherent fraction. Non-treated cells were set as 100%. (**f**) Effect of siRNA-mediated knockdown of Erk1 (siErk1) and Erk2 (siErk2) on cell survival in control or irradiated ($1\times10$ Gy) non-adherent DU145 cells analyzed 48 h after IR and 72 h after transfection by flow cytometry. Non-targeting siRNA (siNT) was used as a negative control. The bars represent relative amount (in percentage, numbers above bars) of viable AnnexinV$^-$/Hoechst$^-$ cells in non-adherent fraction. Irradiated cells transfected with control siRNA (siNT) were set as 100%. (**g**) Effect of Erk1/2 inhibition (ERKi) on Bim (EL) and Bcl-XL levels in control or irradiated ($1\times10$ Gy) DU145 cells assessed by immunoblotting. GAPDH was used as a loading control. (**h**) Immunobloting detection of Bcl-XL in DU145 stable cell lines generated by infection with lentiviruses possesing pCDH-CMV-MCS-EFI-Neo-empty (empty) or pCDH-CMV-MCS-EFI-Neo-Bcl-XL (Bcl-XL) vector. GAPDH was used as a loading control. (**i**) Effect of ERKi (10 $\mu$M for 16 h, added after last dose of fIR) on cell survival in control or irradiated ($10\times2$ Gy) adherent and non-adherent stable DU145 cells constitutively expressing Bcl-XL (Bcl-XL) analyzed by flow cytometry. The bars represent relative amount (in percentage) of viable (AnnexinV$^-$/Hoechst$^-$) cells. Stable DU145 cell line transduced with pCDH-CMV-MCS-EFI-Neo-empty vector (empty) was used as a control. Data in **d–f** represent means $\pm$S.D. from two independent experiments. Data in **i** represent means $\pm$S.D from four (w/o ERKi) or two ($+$ERKi) independent experiments performed in duplicates. ***$P<0.001$

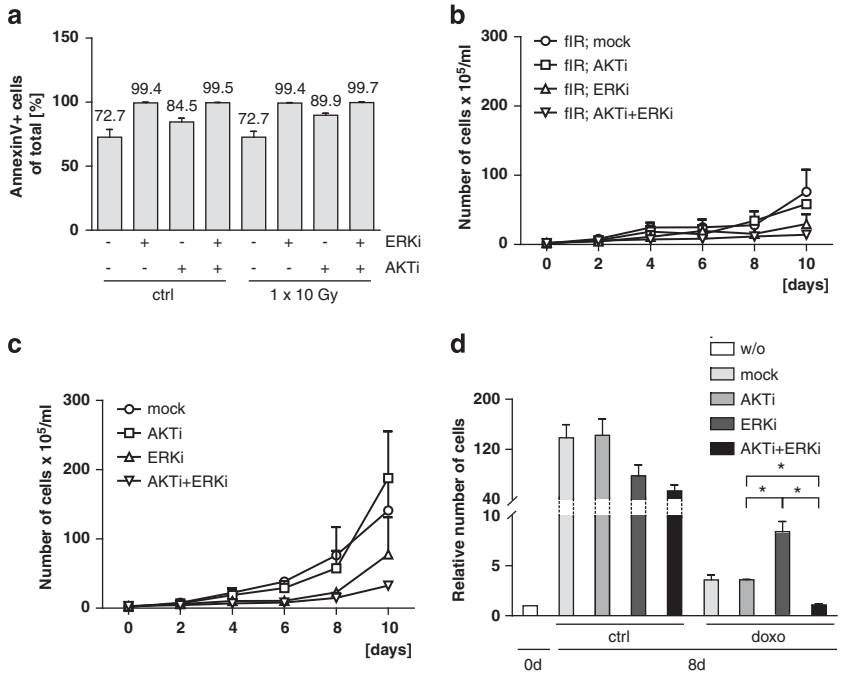


**Figure 6** Differential sensitivity of fIR-surviving adherent and non-adherent DU145 cells to inhibitors of Erk and Akt signaling. (**a**) Effect of Erk1/2 inhibition (ERKi) and/or Akt inhibition (AKTi) on cell survival in control or irradiated ($1 \times 10$ Gy) non-adherent DU145 cells analyzed by flow cytometry 48 h after IR. The bars represent relative amount (in percentage, numbers above bars) of apoptotic cells (AnnexinV$^-$/Hoechst$^-$ plus AnnexinV$^+$/Hoechst$^-$) in total non-adherent fraction. (**b**) Effect of Erk1/2 inhibition (ERKi) and/or Akt inhibition (AKTi) on proliferation of irradiated ($10 \times 2$ Gy) DU145 cells. Trypan blue-negative cells were counted at time points as indicated. (**c**) Effect of Erk1/2 inhibition (ERKi) and/or Akt inhibition (AKTi) on proliferation of control non-irradiated DU145 cells. Trypan blue-negative cells were counted at time points as indicated. (**d**) Effect of Erk1/2 inhibition (ERKi) and/or Akt inhibition (AKTi) on proliferation of control or doxorubicine-treated (0.75 $\mu$M) DU145 cells. Relative numbers of cells were assessed at day 0 (w/o; without any additives) and day 8. Data in all bars are normalized to control cells (i.e. to doxorubicin-untreated cells) at day 8. Data in **a**–**d** represent mean values $\pm$ S.D. from two independent experiments. *$P < 0.05$. In **b**–**d,** control cells were treated with DMSO diluent (mock)

concentrations of both inhibitors only slowed down proliferation without cytotoxic effects (Supplementary Figure 6c).

Complementary to the radiosensitization experiments, the combined inhibition of Akt and Erk1/2 completely suppressed also CaP chemoresistance, otherwise manifested as outgrowth of senescence-resistant colonies of DU145 cells exposed to a subapoptotic, senescence-inducing treatment with doxorubicin (Figure 6d).

Overall, the combined inhibition of Akt and Erk1/2 impaired survival of the anoikis-resistant non-adherent CaP cells and prevented escape from senescence in the adherent CaP population both after irradiation and doxorubicin treatment.

**Acquired radioresistance of CaP cells after fractioned irradiation.** Conceptually and therapeutically relevant issue is whether the adherent or the non-adherent cells feature 'radioresistance memory', that is, enhanced survival on later round(s) of irradiation. We noted that the phenotypic switch (the cycle of irradiation-induced loss of adhesion and subsequent re-adhesion) was repeatable at least three times (not shown) indicating stress-induced reversible phenotypic plasticity. However, several population doublings of the re-adherent cells were necessary to revert the mesenchymal phenotype back to the epithelial one (see Supplementary Figure 7a. for changes in E-cadherin and vimentin after re-adhesion). To assess whether the fIR survivors are more radioresistant than the parental cells, we exposed DU145 cells that survived the 35 doses of 2 Gy as either adherent (adherent survivors) or non-adherent fraction after its re-adhesion (re-adherent survivors) to a single dose of 10 or 40 Gy. Although the overall survival of both adherent and re-adherent survivors did not differ markedly from the parental cells (Figure 7a) and the colony-forming ability was increased only for the adherent survivors compared to the parental cells (Figure 7b; consistent with Skvortsova *et al.*[5]), the colonies of the re-adherent survivors (although equally numerous as from the parental cells) featured fewer colonies composed of senescent-like cells (Figure 7b). Importantly, the anoikis-resistant survival of the re-adherent survivors was enhanced compared with both the parental cells and adherent survivors (Figure 7c).

Altogether, the observed radiation-induced phenotypes likely reflect contributions from both adaptive (partly transient) responses due to plasticity of the metastatic CaP cell populations, and more durable (heritable), selection-acquired resistance to radiation-evoked cellular senescence or anoikis (Supplementary Figure 7b).

## Discussion

As metastatic CaP is essentially incurable due to radioresistance and chemoresistance, we performed this study to better understand the underlying mechanisms to overcome the resistance. Our analyses of human metastatic CaP cell lines DU145, PC-3, LNCaP and 22RV1 during a fractionated ionizing irradiation regimen that mimicked the schedule used

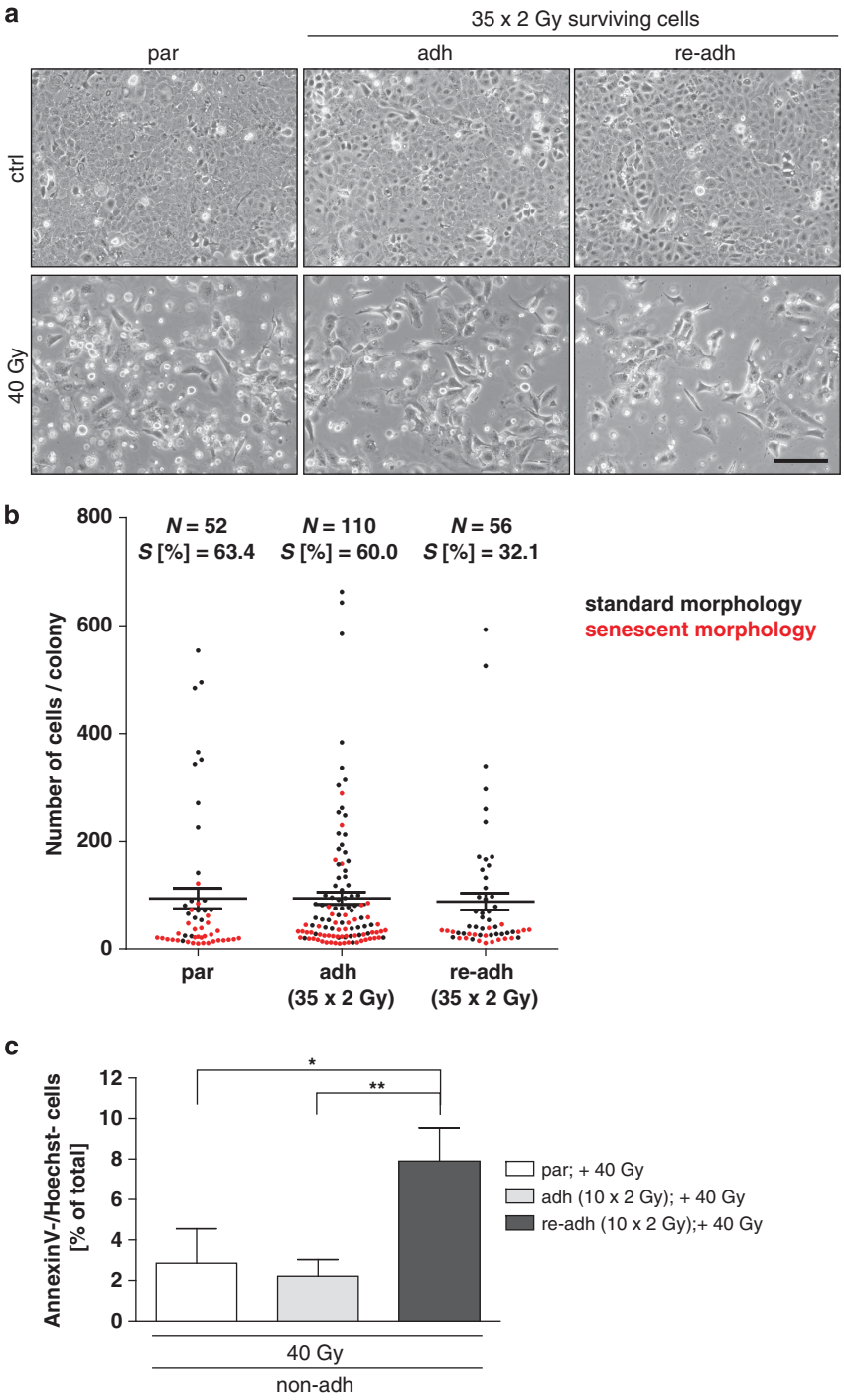


**Figure 7** Evaluation of radioresistance of fIR-surviving cells. (**a**) Phase contrast microscopic images of parental (par) and irradiated (35 × 2 Gy) adherent (adh) and re-adherent (readh) DU145 survivors 3 days after a single dose (40 Gy) or without re-irradiation (ctrl). Scale bar, 100 $\mu$m. (**b**) Clonogenic cell survival assay. Parental or irradiated (35 × 2 Gy) adherent and re-adherent DU145 survivors were counted and $1 \times 10^3$ cells seeded into 6-well plates in triplicates. Number of cells from all colonies (>10 cells) formed at day 13 following re-irradiation (10 Gy) were counted and plotted. *N* = number of total colonies formed. *S* = number of senescent colonies formed/number of total colonies formed × 100. Each dot in the plot represents one colony characterized by number of cells and presence (red dot) or absence (black dot) of senescence according to cell morphology. (**c**) Anoikis-resistant survival of parental (par) and previously irradiated (10 × 2 Gy) adherent (adh) and re-adherent (readh) DU145 survivors after re-irradiation (40 Gy) assessed by flow cytometry 72 h after IR. Bars represent relative amount (in percentage) of viable cells (AnnexinV$^-$/Hoechst$^-$) in total non-adherent fraction. Data represent mean values ± S.D. from three independent experiments performed in duplicates. *$P<0.05$; **$P<0.01$

in clinical radiotherapy revealed three phenotypically distinct radiation-surviving cell populations: (1) adherent cells with senescent/EMT features capable of regrowth after termination of irradiation; (2) non-adherent anoikis-resistant and non-proliferating cells with stem cell traits capable of long-term survival, competent to restore adherent growth and

proliferation; (3) re-adherent cells originating from the non-adherent pool, with epithelial features and tumorigenic potential.

One of our key novel results was the role of the Snail-ERK pathway in the EMT phenotype, loss of adherence, anoikis and radioresistance. Our findings of decreased E-cadherin in the radiation-surviving non-adherent cells, accompanied by enhanced levels of the E-cadherin-repressive EMT-inducer Snail,[21,22] support the role of E-cadherin-mediated intercellular contacts in the maintenance of the epithelial phenotype,[34] the loss of E-cadherin *per se* as an EMT inducer,[35] and association of EMT with radio- and chemoresistance.[36–39] Using MEKi and knockdown of Erk1/2 and Snail, we showed that the loss of adhesion after IR required Erk1/2-mediated expression of Snail. Consistent changes in gene expression, including Snail upregulation, and genes of the Notch pathway, have been independently validated by a comprehensive gene expression profiling analysis (not shown). The radiation-induced phenotypic heterogeneity, we report, might reflect transient cellular plasticity as well as stress-evoked responses of preexistent subsets cells seen in the parental DU145 and PC-3 cell populations.[40–52]

Ionizing radiation can promote traits of EMT in normal human mammary epithelium,[41] lung carcinoma[42,43] and colorectal cancer cells.[44] Furthermore, besides their role in E-cadherin repression,[45,46] Slug and Snail have been implicated in radioresistance-associated EMT.[47,48] Snail enhances resistance to apoptosis by activating the PI3K/Akt and Erk1/2 pathways,[28] consistent with our data showing increased radiosensitivity after inhibition of PI3K/Atk and Erk1/2 and downregulation of Snail. Notably, Snail is a substrate of the major radiation-induced kinase ATM, and this phosphorylation is involved in radiosensitivity.[49]

Another intriguing aspect of our results is the link between EMT and stem-like cell traits. Epithelial cancer cells undergoing EMT exhibit also features of stemness,[50,51] and Snail induces both EMT and stem cell-like features in squamous cell carcinoma.[52] We show that besides elevated Snail, radiation-surviving non-adherent CaP cells featured enhanced expression of stem cell-associated genes CD133,[53] Oct-4, Sox2 and Nanog, the latter three capable of reprogramming various differentiated cells toward stemness.[54,55] Besides these stem cell markers, radiation-surviving non-adherent CaP cells showed increased activity of Notch signaling, a characteristics of diverse progenitor cells.[23,24] In breast cancer, IR induces Notch[56] and stem-like phenotype, including Notch-dependent upregulation of Oct-4.[57] Notch signaling can also activate EMT.[58] Together with other evidence,[59–61] our data support an emerging concept that IR promotes a phenotypic switch towards EMT and stem-like traits in epithelial tumors, also consistent with the intriguing yet mechanistically unclear resistance of cancer stem-like cells to genotoxic treatments.

In contrast to reported sphere-forming growth of irradiated lung cancer cells[43] and IR-induced cell cycle entry of breast CSC,[61] the radiation-induced non-adherent CaP cells were proliferatively dormant even in conditions permissive for self-renewal of CSCs (not shown). This supports the notion that EMT-inducing factors reduce cell proliferation,[28,62] and circulating tumor cells (CTCs) with enhanced Twist1 need to downregulate Twist1 before regaining the ability to proliferate and form macrometastases.[63] We propose that during development of radioresistance in CaP, and possibly other types of cancer, reversion of EMT is necessary for initiation of cell proliferation. This is also supported by our data that the re-adherent CaP cells exhibited an epithelial phenotype and reduced motility (not shown) indicating reversion of stem-like/mesenchymal traits during re-adhesion. The phenotypic changes including cell contact and ECM-adhesive molecules observed in the non-adherent irradiated population reverted after cell re-adhesion, coinciding with regained proliferation and tumorigenicity.

There is evidence that EMT/MET is linked with metastatic spread, as the number of CTCs with epithelial or mesenchymal phenotype captured from patients treated for metastatic breast cancer correlated with type of therapy applied.[64] Whereas positive therapeutic responses were accompanied by fewer CTCs and increased epithelial phenotype, patients with progressive disease unresponsive to chemotherapy possessed higher numbers of predominantly mesenchymal CTCs in post-treatment samples. The simultaneous inhibition of Erk and PI3K–Akt signaling we report here resulted in both suppression of resistance to anoikis and prevention of regrowth of adherent CaP in response to IR and doxorubicin, indicating potential use of this drug combination for radio and chemosensitization with abrogation of radio-/chemotherapy-induced tumor cell heterogeneity. Mechanistically, we speculate that DNA damage signaling from therapy-induced recurrent and/or persistent DNA lesions (e.g. from senescent cells[65]) may promote the observed phenotypic switch via the ATM-induced cytokine network[66] including TGF$\beta$ family members that can shape the phenotype of treated cancer cells toward EMT and stem cell enrichment in a paracrine manner. Finally, we suggest that such treatment resistance (see Supplementary Figure 7) could be overcome, and that the dependency on signaling cascades we report here reveal vulnerabilities potentially exploitable in cancer treatment.

## Materials and Methods

**Chemicals and antibodies.** MEK-Erk inhibitor U0126 (ERKi; 10 $\mu$M), Akt1/2 kinase inhibitor (AKTi; 1 $\mu$M; Cat. No. A6730) doxycycline hydrochloride (dox) and doxorubicin hydrochloride (doxo), were purchased from Sigma (St Louis, MO, USA). Epidermal growth factor (EGF) and fibroblast growth factor (FGF) recombinant proteins were obtained from Peprotech (Rocky Hill, NJ, USA).

The following antibodies were used for immunoblotting: mouse monoclonal antibody against Erk1 (ECM Bioscience, Versailles, KY, USA), goat polyclonal antibody against DLL1 and mouse monoclonal antibody against Twist1 from Santa Cruz Biotechnology (Dallas, TX, USA), rabbit monoclonal antibodies against Snail (SNAI1), Akt, Nanog XP, Oct-4A, Bcl-XL and phosphoserine 473 of Akt, rabbit polyclonal antibodies against Chk2, p53 and Bim and mouse monoclonal antibodies against $p21^{waf/cip}$, phosphoserine 15 of p53 and phosphothreonine 68 of Chk2, all from Cell Signaling Technology (Danvers, MA, USA). Mouse monoclonal antibody against GAPDH was purchased from GeneTEX (Irvine, CA, USA), mouse monoclonal antibody against phosphoserine 139 of histone H2AX from Millipore (Billerica, MA, USA), mouse monoclonal antibody against E-cadherin from BD Biosciences (San Jose, CA, USA) and rabbit polyclonal antibody against phosphothreonine 202/phosphotyrosine 204 of Erk1/2 from Promega (San Luis Obispo, CA, USA). Mouse monoclonal antibody against $\gamma$-tubulin was provided by Pavel Draber (Institute of Molecular Genetics, Prague, Czech Republic). Mouse monoclonal antibody against Erk2 (B3B9) was prepared by Mike Weber and provided by Tomas Vomastek (Institute of Microbiology, Prague, Czech Republic).

The following antibodies were used for indirect immunofluorescence: mouse monoclonal antibody PG-M3 against PML, rabbit polyclonal antibody against 53BP1

both from Santa Cruz Biotechnology, mouse monoclonal antibody against phosphoserine 139 of histone H2AX (Millipore), mouse monoclonal antibody against E-cadherin from BD Biosciences, rabbit polyclonal antibodies against vimentin from Cell Signaling Technology. Secondary antibodies anti-mouse IgG conjugated with Cy3 from Jackson Immunoresearch Laboratories (West Grove, PA, USA), anti-rabbit IgG antibody Alexa 568 and anti-mouse IgG antibody Alexa 488 were from Invitrogen (Carlsbad, CA, USA).

**Cell cultures.** Human prostatic carcinoma cell lines DU145, PC-3, LNCaP, 22RV1, human breast carcinoma cell line MCF-7, human embryonic kidney cells HEK293T stably expressing the SV40 large T antigen and human fibroblast cells BJ were obtained from American Type Culture Collection (ATCC, Manassas, VA, USA). DU145, PC-3, MCF-7 and HEK293T cells were cultivated in DMEM (glucose 4.5 g/l), LNCaP and 22RV1 in RPMI-1640 (both media from Biochrom, Cambridge, UK) and BJ in DMEM (glucose 1 g/l; Invitrogen) supplemented with 10% fetal bovine serum (PAA, Pasching, Austria), 100 U/ml penicillin and 100 $\mu$g/ml streptomycin sulfate (Sigma). Cells were kept at 37 °C under 5% $CO_2$ atmosphere and 95% humidity.

Cells were irradiated with orthovoltage X-ray instrument T-200 (Wolf-Medizintechnik GmbH, St. Gangloff, Germany) using 0.5 Gy/min dose rate and thorium filter daily with 10 or 35 doses 2 Gy (fIR) or with single dose 10 Gy. Non-adherent cells generated during fIR were collected both during fIR ($35 \times 2$ Gy) or 24 h after last dose (10 or $35 \times 2$ Gy). There was no analytical difference between these two modes of cell collection. However, to avoid possible contamination of non-adherent fraction by mitotic cells of adherent fraction ($10 \times 2$ Gy fIR), non-adherent cells were transferred through another cultivation flask to enable attachment of mitotic cell contaminants (6–8 h), then moved to a new flask and daily carefully checked for 'prematurely' attached cells. Using such procedure, potential contamination was practically eliminated.

To obtain re-adherent colonies from non-adherent cells, irradiated non-adherent prostate cancer cells were separated from adherent fraction as stated above and observed for initiation of adherent growth. After re-adherence, cells were cultivated as described above. As non-adherent control, DU145 cells were kept in confluence for 3–5 days and then non-adherent cells were collected.

Images of live cells were captured by inverted tissue culture microscope Nicon Eclipse TE300 (Nicon, Tokyo, Japan) equipped with Leica DFC490 camera and LAS AF software (Leica Microsystems, Germany).

**Lentiviral constructs and transduction.** Lentiviral vector pCDH-EFI-Neo-Bcl-XL, constitutively expressing Bcl-XL, was generated by subcloning the *EcoR*I fragment from pSFFV-Neo-Bcl-XL (#8749 Addgene, Cambridge, MA, USA) into pCDH-CMV-MCS-EFI-Neo (Systems Biosciences, CA, USA). pLKO-Tet-On-shRNA-Snail was generated by ligation of the double stranded oligo 5′-CCGGCCA GGCTCGAAAGGCCTTCAACTCGAGTTGAAGGCCTTTCGAGCCTGGTTTTT-3′ between the *Age*I and *EcoR*I sites in the pLKO-Tet-On vector as described.[67] To produce DU145-empty and DU145-Bcl-XL cell lines, DU145 cells were transduced either with pCDH-CMV-MCS-EFI-Neo or with pCDH-EFI-Neo-Bcl-XL viral particles.[68] For inducible RNAi of Snail, DU145 were transduced with pLKO-Tet-On-shRNA-Snail particles. To obtain stabile expression, 72 h post transduction cells were plated into media containing G418 (800 $\mu$g/ml) or puromycin (2 $\mu$g/ml) and selected for further 10 or 3 days. Snail shRNA expression was induced with 0.7 $\mu$g/ml doxycycline (dox), supplied every 48 h to the cultivation media. Non-transduced DU145 cells (wt) treated with corresponding amounts of dox were used as a control.

**Magnetic-activated cell sorting.** AnnexinV-negative fraction of irradiated non-adherent DU145, PC-3 and MCF-7 cells was obtained by incubation with Dead Cell Removal MicroBeads (Dead Cell Removal Kit, Miltenyi Biotec, Germany) for 15 min and separation in magnetic field of AutoMACS Pro magnetic separator (Miltenyi Biotec). The separated cells were harvested for immunoblotting or real time qRT–PCR analysis.

**Fluorescence-activated cell sorting**

*AnnexinV-FITC/Hoechst 33258 staining and analysis*: Cell survival of non-adherent DU145, PC-3, LNCaP, MCF-7 and 22RV1 cells after single dose or multiple doses of IR was assessed by staining with 1-5 $\mu$g/ml Hoechst 33258 (Invitrogen) in combination with AnnexinV-FITC (AnnexinV: FITC Apoptosis Detection Kit, BD Biosciences) according to manufacturer's protocol. Cells were collected in PBS (300 *g* at 4 °C for 10 min), stained in AnnexinV binding buffer (BD Biosciences) for 15 min at RT and then analyzed using the LSRII flow cytometer (BD Biosciences). Cells from following quadrants were analyzed: viable AnnexinV-FITC$^-$/Hoechst 33258$^-$ cells (A-/H-), early apoptotic AnnexinV-FITC$^+$/Hoechst 33258$^-$ cells (A+/H−) and late apoptotic AnnexinV$^+$/Hoechst 33258$^+$ cells (A+/H+). To assess radiation-induced loss of adhesion, non-adherent control and irradiated cells ($1 \times 10$ Gy) were washed twice with PBS and collected (300 *g* at 4 °C for 5 min) in 300 $\mu$l of AnnexinV binding buffer (BD Biosciences). Defined volume of cell suspension was analyzed to assess the total number of cells. The precision of volume intake by high throughput sampler (HTS) unit of LSRII flow cytometer was checked using fluorescent AlignFlo Flow Cytometry Alignment Beads, 2.5 $\mu$m (Invitrogen) excitable at 488 nm. Volume intake error was estimated as ±5.13%.

*eFluor670 staining and analysis*: Proliferation of irradiated adherent DU145 cells was estimated with Cell Proliferation Dye eFluor670 (eBioscience, San Diego, CA, USA), which binds unspecifically membrane proteins and is distributed equally between daughter cells during division. Dye fluorescence intensity in APC channel was measured by LSRII flow cytometer. Control and irradiated adherent cells were detached by Versene after 10th dose of irradiation (Gibco, Carlsbad, CA, USA), stained with eFluor670 and either immediately analyzed by FACS or further irradiated (five daily doses of 2 Gy) and analyzed after 11, 13 and 15 dose. To assess the proliferation of irradiated ($10 \times 2$ Gy) non-adherent cells, cells were collected in PBS after last dose of irradiation (300 *g* at 4 °C for 10 min), stained with eFluor670 and further cultivated in new Petri dish for 28 days. At 28th day after staining, non-adherent and newly established re-adherent cells were analyzed by FACS as described above.

*Click-iT EdU proliferation assay and analysis*: Proliferation of non-adherent DU145 cells was assessed during fIR (after $7 \times 2$ Gy and $10 \times 2$ Gy) and at several post-fIR time points (3, 7 and 10 days after fIR). First, cells were pulse-labeled with 10 $\mu$M EdU for 3 h, washed with PBS and stained with fixable viability fluorescent dye eFluor780 (eBioscience) according to manufacturer's protocol. Second, cells were fixed (4% formaldehyde, 15 min at RT), washed twice with PBS and stored at 4 °C. In the post-fIR time points, medium with non-adherent cells was transferred to a new Petri dish 1 day before EdU pulse to prevent mitotic cell contamination from adherent layer. DNA replication was measured using the Click-iT EdU Alexa Fluor 488 Imaging Kit (Invitrogen), customized for flow cytometry. EdU was detected after permeabilization (0.2% Triton X-100, 5 min at RT) by staining cells with Click-iT chemistry for 25 min at RT (azide labeled by Alexa Fluor 488, $CuSO_4$ and EdU buffer additive in 100 mM Tris, pH 8.5). Samples were analyzed using LSRII flow cytometer with 488 nm excitation. Background values were estimated by measuring non-EdU labeled, but Click-iT chemistry stained cells.

**Indirect immunofluorescence.** Cells grown on glass coverslips were fixed by methanol:acetone (1:1) at 4 °C or by 4% formaldehyde at RT and permeabilized by 0.2% Triton X-100 15 min at RT. After washing with PBS, cells were incubated in 10% FBS diluted in PBS to block unspecific signal. Cells were subsequently incubated with diluted primary antibodies for 1 h at RT and then extensively washed with PBS. The incubation with secondary antibodies was performed for 1 h at RT. Nuclei were counterstained with 4',6-diamidino-2-phenylindole staining (DAPI; Sigma) followed by mounting in Mowiol (Sigma) or Vectashield HardSet Mounting Medium containing DAPI (Vector Laboratories, Burlingame, CA, USA). Images were captured by fluorescent microscope Leica CTR6000 (Leica Microsystems) equipped with monochrome digital camera DFC350 FX and Leica LAS AF Lite software or Zeiss Axio Imager.A2 equipped with Zeiss AxioCam HR camera and Metamorph software.

**SDS–PAGE and immunoblotting.** Cells were washed with PBS, harvested into Laemmli SDS sample lysis buffer (2% SDS, 50 mM Tris-HCl, 10% glycerol in double-distilled $H_2O$) and sufficiently sonicated ($3 \times 15$ seconds at 4 micron amplitude with 15 sec cooling intervals) on Soniprep 150 (MSE, London, UK). Concentration of proteins was estimated by the BCA method (Pierce Biotechnology, IL, Rockford, USA). A quantity of 100 mM DTT and 0.01% bromphenol blue was added to lysates before separation by SDS–PAGE (10 and 12% gels were used). The same protein amount (25 or 30 $\mu$g) was loaded into each well. Proteins were electrotransferred onto a nitrocellulose membrane using wet transfer and detected by specific antibodies combined with horseradish peroxidase-conjugated secondary antibodies (goat anti-rabbit, goat anti-mouse,

Bio-Rad, Hercules, CA, USA). Peroxidase activity was detected by ECL (Pierce Biotechnology) or SuperSignal West Femto Substrate (Thermo Fisher Scientific, Waltham, MA, USA). GAPDH or $\gamma$-tubulin was used as a marker of equal loading.

**Quantitative real time PCR.** Total RNA samples were isolated using RNeasy Mini Kit (Qiagen Sciences, Germantown, MD, USA) as described.[69] Briefly, first strand cDNA was synthesized from 200 ng of total RNA with random hexamer primers using High-Capacity cDNA Reverse Transcription kit (Applied Biosystems, Foster city, CA, USA).

qRT–PCR was performed in ABI Prism 7300 (Applied Biosystems) using SYBR Select Master Mix containing SYBR GreenE dye (Applied Biosystems). The relative quantity of cDNA was estimated by $\Delta\Delta$CT method and data were normalized to RPL37a, GAPDH or $\beta$-actin. Following primers were purchased from East Port (Prague, Czech Republic): Snail (SNAI1): 5′-TGC CCT CAA GAT GCA CAT CCG A-3′, 5′-GGG ACA GGA GAA GGG CTT CTC-3′; Slug (SNAI2): 5′-ATC TGC GGC AAG GCG TTT TCC A-3′; 5′-GAG CCC TCA GAT TTG ACC TGT C-3′; Twist1: 5′-GCC AGG TAC ATC GAC TTC CTC T-3′, 5′-TCC ATC CTC CAG ACC GAG AAG G-3′; Zeb2: 5′-AAT GCA CAG AGT GTG GCA AGG C-3′, 5′-CTG CTGA TGT GCG AAC TGT AGG-3′; CDH1: 5′-TGA AGG TGA CAG AGC CTC TGG AT-3′, 5′-TGA AGG TGA CAG AGC CTC TGG AT-3′; MMP-7: 5′-TCG GAG GAG ATG CTC ACT TCG A-3′, 5′-GGA TCA GAG GAA TGT CCC ATA CC-3′; ITGA2: 5′-TTG CGT GTG GAC ATC AGT CTG G-3′, 5′-GCT GGT ATT TGT CGG ACA TCT AG-3′; LAMA3: 5′-CCG ATA GTA TCC AGG GCT ACA AC-3′, 5′-AAC CAG ATG AGC ATC ACA TTC CTG-3′; LAMC2: 5′-ACC TGT GAA GCG GTG ACA CTG-3′, 5′-TAC AGA GCT GGA AGG CAG GAT G-3′; CD133: 5′-TTT TGC GGT AAA ACT GGC TAA-3′, 5′-CCA TTT TCC ATA TTT TTC ATG G-3′; Sox2: 5′-CAA GAT GCA CAA CTC GGA GA-3′, 5′-GCT TAG CCT CGT CGA TGA AC-3′; Oct-4: 5′-CAG CTT GGG CTC GAG AAG-3′, 5′-CCT CTC GTT GTG CAT AGT CG-3′; Nanog: 5′-CTC CAA CAT CCT GAA CCT CAG C-3′, 5′-CGT CAC ACC ATT GCT ATT CTT CG-3′; DLL1: 5′-TGC CTG GAT GTG ATG AGC AGC A-3′, 5′-ACA GCC TGG ATA GCG GAT ACA C-3′; DLL4: 5′-CTG CGA GAA GAA AGT GGA CAG G-3′, 5′–3′; Jag1: 5′-TGC TAC AAC CGT GCC AGT GAC T-3′, 5′-TCA GGT GTG TCG TTG GAA GCC A-3′; Hes1: 5′-GGA AAT GAC AGT GAA GCA CCT CC-3′, 5′-GAA GCG GGT CAC CTC GTT CAT G-3′; Hey1: 5′-TGT CTG AGC TGA GAA GGC TGG T-3′, 5′-TTC AGG TGA TCC ACG GTC ATC TG-3′ RPL37a: 5′-AGG AAC CAC AGT GCC AGA TCC-3′, 5′–3′; GAPDH: 5′-GTC GGA GTC AAC GGA TTT GG-3′; $\beta$-actin: 5′-CCA ACC GCG AGA AGA TGA-3′, 5′-CCA GAG GCG TAC AGG GAT AG-3′. The data are expressed as the means $\pm$S.D. of a minimum of two independent experiments performed in triplicates. The *P*-values were estimated using two-tailed Student's *t*-test. *P*-values $<0.05$ were considered statistically significant.

**Senescence-associated $\beta$-galactosidase assay.** Staining for SA-$\beta$-Gal activity was performed by Senescence $\beta$-Galactosidase Staining Kit from Cell Signaling Technology according to manufacturer's protocol. Coverslips were mounted in Mowiol containing 4',6-diamidino-2-phenylindole (DAPI; Sigma) and images were captured by fluorescent microscope Leica DM6000 (Leica Microsystems) equipped with color camera DFC490 and Leica LAS AF Lite software.

**BrdU incorporation assay.** Cells cultured on glass coverslips were pulse-labeled with 10 $\mu$M BrdU (Sigma) for 24 h before fixation with 4% formaldehyde for 15 min at RT. After DNA denaturation in 2 M HCl (30 min), cells were washed in PBS, incubated with mouse monoclonal antibody against BrdU (GeneTex). Images of cells with DAPI-counterstained nuclei were captured by fluorescence microscope Axio Imager.A2 (Zeiss, Germany) using Metamorph software (version 6.2r6; Molecular Devices, Sunnyvale, CA, USA).

**siRNA-mediated gene knockdown.** Specific siRNAs were introduced into cells using Lipofectamine RNAiMAX (Invitrogen). All siRNAs were purchased from Applied Biosystems. Non-targeting siRNA (siNT) sequences were used as a negative control siRNA. Sense sequences of used siRNAs are listed below: siErk1: 5′-GGA CCG GAU GUU AAC CUU Utt-3′, siErk2: 5′-CAA CCA UCG AGC AAA UGA tt-3′ siSnail: 5′-GAA UGU CCC UGC UCC ACA Att-3′, siTwist1: 5′-AGA ACA CCU UUA GAA AUA Att-3′.

**Cell proliferation.** DU145 and BJ proliferation curves were estimated by counting trypan blue-negative cells with Countess automated cell counter (Invitrogen) every 2 days during 8–10 day time course. ERKi (10 $\mu$M) and AKTi (1 $\mu$M) were changed with fresh culture medium every 2 days 30–45 min before irradiation. Data represent the means $\pm$S.D. of two independent experiments.

**Clonogenic cell survival assay.** Clonogenic assay of control (parental) and irradiated 'radioresistant' (adherent and re-adherent) DU145 cells were performed as described.[70] Briefly, cells were seeded on 6-well plates in triplicates and subsequently (6 h post seeding) irradiated with 10 or 40 Gy. Cells were fixed with ice-cold 100% methanol (10 min at $-20\,^{\circ}$C) and stained with 0.5% crystal violet in 20% methanol (10 min at RT) at day 13th, and groups in excess of 10 cells were counted as colonies. In some experiments, the size of the colonies above the threshold and presence of senescence-like cells in colonies were examined.

**Estimation of tumorigenicity.** Immunodeficient male SCID mice (6 weeks old) purchased from AnLab, s.r.o. (Prague, Czech Republic) were acclimated for 2 weeks. Experimental protocols were approved by the Institutional Animal Care Committee of the Institute of Molecular Genetics ASCR, Prague. $1\times10^5$ or $1\times10^6$ control (parental) or irradiated ($10\times2$ Gy) re-adherent DU145 cells in 300 $\mu$l of DMEM were injected subcutaneously into the right flank of the mice. Cells were stained with trypan blue and counted for viability using Countess automated cell counter before injection (Invitrogen). Tumor onset and tumor size were measured weekly with the use of calipers and calculated by length $\times$ width. $N=5$. Statistical significance was estimated by Newman–Keuls multiple comparison test.

**Data processing and statistical analysis.** FACS data were analyzed using FlowJo 9.6.4 cytometric analytical software (TreeStar, Stanford University, USA). Graphs were generated using Prism 5 (GraphPad Software, La Jolla, CA, USA). *P*-values were calculated using Student's *t*-test for two samples assuming unequal variances (Microsoft Excel 2010, Microsoft, Redmond, WA, USA).

## Conflict of Interest

The authors declare no conflict of interest.

**Acknowledgements**. This study was supported by Grant Agency of the Czech Republic (Project 13-17658S), Institutional Grant (Project RVO 68378050), DiaNa21 (Smartbrain s.r.o.), the Danish Research Council (DFF-1331-00262B), the Lundbeck Foundation (R93-A8990), the Danish National Research Foundation, the European Commission (Project DDResponse 259893) and the Grant Agency of the Ministry of Health of the Czech Republic (Project NT14461). LK, SH and TI were supported in part by the Faculty of Science, Charles University, Prague. We acknowledge P. Hamerlik for helpful discussions, D. Hladovcova for help with the mouse model, M. Vancurova for technical assistance with cell culture, O. Horvath and Z. Cimburek for their help with flow cytometry and cell sorting, R. Liska and S. Pavelka for help with cell irradiation, L. Andera for providing the anti-Bcl-XL and RPL37a forward and reverse primers for qRT–PCR, J. Švadlenka for providing the pCDH-EFI-Neo-empty and pCDH-EFI-Neo-Bcl-XL lentiviral vectors, T. Vomastek for the anti-Erk2 antibody and P. Draber for the anti-gamma-tubulin antibody.

1. Jemal A, Bray F, Center MM, Ferlay J, Ward E, Forman D. Global cancer statistics. *CA Cancer J Clin* 2011; **61**: 69–90.
2. Heidenreich A, Bellmunt J, Bolla M, Joniau S, Mason M, Matveev V *et al.* EAU guidelines on prostate cancer. Part 1: screening, diagnosis, and treatment of clinically localised disease. *Eur Urol* 2011; **59**: 61–71.
3. Mottet N, Bellmunt J, Bolla M, Joniau S, Mason M, Matveev V *et al.* EAU guidelines on prostate cancer. Part II: treatment of advanced, relapsing, and castration-resistant prostate cancer. *Eur Urol* 2011; **59**: 572–583.
4. Kong Z, Xie D, Boike T, Raghavan P, Burma S, Chen DJ *et al.* Downregulation of human DAB2IP gene expression in prostate cancer cells results in resistance to ionizing radiation. *Cancer Res* 2010; **70**: 2829–2839.
5. Skvortsova I, Skvortsov S, Stasyk T, Raju U, Popper BA, Schiestl B *et al.* Intracellular signaling pathways regulating radioresistance of human prostate carcinoma cells. *Proteomics* 2008; **8**: 4521–4533.
6. Sakai I, Miyake H, Terakawa T, Fujisawa M. Inhibition of tumor growth and sensitization to chemotherapy by RNA interference targeting interleukin-6 in the androgen-independent human prostate cancer PC3 model. *Cancer Sci* 2011; **102**: 769–775.

7. Huang HF, Murphy TF, Shu P, Barton AB, Barton BE. Stable expression of constitutively-activated STAT3 in benign prostatic epithelial cells changes their phenotype to that resembling malignant cells. *Mol Cancer* 2005; **4**: 2.
8. Kajanne R, Miettinen P, Tenhunen M, Leppa S. Transcription factor AP-1 promotes growth and radioresistance in prostate cancer cells. *Int J Oncol* 2009; **35**: 1175–1182.
9. Kim BY, Kim KA, Kwon O, Kim SO, Kim MS, Kim BS *et al.* NF-kappaB inhibition radiosensitizes Ki-Ras-transformed cells to ionizing radiation. *Carcinogenesis* 2005; **26**: 1395–1403.
10. Rojas A, Liu G, Coleman I, Nelson PS, Zhang M, Dash R *et al.* IL-6 promotes prostate tumorigenesis and progression through autocrine cross-activation of IGF-IR. *Oncogene* 2011; **30**: 2345–2355.
11. Mora LB, Buettner R, Seigne J, Diaz J, Ahmad N, Garcia R *et al.* Constitutive activation of Stat3 in human prostate tumors and cell lines: direct inhibition of Stat3 signaling induces apoptosis of prostate cancer cells. *Cancer Res* 2002; **62**: 6659–6666.
12. Sun M, Liu C, Nadiminty N, Lou W, Zhu Y, Yang J *et al.* Inhibition of Stat3 activation by sanguinarine suppresses prostate cancer cell growth and invasion. *Prostate* 2012; **72**: 82–89.
13. Reddy KR, Guan Y, Qin G, Zhou Z, Jing N. Combined treatment targeting HIF-1alpha and Stat3 is a potent strategy for prostate cancer therapy. *Prostate* 2011; **71**: 1796–1809.
14. Gao L, Zhang L, Hu J, Li F, Shao Y, Zhao D *et al.* Down-regulation of signal transducer and activator of transcription 3 expression using vector-based small interfering RNAs suppresses growth of human prostate tumor *in vivo*. *Clin Cancer Res* 2005; **11**: 6333–6341.
15. Ni Z, Lou W, Leman ES, Gao AC. Inhibition of constitutively activated Stat3 signaling pathway suppresses growth of prostate cancer cells. *Cancer Res* 2000; **60**: 1225–1228.
16. Shin J, Lee HJ, Jung DB, Jung JH, Lee EO, Lee SG *et al.* Suppression of STAT3 and HIF-1 alpha mediates anti-angiogenic activity of betulinic acid in hypoxic PC-3 prostate cancer cells. *PLoS One* 2011; **6**: e21492.
17. Lim S, Becker A, Zimmer A, Lu J, Buettner R, Kirfel J. SNAI1-mediated epithelial-mesenchymal transition confers chemoresistance and cellular plasticity by regulating genes involved in cell death and stem cell maintenance. *PLoS One* 2013; **8**: e66558.
18. Miyoshi A, Kitajima Y, Sumi K, Sato K, Hagiwara A, Koga Y *et al.* Snail and SIP1 increase cancer invasion by upregulating MMP family in hepatocellular carcinoma cells. *Br J Cancer* 2004; **90**: 1265–1273.
19. Neal CL, McKeithen D, Odero-Marah VA. Snail negatively regulates cell adhesion to extracellular matrix and integrin expression via the MAPK pathway in prostate cancer cells. *Cell Adh Migr* 2011; **5**: 249–257.
20. Haraguchi M, Okubo T, Miyashita Y, Miyamoto Y, Hayashi M, Crotti TN *et al.* Snail regulates cell-matrix adhesion by regulation of the expression of integrins and basement membrane proteins. *J Biol Chem* 2008; **283**: 23514–23523.
21. Cano A, Perez-Moreno MA, Rodrigo I, Locascio A, Blanco MJ, del Barrio MG *et al.* The transcription factor snail controls epithelial-mesenchymal transitions by repressing E-cadherin expression. *Nat Cell Biol* 2000; **2**: 76–83.
22. Batlle E, Sancho E, Franci C, Dominguez D, Monfar M, Baulida J *et al.* The transcription factor snail is a repressor of E-cadherin gene expression in epithelial tumour cells. *Nat Cell Biol* 2000; **2**: 84–89.
23. Dontu G, Jackson KW, McNicholas E, Kawamura MJ, Abdallah WM, Wicha MS. Role of Notch signaling in cell-fate determination of human mammary stem/progenitor cells. *Breast Cancer Res* 2004; **6**: R605–R615.
24. Fre S, Huyghe M, Mourikis P, Robine S, Louvard D, Artavanis-Tsakonas S. Notch signals control the fate of immature progenitor cells in the intestine. *Nature* 2005; **435**: 964–968.
25. Jarriault S, Brou C, Logeat F, Schroeter EH, Kopan R, Israel A. Signalling downstream of activated mammalian Notch. *Nature* 1995; **377**: 355–358.
26. Maier MM, Gessler M. Comparative analysis of the human and mouse Hey1 promoter: Hey genes are new Notch target genes. *Biochem Biophys Res Commun* 2000; **275**: 652–660.
27. Barbera MJ, Puig I, Dominguez D, Julien-Grille S, Guaita-Esteruelas S, Peiro S *et al.* Regulation of Snail transcription during epithelial to mesenchymal transition of tumor cells. *Oncogene* 2004; **23**: 7345–7354.
28. Vega S, Morales AV, Ocana OH, Valdes F, Fabregat I, Nieto MA. Snail blocks the cell cycle and confers resistance to cell death. *Genes Dev* 2004; **18**: 1131–1143.
29. Reginato MJ, Mills KR, Paulus JK, Lynch DK, Sgroi DC, Debnath J *et al.* Integrins and EGFR coordinately regulate the pro-apoptotic protein Bim to prevent anoikis. *Nat Cell Biol* 2003; **5**: 733–740.
30. Marani M, Hancock D, Lopes R, Tenev T, Downward J, Lemoine NR. Role of Bim in the survival pathway induced by Raf in epithelial cells. *Oncogene* 2004; **23**: 2431–2441.
31. Weston CR, Balmanno K, Chalmers C, Hadfield K, Molton SA, Ley R *et al.* Activation of ERK1/2 by deltaRaf-1:ER* represses Bim expression independently of the JNK or PI3K pathways. *Oncogene* 2003; **22**: 1281–1293.
32. Ley R, Balmanno K, Hadfield K, Weston C, Cook SJ. Activation of the ERK1/2 signaling pathway promotes phosphorylation and proteasome-dependent degradation of the BH3-only protein, Bim. *J Biol Chem* 2003; **278**: 18811–18816.
33. Kumar P, Benedict R, Urzua F, Fischbach C, Mooney D, Polverini P. Combination treatment significantly enhances the efficacy of antitumor therapy by preferentially targeting angiogenesis. *Lab Invest* 2005; **85**: 756–767.
34. Imhof BA, Vollmers HP, Goodman SL, Birchmeier W. Cell-cell interaction and polarity of epithelial cells: specific perturbation using a monoclonal antibody. *Cell* 1983; **35**(3 Pt 2): 667–675.
35. Behrens J, Mareel MM, Van Roy FM, Birchmeier W. Dissecting tumor cell invasion: epithelial cells acquire invasive properties after the loss of uvomorulin-mediated cell-cell adhesion. *J Cell Biol* 1989; **108**: 2435–2447.
36. Singh A, Settleman J. EMT cancer stem cells and drug resistance: an emerging axis of evil in the war on cancer. *Oncogene* 2010; **29**: 4741–4751.
37. Sarkar FH, Li Y, Wang Z, Kong D. Pancreatic cancer stem cells and EMT in drug resistance and metastasis. *Minerva Chir* 2009; **64**: 489–500.
38. Kong D, Li Y, Wang Z, Sarkar FH. Cancer stem cells and epithelial-to-mesenchymal transition (EMT)-phenotypic cells: are they cousins or twins? *Cancers* 2011; **3**: 716–729.
39. Izumiya M, Kabashima A, Higuchi H, Igarashi T, Sakai G, Iizuka H *et al.* Chemoresistance is associated with cancer stem cell-like properties and epithelial-to-mesenchymal transition in pancreatic cancer cells. *Anticancer Res* 2012; **32**: 3847–3853.
40. Li H, Chen X, Calhoun-Davis T, Claypool K, Tang DG. PC3 human prostate carcinoma cell holoclones contain self-renewing tumor-initiating cells. *Cancer Res* 2008; **68**: 1820–1825.
41. Andarawewa KL, Erickson AC, Chou WS, Costes SV, Gascard P, Mott JD *et al.* Ionizing radiation predisposes nonmalignant human mammary epithelial cells to undergo transforming growth factor beta induced epithelial to mesenchymal transition. *Cancer Res* 2007; **67**: 8662–8670.
42. Jung JW, Hwang SY, Hwang JS, Oh ES, Park S, Han IO. Ionising radiation induces changes associated with epithelial-mesenchymal transdifferentiation and increased cell motility of A549 lung epithelial cells. *Eur J Cancer* 2007; **43**: 1214–1224.
43. Gomez-Casal R, Bhattacharya C, Ganesh N, Bailey L, Basse P, Gibson M *et al.* Non-small cell lung cancer cells survived ionizing radiation treatment display cancer stem cell and epithelial-mesenchymal transition phenotypes. *Mol Cancer* 2013; **12**: 94.
44. Kawamoto A, Yokoe T, Tanaka K, Saigusa S, Toiyama Y, Yasuda H *et al.* Radiation induces epithelial-mesenchymal transition in colorectal cancer cells. *Oncol Rep* 2012; **27**: 51–57.
45. Thiery JP. Epithelial-mesenchymal transitions in tumour progression. *Nat Rev Cancer* 2002; **2**: 442–454.
46. Thiery JP, Acloque H, Huang RY, Nieto MA. Epithelial-mesenchymal transitions in development and disease. *Cell* 2009; **139**: 871–890.
47. Escrivà M, Peiró S, Herranz N, Villagrasa P, Dave N, Montserrat-Sentís B *et al.* Repression of PTEN phosphatase by Snail1 transcriptional factor during gamma radiation-induced apoptosis. *Mol Cell Biol* 2008; **28**: 1528–1540.
48. Kurrey NK, Jalgaonkar SP, Joglekar AV, Ghanate AD, Chaskar PD, Doiphode RY *et al.* Snail and slug mediate radioresistance and chemoresistance by antagonizing p53-mediated apoptosis and acquiring a stem-like phenotype in ovarian cancer cells. *Stem Cells* 2009; **27**: 2059–2068.
49. Sun M, Guo X, Qian X, Wang H, Yang C, Brinkman KL *et al.* Activation of the ATM-Snail pathway promotes breast cancer metastasis. *J Mol Cell Biol* 2012; **4**: 304–315.
50. Mani SA, Guo W, Liao MJ, Eaton EN, Ayyanan A, Zhou AY *et al.* The epithelial-mesenchymal transition generates cells with properties of stem cells. *Cell* 2008; **133**: 704–715.
51. Scheel C, Eaton EN, Li SH, Chaffer CL, Reinhardt F, Kah KJ *et al.* Paracrine and autocrine signals induce and maintain mesenchymal and stem cell states in the breast. *Cell* 2011; **145**: 926–940.
52. Zhu LF, Hu Y, Yang CC, Xu XH, Ning TY, Wang ZL *et al.* Snail overexpression induces an epithelial to mesenchymal transition and cancer stem cell-like properties in SCC9 cells. *Lab Invest* 2012; **92**: 744–752.
53. Richardson GD, Robson CN, Lang SH, Neal DE, Maitland NJ, Collins AT. CD133, a novel marker for human prostatic epithelial stem cells. *J Cell Sci* 2004; **117**(Pt 16): 3539–3545.
54. Takahashi K, Yamanaka S. Induction of pluripotent stem cells from mouse embryonic and adult fibroblast cultures by defined factors. *Cell* 2006; **126**: 663–676.
55. Yu J, Vodyanik MA, Smuga-Otto K, Antosiewicz-Bourget J, Frane JL, Tian S *et al.* Induced pluripotent stem cell lines derived from human somatic cells. *Science* 2007; **318**: 1917–1920.
56. Lagadec C, Vlashi E, Alhiyari Y, Phillips TM, Dratver MB, Pajonk F. Radiation-induced notch signaling in breast cancer stem cells. *Int J Radiat Oncol Biol Phys* 2013; **87**: 609–618.
57. Lagadec C, Vlashi E, Della Donna L, Dekmezian C, Pajonk F. Radiation-induced reprogramming of breast cancer cells. *Stem Cells* 2012; **30**: 833–844.
58. Sahlgren C, Gustafsson MV, Jin S, Poellinger L, Lendahl U. Notch signaling mediates hypoxia-induced tumor cell migration and invasion. *Proc Natl Acad Sci USA* 2008; **105**: 6392–6397.
59. Woodward WA, Chen MS, Behbod F, Alfaro MP, Buchholz TA, Rosen JM. WNT/beta-catenin mediates radiation resistance of mouse mammary progenitor cells. *Proc Natl Acad Sci USA* 2007; **104**: 618–623.
60. Phillips TM, McBride WH, Pajonk F. The response of CD24(-/low)/CD44 + breast cancer-initiating cells to radiation. *J Natl Cancer Inst* 2006; **98**: 1777–1785.
61. Lagadec C, Vlashi E, Della Donna L, Meng Y, Dekmezian C, Kim K *et al.* Survival and self-renewing capacity of breast cancer initiating cells during fractionated radiation treatment. *Breast Cancer Res* 2010; **12**: R13.
62. Evdokimova V, Tognon C, Ng T, Ruzanov P, Melnyk N, Fink D *et al.* Translational activation of snail1 and other developmentally regulated transcription factors by YB-1 promotes an epithelial-mesenchymal transition. *Cancer Cell* 2009; **15**: 402–415.

63. Tsai JH, Donaher JL, Murphy DA, Chau S, Yang J. Spatiotemporal regulation of epithelial-mesenchymal transition is essential for squamous cell carcinoma metastasis. *Cancer Cell* 2012; **22**: 725–736.
64. Yu M, Bardia A, Wittner BS, Stott SL, Smas ME, Ting DT *et al.* Circulating breast tumor cells exhibit dynamic changes in epithelial and mesenchymal composition. *Science* 2013; **339**: 580–584.
65. Laberge RM, Awad P, Campisi J, Desprez PY. Epithelial-mesenchymal transition induced by senescent fibroblasts. *Cancer Microenviron* 2012; **5**: 39–44.
66. Rodier F, Coppe JP, Patil CK, Hoeijmakers WA, Munoz DP, Raza SR *et al.* Persistent DNA damage signalling triggers senescence-associated inflammatory cytokine secretion. *Nat Cell Biol* 2009; **11**: 973–979.
67. Wiederschain D, Wee S, Chen L, Loo A, Yang G, Huang A *et al.* Single-vector inducible lentiviral RNAi system for oncology target validation. *Cell Cycle* 2009; **8**: 498–504.
68. Velimezi G, Liontos M, Vougas K, Roumeliotis T, Bartkova J, Sideridou M *et al.* Functional interplay between the DNA-damage-response kinase ATM and ARF tumour suppressor protein in human cancer. *Nat Cell Biol* 2013; **15**: 967–977.
69. Vlasakova J, Novakova Z, Rossmeislova L, Kahle M, Hozak P, Hodny Z. Histone deacetylase inhibitors suppress IFN{alpha}-induced up-regulation of promyelocytic leukemia protein. *Blood* 2007; **109**: 1373–1380.
70. Franken NAP, Rodermond HM, Stap J, Haveman J, van Bree C. Clonogenic assay of cells in vitro. *Nat Protoc* 2006; **1**: 2315–2319.

Supplementary Information accompanies this paper on Cell Death and Differentiation website (http://www.nature.com/cdd)

**Titles and Legends to Supplementary Figures**

**Supplementary Figures**

**Supplementary Figure 1. fIR-associated senescence-like phenotype in carcinoma cell lines.** (**a**) Flow cytometric estimation of cell proliferation by eFluor670 dye dilution in adherent control (red line) and irradiated (blue line) DU145 cells (11, 13 and 15 x 2 Gy daily; see Material and Methods for details) expressed as histogram of fluorescence intensity. Note, control (orange line) and irradiated (10 x 2 Gy; green line) were labeled and analyzed immediately after staining (day 0). (**b**) Fluorescence detection of micronuclei formation (arrowheads) using DAPI (blue) in DU145 and PC-3 cells estimated three days after 10 x 2 Gy. Bar, 15 μm. (**c**) Indirect immunofluorescence detection of BrdU incorporation (green) after 1 x 10 Gy in DU145 cells. Nuclei were visualized by DAPI (blue). Yellow arrows illustrate sites of active replication. (**d**) Senescence-associated β-galactosidase activity in DU145 and PC-3 cells estimated 10 days after 10 x 2 Gy. Yellow arrowheads indicate senescent cells. Bar, 100 μm. (**e**) Flow cytometry viability analysis of DU145, PC-3, LNCaP, 22RV1 and MCF-7 non-adherent cells exposed to different irradiation regimens (1 x 10 Gy, 10 x 2 Gy and 35 x 2 Gy) expressed as relative amount (in percentage, numbers above bars) of viable AnnexinV$^-$/Hoechst$^-$ cells in total non-adherent fraction. Values represent means ±S.D. from two independent experiments. (**f**) Phase contrast image of irradiated re-adherent MCF-7 single-cell colony. Note, non-adherent cells (yellow arrowheads) starting to attach to the layer of adherent cells. Bar, 100 μm. (**g**) Phase contrast microscopic images of non-irradiated parental cells (par) and radiation-surviving MCF-7 cell populations after 10 x 2 Gy fIR (adh and non-adh) or 14 days after fIR (re-adh). Representative phase contrast images of one of two independent experiments are shown. Bar, 100 μm. Representative images from two (**f** and **g**) or three (**b - d**) independent experiments are shown.

**Supplementary Figure 2.** (**a**) Immunoblotting detection of total Chk2, phosphothreonine 68 of Chk2, total p53, phosphoserine 15 of p53, phosphoserine 139 of H2AX and p21$^{waf/cip}$ (p21) in control and irradiated (2 – 10 x 2 Gy) DU145 and PC-3 cells. GAPDH was used as a loading control. (**b**) Indirect immunofluorescence detection of PML (red) in irradiated (10 x 2 Gy) DU145 and PC-3 three weeks and three days after irradiation, respectively. Nuclei were visualized by DAPI (blue). Bars, 50 μm. (**c**) Immunofluorescence detection of 53BP1 (red) and γH2AX (green) foci in DU145 and PC-3 cells three days after irradiation (10 x 2 Gy). Nuclei were visualized by DAPI (blue). Bar, 50 μm. **(d)** Phase contrast microscopic images of radiation surviving re-adherent DU145 cell populations after 35 x 2 Gy fIR. Non-adherent cells with membrane blebbing (arrowheads) attaching to the layer of adherent cells are shown. (**e**) Kaplan-Meier survival plot (left) and tumor growth curve (right) reflecting percentage of tumor-free SCID mice and mean tumor area, respectively, at indicated times after subcutaneous injection of either control or 10 x 2 Gy-irradiated re-adherent DU145 cells. $P < 0.05$ estimated by the Newman-Keuls multiple-comparison test ($N = 5$).

**Supplementary Figure 3. Radiation-induced EMT and stem cell-related factors in prostate cancer cells.** (**a**) Real time qRT-PCR quantification of Slug, Twist1 and Zeb2 in control (parental) and irradiated (10 x 2 Gy) adherent, non-adherent and re-adherent DU145 (left) and PC-3 (right) cells. RPL37a was used as a reference gene. (**b**) Real time qRT-PCR estimation of Snail mRNA level detected in control (parental) and irradiated (35 x 2 Gy) adherent and non-

adherent DU145 cells. RPL37a was used as a reference gene. (**c**) Immunoblotting detection of Twist1 in non-treated DU145 and PC-3 cells. Gamma-tubulin was used as a loading control. (**d**) Effectiveness of doxycycline-induced (dox, 0.7 μg/ml) shRNA-mediated Snail knock-down in lentivirally transduced DU145 cells during fIR (10 x 2 Gy) verified by immunoblotting. Gamma-tubulin was used as a loading control. Non-transduced cells were used as a control (wt). (**e**) Effect of doxycycline-induced shRNA-mediated Snail knock-down on loss of adhesion during fIR (10 x 2 Gy) expressed as the relative number of detached cells (40 μl/sample) assessed by flow cytometry in control non-transduced DU145 cells (wt) and stable DU145 cell line generated by lentiviral transduction with the pLKO-Tet-On-shRNA-Snail (shSnail) vector. Non-transduced control cells (wt) were set as "1". (**f**) Effect of doxycycline-induced (dox, 0.7 μg/ml) shRNA-mediated Snail knock-down in lentivirally transduced DU145 (shSnail) cells on integrin alpha2 (ITGA2) protein level with or w/o irradiation (10 x 2 Gy) detected by immunoblotting. Gamma-tubulin was used as a loading control. (**g**) Real time qRT-PCR quantification of stem cell-related genes CD133, Sox2, Oct-4 and Nanog in control and irradiated (35 x 2 Gy) adherent and non-adherent DU145 cells. (**h**) Immunoblotting detection of DLL1 in control (parental) and irradiated (10 x 2 Gy) adherent, non-adherent and re-adherent DU145 cells. GAPDH was used as a loading control. Values in **a**, **b** and **g** represent means ±S.D. from at least two independent experiments performed in triplicates. Bars in panel **e** represent mean ±S.D from two independent experiments performed in duplicates. **P*<0.05.

**Supplementary Fig. 4. Proliferation of radiation-surviving non-adherent and re-adherent DU145 cells.** (**a**) Schematic representation of the irradiation protocol using 2 Gy every 24 hours for 10 days. Generation of radiation surviving non-adherent population of DU145 cell line is depicted. Non-adherent cells were stained with eFluor670 immediately after last dose of irradiation. Approximately one week after staining small fraction of non-adherent cells became re-adherent. Both non-adherent and re-adherent cells were analyzed by FACS at 28th day after staining. (**b**) Flow cytometric estimation of proliferation of irradiated (10 x 2 Gy) non-adherent and re-adherent DU145 cells using the eFluor670 dye dilution assay at 28th day after staining. Note, the eFluor670 dye is diluted with progression of cell divisions, see the left side "shift" of the peak in the histogram in case of proliferation. Fraction of irradiated non-adherent DU145 cells reattached and were FACS-analyzed simultaneously with residual non-adherent cells. Non-stained cells were used as a negative control (NC).

**Supplementary Figure 5.** (**a**) Effect of Erk1/2 inhibition by ERKi (49 hours) on irradiation-induced (1 x 10 Gy) loss of adhesion expressed as the relative number of detached cells in control or irradiated non-adherent DU145 cells assessed by flow cytometry 48 hours after IR. Bars represent relative amount (in percentage) of total cells. Non-irradiated control cells were set as 100%. (**b**) Efficiency of Erk1/2 inhibition (ERKi) and/or activation (mixture of 10 ng/ml EGF and 50 ng/ml FGF) on Erk1/2 activity in control or irradiated (1 x 10 Gy) DU145 cells detected by immunoblotting. GAPDH was used as a loading control. (**c**) Effect of Erk1/2 activation (mixture of 10 ng/ml EGF and 50 ng/ml FGF) or chemical inhibition (ERKi) on irradiation-induced (10 Gy) loss of cell adhesion expressed as the relative number of detached DU145 cells analyzed 48 hours after IR by flow cytometry. The bars represent relative amount (in percentage) of total cells. Non-irradiated control cells were set as 100%. (**d**) Effect of siRNA-mediated knock-down of Erk1 (siErk1) and Erk2 (siErk2) on irradiation-induced (10 Gy) loss of cell adhesion expressed as the relative number of detached DU145 cells analyzed 48 hours after IR

(72 hours after transfection) by flow cytometry. Non-targeting siRNA (siNT) was used as a control. The bars represent relative amount (in percentage) of total cells. Non-irradiated control cells were set as 100%. (**e**) Efficiency of siRNA-mediated knock-down of Erk1 (siErk1) and Erk2 (siErk2) on Erk1/2 activity in control or irradiated (1 x 10 Gy) DU145 cells detected by immunoblotting. Non-targeting siRNA (siNT) was used as a control. GAPDH was used as a loading control. (**f**) Immunoblotting detection of Bim (EL, extra large form) and Bcl-XL levels in control or irradiated (1 x 10 Gy or 10 x 2 Gy) adherent or non-adherent DU145 cells. GAPDH was used as a loading control. Data in **a**, **c** and **d** represent means ±S.D. from two independent experiments. **P*<0.05; ***P*<0.01.

**Supplementary Figure 6. Effect of Erk and Akt inhibition on survival of prostate cancer cells.** (**a**) Phase contrast microscopic images of control or irradiated adherent (10 x 2 Gy) DU145 cells after Erk (ERKi) and/or Akt (AKTi) inhibition captured at day 10 after IR. Bar, 100 μm. (**b**) Immunoblotting estimation of efficiency of Erk1/2 inhibition (ERKi) and/or Akt inhibition (AKTi) detected as activity of Erk1/2 (phosphothreonine 204/phosphotyrosine 204) and Akt (phosphoserine 473), respectively, in control or irradiated (1 x 10 Gy) DU145 cells. GAPDH was used as a loading control. (**c**) Effect of Erk inhibition (ERKi) and/or Akt inhibition (AKTi) on proliferation of control (untreated) BJ cells. Trypan blue negative cells were counted during the time course of 10 days. Data represent mean values ±S.D. from two (BJ) or three (DU145) independent experiments.

**Supplementary Fig. 7.** (**a**) Indirect immunofluorescence detection of the epithelial marker E-cadherin (green) and mesenchymal marker vimentin (red) in control (parental) and irradiated (10 x 2 Gy) adherent and re-adherent (passages 2, 4 and 9) DU145. Nuclei were visualized by DAPI (blue). Bar, 100 μm. Representative images from two independent experiments are shown. (**b**) Schematic representation of fIR-induced EMT/MET-associated changes. The differential sensitivity of adherent and non-adherent cells to Erk and Akt inhibitors is depicted.

# Suppl. Fig. 1

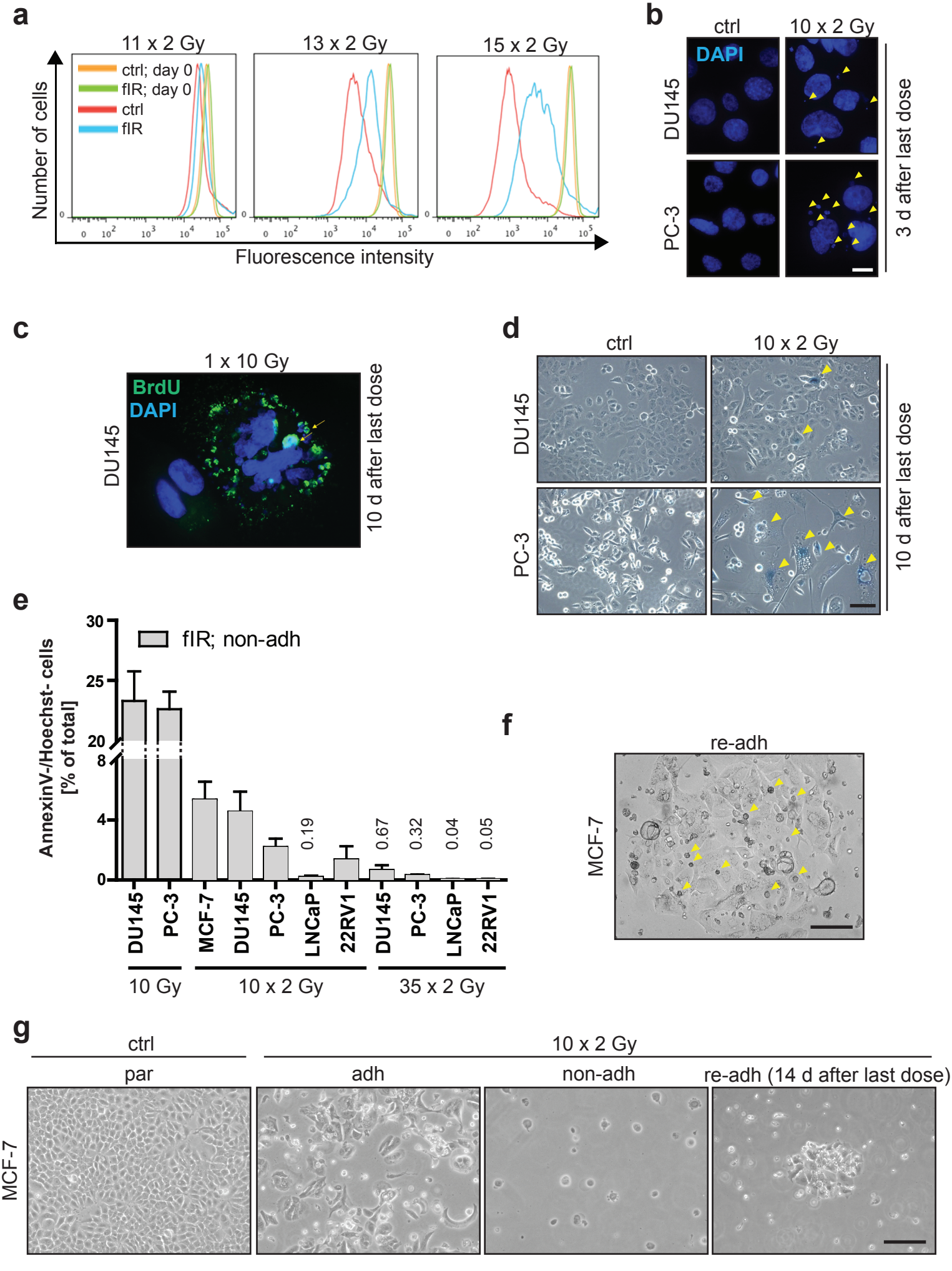
a
11 x 2 Gy
13 x 2 Gy
15 x 2 Gy
ctrl; day 0
fIR; day 0
ctrl
fIR
Number of cells
Fluorescence intensity
b
ctrl
10 x 2 Gy
DAPI
DU145
PC-3
3 d after last dose
c
1 x 10 Gy
BrdU
DAPI
DU145
10 d after last dose
d
ctrl
10 x 2 Gy
DU145
PC-3
10 d after last dose
e
fIR; non-adh
AnnexinV-/Hoechst- cells [% of total]
30
25
20
8
4
0
0.19
0.67
0.32
0.04
0.05
DU145
PC-3
MCF-7
DU145
PC-3
LNCaP
22RV1
DU145
PC-3
LNCaP
22RV1
10 Gy
10 x 2 Gy
35 x 2 Gy
f
re-adh
MCF-7
g
ctrl
10 x 2 Gy
par
adh
non-adh
re-adh (14 d after last dose)
MCF-7

# Suppl. Fig. 2

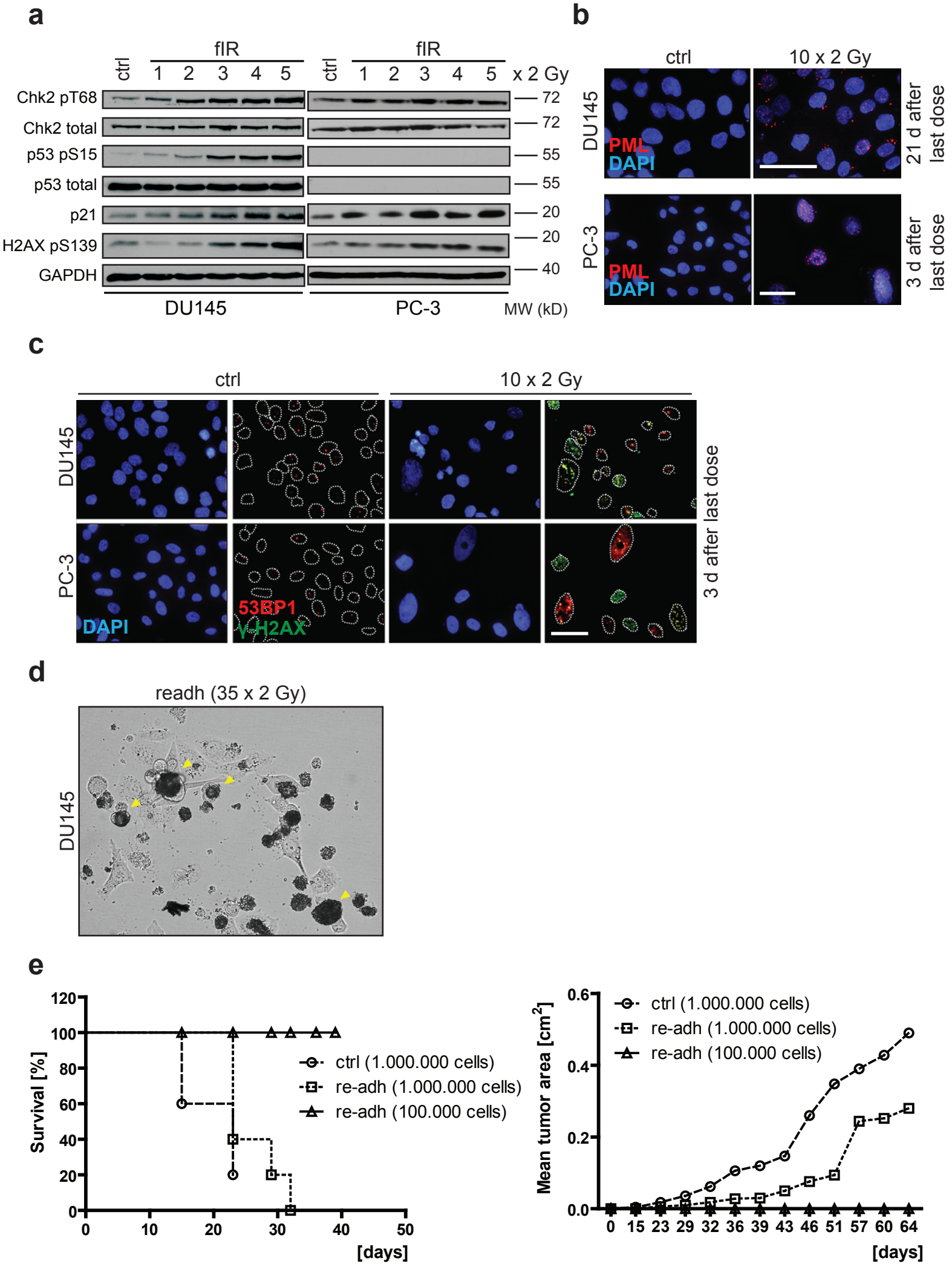
a
ctrl
fIR
1 2 3 4 5
x 2 Gy
Chk2 pT68
Chk2 total
p53 pS15
p53 total
p21
H2AX pS139
GAPDH
72
72
55
55
20
20
40
DU145
PC-3
MW (kD)
b
ctrl
10 x 2 Gy
DU145
PC-3
PML
DAPI
21 d after last dose
3 d after last dose
c
ctrl
10 x 2 Gy
DU145
PC-3
DAPI
53BP1
γ-H2AX
3 d after last dose
d
readh (35 x 2 Gy)
DU145
e
Survival [%]
120
100
80
60
40
20
0
0
10
20
30
40
50
[days]
ctrl (1.000.000 cells)
re-adh (1.000.000 cells)
re-adh (100.000 cells)
Mean tumor area [cm²]
0.6
0.4
0.2
0.0
0 15 23 29 32 36 39 43 46 51 57 60 64
[days]
ctrl (1.000.000 cells)
re-adh (1.000.000 cells)
re-adh (100.000 cells)

# Suppl. Fig. 3

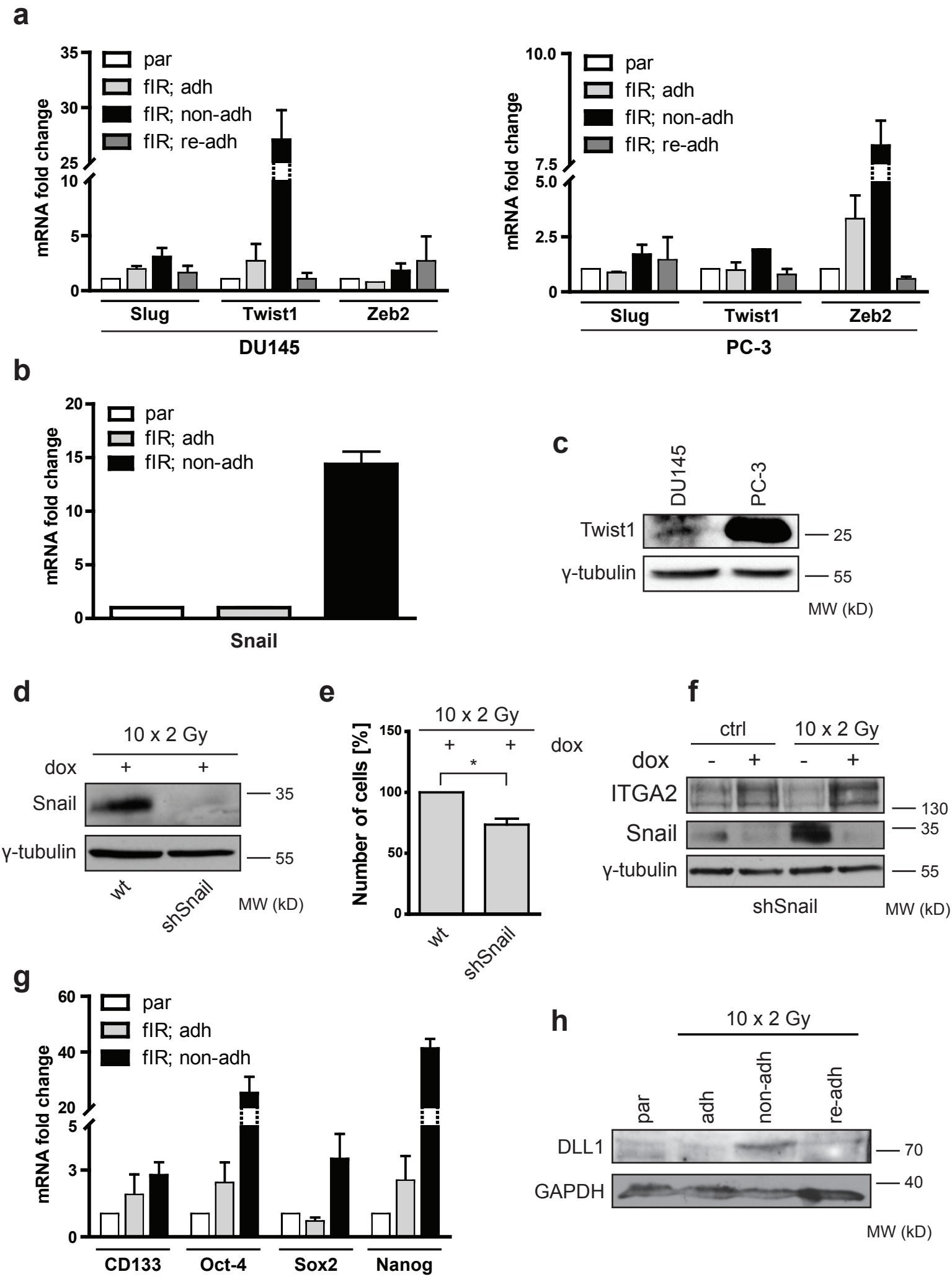
a
mRNA fold change
par
fIR; adh
fIR; non-adh
fIR; re-adh
Slug
Twist1
Zeb2
DU145
PC-3
b
Snail
c
DU145
PC-3
Twist1
γ-tubulin
MW (kD)
d
10 x 2 Gy
dox
Snail
γ-tubulin
wt
shSnail
e
Number of cells [%]
f
ctrl
ITGA2
shSnail
g
CD133
Oct-4
Sox2
Nanog
h
DLL1
GAPDH

# Suppl. Fig. 4

**a**

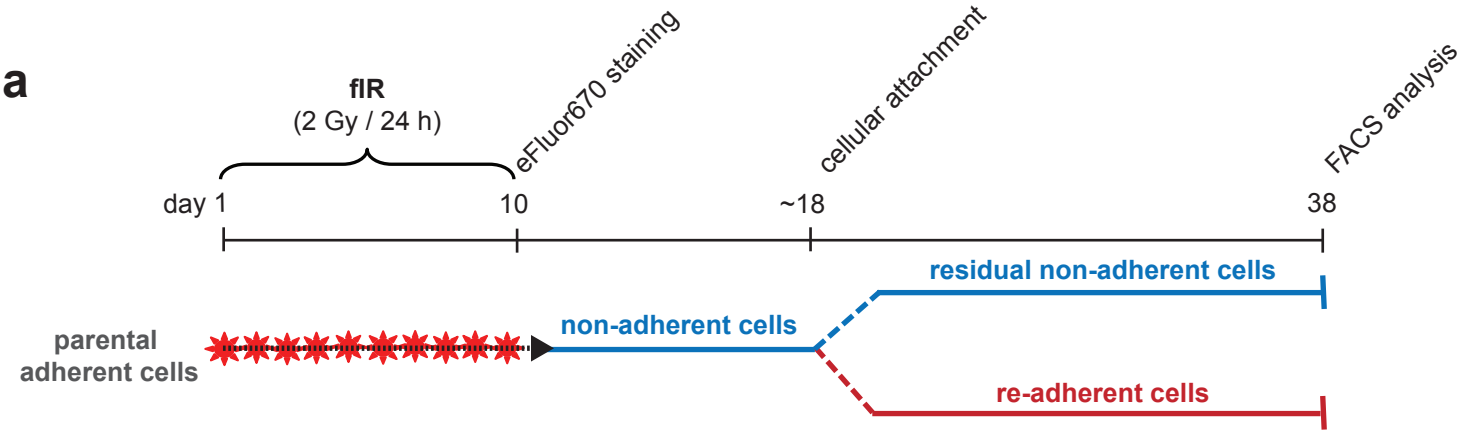


**b**

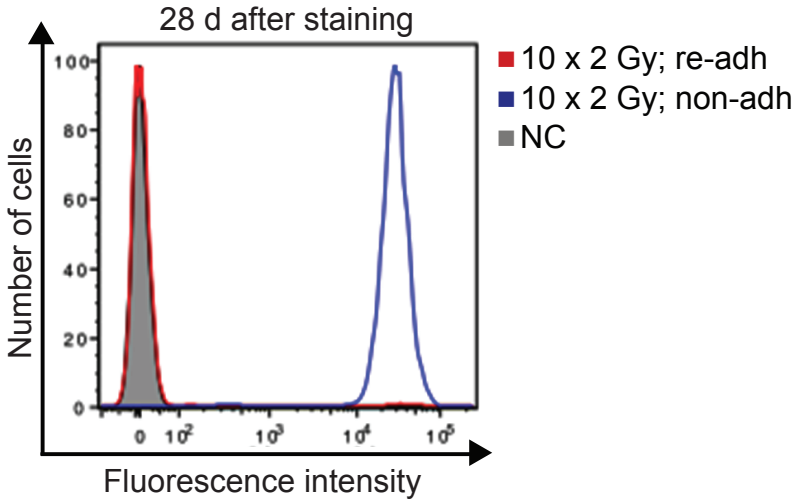

# Suppl. Fig. 5

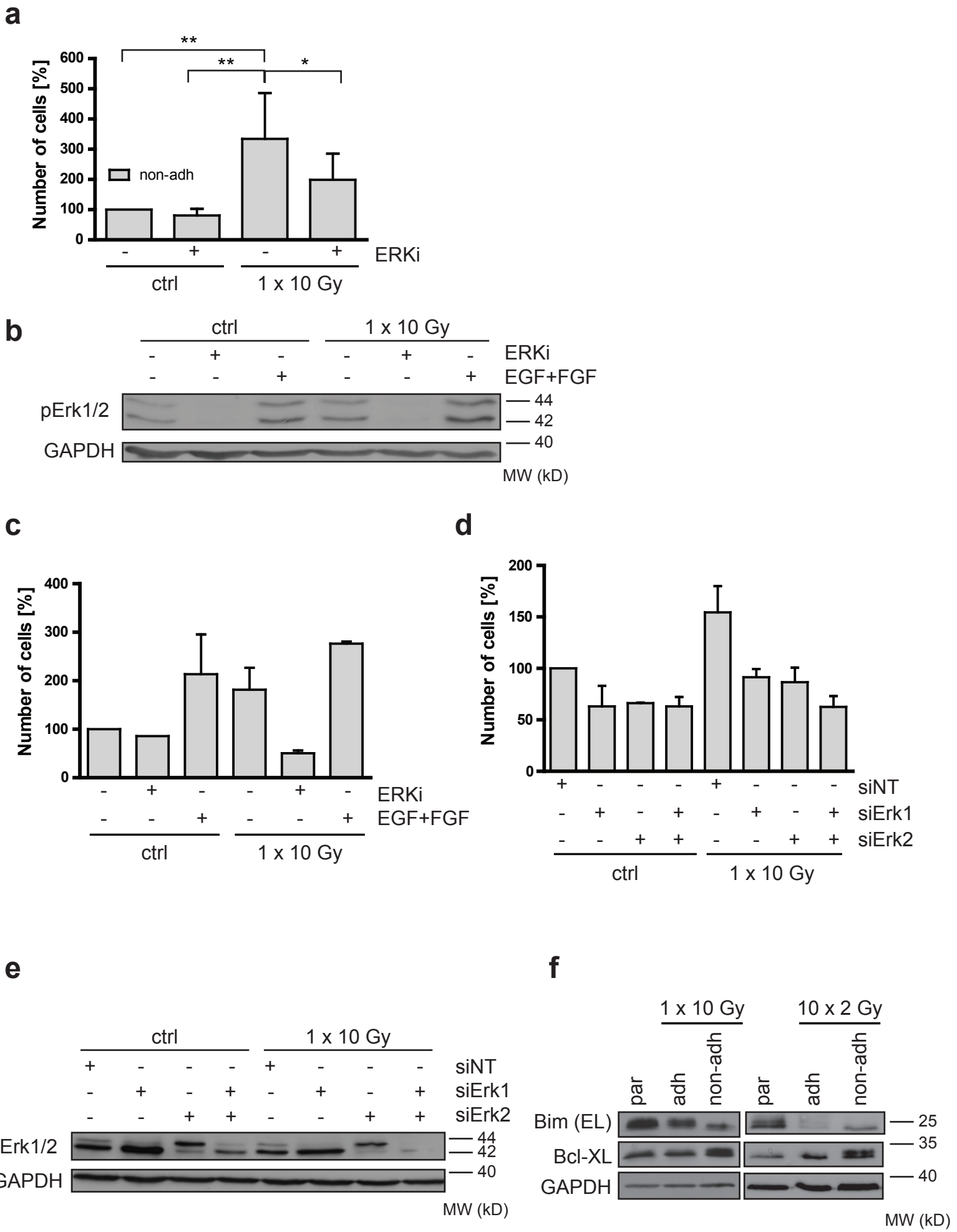
a
Number of cells [%]
non-adh
ERKi
ctrl
1 x 10 Gy
b
ctrl
1 x 10 Gy
ERKi
EGF+FGF
pErk1/2
GAPDH
MW (kD)
c
Number of cells [%]
ERKi
EGF+FGF
ctrl
1 x 10 Gy
d
Number of cells [%]
siNT
siErk1
siErk2
ctrl
1 x 10 Gy
e
ctrl
1 x 10 Gy
siNT
siErk1
siErk2
pErk1/2
GAPDH
MW (kD)
f
1 x 10 Gy
10 x 2 Gy
par
adh
non-adh
Bim (EL)
Bcl-XL
GAPDH
MW (kD)

# Suppl. Fig. 6

**a**

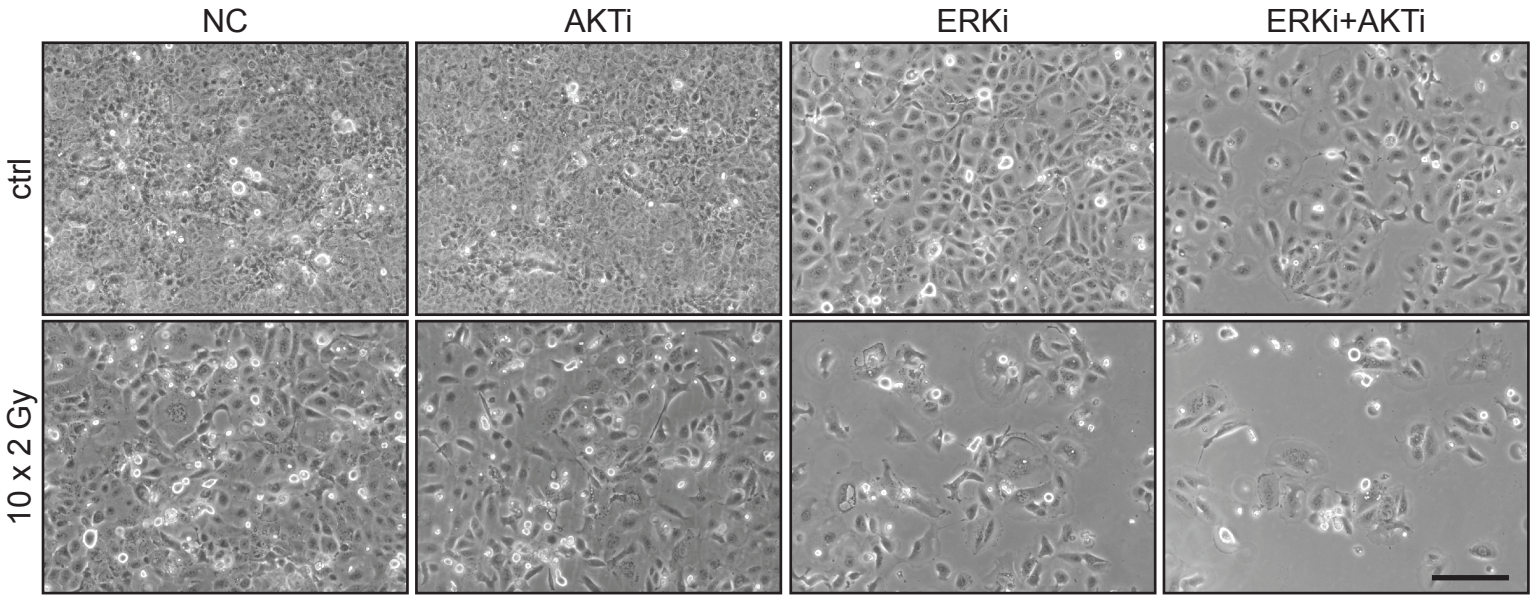


**b**

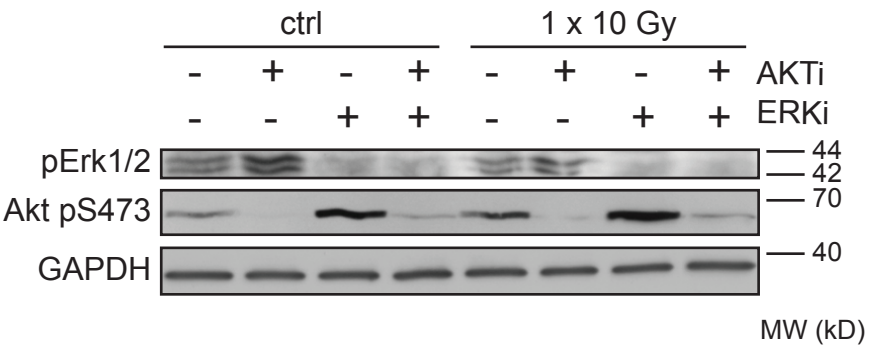


**c**

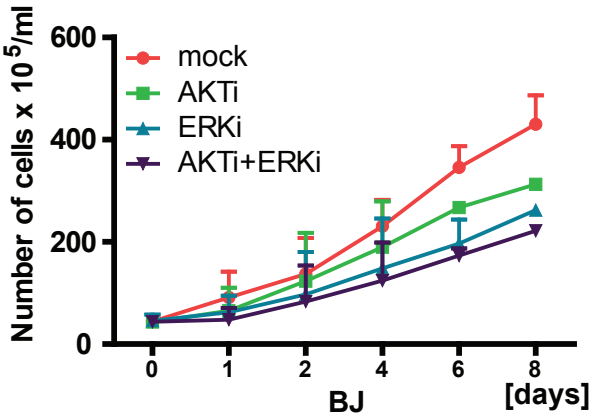

# Suppl. Fig. 7

**a**

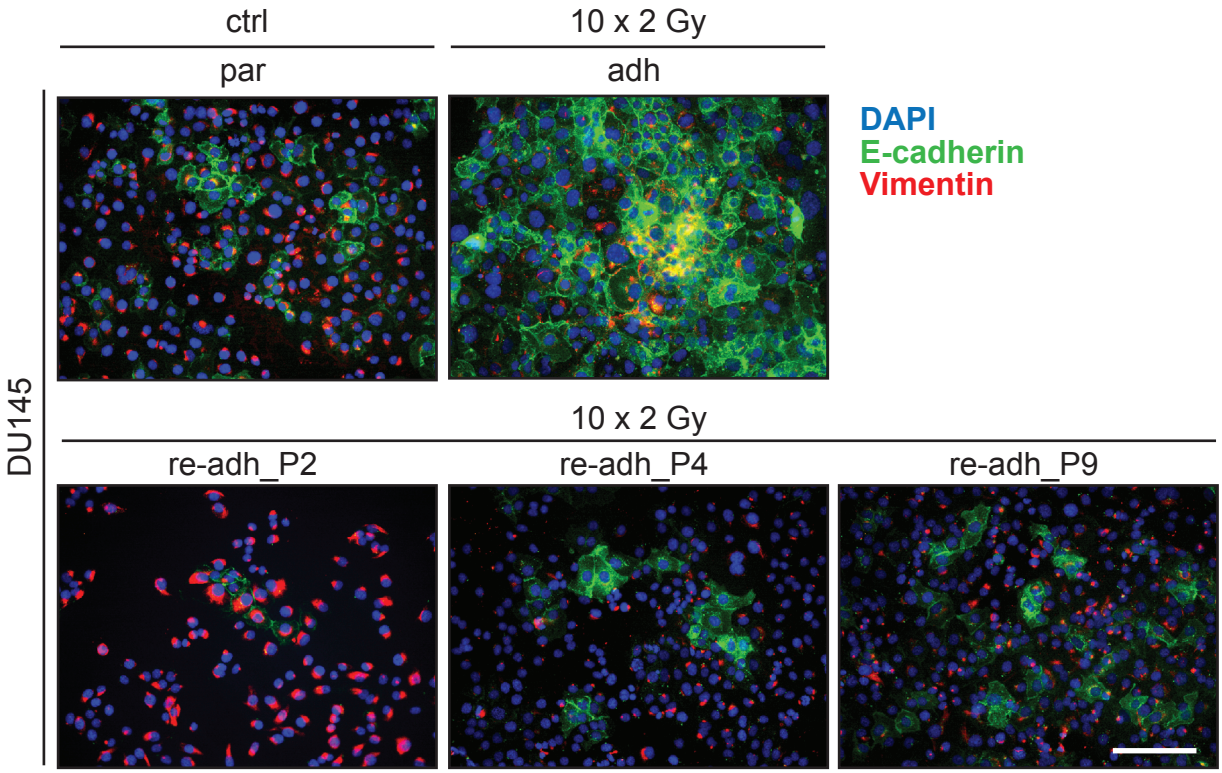


**b**

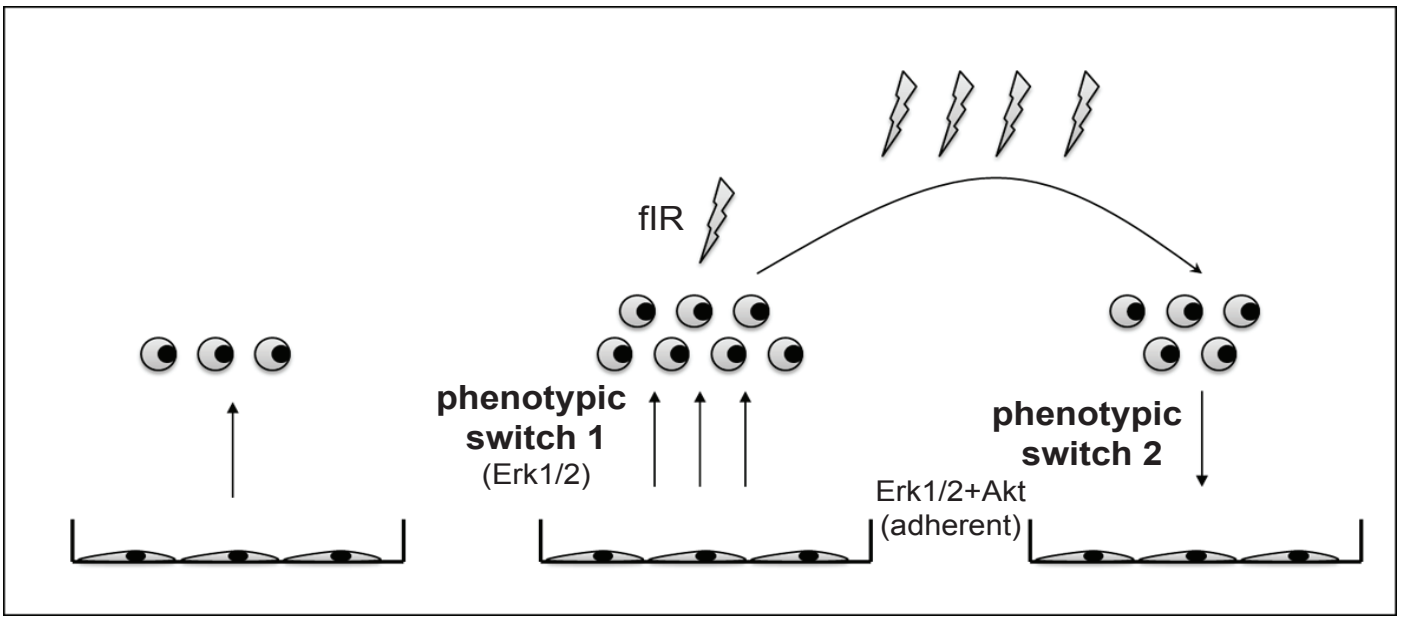

Research Paper

# Tumor growth accelerated by chemotherapy-induced senescent cells is suppressed by treatment with IL-12 producing cellular vaccines

**Jana Simova[1], Olena Sapega[1], Terezie Imrichova[2], Ivan Stepanek[1], Lenka Kyjacova[2], Romana Mikyskova[1], Marie Indrova[1], Jana Bieblova[1], Jan Bubenik[3], Jiri Bartek[2,4,5], Zdenek Hodny[2], Milan Reinis[1]**

[1]Immunology Unit, Czech Centre for Phenogenomics, BIOCEV and Department of Transgenic Models of Diseases, Institute of Molecular Genetics of the ASCR, v.v.i., Prague 14220, Czech Republic

[2]Department of Genome Integrity, Institute of Molecular Genetics, v.v.i., Academy of Sciences of the Czech Republic, Prague 14220, Czech Republic

[3]First Faculty of Medicine, Charles University in Prague, Prague 12000, Czech Republic

[4]Danish Cancer Society Research Center, Copenhagen DK-2100, Denmark

[5]Department of Medical Biochemistry and Biophysics, Science For Life Laboratory, Division of Translational Medicine and Chemical Biology, Karolinska Institute, 17121 Solna, Sweden

**Correspondence to:** Zdenek Hodny, **email:** hodny@img.cas.cz
Milan Reinis, **email:** reinis@img.cas.cz

**Keywords:** *cellular senescence, cancer chemotherapy, docetaxel, IL-12, cell therapy*

***Received:*** *April 18, 2016* ***Accepted:*** *May 29, 2016* ***Published:*** *July 19, 2016*

## ABSTRACT

**Standard-of-care chemo- or radio-therapy can induce, besides tumor cell death, also tumor cell senescence. While senescence is considered to be a principal barrier against tumorigenesis, senescent cells can survive in the organism for protracted periods of time and they can promote tumor development. Based on this emerging concept, we hypothesized that elimination of such potentially cancer-promoting senescent cells could offer a therapeutic benefit. To assess this possibility, here we first show that tumor growth of proliferating mouse TC-1 HPV-16-associated cancer cells in syngeneic mice becomes accelerated by co-administration of TC-1 or TRAMP-C2 prostate cancer cells made senescent by pre-treatment with the anti-cancer drug docetaxel, or lethally irradiated. Phenotypic analyses of tumor-explanted cells indicated that the observed acceleration of tumor growth was attributable to a protumorigenic environment created by the co-injected senescent and proliferating cancer cells rather than to escape of the docetaxel-treated cells from senescence. Notably, accelerated tumor growth was effectively inhibited by cell immunotherapy using irradiated TC-1 cells engineered to produce interleukin IL-12. Collectively, our data document that immunotherapy, such as the IL-12 treatment, can provide an effective strategy for elimination of the detrimental effects caused by bystander senescent tumor cells *in vivo*.**

## INTRODUCTION

Cellular senescence, an irreversible cell-cycle arrest, represents a principal barrier against tumorigenesis [1–3]. Senescent cells do not proliferate, however, they remain metabolically active and are able to further influence biological processes within the body [4]. These 'bystander' effects are mediated by numerous molecules produced by the senescent cells, commonly termed senescence-associated secretory phenotype (SASP; [5, 6]). SASP comprises mainly growth factors, extracellular matrix components and remodeling factors, cytokines and chemokines including proinflammatory species as well as other factors mediating intercellular communications [7]. Besides cell death, senescence can be induced in tumor cells during chemotherapy or radiotherapy [8, 9]. In such case, the fate and the function of surviving senescent tumor cells, including the effects of SASP on tumor microenvironment, are considered to play an important role in tumor progression with influence on the effectiveness of antitumor therapy. There is accumulating evidence that the presence of senescent cells in the tumor

and their SASP-related effects can be tumor growth-promoting [10]. It can be presumed therefore that not only the induction of cancer cell senescence itself, but also subsequent elimination of senescent cells will contribute, in a tumor-stage-dependent manner, to the overall anti-tumor barrier capacity. Indeed, it has been shown that oncogene-induced senescent murine hepatocytes were cleared by the immune system, through a process termed 'senescence surveillance' [11]. Importantly, impaired senescence surveillance in this model resulted in the induction of hepatocarcinoma. Furthermore, in MMTV-Wnt1-driven mammary tumors, persistence of senescent cells secreting senescence-associated cytokines displayed protumorigenic potential and contributed to tumor relapse [12]. The importance of senescence surveillance in aging has also been demonstrated in a study in which clearance of senescent cells ($p16^{Ink4a}$) suppressed and/or delayed development of ageing-associated symptoms in a progeroid mouse model [13].

The first example documenting tumor-promoting effects of senescent cells co-administered with proliferating tumor cells was reported by Krtolica et al. [14] who showed that co-injection of senescent fibroblasts with human mammary tumor cells accelerated tumor growth in immunocompromised mice. Later on, however, it was shown that although senescent human prostate cancer cells increased proliferation of co-cultured tumor cells *in vitro,* such accelerating impact on xenograft tumor cell growth in nude mice was not observed [8] indicating impact of some still unidentified factors on this phenomenon.

Interleukin 12 (IL-12), a cytokine connecting innate and adaptive immunity, represents one of the important players in induction of anti-tumor immune response [15]. Produced mainly by antigen presenting cells, such as dendritic cells, macrophages, monocytes or B cells upon their activation, IL-12 exerts its effects mainly through induction of IFNγ, as well as NK and T cell activation [16, 17]. Antitumor immunotherapy with IL-12 administered in different forms, including the usage of irradiated tumor cells producing IL-12, has been studied [15, 18, 19]. In several experimental tumor models, including those used in our laboratory, anti-tumor immunogenicity could be enhanced by administration of IL-12 or by gene therapy with tumor cells engineered to produce IL-12 (for reviews, see [20–22]).

This intriguing accumulating data inspired our present working hypothesis, namely that IL-12-based immunotherapy might be able to mitigate or entirely eliminate the pro-tumorigenic effects of bystander senescent cells. Indeed, here we document an acceleration of tumor growth, when proliferating TC-1 tumor cells were co-administered into syngeneic mice together with syngeneic tumor cells that had been subjected to senescence-inducing treatment with docetaxel (DTX). Furthermore, we also document effective treatment of such tumors by cell therapy using irradiated IL-12-producing tumor cells.

## RESULTS

### DTX induces senescence in mouse tumor cells TC-1 and TRAMP-C2

First, we evaluated the impact of DTX in terms of senescence induction, using two C57Bl/6 mice-derived tumor cell lines TC-1 and TRAMP-C2 of lung and prostate epithelial origin, respectively. Both TC-1 and TRAMP-C2 cells were susceptible to DTX and underwent senescence after a four-day incubation with 7.5 μM DTX [23]. After this treatment, the vast majority of TC-1 and TRAMP-C2 cells were alive but senescent, as characterized by the lack of cell proliferation, increased senescence-associated-β-galactosidase activity, characteristic cell morphology and increased expression of p16INK4a and p21waf1 inhibitors of cyclin-dependent kinases. Most of the senescent cells showed persistent DNA damage response, as judged from the presence of DNA damage foci positive for serine 139-phosphorylated histone H2AX (γH2AX; Figure 1, Figure 3B). Cessation of DNA replication was verified by incorporation of EdU. Only limited subsets of EdU-positive cells were observed in both TC-1 and TRAMP-C2 cell populations by FACS analysis (Figure 2A). Such residual EdU positivity can most likely be accounted for by ongoing DNA repair of the observed DNA damage (γH2AX) and/or aberrant endoreduplication uncoupled from cell division (Figure 2B) as we did not observe any proliferation of cells upon the DTX-treatment (Figure 3A). Most importantly for our subsequent experiments, subcutaneous administration of such senescent cells into animals did not lead to development of tumors (Figure 3C).

Pro-tumorigenic effects of senescent cells are believed to be mediated through their secretome [5]. Therefore, we analyzed any potential expression changes among 84 cytokines/chemokines evaluated during the course of the DTX-induced senescence in TC-1 and TRAMP-C2 cell lines. Indeed, expression of more than two dozens of cytokines was altered (either upregulated or downregulated; fold change > 2) in both TC-1 and TRAMP-C2 tumor cell lines. Elevated mRNA levels of a number of inflammatory and immunoregulatory factors, such as CSF2, CXCL1, CXCL16, TNFSF13b, adiponectin, CCL19, CCLl20, CCL4, CCL5, CD70, CNTF, CSF3, CXCL10, HC, IL-10, IL-13, IL-17f, IL-27, IL-6, LIF, TNF were observed (Supplementary Table 1). Notably, some of these factors are endowed with documented pro-tumorigenic properties, such as CXCL1 or IL-6 [7]. Elevated mRNA levels of the TNF family (FasL, TNSFS13b, TNF-α) were observed as well.

### Admixture of senescent cells accelerates tumorigenic potential of proliferating TC-1 cells

In order to test whether 'bystander' senescent cells can influence tumor growth, proliferating TC-1 tumor cells were injected into mice either alone ($3 \times 10^4$ cells/mouse) or admixed with docetaxel-induced senescent TC-1 cells ($3 \times 10^5$ cells/mouse). As shown in Figure 4A, co-administration of the bystander DTX-treated (senescent) cells and proliferating TC-1 cells into syngeneic animals resulted in significantly accelerated tumor growth, as compared to the tumors when the proliferating TC-1 cells were injected alone. Next, we performed an analogous experiment in which TC-1 proliferating cells were co-administered with senescent TRAMP-C2 cells (Figure 4B). Again, the presence of syngeneic bystander senescent cells accelerated the tumor growth. Significantly accelerated tumorigenicity was achieved also with admixture of proliferating TRAMP-C2 cancer cells (Figure 4C), as expected, and, interestingly, by adding lethally irradiated tumor cells (Figure 4D). Flow cytometry phenotypic analysis of cells explanted from the tumors and cultured for seven days *ex vivo*, taking advantage of the TC-1 and TRAMP-C2 mutual discrimination using the CD80 cell surface marker (TC-1 cells are CD80-positive while TRAMP-C2 are CD80-negative), revealed that the vast majority of tumor cells present in the tumors that had arisen from co-injection of TC-1 proliferating cells with senescent TRAMP-C2 cells were TC-1 tumor cells (Figure 5). This indicates that the senescent cells did not

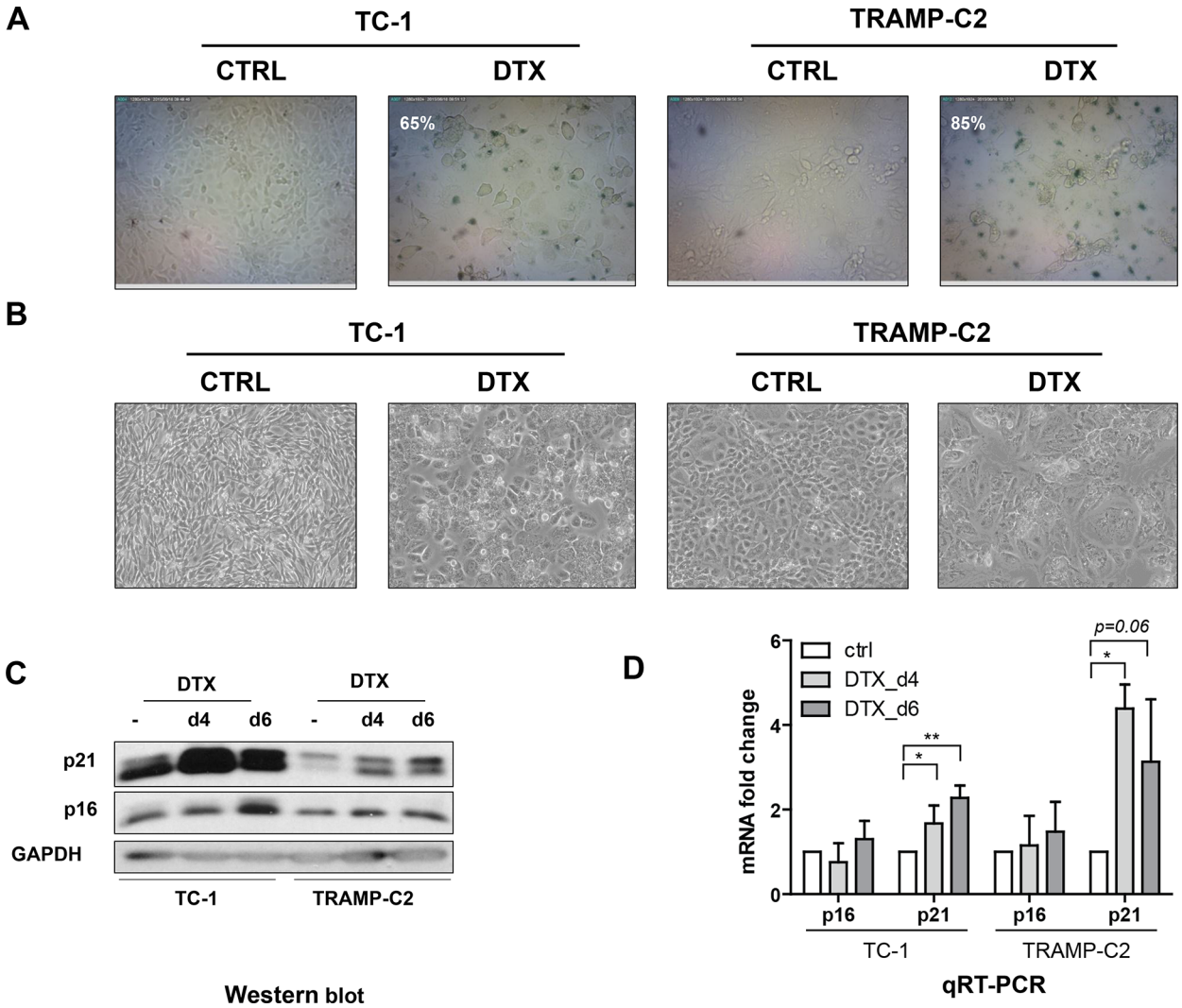


**Figure 1: Docetaxel induces senescence in TC-1 and TRAMP-C2 cells.** Senescence-associated β-galactosidase activity in TC-1 and TRAMP-C2 cells treated with DTX (7.5 μM) for 4 days (**A**). Phase contrast microscopic images of control and DTX-treated (7.5 μM) TC-1 and TRAMP-C2 cells at day 4 after the treatment (**B**). Immunoblotting detection of mouse p16INK4A (p16) and p21waf1/cip1 (p21) in control and DTX-treated (7.5 μM) TC-1 and TRAMP-C2 cells harvested at day 4 and 6 after the treatment. GAPDH was used as a loading control (**C**). qRT-PCR quantification of p16 and p21 in control and DTX-treated (7.5 μM) TC-1 and TRAMP-C2 cells harvested at day 4 and 6 after the treatment. Data represent means ± S.D. *$p < 0.05$, **$p < 0.005$ (**D**).

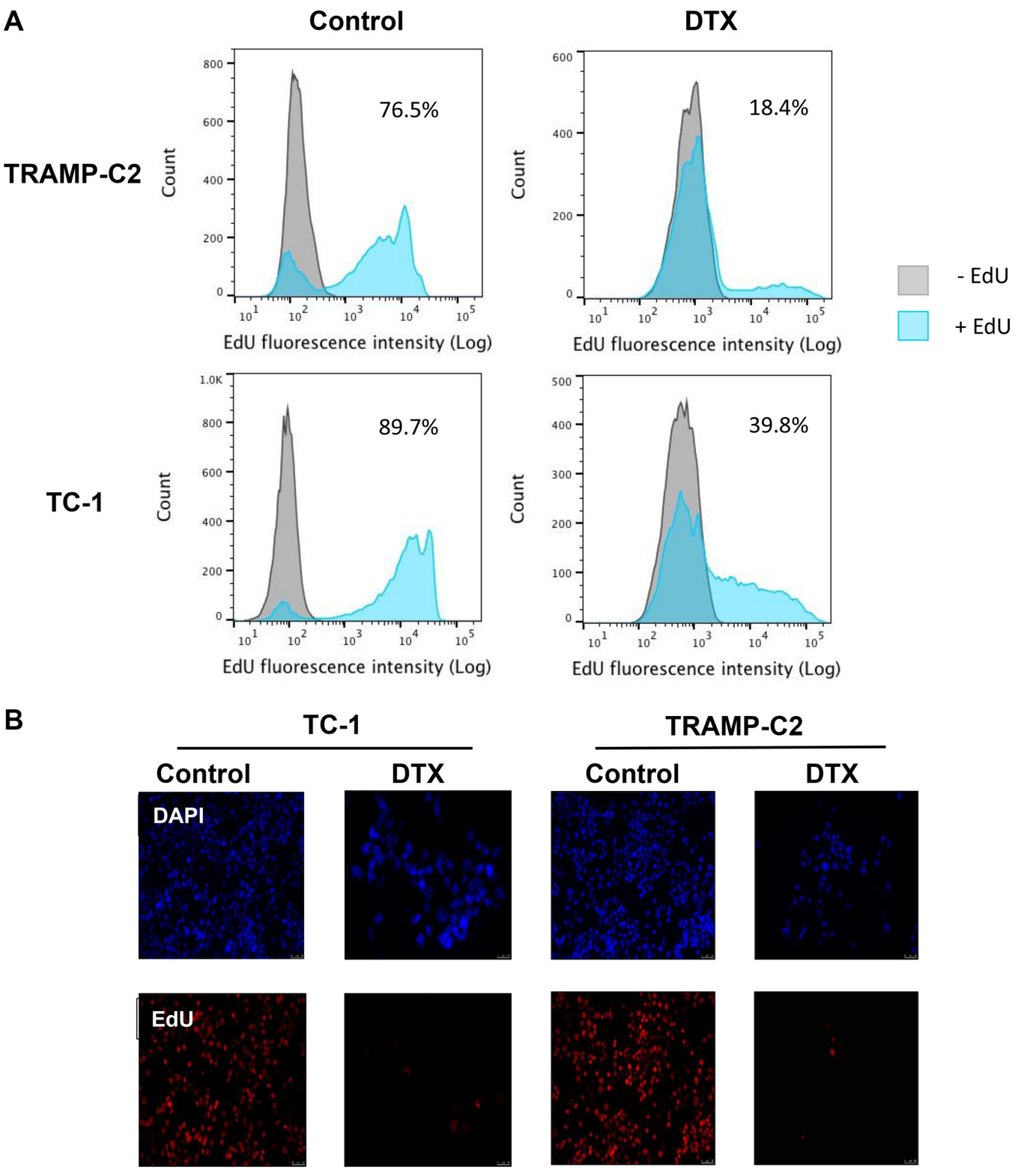


**Figure 2: Analysis of TC-1 and TRAMP-C2 cell proliferation by EdU incorporation.** The cells were driven to senescence by 4-day treatment with 7.5 μM docetaxel (DTX) and then incubated with 10 μM EdU for 6 h. Click-iT reaction was performed on fixed cells and FACS analysis was carried out to determine the fraction of proliferating cells in DTX-treated and control samples (**A**). Control and DTX-treated TC-1 and TRAMP-C2 cells were incubated with 10 μM EdU for 6 h. Following fixation, Click-iT reaction was performed and the coverslips were mounted with Mowiol containing DAPI (**B**).

bypass senescence *in vivo* in our settings and thus they did not contribute to the growing cell mass of the tumor. On the other hand, admixture of proliferating instead of senescent TRAMP-C2 cells resulted in tumors consisting of both TC-1 and TRAMP-C2 cells, in spite of the fact that the TRAMP-C2 cells were injected in a number lower than the number of cells sufficient to ensure tumor growth in all injected animals. Collectively, these data demonstrate that bystander senescent tumor cells can evoke a tumor growth-promoting microenvironment, a property shared by bystander lethally irradiated tumor cells.

## IL-12-based immunotherapy suppresses senescence-accelerated tumor growth

We have previously reported induction of IFNγ upon *in vivo* administration of an IL-12-producing cellular vaccine by ELISPOT analysis of spleen cells, as well as

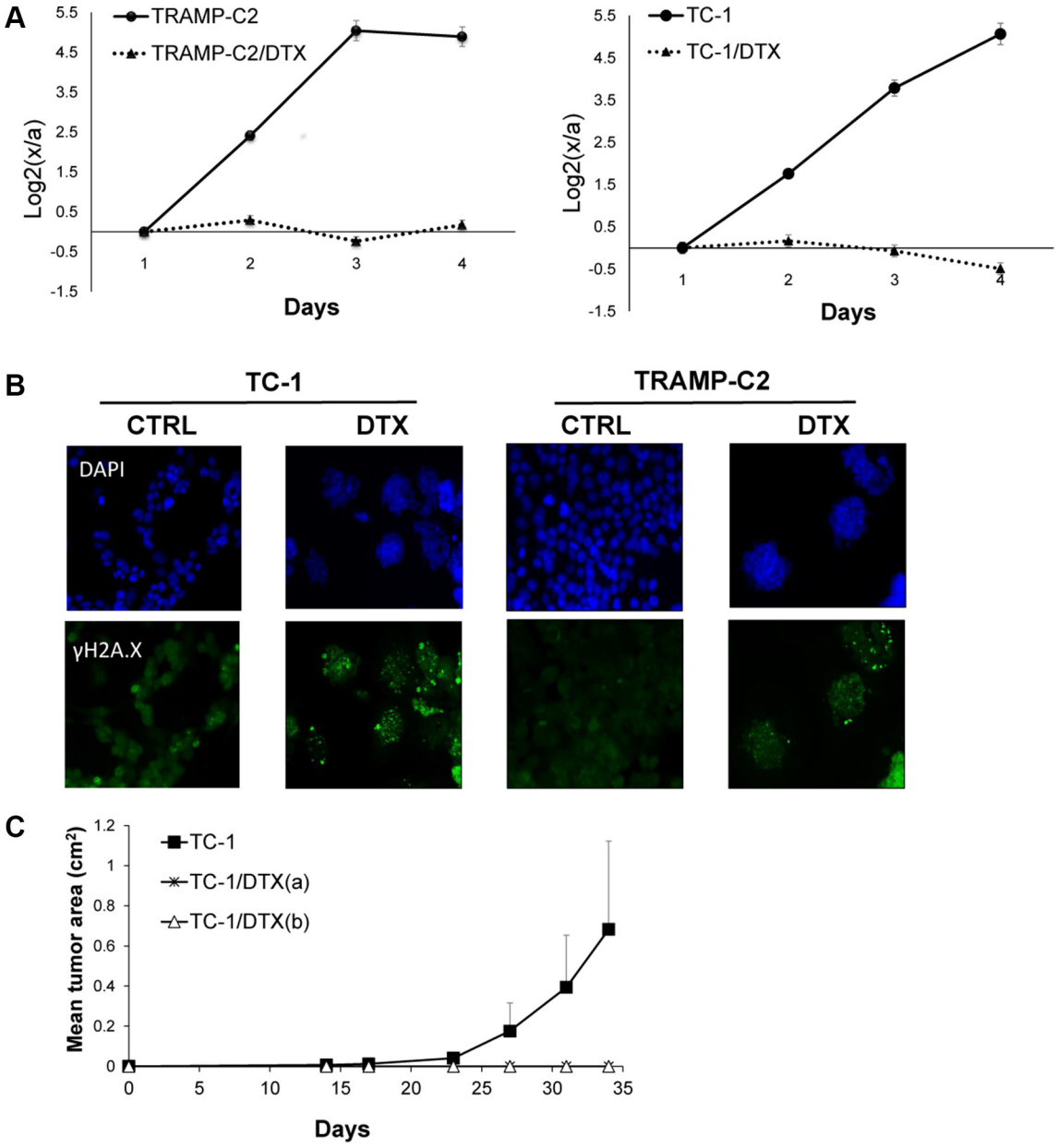


**Figure 3: Docetaxel-induced DNA damage and senescence in TC-1 and TRAMP-C2 cell lines *in vitro* and *in vivo*.** Cells were seeded onto 6-well plates in triplicates and treated with 7.5 μM docetaxel (DTX) or left untreated (control). Cell proliferation was determined by counting cell number every 24 h and plotted as $\log_2$ ratio of final cell number to number of seeded cells, to compensate for differential seeding capacity of control versus the DTX-treated cells (**A**). To detect DNA damage, control and DTX-treated cells were stained with phosphoSer139 H2AX (γH2AX) antibody and mounted with Mowiol containing DAPI (**B**). Mice were transplanted s.c. on day 0 with TC-1 cells ($3 \times 10^4$) or with senescent DTX-treated cells at the doses $3 \times 10^4$ [TC-1/DTX(a)] or $5 \times 10^5$ [TC-1/DTX(b)] tumor cells, respectively, and the tumor growth was monitored. The experiment was repeated three times with similar results (**C**).

determination of the IFNγ levels in plasma by ELISA [24]. Given that IL-12-mediated antitumor effects are associated with induction of IFNγ, we have hypothesized that immunotherapy with IL-12 could be effective against both the proliferating and senescent tumor cells by concomitantly inducing non-specific as well as specific immune responses and thereby inhibiting growth of the senescent cell-accelerated tumors. To test this working hypothesis, here we employed irradiated IL-12-producing TC-1-derived cells, injected into the vicinity of *in vivo* growing tumors in two scenarios: i) either tumors growing from proliferating TC-1 cells alone, or ii) tumors growing in an accelerated fashion upon co-injection of the proliferating TC-1 cells with TC-1/DTX senescent cells. Consistent with our hypothesis, compared to rapid growth of mock-treated tumors, treatment with the IL-12-producing TC-1-based cellular vaccine greatly inhibited tumor growth under both tumorigenic scenarios (Figure 6). We conclude from these *in vivo* experiments that IL-12-based immunotherapy strategies analogous to the one we evaluated in this pre-clinical study may be effective also against the accelerated tumor growth fueled by the local microenvironment modified by the presence of bystander tumor senescent cells.

## DISCUSSION

From a broader perspective, our present results contribute to the field of tumor cell senescence and immunotherapy in several ways.

First, we show that chemotherapy-induced (here by DTX treatments) tumor cell senescence can indeed exert a tumor-promoting effect under syngeneic *in vivo* conditions. DTX, a chemotherapeutic agent used either alone or in standard-of-care combination treatments

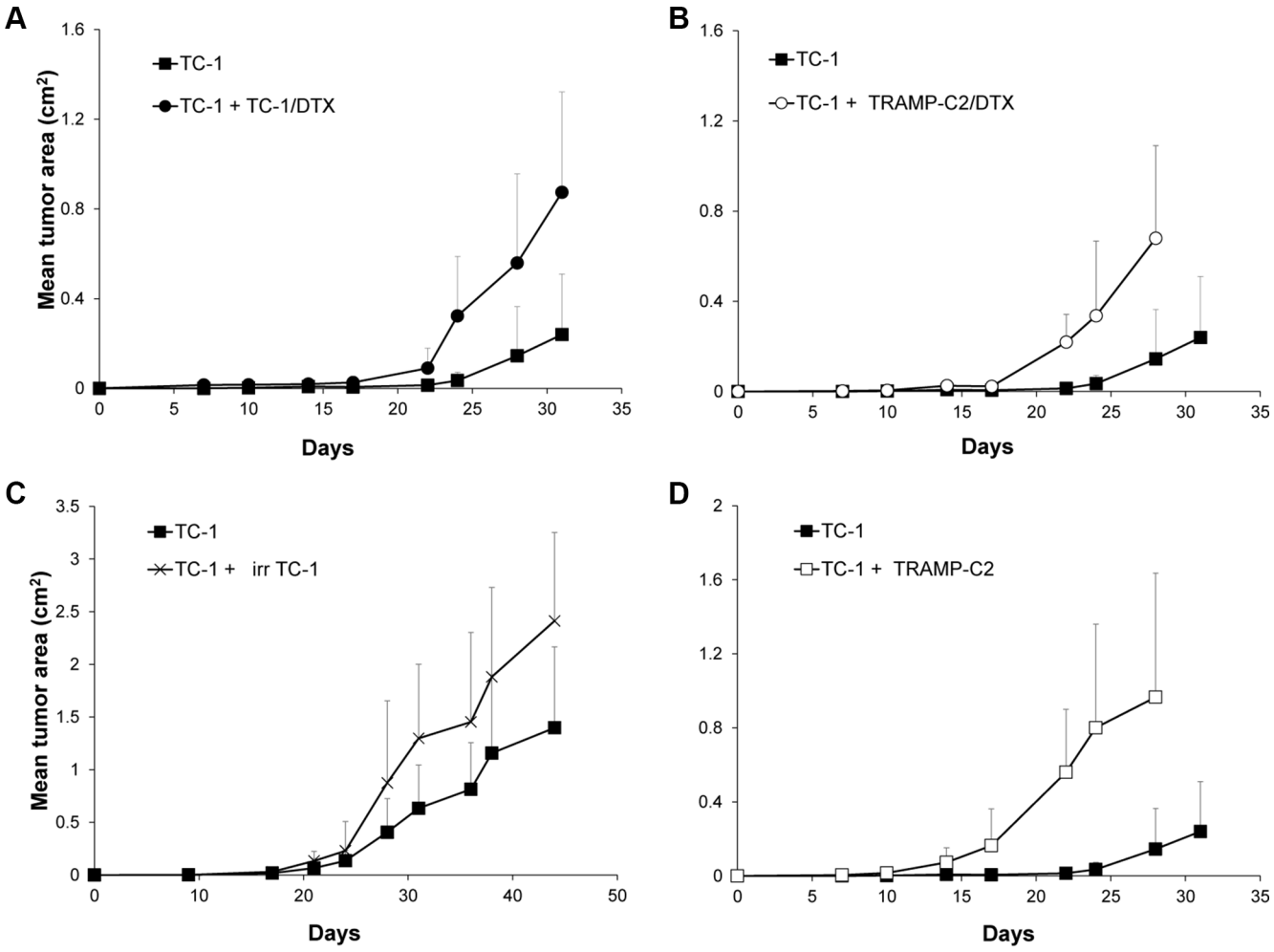


**Figure 4: Co-administration of DTX-treated senescent cells accelerates tumor growth.** Mice were transplanted s.c. on day 0 with TC-1 cells ($3 \times 10^4$ cells per mouse) admixed with senescent, DTX-treated TC-1 cells (TC-1/DTX; $3 \times 10^5$) (**A**); with senescent, DTX-treated TRAMP-C2 cells (TRAMP-C2/DTX; $3 \times 10^5$ cells per mouse) (**B**); with irradiated TC-1 cells (150 Gy; $3 \times 10^5$ cells per mouse) (**C**); or proliferating TRAMP-C2 cells ($3 \times 10^5$) (**D**). Controls were mice transplanted s.c. on day 0 with proliferating TC-1 cells ($3 \times 10^4$ cells per mouse) only. In all experiments, significant acceleration of the tumor growth was observed ($p < 0.05$). The experiments were repeated three times with similar results.

for various types of human malignancies, has been previously shown to induce massive cellular senescence in several tumor cell lines [23, 25]. In this study, we have demonstrated that DTX, when administered to two tumorigenic cell lines TC-1 and TRAMP-C2 *in vitro* in subapoptotic doses, induced persistent DNA damage response, cell cycle arrest and development of senescence-like phenotype accompanied by complex alteration of cytokine expression/secretion. This is in agreement with the current views that DNA damage signaling and repair networks are closely tied with the immune response signaling pathways [26]. Dependent on (patho) physiological context, such links can have either positive or detrimental impact on organismal health. Although pro-tumorigenic effects of senescent cells, namely fibroblasts, mediated by their SASP have been studied in the past [6], there has been paucity of studies documenting pro-tumorigenic effects of tumor cells brought into senescence by genotoxic chemotherapeutic agents, a gap in our knowledge partly filled by our present results.

Second, our major objective was to set up an *in vivo* model in which the impact of senescent cells on tumor growth could be investigated in the context of non-immunocompromised syngeneic animals, to better

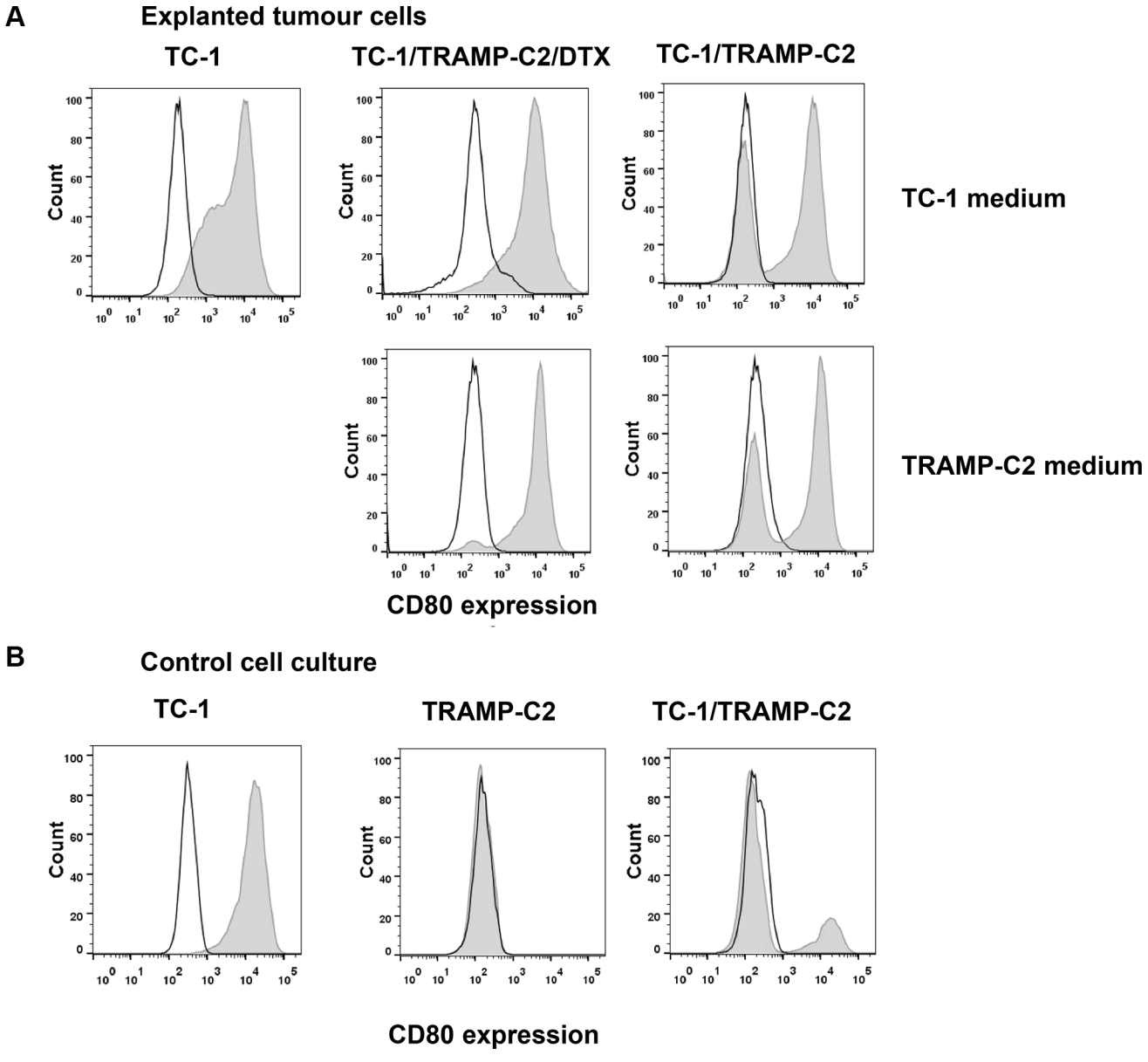


**Figure 5: Cell surface marker analysis of explanted tumor cells.** Explanted tumor cells were cultured for seven days and analyzed for the proportion of TC-1 ($CD80^+$) and TRAMP-C2 ($CD80^-$) cells by flow cytometry using CD80 as a marker (filled histograms; empty histograms represent isotype controls). To exclude leukocytes from the analysis, $CD45^+$ cells were gated out. For comparison, explanted cells were cultured in the culture medium optimized either for TC-1 cells (upper row) or for TRAMP-C2 cells (lower row) (**A**). Flow cytometry analysis of the CD80 cell surface expression on cultured TC-1 and TRAMP-C2 cells, as well as their mixed culture (**B**).

mimic the clinical human scenario. We argued that such model would help elucidate the biological impact of bystander senescent tumor cells under conditions permissive for interactions of the growing tumor with the host immune system, a complex interplay that can dramatically influence tumor microenvironment and cancer development in general. This fundamental biological aspect of tumorigenesis is unfortunately missing in the widely used xenograft tumor models based on immunodeficient animals, and it is a major advantage of the dataset presented here.

Another major advantage of our present study is the nature of the senescent cells used in our *in vivo* experiments. Thus, most previous studies dealt with the effects of senescent fibroblasts present in the tumor stroma on the proliferation of human tumor cells. Bavik et al. have demonstrated that both direct co-culture and conditioned medium from senescent fibroblasts stimulated neoplastic epithelial cells proliferation *in vitro* [27]. Further, senescent fibroblasts have been shown to promote neoplastic transformation of partially transformed ovarian epithelial cells in a three dimensional spheroid cell culture model [28]. Moreover, *in vivo* experiments were performed using nude mice in which xenograft tumor growth was monitored. Accelerated tumor growth was observed when senescent fibroblasts ($1.5 \times 10^6$ cells) were co-injected with the same number of proliferating MDA-231 human breast cancer cells into (*nu/nu*) mice [14]. However, in the study performed by Ewald et al., the admixture of $0.5 \times 10^6$ senescent doxorubicin-treated DU-145 human prostate cancer cells with the equal number of proliferating cells did not result in any growth acceleration of the xenografted tumor [8]. In contrast, in our present study using syngeneic immunocompetent C57BL/6 model, we observed that the presence of senescent syngeneic tumor cells did augment the growth of tumors *in vivo*. We propose that the apparent discrepancy between the negative data of Ewald et al. [14] on the one hand, and our positive results documenting tumor growth acceleration on the other, might be attributable to better fitness and proliferation potential of tumor cells in the syngeneic system, cell type specific sensitivity or differences in the SASP of senescent cells or, importantly, the requirement of interactions between the senescent cells and the immune system or developing tumor stroma. Indeed, these important factors that are present in our syngeneic, immunocompetent model system, cannot be established in any heterologous system due to an uneven compatibility of mouse and human signaling components and compromised immunity. In addition, we believe that using much fewer senescent cells in our present experiments (we used the ratio between the proliferating tumor cells: $3 \times 10^4$ cells/mouse, and the admixed docetaxel-treated senescent TC-1 or TRAMP-C2 cells at $3 \times 10^5$ cells/mouse), compared to higher amounts of senescent cells in the previous studies [14], is a more realistic scenario that further supports the value of our model system.

Notably, our analysis of cytokine and chemokine transcript levels in the DTX-treated senescent tumor cells demonstrated upregulation of numerous cytokine species including those implicated in supporting tumor growth (such as CXCL1, IL-1 or IL-6). This effect of docetaxel is in accord with previous studies showing that persistent DNA damage response induced by various chemotherapeutics results in complex changes in cytokine expression and secretion (reviewed in [6]). As expected,

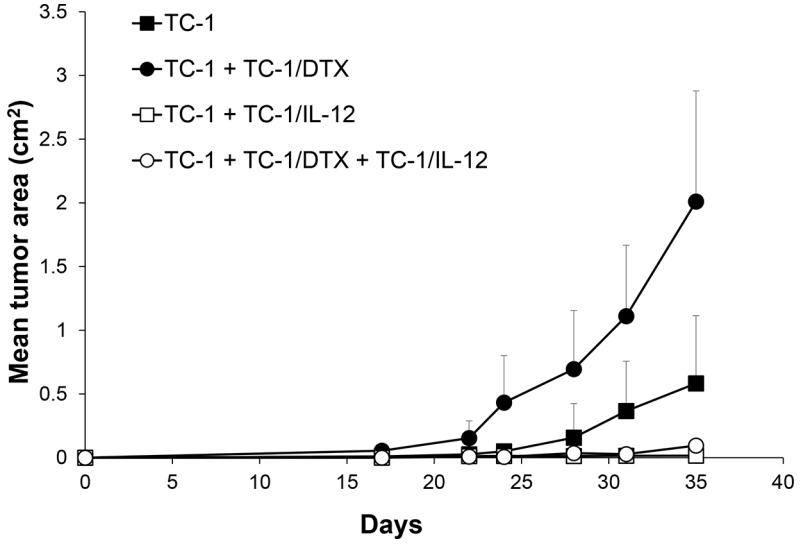


**Figure 6: IL-12-based immunotherapy suppresses senescence-accelerated tumor growth.** Mice were transplanted on day 0 s.c. with TC-1 cells ($3 \times 10^4$), docetaxel-induced senescent TC-1/DTX ($3 \times 10^5$) or TC-1 cells ($3 \times 10^4$) admixed with TC-1/DTX. IL-12 producing TC-1/IL-12 cells were administered on day 3 in the vicinity of transplanted control TC-1 cells and TC-1 cells admixture with TC-1/DTX senescent cells. The experiment was repeated twice with similar results. $p < 0.05$ TC-1 as compared to TC-1/DTX; $p < 0.05$ TC-1 as compared to TC-1 + TC-1/IL-12; $p < 0.05$ TC-1 + TC-1/DTX vs. TC-1 + TC-1/DTX + TC-1/IL-12.

when comparing cytokine profiles among different cell lines, there are some variations in the levels of specific cytokines. However, some shared, consistently altered species found in human senescent cells such as IL6 and CSF2 are also present in the secretome of the DXT-induced mouse senescent cells used here. For given tumor cells, these variations in secreted signaling ligands can have specific contributions to their respective tumor microenvironment and can possibly result in distinct responses to the same therapeutics.

In control experiments, we have proved that the growth acceleration could be achieved also by a senescent tumor cell type distinct from the proliferating one. This suggests that senescent cells can promote growth of tumor cells of different tissue origin, thus potentially fueling secondary malignancies of either the same or different tissues exposed to chemotherapy. Furthermore, relevant to radiotherapy and its potential late adverse effects, we show here in yet another set of experiments that also cells in which genotoxic stress was induced by irradiation, rather than chemotherapy, share the capacity to promote accelerated tumor growth.

There is still debate on 'stability' versus reversibility of the senescence phenotype, and there is mounting evidence that senescent cells can sometimes bypass their growth arrest and re-enter the cell cycle [29]. Interestingly, docetaxel-treated tumor cells can form polyploid senescent cells and subsequently re-enter the cell cycle and acquire a chemoresistant phenotype [30]. However, our analyses of the cell surface markers of the explanted tumor cells that formed the established tumors after TC-1 inoculation, the growth of which had been accelerated by the presence of senescent TRAMP-C2 cells, did not suggest any significant degree of senescence bypass among the TRAMP-C2 cells, since the vast majority of the explanted tumor cells were of TC-1 origin. These data suggest that the tumor growth was accelerated by paracrine pro-tumorigenic effects of the bystander senescent tumor cells. Unfortunately, in the scenario we have used, it is impossible to distinguish between direct effects on tumor cell proliferation versus more indirect impact through the tumor microenvironment or antitumor immunity, as the critical processes probably occurred shortly upon tumor cell administration when they are very difficult to follow. In a control experiment, in which TC-1 tumor cells were co-administered with proliferating TRAMP-C2 cells (although in suboptimal dose), analysis of cells from explanted tumors revealed that both TC-1 and TRAMP-C2 cells were present, as expected.

The major objective of our study was to develop a murine model that would enable us to test the immunotherapy efficacy in elimination of senescent cells and/or their detrimental tumor promoting effects and to demonstrate the effectiveness of the immunotherapy approach. Although senescent cells do not proliferate, they remain alive *in vitro* for long periods of time. Using a mouse liver carcinoma model, it has been demonstrated, that senescent tumor cells induced innate immune response due to their inflammatory cytokine secretion, accompanied by increase of leukocyte attracting molecules like ICAM1 or VCAM1. Consequently, senescent tumor cells were cleared from the organism [31]. Senescent cells can also induce specific immunity, as has been illustrated through their use as experimental cellular vaccines [32]. These facts suggest that detrimental effects of senescent cells can be eliminated using effective immunotherapy. IL-12, as a cytokine bridging innate and adaptive immunity, capable of activating NK cells, as well as inducing Th1 immune responses, appears to be a suitable candidate for such treatment. We have previously demonstrated the potential of IL-12-producing cellular vaccines that can be conveniently administered in the tumor vicinity, in several therapeutic chemo-immunotherapeutic settings. Here, we advance such studies and clearly document that the IL-12-based therapy can effectively inhibit development of tumors, including those whose growth was accelerated by the presence of bystander senescent cells.

Collectively, our work presented here has established a murine model that is beneficial for research into pro-tumorigenic effects of senescent cells, as well as innovative therapeutic strategies. Last but not least, our present dataset has documented that IL-12-mediated therapy may represent a feasible way to minimize or eliminate the adverse tumor-promoting effects of bystander senescent cells that may accumulate *in vivo* either due to endogenous oncogene-induced stimuli or insults caused by genotoxic chemotherapy and radiotherapy.

## MATERIALS AND METHODS

### Cell culture

TC-1 cell line was obtained by *in vitro* co-transfection of murine lung C57BL/6 cells with HPV16 *E6/E7* and activated human *H-Ras* (G12V) oncogenes [33]. IL-12-gene modified TC-1/IL-12 (231/clone 15) cells used for immunotherapy produced *in vitro* 40 ng IL-12/1 × $10^5$ cells/ml medium/48 h and were irradiated (150 Gy) before use [34]. TC-1 cells were cultured in RPMI 1640 medium supplemented with 10% fetal calf serum, L-glutamine and antibiotics. TRAMP-C2 prostate carcinoma cells [35] were obtained from ATCC collection. TRAMP-C2 cells were maintained in D-MEM medium (Sigma-Aldrich, Saint Louis, MO, USA) supplemented with 5% FCS, Nu-Serum IV (5%; BD Biosciences, Bedford, MA, USA), 5 mg/ml human insulin (Sigma-Aldrich), dehydroisoandrosterone (DHEA, 10 nM; Sigma-Aldrich) and antibiotics [36].

### Induction of senescence and characterization of senescent cells

To induce senescence in tumor cells, cells were cultured for 4 days in medium containing 7.5 μM DTX (Actavis, North Brunswick, NJ). Senescence was evaluated by using Senescence β-galactosidase Staining Kit (Cell Signaling Technology, Danvers, MA, USA) according to manufacturer's instructions. Images were captured by Dino-Lite (Dino-Lite Europe (Naarden, Netherlands) by using inverted tissue culture microscope Nicon TMS (Nicon, Tokyo, Japan) and by inverted tissue culture microscope Nicon Eclipse TE300 (Nicon, Tokyo, Japan) equipped with Leica DFC490 camera and LAS AF software (Leica Microsystems, Wetzlar, Germany).

### Antibodies

The following antibodies were used for immunoblotting: anti-mouse $p21^{waf1/cip1}$ (p21) rabbit monoclonal antibody (ab109199) and anti-mouse p16INK4A (p16) rabbit polyclonal antibody (ab189034) were purchased from Abcam (Cambridge, UK), anti-mouse GAPDH rabbit monoclonal antibody (14C10) was purchased from Cell Signaling Technology (Danvers, MA, USA). IgG-HRP anti-rabbit secondary antibody produced in goat (170–6515) was purchased from Bio-Rad Laboratories (Hercules, CA, USA).

### SDS-PAGE and immunoblotting

Cells were washed with PBS, harvested into Laemmli SDS sample lysis buffer (2% SDS, 50 mM Tris-Cl, 10% glycerol in double distilled water) and sufficiently sonicated (3 × 15 seconds at 4 micron amplitude with 15 seconds cooling intervals) on Soniprep 150 (MSE, London, UK). Concentration of proteins was estimated by the BCA method (Pierce Biotechnology, IL, Rockford, USA). 100 mM DTT and 0.01% bromphenol blue was added to lysates before separation by SDS-PAGE (14% gel was used). The same protein amount (35 μg) was loaded into each well. Proteins were electrotransferred onto a nitrocellulose membrane using wet transfer and detected by specific antibodies combined with horseradish peroxidase-conjugated secondary antibody. Peroxidase activity was detected by ECL (Pierce Biotechnology). GAPDH was used as a marker of equal loading.

### Quantitative real time PCR (qRT-PCR)

Total RNA samples were isolated using RNeasy Mini Kit (Qiagen Sciences, Germantown, MD, USA). First strand cDNA was synthesized from 500 ng of total RNA with random hexamer primers using High-Capacity cDNA Reverse Transcription kit (Applied Biosystems, Foster City, CA, USA). qRT-PCR was performed in ABI Prism 7300 (Applied Biosystems) using SYBR Select Master Mix containing SYBR GreenE dye (Applied Biosystems). The relative quantity of cDNA was estimated by ΔΔCT method and data were normalized to β-actin (ACTB). Following primers were purchased from East Port (Prague, Czech Republic): ACTB_fw: 5′-CATTGCTGACAGGATGCAGAAGG-3′, ACTB_rev: 5′-TGCTGGAAGGTGGACAGTGAGG-3′; p21_fw: 5′-CAGATCCACAGCGATATCCA-3′, p21_rev: 5′-ACGGGACCGAAGAGACAAC-3′; and p16_fw: 5′-CGTGAACATGTTGTTGAGGC-3′, p16_rev: 5′-GCAGAAGAGCTGCTACGTGA-3′. Data represent values from three independent experiments performed in 3 technical replicates.

### EdU incorporation, Click-iT reaction and FACS analysis

TRAMP-C2 and TC-1 cells were driven to senescence by DTX as described above. On the fourth day of DTX treatment, cells were incubated with 10 μM 5-ethynyl-2′-deoxyuridine (EdU) for 6 h. For Click-iT reaction cells were washed by PBS, detached by trypsin, washed by PBS again and fixed by 4% formaldehyde for 15 min. The fixed cells were washed in PBS, permeabilized by 0.2% Triton X-100 for 5 min and washed by 1% BSA/PBS. Click-iT reaction was performed with Click-iT EdU Alexa Fluor 647 Kit (Invitrogen, Carlsbad, CA, USA) according to manufacturer's instructions. After that, cells were washed twice in PBS and resuspended in fresh PBS for FACS analysis. FACS analysis was performed using an LSR II flow cytometer (BD Biosciences) and data analyzed by FlowJo 7.6.5 software.

### FACS analysis of explanted tumor cells

Cell surface expression of CD45 and CD80 on the tumor cells explanted from tumor bearing mice was analyzed by flow cytometry. Cell suspensions were washed and preincubated with anti-CD16/CD32 antibody to minimize non-specific binding for 15 min at 4°C following washing step and incubation with labeled primary antibody for 30 min at 4°C. Relevant isotype controls of irrelevant specificity were used. FACS buffer (PBS, 1% FBS, 0.1% $NaN_3$) was used for all washing steps and analysis. The following antibodies were used: PE anti-CD80 (16-10A1), PE anti-CD86 (GL1), BV421 anti-CD45 (30-F11) (BD Biosciences, San Jose, CA); FACS analysis was performed using an LSR II flow cytometer (BD Biosciences) and data analyzed by FlowJo 7.6.5 software.

### Immunolabeling and fluorescence microscopy

Cells were grown on glass coverslips were driven to senescence by DTX as described above. On the fourth day of DTX treatment, cells were fixed by 4% formaldehyde

for 20 min and permeabilized by 0.2% Triton X-100 for 5 min. Subsequently, cells were washed with PBS, blocked in 25% FBS/PBS for 30 min and stained with primary antibodies diluted in 1% BSA/PBS for 1 h. After double-wash by PBS cells were stained with secondary antibody diluted in 1% BSA/PBS for 45 min, double-washed by PBS again and mounted in Mowiol, containing 4′,6-diamidine-2-phenylindole (DAPI; Sigma) counter-stain (1 mg/ml). Fluorescence microscopy was performed using fluorescence microscope Leica CTR6000 (Leica Microsystems) equipped with monochrome digital camera DFC350 FX and Leica LAS AF Lite software.

The antibodies used: phospho-Ser139 H2AX, rabbit, polyclonal, Cell Signaling, 1 : 200; Alexa 488 goat anti-rabbit, Invitrogen, 1 : 1000.

### Cytokine array

Cells were seeded into 75 $cm^2$ flasks (1 – 3 × $10^6$ cells/flask) and after 6 h, DTX was added to a final concentration of 7.5 μM and cells were cultivated for 96 h with/without DTX (7.5 μM). Expression of selected chemokines/cytokines by tumor cells was analyzed using Mouse Cytokines & Chemokines PCR Array (PAMM-150ZG-4, QIAGEN) according to the manufacturer's instructions.

### Mice

C57BL/6 male mice, 6 - 8 weeks old, were obtained from AnLab Co., Prague, Czech Republic. Experimental protocols were approved by the Institutional Animal Care Committee of the Institute of Molecular Genetics, Prague.

### *In vivo* experiments

Mice (8 - 10 per group) were transplanted on day 0 s.c. with control TC-1 cells (3 × $10^4$), DTX-induced senescent TC-1/DTX or TRAMP-C2/DTX cells (3 × $10^5$) or control TC-1 cells (3 × $10^4$) admixed with TC-1/DTX or TRAMP-C2/DTX cells. For control, irradiated TC-1 cells (150 Gy), TRAMP-C2 cells injected in admixture with TC-1 cells were used. To characterize growing tumors, some tumors were explanted, cultured *in vitro* for 7 days and the surface expression of CD80 was analyzed by FACS. IL-12 producing TC-1/IL-12 cells were used in therapeutic experiments. Cells were administered on day 3 in the vicinity of transplanted control TC-1 cells and TC-1 cells admixture with TC-1/DTX senescent cells. Mice were observed twice a week and the size of the tumors was recorded. Two perpendicular diameters of the tumors were measured with a caliper and the tumor size was expressed as the tumor area ($cm^2$).

### Data processing and statistical analyses

For evaluation of *in vitro* experiments, graph concerning qRT-PCR data was generated using Prism 5 (GraphPad Software, La Jolla, CA USA). qRT-PCR data represent mean ± S.D. *p*-values were calculated using student *t*-Test for two samples assuming unequal variances (Microsoft Excel 2010, Microsoft, Redmond, WA, USA). $p < 0.05$ was considered statistically significant.

For evaluation of *in vivo* experiments, Analysis of Variance (ANOVA) from the NCSS, Number Cruncher Statistical System (Kaysville, Utah, USA) statistical package was utilized. Standard deviations are indicated in the Figures.

## ACKNOWLEDGMENTS

The authors are grateful to Mrs. Renata Tureckova for skillful technical assistance.

## CONFLICTS OF INTEREST

All authors declare no competing financial interests.

## GRANT SUPPORT

This work was supported by research grant NT14461 grant from the Grant Agency of the Ministry of Health of the Czech Republic.

## REFERENCES

1. Bartkova J, Rezaei N, Liontos M, Karakaidos P, Kletsas D, Issaeva N, Vassiliou LV, Kolettas E, Niforou K, Zoumpourlis VC, Takaoka M, Nakagawa H, Tort F, et al. Oncogene-induced senescence is part of the tumorigenesis barrier imposed by DNA damage checkpoints. Nature. 2006; 444:633–637.
2. Di Micco R, Fumagalli M, Cicalese A, Piccinin S, Gasparini P, Luise C, Schurra C, Garre M, Nuciforo PG, Bensimon A, Maestro R, Pelicci PG, d'Adda di Fagagna F. Oncogene-induced senescence is a DNA damage response triggered by DNA hyper-replication. Nature. 2006; 444:638–642.
3. Sager R. Senescence as a mode of tumor suppression. Environ Health Perspect. 1991; 93:59–62.
4. Campisi J. Senescent cells, tumor suppression, and organismal aging: good citizens, bad neighbors. Cell. 2005; 120:513–522.
5. Coppe JP, Patil CK, Rodier F, Sun Y, Munoz DP, Goldstein J, Nelson PS, Desprez PY, Campisi J. Senescence-associated secretory phenotypes reveal cell-nonautonomous functions of oncogenic RAS and the p53 tumor suppressor. PLoS Biol. 2008; 6:2853–2868.

6. Davalos AR, Coppe JP, Campisi J, Desprez PY. Senescent cells as a source of inflammatory factors for tumor progression. Cancer Metastasis Rev. 2010; 29:273–283.
7. Coppe JP, Desprez PY, Krtolica A, Campisi J. The senescence-associated secretory phenotype: the dark side of tumor suppression. Annu Rev Pathol. 2010; 5:99–118.
8. Ewald J, Desotelle J, Almassi N, Jarrard D. Drug-induced senescence bystander proliferation in prostate cancer cells *in vitro* and *in vivo*. Br J Cancer. 2008; 98:1244–1249.
9. Gewirtz DA, Holt SE, Elmore LW. Accelerated senescence: an emerging role in tumor cell response to chemotherapy and radiation. Biochem Pharmacol. 2008; 76:947–957.
10. Hoenicke L, Zender L. Immune surveillance of senescent cells—biological significance in cancer- and non-cancer pathologies. Carcinogenesis. 2012; 33:1123–1126.
11. Kang TW, Yevsa T, Woller N, Hoenicke L, Wuestefeld T, Dauch D, Hohmeyer A, Gereke M, Rudalska R, Potapova A, Iken M, Vucur M, Weiss S, et al. Senescence surveillance of pre-malignant hepatocytes limits liver cancer development. Nature. 2011; 479:547–551.
12. Jackson James G, Pant V, Li Q, Chang Leslie L, Quintás-Cardama A, Garza D, Tavana O, Yang P, Manshouri T, Li Y, El-Naggar Adel K, Lozano G. p53-Mediated Senescence Impairs the Apoptotic Response to Chemotherapy and Clinical Outcome in Breast Cancer. Cancer Cell. 2012; 21:793–806.
13. Baker DJ, Wijshake T, Tchkonia T, LeBrasseur NK, Childs BG, van de Sluis B, Kirkland JL, van Deursen JM. Clearance of p16Ink4a-positive senescent cells delays ageing-associated disorders. Nature. 2011; 479:232–236.
14. Krtolica A, Parrinello S, Lockett S, Desprez PY, Campisi J. Senescent fibroblasts promote epithelial cell growth and tumorigenesis: a link between cancer and aging. Proc Natl Acad Sci U S A. 2001; 98:12072–12077.
15. Tugues S, Burkhard SH, Ohs I, Vrohlings M, Nussbaum K, Vom Berg J, Kulig P, Becher B. New insights into IL-12-mediated tumor suppression. Cell Death Differ. 2015; 22:237–246.
16. Grufman P, Karre K. Innate and adaptive immunity to tumors: IL-12 is required for optimal responses. Eur J Immunol. 2000; 30:1088–1093.
17. Dranoff G. Cytokines in cancer pathogenesis and cancer therapy. Nat Rev Cancer. 2004; 4:11–22.
18. Indrova M, Bieblova J, Bubenik J, Reinis M. IL-12 immunotherapy of minimal residual disease in murine models of HPV16-associated tumours: induction of immune responses, cytokine production and kinetics of immune cell subsets. Int J Oncol. 2008; 32:499–507.
19. Indrova M, Bieblova J, Rossowska J, Kuropka P, Pajtasz-Piasecka E, Bubenik J, Reinis M. HPV 16-associated tumours: IL-12 can repair the absence of cytotoxic and proliferative responses of tumour infiltrating cells after chemotherapy. Int J Oncol. 2009; 34:173–179.
20. Bubenik J. Cytokine gene-modified vaccines in the therapy of cancer. Pharmacol Ther. 1996; 69:1–14.
21. Bubenik J. Genetically modified tumour vaccines carrying inserted genes for immunoregulatory molecules. Folia Biol (Praha). 1996; 42:295–304.
22. Bubenik J. Interleukin 12 in cancer treatment. Folia Biol (Praha). 2011; 57:1–2.
23. Schwarze SR, Fu VX, Desotelle JA, Kenowski ML, Jarrard DF. The identification of senescence-specific genes during the induction of senescence in prostate cancer cells. Neoplasia. 2005; 7:816–823.
24. Simova J, Pollakova V, Indrova M, Mikyskova R, Bieblova J, Stepanek I, Bubenik J, Reinis M. Immunotherapy augments the effect of 5-azacytidine on HPV16-associated tumours with different MHC class I-expression status. Br J Cancer. 2011; 105:1533–1541.
25. Di Mitri D, Toso A, Chen JJ, Sarti M, Pinton S, Jost TR, D'Antuono R, Montani E, Garcia-Escudero R, Guccini I, Da Silva-Alvarez S, Collado M, Eisenberger M, et al. Tumour-infiltrating Gr-1+ myeloid cells antagonize senescence in cancer. Nature. 2014; 515:134–137.
26. Pateras IS, Havaki S, Nikitopoulou X, Vougas K, Townsend PA, Panayiotidis MI, Georgakilas AG, Gorgoulis VG. The DNA damage response and immune signaling alliance: Is it good or bad? Nature decides when and where. Pharmacology & Therapeutics. 2015; 154:36–56.
27. Bavik C, Coleman I, Dean JP, Knudsen B, Plymate S, Nelson PS. The gene expression program of prostate fibroblast senescence modulates neoplastic epithelial cell proliferation through paracrine mechanisms. Cancer Res. 2006; 66:794–802.
28. Lawrenson K, Grun B, Benjamin E, Jacobs IJ, Dafou D, Gayther SA. Senescent fibroblasts promote neoplastic transformation of partially transformed ovarian epithelial cells in a three-dimensional model of early stage ovarian cancer. Neoplasia. 2010; 12:317–325.
29. Beausejour CM, Krtolica A, Galimi F, Narita M, Lowe SW, Yaswen P, Campisi J. Reversal of human cellular senescence: roles of the p53 and p16 pathways. Embo J. 2003; 22:4212–4222.
30. Ogden A, Rida PC, Knudsen BS, Kucuk O, Aneja R. Docetaxel-induced polyploidization may underlie chemoresistance and disease relapse. Cancer Lett. 2015; 367:89–92.
31. Xue W, Zender L, Miething C, Dickins RA, Hernando E, Krizhanovsky V, Cordon-Cardo C, Lowe SW. Senescence and tumour clearance is triggered by p53 restoration in murine liver carcinomas. Nature. 2007; 445:656–660.
32. Meng Y, Efimova EV, Hamzeh KW, Darga TE, Mauceri HJ, Fu YX, Kron SJ, Weichselbaum RR. Radiation-inducible immunotherapy for cancer: senescent tumor cells as a cancer vaccine. Mol Ther. 2012; 20:1046–1055.
33. Lin KY, Guarnieri FG, Staveley-O'Carroll KF, Levitsky HI, August JT, Pardoll DM, Wu TC. Treatment of established

tumors with a novel vaccine that enhances major histocompatibility class II presentation of tumor antigen. Cancer Res. 1996; 56:21–26.

34. Indrova M, Bieblova J, Jandlova T, Vonka V, Pajtasz-Piasecka E, Reinis M. Chemotherapy, IL-12 gene therapy and combined adjuvant therapy of HPV 16-associated MHC class I-proficient and -deficient tumours. Int J Oncol. 2006; 28:253–259.

35. Foster BA, Gingrich JR, Kwon ED, Madias C, Greenberg NM. Characterization of prostatic epithelial cell lines derived from transgenic adenocarcinoma of the mouse prostate (TRAMP) model. Cancer Res. 1997; 57:3325–3330.

36. Mikyskova R, Stepanek I, Indrova M, Bieblova J, Simova J, Truxova I, Moserova I, Fucikova J, Bartunkova J, Spisek R, Reinis M. Dendritic cells pulsed with tumor cells killed by high hydrostatic pressure induce strong immune responses and display therapeutic effects both in murine TC-1 and TRAMP-C2 tumors when combined with docetaxel chemotherapy. Int J Oncol. 2016; 48:953–964.

**Supplementary Table S1: Cytokine and chemokine mRNA levels of TC-1 and TRAMP-C2 cell lines treated with DTX**

| | | TC-1 | TRAMP-C2 |
|---|---|---|---|
| **Gene** | **Description** | **Fold change*** | **Fold change*** |
| Csf3 | Colony stimulating factor 3 (granulocyte) | 22.94 | 5.94 |
| Tnfsf13b | Tumor necrosis factor (ligand) superfamily, member 13b | 12.21 | 7.89 |
| Csf2 | Colony stimulating factor 2 (granulocyte-macrophage) | 8.94 | 11.39 |
| Tnf | Tumor necrosis factor | 8.57 | 10.13 |
| Ccl4 | Chemokine (C-C motif) ligand 4 | 8.57 | 7.84 |
| Ccl3 | Chemokine (C-C motif) ligand 3 | 6.32 | 1.73 |
| Fasl | Fas ligand (TNF superfamily, member 6) | 6.28 | 4.66 |
| Ccl20 | Chemokine (C-C motif) ligand 20 | 5.70 | 4.96 |
| Il13 | Interleukin 13 | 5.70 | 3.63 |
| Il22 | Interleukin 22 | 5.58 | 1.73 |
| Il10 | Interleukin 10 | 5.39 | 4.92 |
| Cxcl1 | Chemokine (C-X-C motif) ligand 1 | 5.35 | 3.10 |
| Cxcl16 | Chemokine (C-X-C motif) ligand 16 | 4.76 | 3.53 |
| Hc | Hemolytic complement | 4.69 | 13.74 |
| Bmp2 | Bone morphogenetic protein 2 | 4.59 | 1.33 |
| Nodal | Nodal | 4.32 | 1.87 |
| Cxcl10 | Chemokine (C-X-C motif) ligand 10 | 4.14 | 18.00 |
| Il27 | Interleukin 27 | 3.84 | 2.30 |
| Adipoq | Adiponectin, C1Q and collagen domain containing | 3.76 | 7.84 |
| Ccl5 | Chemokine (C-C motif) ligand 5 | 3.66 | 2.97 |
| Il1a | Interleukin 1 alpha | 3.53 | 1.28 |
| Cd70 | CD70 antigen | 2.89 | 2.14 |
| Il17f | Interleukin 17F | 2.73 | 2.95 |
| Ifng | Interferon gamma | 2.68 | 1.73 |
| Lif | Leukemia inhibitory factor | 2.66 | 5.28 |
| Cxcl11 | Chemokine (C-X-C motif) ligand 11 | 2.66 | 1.73 |
| Ccl22 | Chemokine (C-C motif) ligand 22 | 2.62 | 1.73 |
| Bmp6 | Bone morphogenetic protein 6 | 2.58 | –1.27 |
| Il3 | Interleukin 3 | 2.48 | 1.73 |
| Il6 | Interleukin 6 | 2.45 | 3.10 |

| | | | |
|---|---|---|---|
| Cntf | Ciliary neurotrophic factor | 2.40 | 2.36 |
| Ccl19 | Chemokine (C-C motif) ligand 19 | 2.35 | 5.46 |
| Il1b | Interleukin 1 beta | 2.14 | 1.73 |
| Il4 | Interleukin 4 | 1.97 | –1.35 |
| Il23a | Interleukin 23, alpha subunit p19 | 1.88 | 16.00 |
| Il12a | Interleukin 12A | 1.88 | 7.41 |
| Bmp7 | Bone morphogenetic protein 7 | 1.88 | 1.73 |
| Il24 | Interleukin 24 | 1.78 | 4.89 |
| Ifna2 | Interferon alpha 2 | 1.78 | 3.05 |
| Cxcl13 | Chemokine (C-X-C motif) ligand 13 | 1.69 | 25.63 |
| Ccl2 | Chemokine (C-C motif) ligand 2 | 1.51 | 4.72 |
| Cxcl3 | Chemokine (C-X-C motif) ligand 3 | 1.32 | 5.98 |
| Il1rn | Interleukin 1 receptor antagonist | 1.29 | 4.08 |
| Il5 | Interleukin 5 | 1.23 | 5.39 |
| Il7 | Interleukin 7 | 1.14 | −1.62 |
| Tnfsf11 | Tumor necrosis factor (ligand) superfamily, member 11 | 1.13 | −1.15 |
| Ltb | Lymphotoxin B | 1.12 | 1.69 |
| Pf4 | Platelet factor 4 | 1.10 | 8.63 |
| Xcl1 | Chemokine (C motif) ligand 1 | 1.10 | 8.17 |
| Cxcl9 | Chemokine (C-X-C motif) ligand 9 | 1.10 | 7.06 |
| Ccl12 | Chemokine (C-C motif) ligand 12 | 1.10 | 6.02 |
| Ppbp | Pro-platelet basic protein | 1.10 | 3.68 |
| Osm | Oncostatin M | 1.10 | 2.99 |
| Ccl1 | Chemokine (C-C motif) ligand 1 | 1.10 | 2.58 |
| Tnfrsf11b | Tumor necrosis factor receptor superfamily, member 11b | 1.10 | 1.93 |
| Ccl24 | Chemokine (C-C motif) ligand 24 | 1.10 | 1.73 |
| Cd40lg | CD40 ligand | 1.10 | 1.73 |
| Il17a | Interleukin 17A | 1.10 | 1.73 |
| Il2 | Interleukin 2 | 1.10 | 1.73 |
| Il21 | Interleukin 21 | 1.10 | 1.73 |
| Il9 | Interleukin 9 | 1.10 | 1.73 |
| Mstn | Myostatin | 1.10 | 1.73 |
| Il12b | Interleukin 12B | 1.10 | 1.69 |

| | | | |
|---|---|---|---|
| Tgfb2 | Transforming growth factor, beta 2 | 1.10 | −1.09 |
| Mif | Macrophage migration inhibitory factor | 1.05 | 2.73 |
| Vegfa | Vascular endothelial growth factor A | −1.04 | 1.53 |
| Lta | Lymphotoxin A | −1.08 | 1.73 |
| Il11 | Interleukin 11 | −1.09 | 1.10 |
| Spp1 | Secreted phosphoprotein 1 | −1.14 | −4.00 |
| Cxcl5 | Chemokine (C-X-C motif) ligand 5 | −1.19 | 4.92 |
| Ccl11 | Chemokine (C-C motif) ligand 11 | −1.21 | 3.76 |
| Il15 | Interleukin 15 | −1.25 | 2.99 |
| Thpo | Thrombopoietin | −1.32 | 1.06 |
| Ctf1 | Cardiotrophin 1 | −1.37 | 7.62 |
| Cx3cl1 | Chemokine (C-X3-C motif) ligand 1 | −1.56 | −2.22 |
| Csf1 | Colony stimulating factor 1 (macrophage) | −1.58 | 1.39 |
| Bmp4 | Bone morphogenetic protein 4 | −1.84 | 1.32 |
| Gpi1 | Glucose phosphate isomerase 1 | −1.93 | 1.28 |
| Il18 | Interleukin 18 | −2.09 | 3.71 |
| Tnfsf10 | Tumor necrosis factor (ligand) superfamily, member 10 | −2.22 | 4.56 |
| Ccl7 | Chemokine (C-C motif) ligand 7 | −2.79 | 1.28 |
| Il16 | Interleukin 16 | −2.95 | 3.36 |
| Cxcl12 | Chemokine (C-X-C motif) ligand 12 | −2.97 | 3.94 |
| Ccl17 | Chemokine (C-C motif) ligand 17 | −4.03 | −1.45 |

*Fold change: treated cells vs. untreated cells.

Research Paper

# Induction, regulation and roles of neural adhesion molecule L1CAM in cellular senescence

**Blanka Mrazkova[1], Rastislav Dzijak[1], Terezie Imrichova[1], Lenka Kyjacova[1], Peter Barath[2], Petr Dzubak[3], Dusan Holub[3], Marian Hajduch[3], Zuzana Nahacka[4], Ladislav Andera[4], Petr Holicek[4], Pavla Vasicova[1], Olena Sapega[5], Jiri Bartek[1,6,7], Zdenek Hodny[1]**

[1]Department of Genome Integrity, Institute of Molecular Genetics of the ASCR, Prague 14220, Czech Republic
[2]Institute of Chemistry, Slovak Academy of Sciences, Bratislava 84538, Slovakia
[3]Institute of Molecular and Translational Medicine, Palacky University, Olomouc 77147, Czech Republic
[4]Laboratory of Molecular Therapy, Institute of Biotechnology of the ASCR, Prague 14220, Czech Republic
[5]Laboratory of Immunological and Tumour Models, Institute of Molecular Genetics of the ASCR, Prague 14220, Czech Republic
[6]Danish Cancer Society Research Center, Copenhagen DK-2100, Denmark
[7]Division of Genome Biology, Department of Medical Biochemistry and Biophysics, Karolinska Institute, Stockholm, Sweden

**Correspondence to:** Zdenek Hodny, Jiri Bartek; **email:** hodny@img.cas.cz, jb@cancer.dk
**Keywords:** mass spectrometry, SILAC, proteomics, MAPK pathway, aging
**Received:** December 20, 2017 **Accepted:** March 22, 2018 **Published:** March 28, 2018



## ABSTRACT

**Aging involves tissue accumulation of senescent cells (SC) whose elimination through senolytic approaches may evoke organismal rejuvenation. SC also contribute to aging-associated pathologies including cancer, hence it is imperative to better identify and target SC. Here, we aimed to identify new cell-surface proteins differentially expressed on human SC. Besides previously reported proteins enriched on SC, we identified 78 proteins enriched and 73 proteins underrepresented in replicatively senescent BJ fibroblasts, including L1CAM, whose expression is normally restricted to the neural system and kidneys. L1CAM was: 1) induced in premature forms of cellular senescence triggered chemically and by gamma-radiation, but not in Ras-induced senescence; 2) induced upon inhibition of cyclin-dependent kinases by $p16^{INK4a}$; 3) induced by TGFbeta and suppressed by RAS/MAPK(Erk) signaling (the latter explaining the lack of L1CAM induction in RAS-induced senescence); and 4) induced upon downregulation of growth-associated gene ANT2, growth in low-glucose medium or inhibition of the mevalonate pathway. These data indicate that L1CAM is controlled by a number of cell growth- and metabolism-related pathways during SC development. Functionally, SC with enhanced surface L1CAM showed increased adhesion to extracellular matrix and migrated faster. Our results provide mechanistic insights into senescence of human cells, with implications for future senolytic strategies.**

## INTRODUCTION

Human population is aging rapidly, raising serious global health and societal concerns, at the same time highlighting the urgent need to better understand the process of aging at the molecular, cellular and organismal levels. Recent research has revealed aging-associated accumulation in diverse tissues of the so-

called senescent cells (SC) which, along with their secreted products, appear to causally contribute to aging [1, 2]. From a broader perspective, the process of senescence is a cellular stress response leading to persistent activation of cell-cycle checkpoints and long-lasting cell-cycle arrest caused predominantly by lasting DNA damage signaling. SC play important patho-physiological roles in a number of processes during ontogenetic development of the mammalian organism [3]; for instance, senescence response takes part in wound healing [4] and tissue regeneration [5]. As a cellular fate commonly triggered by DNA damage response, cellular senescence is considered as a primary tumorigenesis barrier [6-8]. DNA damage-induced cellular senescence also accompanies genotoxic cancer therapies [9, 10]. Long-lasting persistence of senescent cells in tissues can also induce various pathological changes affecting organismal homeostasis (see, e.g. references [1, 2]). These effects are thought to be elicited by secretion from SC of a complex mixture of factors comprising components of the extracellular matrix, its modifiers such as proteases and their regulators, reactive oxygen species [11] and particularly cytokines including morphogens from the TGFβ family, pro-inflammatory species (e.g., IL1, IL6, IL8; [12]), and chemokines (such as MCP-1; [13]). The composition of the SC secretome (denoted as senescence-associated secretory phenotype; SASP) varies according to the cell type and mechanism of senescence induction [14]. Additional factors influencing the secretory response of SC, such as interactions of SC with surrounding cells and specific tissue microenvironment, likely exist at the organismal level. This complexity and variability of SASP is the reason why the effects of SASP on the tissue microenvironment and the pathogenic role of various types of SC remain poorly understood. Nevertheless, it was plausibly demonstrated that senescent cells can affect neighboring cells by induction of oxidative stress and DNA damage resulting in secondary ('bystander') senescence [11, 15, 16]. This 'domino' effect might contribute to the spread of a mild but chronic inflammatory environment especially in aging tissues [17]. It should also be noted that certain chemotherapeutic drugs are able to induce cellular senescence in normal tissues within the close proximity of tumors, which can also promote local inflammation and self-sustaining genotoxic environment.

Of the various interactions of SC with their milieu, the interaction with the immune system is especially important. SC interact with the immune system in a mutual way – besides being a target of the immune system (senescence immunosurveillance; [18]), SC can modulate the immune system function by either immunoactivation [18] or immunosuppression [19, 20]. Intriguingly, observations that genetically engineered removal of SC from the mouse organism induced a 'rejuvenating' effect [2] and the presence of SC affected the rate of mouse aging [1] both indicate aging-promoting harmful effects of SC *in vivo*. Indeed, there is accumulating evidence that SC contribute to pathogenesis of several aging-associated degenerative diseases including atherosclerosis [21], cartilage degeneration leading to osteoarthritis [22, 23], cardiac fibrosis [24], liver fibrosis [25], type 2 diabetes [26], and Alzheimer's and Parkinson's diseases [27, 28]. In addition, elimination of senescent cells from the tumor environment is believed to improve the health condition of patients with cancer [29].

Based on the negative effects of SC in tissues, there is a prevailing view that prevention of SC accumulation or support of their elimination would be beneficial for the health span of the organism. The prerequisite for this ambition is our ability to unambiguously detect SC in tissues. However, reliable biomarkers strictly specific to SC are still missing, despite the SC undergo profound changes of their phenotype deviating extensively from their parental cells [30]. The purpose of this study was to identify candidate protein markers differentially expressed on the cell surface of proliferating versus replicatively senescent human fibroblasts using quantitative proteomic analysis. Apart from several previously reported proteins such as PVR, TIMP3, GGT2, and ADAMTS1, we identified the neural adhesion factor L1CAM as being overrepresented on the surface of the replicatively SC. Further analysis of L1CAM whose expression is physiologically restricted to neural and kidney tissues revealed that except for oncogenic Ras-induced senescence, other pro-senescence stimuli can induce L1CAM. Also intrigued by the known association of L1CAM with cancer and poor prognosis of cancer patients [31-37], we then pinpointed several cellular signaling and metabolic pathways involved in regulation to L1CAM expression, as well as functional impact of elevated L1CAM expression, using several human models of SC. Both the overall spectrum of the cell-surface proteins identified in our unbiased proteomic screen, and the insights into L1CAM regulation and potential roles in senescence are presented in this dataset.

## RESULTS

### L1CAM is enriched on the cell surface of replicatively senescent fibroblasts

In our search to identify proteins differently expressed on the plasma membrane of senescent cells, we performed quantitative proteomic analysis of cell surface proteins of proliferating (PD 28) and replicatively

senescent (PD 84) BJ fibroblasts (see Supplementary Figure 1A, B for activity of senescence-associated β-galactosidase and markers of persistent DNA damage response, respectively). For enrichment of cell surface proteins we utilized biotin labeling of cell surface proteins (see Materials and Methods for details). Out of 650 quantified proteins identified by mass spectrometry, 151 proteins showed differential expression (Supplementary Table 1). Within this group we focused on the candidate proteins whose expression on the surface of senescent fibroblasts was increased more than four fold over the level in proliferating counterpart cells. In addition to several proteins already reported as overexpressed in senescent cells, such as metalloproteinase inhibitor 3 (TIMP3) [38], γ-glutamyl-transpeptidase 2 (GGT2) [39] and ADAMTS1 [40], our analysis revealed some previously unrecognized proteins such as THY1, BST1, FAT1 (for full list of differentially changed proteins, see Supplementary Table 1) and neural cell adhesion molecule L1, L1CAM (Figure 1A). Thirty six most upregulated proteins were selected and analyzed for mRNA levels, of which more than dozen was significantly elevated (see Supplementary Figure 1C). The changes of total protein level of five selected proteins (fibronectin, L1CAM, collagen IV, integrin α2 and PVR) in replicative senescent BJ cells were verified by immunoblotting (see Supplementary Figure 1D).

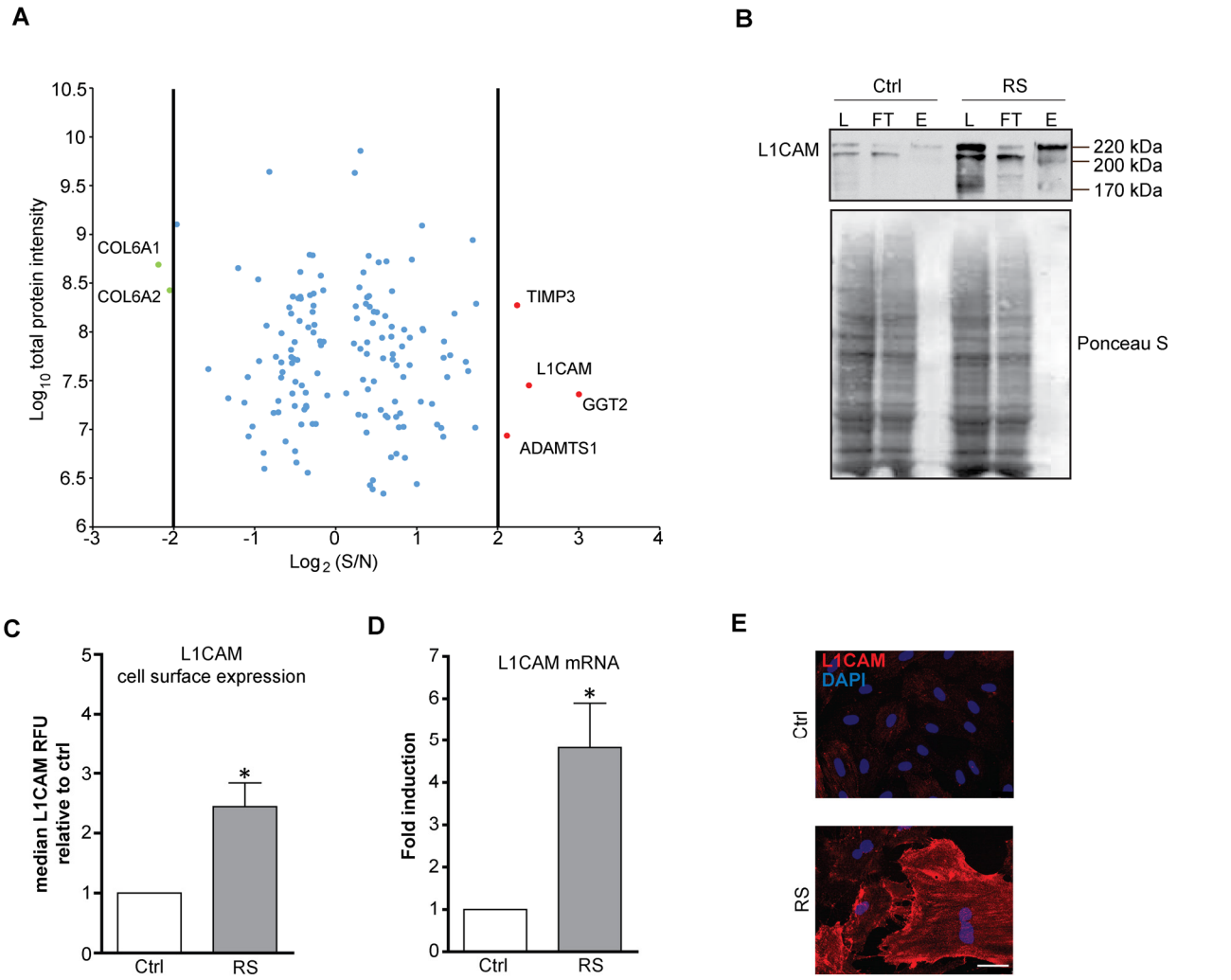


**Figure 1. L1CAM is enriched on the surface of replicatively senescent fibroblasts.** (**A**) Proteomic analysis of the surface of senescent cells. Down- (green dots < four fold) and up-regulated (red dots > four fold) proteins in senescent cells. (**B**) Cell surface proteins of proliferating (Ctrl) and replicatively senescent (RS) BJ fibroblasts were modified by biotin and captured on a streptavidin column (see Material and Methods for details), and fractions were validated for the presence of L1CAM by Western blotting. L – load (total protein); FT – flow through (non-biotinylated protein fraction), E – elution (biotinylated protein fraction). Ponceau S staining is shown to demonstrate protein loading. (**C**) FACS analysis of the surface level of L1CAM in BJ fibroblasts. (**D**) mRNA level of L1CAM normalized to GAPDH in replicatively senescent BJ cells. (**E**) Live cell immunofluorescence detection of L1CAM in proliferating (Ctrl) and replicatively senescent (RS) BJ (upper panel) and MRC5 (lower panel) fibroblasts. Scale bar, 50 μm. All experiments were performed in biological triplicates. For statistics, two-tailed Student's t-test was used: $p < 0.05$ (*); $p < 0.01$ (**); $p < 0.001$ (***).

L1CAM attracted our attention as it is expressed physiologically in neural and renal tissues and pathologically in several types of human tumors (see Discussion for further details). To validate the mass spectrometry data, we compared the L1CAM mRNA, total and surface protein expression in young/proliferating versus senescent BJ cells. As shown by immunoblotting of biotin/streptavidin immunoprecipitates, the total level of L1CAM was increased in replicatively senescent BJ cells compared to the proliferating cells (compare lanes 'L' for proliferating and replicatively senescent cells in Figure 1B). The increased cell surface protein level in replicatively senescent cells was verified by comparing the amount of eluted biotinylated L1CAM from streptavidin matrix (see lines 'E' in Figure 1B). This was further confirmed by flow cytometry analysis using live cell staining with L1CAM antibody, where the surface protein level of L1CAM was markedly elevated in replicatively senescent BJ cells (Figure 1C). Note, similar cell surface enhancement of L1CAM in replicative senescent BJ cells was observed also for fibronectin and PVR (Supplementary Figure 1E). The L1CAM protein elevation was concordant with the changes of the L1CAM mRNA levels (Figure 1D and Supplementary Figure 1C, D). Using indirect immunofluorescence, we observed marked heterogeneity of L1CAM cell surface levels among individual cells in both populations of proliferating and senescent BJ cells (Figure 1E; for validation of antibody specificity, see Supplementary Figure 1F, G; note that the L1CAM antibody staining of formaldehyde-fixed cells was nonspecific).

Altogether, our data show that L1CAM is overrepresented on the cell surface of replicatively senescent BJ fibroblasts; and L1CAM's enhanced surface protein level corresponds to the increased expression of *L1CAM* mRNA.

**L1CAM expression is cell type- and senescence stimulus-dependent**

During serial cultivation of cells *in vitro* there is a likelihood of selection of clones with enhanced replicative potential [41]. To examine whether increased L1CAM expression in replicatively senescent

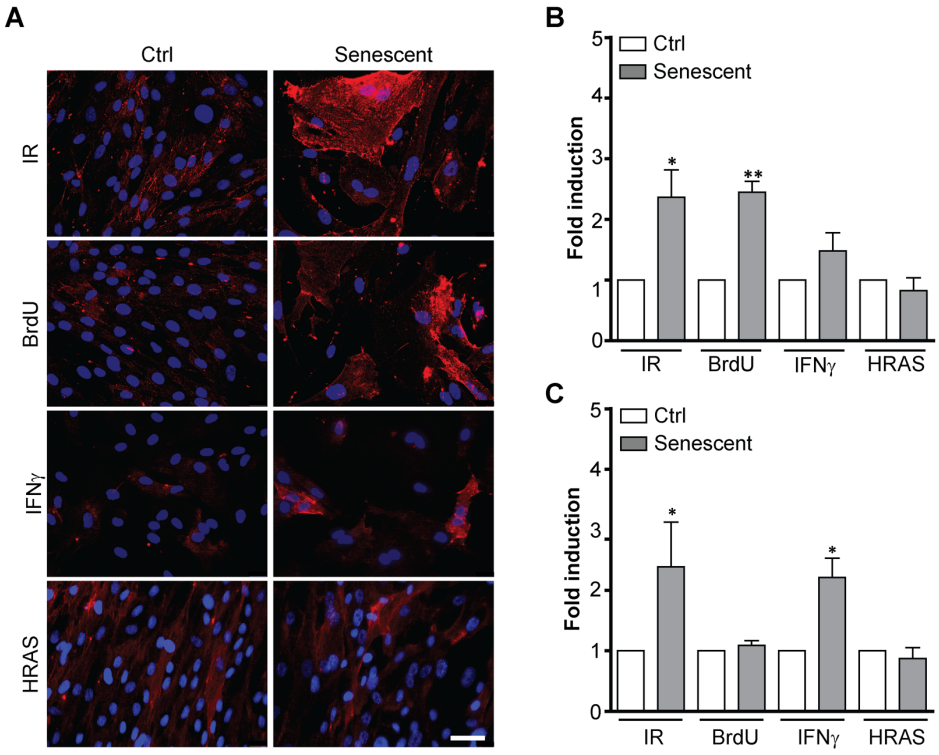


**Figure 2. L1CAM expression in premature senescence induced by various stimuli.** BJ fibroblasts were brought to premature senescence by γ-irradiation (PD 32, IR 20 Gy), 100 μM 5-bromo-2'-deoxyuridine (PD 32, BrdU), 500 U/ml IFNγ (PD35), or by induction of oncogenic HRAS using the Tet on system (see Materials and Methods). Cell surface expression of L1CAM estimated by live cell immunostaining with L1CAM antibody was detected microscopically (**A**) or (**B**) by FACS. The values representing three independent experiments are shown as a fold induction relative to control. (**C**) Real time RT-qPCR quantification of mRNA levels of L1CAM in BJ cells brought to premature senescence as in A. The values representing three independent experiments are shown as a fold induction relative to control. GAPDH was used as a reference gene. For statistics, two-tailed Student's t-test was used; $p < 0.05$ (*); $p < 0.01$ (**); $p < 0.001$ (***). Scale bar, 50 μm.

BJ cells was due to clonal selection of cells bearing higher L1CAM expression, we followed the expression of L1CAM in a scenario of prematurely induced senescence in BJ cells triggered by ionizing radiation (IR) [42], 5-bromo-2'-deoxyuridine (BrdU) [43], and interferon-γ (IFNγ) [16, 44], or overexpression of oncogenic H-Ras(V12) [46]. With the exception of H-Ras-induced senescence, the cell surface expression of L1CAM was increased in BJ fibroblasts upon exposure to all other stimuli (Figure 2A, B; see Supplementary Figure 1A for SA-β-gal staining), indicating that cell surface expression of L1CAM is not the result of a clonal selection during serial passaging. The lack of L1CAM induction in H-Ras oncogene-induced senescence suggested the dependence of L1CAM expression on the type of senescence-inducing stimulus. Moreover, we observed that the *L1CAM* transcript level remained unchanged after BrdU treatment despite enhanced L1CAM cell surface expression (Figure 2C), indicating that both *de novo* synthesis and/or enhanced (re)localization of L1CAM to the cell surface can take part in a mechanism of its enhanced cell surface expression. The heterogeneity of L1CAM expression in the population of SC was apparent among prematurely senescent cells as well.

To determine whether the heterogeneous expression of L1CAM in senescent cells stems from clonal heterogeneity present already in proliferating BJ cells, we sorted proliferating BJ cells according to their surface L1CAM level by FACS to populations with low ($L1CAM^{low}$) and high ($L1CAM^{high}$) expression (Supplementary Figure 2A) and followed the L1CAM levels for several population doublings. Notably, the differences in L1CAM levels between the sorted subpopulations balanced out after approximately ten population doublings (Supplementary Figure 2B) indicating that epigenetic rather than genetic factors likely determine the L1CAM heterogeneity. No differences in proliferation of L1CAM 'high' versus 'low' cells were observed (Supplementary Figure 2C), consistent with the notion that L1CAM expression is not linked with proliferation advantage of any subpopulation. In addition, there were no significant differences in the occurrence of DNA damage foci (detected as 53BP1 and serine 139 phosphorylated histone H2A.X) between $L1CAM^{high}$ and $L1CAM^{low}$ cells (see Supplementary Figure 2 D and E). We also did not observe any marked morphological differences among senescent $L1CAM^{high}$ and $L1CAM^{low}$ populations of BJ cells, except that $L1CAM^{high}$ cells were slightly larger in size (mean area ± SEM: 327.6 ± 5.317 $\mu m^2$ for $L1CAM^{low}$ and 344.9 ± 4.113 $\mu m^2$ for $L1CAM^{high}$; two-tailed paired test, $p = 0.0123$; Supplementary Figure 2F). Furthermore, down-regulation of L1CAM in replicatively senescent cells did not result in escape of cells from senescence (Supplementary Figure 2G), indicating that L1CAM is not involved in senescent cell cycle arrest.

Next we tested a panel of other human cell types, including normal and cancerous cells, for L1CAM expression during the development of premature senescence. Figure 3 summarizes L1CAM mRNA, total and cell surface protein levels in a variety of cell types brought to senescence by IR or BrdU (Supplementary Figure 3A). In accord with a previous study [47], pancreatic carcinoma PANC-1 cells featured high L1CAM cell surface expression even under unperturbed conditions (see Supplementary Figure 3B for the relative transcript level of L1CAM in all cell types analyzed). IR but not BrdU induced both L1CAM transcript level and cell surface expression in PANC-1 and similarly in osteosarcoma U2OS cells (Figure 3A, B). In contrast, BrdU induced L1CAM expression in prostate cancer PC3 and melanoma A375 cells more potently than IR. Normal diploid fibroblasts MRC-5 and HSF-1, and immortalized retinal pigment epithelial RPE-1 cells responded by elevation of L1CAM mRNA and total protein levels in dependence on the stimulus but without concomitant protein expression on the cell surface, indicating again that cell surface exposure of L1CAM is regulated. Note that the expression of L1CAM is the lowest in RPE-1 among the tested cell lines (Supplementary Figure 3B); therefore, it is possible that the observed elevation of the L1CAM level after senescence induction was not sufficient for detection of the surface protein level. The transcript levels of L1CAM were only slightly induced in prostate cancer DU145 cells exposed to either IR or BrdU; and the L1CAM protein remained undetectable (Figure 3C). In general, our data showed that higher levels of L1CAM transcriptional induction appear to be necessary for the increase of the total protein level; however, even an increased total protein level is not always expressed as the enhanced presence of protein on the cell surface.

To investigate whether the L1CAM is also induced during senescence in different species, we triggered premature senescence in three mouse cell lines TRAMPC2, TC1 and B16F10 by exposure to docetaxel (7.5 μM, 4 days) as reported previously [48, 49]. In all three cell lines, L1CAM transcript levels were elevated after docetaxel treatment (see Supplementary Figure 4A for L1CAM level and Supplementary Figure 4B for senescence-associated beta-galactosidase staining) indicating that L1CAM induction during senescence is not restricted to human cells.

To conclude, the senescence-associated expression of L1CAM on the cell surface is feature shared in normal and cancerous cells of human and mouse origin, but

dependent on cell type and senescence-inducing stimulus. Our findings also indicate that L1CAM cell surface expression is a complex process regulated both at the level of transcription and posttranscriptionally.

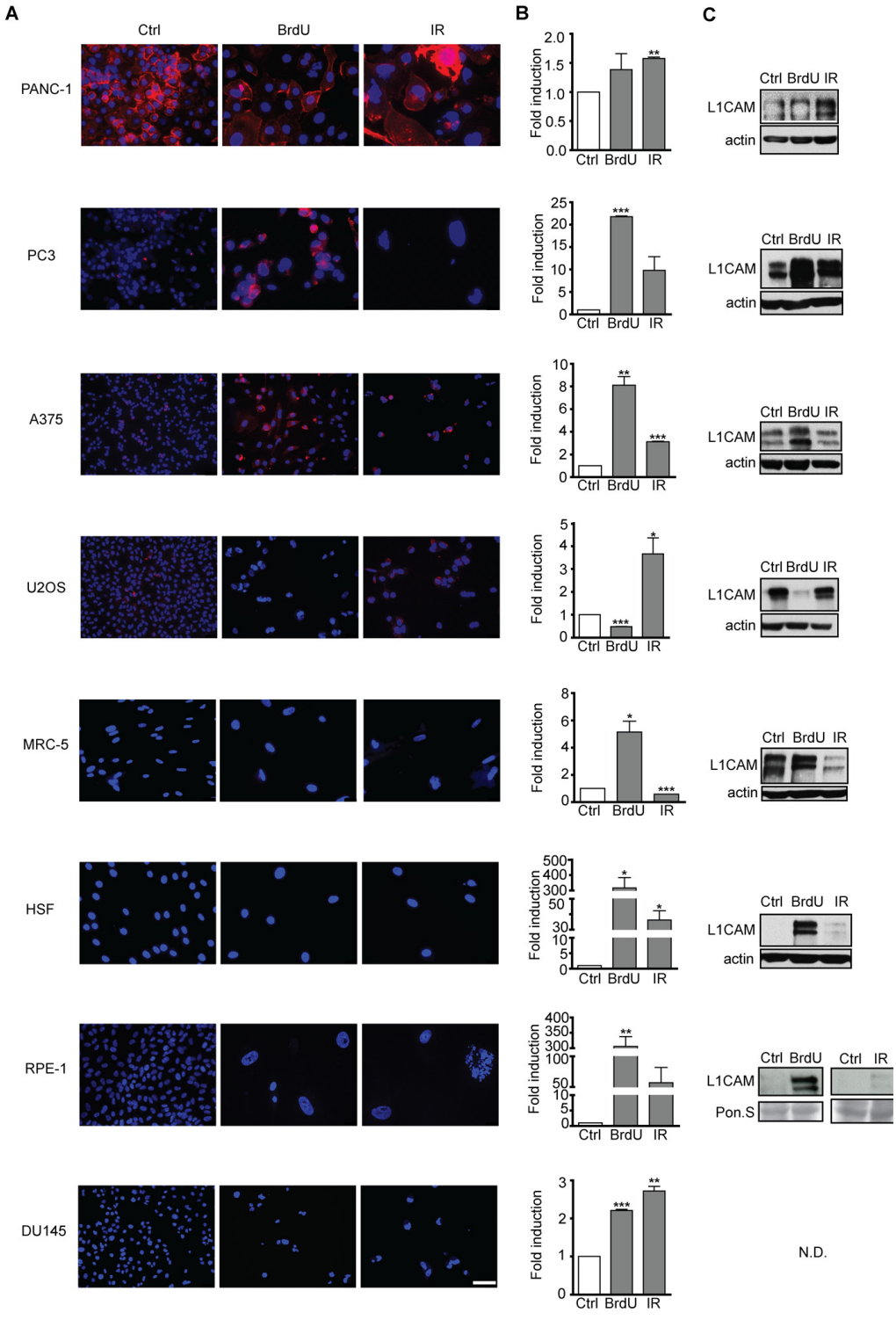


**Figure 3**. **L1CAM expression in normal and tumor senescent cells depends on the cell type and senescence-inducing stimulus**. Normal (MRC5, HSF), immortalized (RPE-1) and tumor (PANC-1, PC3, A375, U2OS, and DU145) cells were brought to senescence either by BrdU (10 μM for A375, 100 μM for rest of cell types) or IR (10 Gy) and assayed for cell surface L1CAM protein expression by live cell immunostaining with L1CAM antibodies. (**A**) L1CAM mRNA expression by real time RT-qPCR quantification (**B**) and total L1CAM protein level by immunoblotting (**C**). GAPDH was used as a reference gene; β-actin was used as a loading control. The values representing two independent experiments are shown as a fold induction relative to control. N.D., not detected. Scale bar, 50 μm.

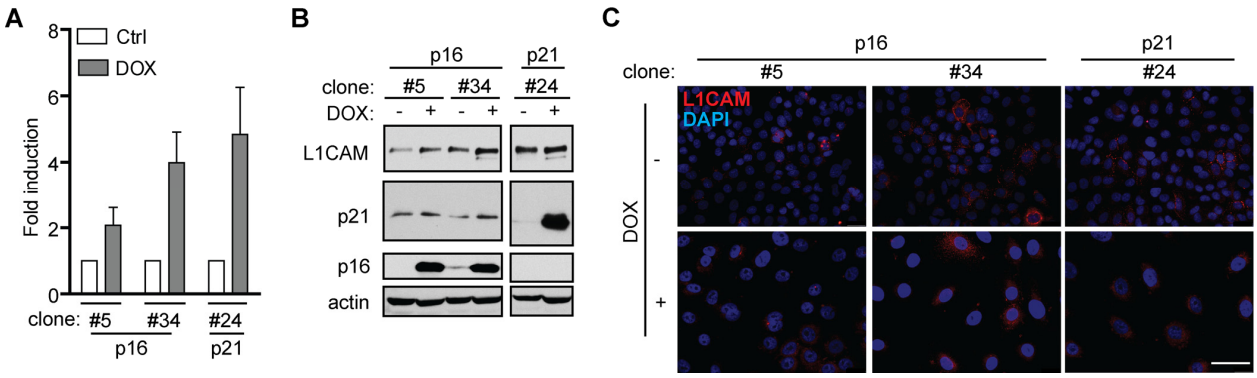


**Figure 4. L1CAM expression is a downstream event linked to inhibition of cyclin-dependent kinases.** L1CAM mRNA (**A**), total protein (B) and surface expression in control cells (ctrl; DOX-) and doxycycline-induced (DOX+) H28 cell clones #5, #34 (expressing p16) and #24 (expressing p21). L1CAM mRNA level was normalized to GAPDH. All experiments were performed in three independent replicates. Scale bar, 100 µm.

### L1CAM expression is a downstream event linked to inhibition of cyclin-dependent kinases by p16ink4a

Next, to decipher the mechanisms mediating L1CAM expression during induction of senescence, we first investigated to which phase of the cell cycle checkpoint cascade the expression of L1CAM is linked. To uncouple the inhibition of cell cycle from upstream events of DNA damage response we utilized ectopic expression of tetracycline-regulatable inhibitor of cyclin-dependent kinases $p16^{ink4a}$ (p16) in human mesothelioma H28 cells in comparison to ectopic expression of $p21^{waf1}$ (p21) known to induce DNA damage response [50]. Doxycycline induction of both p16 and p21 in two single cell-derived clones (p16) and one single-derived p21 clone led to cell cycle arrest (Supplementary Figure 5A; for senescence-associated β-galactosidase staining, see Supplementary Figure 5B), as observed previously [51]. In contrast to p21, no signs of enhanced DNA damage response detected as 53BP1/γH2AX foci were observed after p16 induction when compared to non-induced cells (Supplementary Figure 5C). A reproducible increase of L1CAM mRNA (Figure 4A) and protein (Figure 4B) was observed after induction of both p16 (Figure 4C) and p21 (not shown), however, without detectable increase of the L1CAM cell surface protein level. These findings indicated that the induction of L1CAM expression is a downstream event following induction of cdk protein inhibitor(s).

### Cell type-dependent and mutual interaction of L1CAM and Erk signaling pathways

It has been reported that activation of the L1CAM signaling pathway by antibody-mediated L1CAM cross-linking or manipulation with its level affect the activity of Erk1/2 [52-54]. Indeed, we observed that the basal activity of Erk1/2 was higher in $L1CAM^{low}$ human melanoma A375 and BJ cells when compared to $L1CAM^{high}$ cells (Figure 5A). Additionally, knockdown of L1CAM in BJ cells increased Erk1/2 phosphorylation (Figure 5B). This data obtained in unperturbed cell culture conditions underscored the role of L1CAM in the regulation of activity of Erk1/2.

The other way around, inhibition of Erk1/2 activation by selumetinib, a chemical inhibitor of MEK, in A375 (Figure 5C) and HeLa (data not shown) cells resulted in marked elevation of L1CAM mRNA, total and cell surface protein expression (Figure 5D, E), which indicated that the MAPK pathway may operate in a negative feedback loop to suppress L1CAM, thus balancing its own activity. Further, combined knockdown of Erk1 and/or Erk2 by RNA interference resulted in elevation of L1CAM mRNA (Figure 5F) and surface protein expression (Figure 5G), further supporting the interplay between L1CAM and Erk pathways. Nevertheless, the exposure of BJ cells to selumetinib did not show any effect on L1CAM mRNA and protein levels (not shown), indicating cell type-specific regulation of the L1CAM expression.

These findings fit well with the absence of L1CAM expression during H-RAS oncogene-induced senescence (OIS). To exclude the possibility that our strain of BJ fibroblasts with tetracycline-inducible RAS oncogene lost the competence to induce L1CAM (due to cloning of cells with aberrant L1CAM regulation), we exposed Ras-induced senescent BJ cells presorted for low level of L1CAM to MEK inhibitor selumetinib. As shown in Figure 5J, the inhibition of MEK resulted in an increased L1CAM protein level, indicating unperturbed sensitivity of L1CAM to Erk1/2 inhibition in OIS cells, supporting the suppressive role of the Ras/MAPK pathway on L1CAM expression.

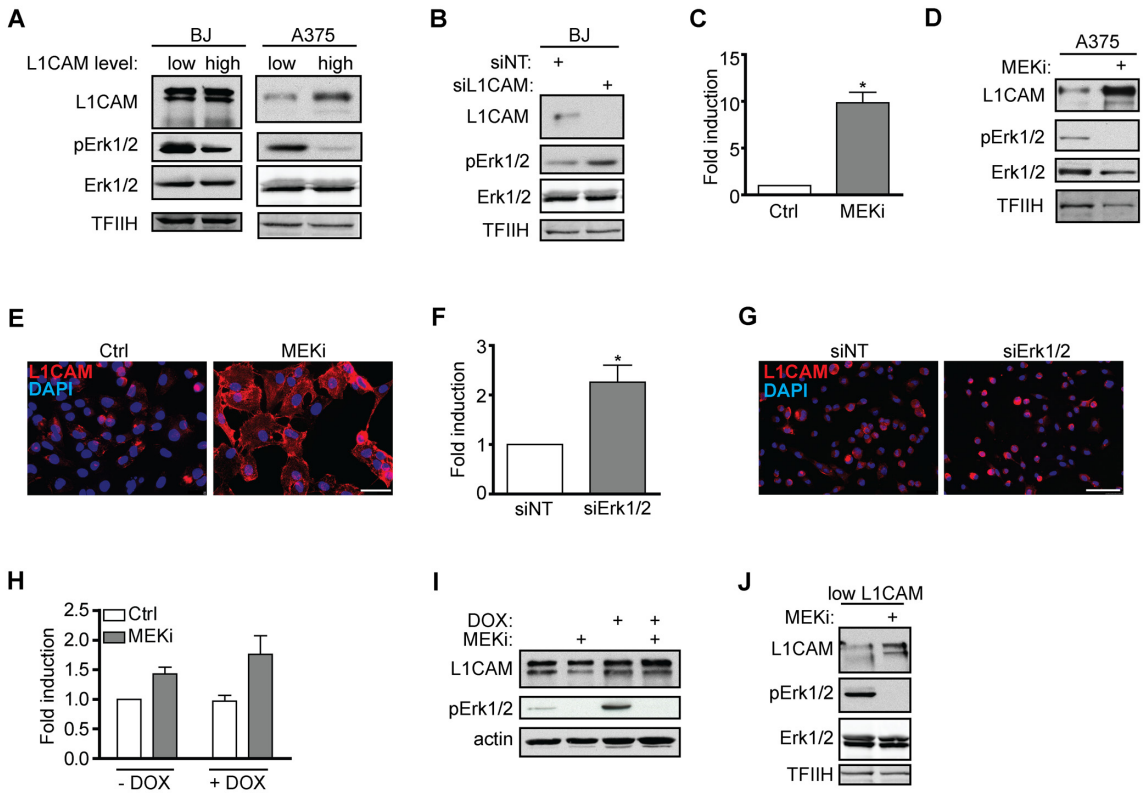


**Figure 5. Interaction of L1CAM with the Erk signaling pathway.** (**A**) Erk 1/2 activity detected as phosphorylation of Erk1/2 (pErk1/2) compared in BJ and A375 cells sorted for L1CAM high and low cell surface level. (**B**) The effect of L1CAM downregulation using RNA interference on Erk1/2 activity detected by immunoblotting in BJ fibroblasts. (**C**) L1CAM mRNA level estimated by real time RT-PCR after inhibition of MEK by selumetinib (10 μM; MEKi) in A375 cells. Total (**D**) and surface L1CAM levels (**E**) detected by immunoblotting and live cell staining, respectively, in A375 cells after MEK inhibition using selumetinib (10 μM; MEKi). L1CAM mRNA (**F**) and surface protein level (**G**) in A375 after downregulation of Erk1/2 using RNA interference (siErk1/2). L1CAM mRNA (**H**) and total protein (**I**) levels in control (-DOX) and H-RAS-induced (+DOX) BJ cells before (ctrl) and after inhibition of MEK using selumetinib (10 μM; MEKi). (**J**) The effect of MEK inhibition by selumetinib (10 μM; MEKi) on the L1CAM total protein level in H-RAS-induced senescent BJ cells sorted for low L1CAM level. Non-template siRNA was used as a control (siNT). For immunoblotting, TFIIH or β-actin were used as a control of equal protein loading. For real time RT-PCR, GAPDH was used as the reference gene. Scale bar, 100 μm. All experiments were performed in three independent replicates. $p < 0.05$ (*), two-tailed Student's t-test.

Overall, our results indicate a crosstalk between L1CAM and Ras/MAPK pathways, where the elevated level of L1CAM is associated with lower Erk1/2 activity and the Ras/MAPK signaling exerts a suppressive effect on L1CAM gene expression.

### L1CAM expression is linked to metabolic changes

Given that *L1CAM* transcription is regulated by hypoxia in tumor cells [55], we asked whether metabolic changes associated with senescence (see e.g. references [56-58]) contribute to regulation of *L1CAM* gene expression. We noted that the concentration of glucose in culture medium affected the expression of *L1CAM* in U2OS and HeLa cells. Both cell types cultured in higher concentration of glucose (4.5 g/L) expressed lower levels of L1CAM compared to cells cultured in 1 g/L glucose, indicating that the expression of L1CAM might be linked to glycolytic energy metabolism of tumor cells (Figure 6A, B). Furthermore, the level of *L1CAM* transcript and protein increased after inhibition of the mevalonate pathway (chosen here for being one of the pathways that utilize acetyl-CoA, derived from glucose metabolism) in BJ fibroblasts by cerivastatin (Figure 6C). As reported previously, various forms of cellular senescence are accompanied by repression of solute carrier family 25 member 5 (SCL25A5) coding for ADP/ATP translocase 2 (ANT2; [59, 60]), which has been implicated in glycolytic metabolism of tumor cells [61-63]. RNA interference-mediated downregulation of ANT2 but not ANT3 (Supplementary Figure 6A) in HeLa and BJ cells led to marked elevation of L1CAM both at mRNA and protein levels (Figure 6E). The intrapopulation heterogeneity of L1CAM expression

was diminished after ANT2 knockdown (data not shown). Interestingly, the inhibition of MEK by selumetinib in A375 cells resulted in suppression of the ANT2 mRNA level associated with the increase of L1CAM expression (see Figure 5C and Figure 6F), suggesting a reciprocal link between ANT2 and L1CAM expression. In support of this notion, there was also an inverse relationship between the mRNA levels of both genes in A375 cells exposed to IFNγ and TGFβ (Figure 6G), the cytokines reported to induce senescence [16, 60]. Note that TGFβ alone strongly induced cell surface expression of L1CAM in A375 cells (Figure 6H), which was associated with stronger cytostatic effect compared to IFNγ (Supplementary Figure 6B).

Altogether our data indicate that the induction of L1CAM during senescence might be linked to accompanying metabolic changes, specifically to suppression of the *SCL25A5/ANT2* gene expression.

**L1CAM increases cell migration and adhesion of both proliferating and senescent BJ cells**

Several studies reported the role of L1CAM in enhanced migration of tumor cells (see, e.g., references [31, 64]). Indeed, in a wound healing assay, young BJ cells with downregulated L1CAM using lentivirally transduced short hairpin RNA recovered the disrupted area significantly slower than control cells (Figure 7A), indicating that migration of normal cells can also be affected by L1CAM surface expression (see reference [54]). Next we asked whether enhanced expression of L1CAM is linked with the migratory properties of senescent cells. Utilizing heterogeneity of L1CAM expression in the cell population of BJ senescent cells, we tested migration of BJ cells sorted by FACS according to L1CAM cell surface expression. Replicatively senescent BJ cells sorted for higher surface L1CAM levels healed the scratch more efficiently than their counterparts with lower cell surface expression of

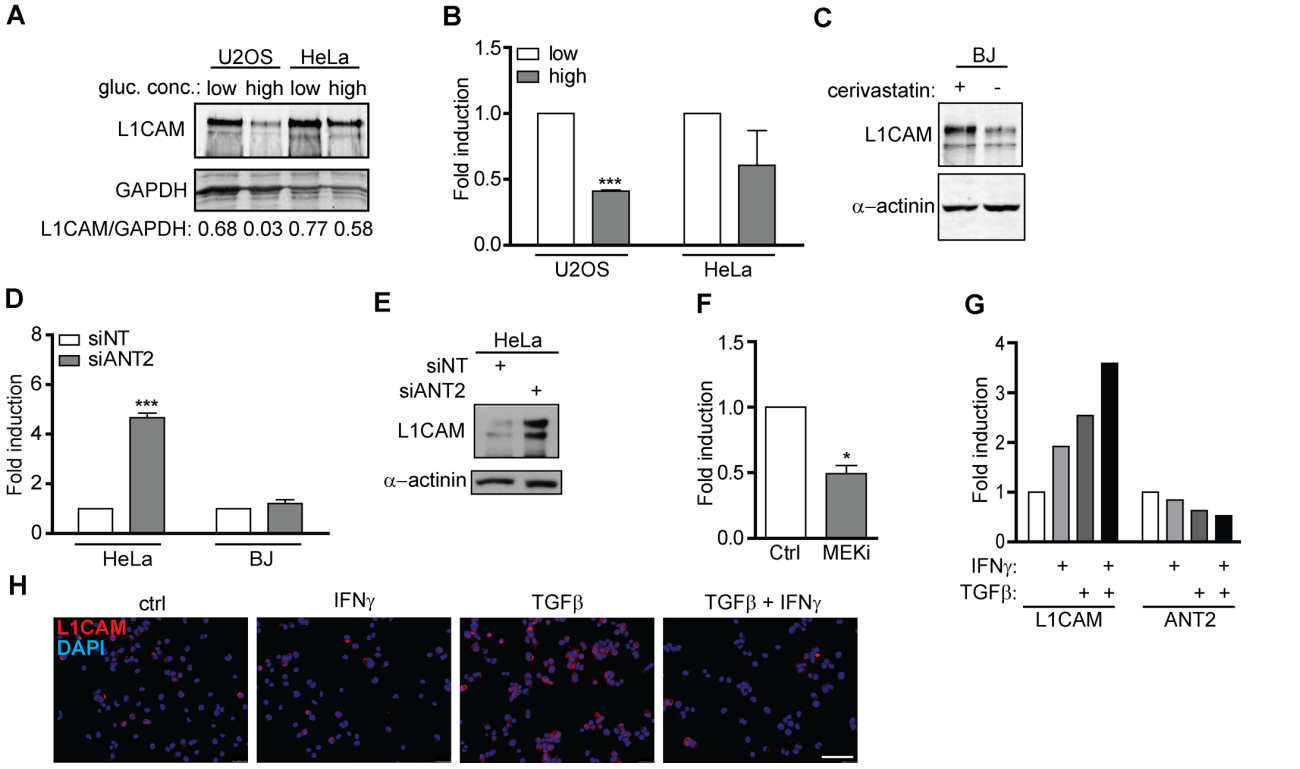


**Figure 6. L1CAM expression is linked to metabolic changes.** The effect of high (4.5 g/L) and low (1.0 g/L) glucose concentration in cultivation medium on total L1CAM protein (**A**) and L1CAM mRNA levels (**B**) in U2OS and HeLa cells detected by Western blotting and real time RT-PCR, respectively. (**C**) The effect of inhibition of the mevalonate pathway by cerivastatin on the L1CAM total protein level in BJ fibroblasts. L1CAM mRNA in HeLa and BJ cells (**D**) and total L1CAM protein in Hela cells (**E**) after downregulation of ANT2 using RNA interference. (**F**) ANT2 mRNA level after inhibition of MEK by selumetinib (10 μM; MEKi) in A375 cells. L1CAM and ANT2 transcripts (**G**) and L1CAM surface expression (**H**) in A375 cells exposed to 500 U/ml IFNγ, 10 ng/ml TGFβ, or their combination for 4 days. For real time RT-qPCR experiments, GAPDH was used as the reference gene. For immunoblotting, GAPDH or α-actinin were used as loading controls. $p < 0.05$ (*); $p < 0.01$ (**); $p < 0.001$ (***), two-tailed Student's t-test. Scale bar, 100 μm. All experiments were performed in three independent replicates.

L1CAM (Figure 7B). To further corroborate these findings, we employed a 3D migration assay to follow cell motility induced by fetal bovine serum as attractant. Using time-lapse cell tracking, several parameters such as velocity, Euclidean distance (length of migration that the cell overcomes directly from the start point to the endpoint), and accumulated distance (cell's trajectory) were evaluated. Notably, senescent BJ cells with high L1CAM cell surface expression migrated faster and covered longer Euclidean and accumulated distances

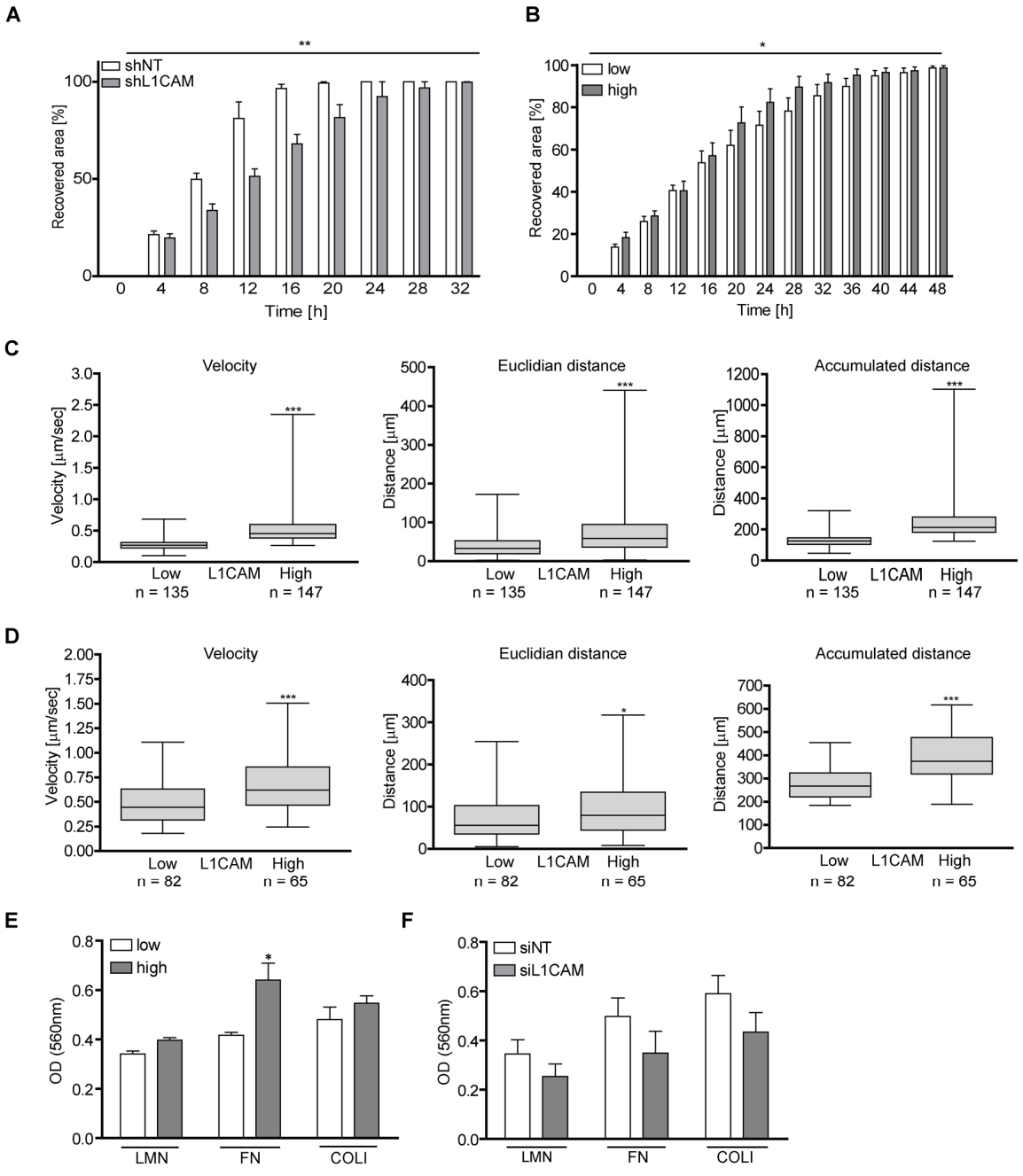


**Figure 7. L1CAM levels correlate with enhanced cell migration and adhesion both in proliferating and senescent cells.** (**A**) Wound healing assay of proliferating BJ after RNA interference-mediated knockdown of L1CAM and (**B**) replicatively senescent BJ fibroblasts sorted according to cell surface expression of L1CAM. (**C**) 3D migration assay of replicatively senescent BJ sorted according to L1CAM cell surface expression presented as velocity (left chart), Euclidian distance (middle chart) and accumulated distance (right chart). (**D**) 3D migration assay of unsorted replicatively senescent BJ. Left chart – velocity; middle chart – Euclidian distance; and right chart – accumulated distance. (**E**) Adhesion assay of replicatively senescent BJ fibroblasts sorted according to cell surface L1CAM expression and (**F**) after L1CAM knockdown. All experiments were performed in three independent replicates. $p < 0.05$ (*); $p < 0.01$ (**); $p < 0.001$ (***), two-tailed Student's t-test.

(Figure 7C). To exclude the possibility of an impact of growth conditions on the tested subpopulations, a 3D random migration assay of non-sorted but L1CAM antibody-labeled senescent BJ fibroblasts was also performed. The results revealed a similar trend as in the case of L1CAM-sorted BJ cells. L1CAM$^{high}$ BJ cells migrated faster and travelled further distances (Figure 7D) compared to L1CAM$^{low}$ BJ cells. The migration of proliferating BJ fibroblasts in the wound healing assay was faster compared to replicatively senescent cells, where young BJ covered the disrupted area approximately three times faster (by 16 hours) compared to senescent cells (48 hours; see references [65, 66]). The proliferation of young cells contributed to faster wound recovering as well; however, the difference in the velocity was significant (Supplementary Video 1 and 2).

Next we asked whether the cell surface level of L1CAM correlates with the cell adhesive properties. As shown in Figure 7E, replicatively senescent L1CAM$^{high}$ BJ cells showed 10, 17 and 20% higher adhesion to the components of extracellular matrix laminin, fibronectin, and collagen 1, respectively, compared to senescent L1CAM$^{low}$ BJ cells. To confirm the contribution of L1CAM to cell adhesive properties, L1CAM was down-regulated in senescent BJ fibroblasts by RNA interference (Figure 7F; for the level of L1CAM down-regulation, see Supplementary Figure 6C). Indeed, control cells adhered more efficiently compared to the cells with a decreased L1CAM level.

Taken together, the enhanced level of L1CAM correlates with increased migratory properties not only of proliferating but also senescent BJ cells. The expression of L1CAM affects the adhesion of BJ cells to the components of extracellular matrix.

## DISCUSSION

Despite that cellular senescence is a phenomenon well characterized and recognizable *in vitro* and the detection of SC in tissues is now less problematic due to the recently published robust method for their detection [67], there is a lack of strictly specific markers that would unambiguously allow targeting of SC for therapeutic purposes [68]. In search of cell-surface determinants overrepresented on senescent cells, we identified adhesion molecule L1CAM as being enhanced on replicatively senescent BJ fibroblasts. Further analysis of L1CAM expression in different senescence-inducing scenarios revealed that L1CAM expression depends on cell type and senescence-inducing stimulus, it shows marked intra-population heterogeneity and multiple levels of control, including regulation of the cell surface exposure. Our data also show that the L1CAM signaling pathway is interlinked with Erk signaling in a reciprocal manner. Stimuli changing cellular metabolism such as glucose levels, inhibition of the mevalonate pathway, and suppression of ANT2 (SCL325A5) all affected the level of L1CAM expression, suggesting that *L1CAM* gene expression might be controlled by the metabolic changes accompanying the development of cellular senescence. The L1CAM level correlated with increased migratory properties of both proliferating and senescent BJ cells and with enhanced adhesion of cells to the components of extracellular matrix.

Our proteomic comparative analysis of cell surface proteins of proliferating and senescent BJ cells based on surface protein biotinylation revealed more than 70 proteins significantly enhanced on the plasma membrane of senescent cells. In previous studies using different methodological approaches, several of these proteins, such as tissue inhibitor of metalloproteinase 3 (TIMP3) [38], γ-glutamyltranspeptidase 2 (GGT2) [39] and ADAMTS1 [40] have already been reported as being overrepresented in senescent cells, thereby validating the technique employed in this study.

The L1CAM/L1 cell adhesive molecule is a transmembrane glycoprotein originally discovered as a cell adhesion molecule in the nervous system [69], where it plays a crucial role during the brain development, being specifically involved in the neurite outgrowth [70] and fasciculation [71], adhesion of neurons and astrocytes [72], and cell migration [73]. L1CAM attracted our attention due to its aberrant expression in several types of human tumors, where it acts as a promalignant factor and progression marker. For instance, L1CAM expression increases with progression of breast cancer [31]. Further, L1CAM promotes tumor progression and metastasis in melanoma [32] and ovarian [33], gastric [34], lung [35], and pancreatic cancers [36, 37], where its presence is associated with a poor prognosis. Besides promoting cancer cell migration (see, e.g., [36]), including perineural invasion of cancer cells (for a review, see ref. [74]), L1CAM confers anti-apoptotic protection, chemoresistance [75] and radioresistance [76], stimulates cell survival [77] and acts as a pro-angiogenic factor [78].

Analysis of L1CAM induction in various cell types and senescence conditions revealed that the increase of the L1CAM total protein level during senescence was mostly associated with the increase of *L1CAM* transcript, indicating senescence-induced *de novo* transcription. Nevertheless, as in the case of HSF and RPE-1, the elevation of the total L1CAM protein must not necessarily be accompanied by the increase of its mRNA level indicative of senescence-mediated

posttranscriptional regulation of L1CAM. Moreover, the increase of the L1CAM total protein level was not always associated with its enhanced cell surface presence, indicating that the exposure of L1CAM on the cell surface of senescent cells is a complex process involving regulation at the transcriptional, post-transcriptional, and posttranslational levels.

Regulation of the *L1CAM* gene expression is controlled by diverse stimuli such as hypoxia or TGFβ signaling. It has been shown that inhibition of HIF-1 leads to inhibition of L1CAM and subsequent blockage of tumor growth and metastasis in lung cancer [55].

The cell cycle block responsible for premature senescence provoked by BrdU or IR is mediated by DNA damage response-induced expression of p21 and/or p16. In our attempt to understand the mechanism of L1CAM induction in premature senescence we found out that artificial expression of p16 itself is capable of elevating *L1CAM* transcript and protein levels, indicating that upstream DNA response signaling is not a prerequisite for senescence-mediated transcriptional induction of *L1CAM*. The notion that induction of *L1CAM* transcription was entirely absent in oncogenic Ras-induced senescence (Figure 2) led us to investigate the role of Ras/MAPK signaling in the control of *L1CAM* gene expression. Several reports point to the role of L1CAM signaling in augmentation of Erk activity ([52-54]). Based on observed intrapopulation variability where the L1CAM levels inversely correlated with Erk1/2 'basal' activity which increased after L1CAM downregulation, our results showed rather opposite relationship indicating cell type differences. In contrast, chemical inhibition of MAP kinase MEK or downregulation of Erk1 or Erk2 resulted in elevation of the L1CAM transcript and protein levels. This suggests the suppressive role of the Ras/MAPK pathway on the L1CAM expression and the existence of a regulatory circuit controlling the mutual balance of L1CAM and the Ras/MAPK signaling, where the expression of L1CAM is controlled by the Erk pathway in a negative feedback loop. It is therefore likely that the level of L1CAM expression in a particular cell type depends on the equilibrium of interlinked activities of Erk and L1CAM pathways. Furthermore, we found that L1CAM expression was also upregulated in A375 cells exposed to TGFβ in concordance with previous reports [79, 80]. Multiple interactions between TGFβ/SMAD and the Ras/MAPK pathways have been described (reviewed, e.g., in [81]). For instance, the Ras/MAPK pathway can suppress the activity of SMAD3 by Erk-dependent phosphorylation of SMAD3 [82]. It is therefore likely that chemical inhibition of MEK relieves the Ras/MAPK-mediated inhibition of the TGFβ pathway, resulting in increased expression of L1CAM; however, this warrants further investigation. The reciprocal expression of *SCL25A5/ANT2* and *L1CAM* genes could reflect their reverse transcriptional regulation by the TGFβ pathway. The *ANT2* gene belongs to early immediate genes induced by mitogens such as platelet-derived growth factor and epidermal growth factor [83], indicating the role of the MAPK pathway in *ANT2* gene expression. Expression of ANT2 is strictly growth-dependent, and ANT2 is suppressed during growth cessation mediated by TGFβ-activated NFI/SMAD transcription factor complexes [59, 84]. In contrast, L1CAM expression is induced by TGFβ ([79, 80] and this study) and suppressed by Ras/MAPK signaling (Figure 5). However, it seems that L1CAM expression might be ANT2-dependent, as RNA interference-mediated knockdown of ANT2 resulted in L1CAM induction. As L1CAM is induced by metabolic signals, we propose that changes in the energy metabolism in response to the cell cycle arrest induce L1CAM. Further study is needed to reveal the mechanism of L1CAM induction in SC.

The cause of heterogeneous expression of L1CAM in proliferating and senescent cell populations *in vitro* is unclear. We observed that cells sorted according to the L1CAM surface level sustained its level of expression for several consecutive population doublings prior the establishment/return to the original heterogeneity, indicative of the role of epigenetic rather than genetic factors (clonal evolution) in the L1CAM intra-population heterogeneity. Based on our results we propose that the individual cell-specific sensitivity to Ras/MAPK and TGFβ signaling sets the level of the L1CAM surface expression.

In accord with previous study showing that manipulation of the level of L1CAM affects the migration properties of breast cancer cells [31], we observed that downregulation of L1CAM attenuates migration of proliferating BJ cells, supporting the role of L1CAM in cell locomotion. Intriguingly, also SC with a higher level of L1CAM surface expression migrated faster, which was accompanied by increased adhesion to extracellular matrix proteins laminin-1, collagen-1, and fibronectin. Senescent cells migrated significantly slower compared to proliferating cells, which may reflect overall changes in the adhesion apparatus and cytoskeleton of senescent cells, and likely an aberrant cell polarity and response to chemotactic stimuli. We attempted to decipher the mechanism of enhanced locomotory properties of cells with elevated L1CAM. To this end, we analyzed the number and shape of focal adhesions, the RhoA activity, integrin α2β1 and integrin αV levels, and the cell polarization to a wound; however, we did not find any significant

differences among L1CAM high and low cell subpopulations (see Supplementary Figure 7A, B, C, D, E, and F). Our results are also broadly consistent with the L1CAM participation in axon guidance and neuronal migration, in a pathway culminating in MEK and Erk activation [85]. Furthermore, a very recent study showed that ionizing radiation reduces ADAM10 expression in brain microvascular endothelial cells and this indirectly leads to enhanced L1CAM protein level [86], suggesting yet another level of stress-responding L1CAM regulation.

Senescent cells represent premalignant cellular forms [6], and the expression of the L1CAM oncoprotein in senescent cells may provide them with specific features that can be inherited by tumor cells bypassing the senescence state [87]. There is accumulating evidence supported by experimental animal models that cancer cells can disseminate early during tumor development to form metastases later, after a shorter or longer period of dormancy (see, e.g. [88, 89], for a review, see [90]), sometimes even without observable formation of a primary tumor. Although it has not yet been proved experimentally that senescent cells can spread to distant tissues from the site of their origin, such possibility cannot be ruled out. Provided cellular senescence may be bypassed, as supported by several experimental findings (see, e.g., refs. [91, 92]), the migratory and invasive properties of senescent cells might become important. Based on the correlation between the L1CAM level and tumor invasiveness it cannot be excluded that migration of senescent cells in the tissues might also be affected by L1CAM expression. Given the emerging roles of SC in promoting both tumorigenesis and organismal aging, our present results may inspire future senolytic approaches through exploiting the cell-surface expression of L1CAM in cellular senescence.

## MATERIALS AND METHODS

### Chemicals and antibodies

Laminin-1 (human fibroblast-derived) and fibronectin (human plasma) were obtained from Sigma-Aldrich (St. Louis, MO, USA). Rat tail collagen type I was purchased from Millipore. Recombinant IFNγ was purchased from Peprotech (Rocky Hill, NJ, USA). Mouse monoclonal antibody against L1CAM from Sigma-Aldrich (Sigma-Aldrich), mouse monoclonal antibody against phosphoserine 139 of histone H2AX (Millipore, Billerica, MA, USA), rabbit polyclonal antibody against 53BP1 (Santa Cruz, CA, USA), and rabbit polyclonal antibody against γ-tubulin (Sigma Aldrich) were used for indirect immunofluorescence. Mouse monoclonal antibody against GAPDH (GeneTEX), rabbit polyclonal antibody against pan-actin (Sigma-Aldrich, St. Louis, MO, USA), and rabbit polyclonal against αTFIIH (Santa Cruz), rabbit polyclonal antibody against integrin αV (Cell Signaling), and mouse monoclonal antibody against integrin α2β1(Abcam) were used for immunoblotting. Anti-mouse IgG antibody Alexa 555 (Invitrogen, Carlsbad, CA, USA) and anti-rabbit IgG antibody Alexa 488 (Invitrogen) were used as secondary antibodies.

### Cell cultures and senescence induction

Human cancer cell lines (PC3 (ATCC® CRL-1435™), DU145 (ATCC® HTB-81™), A375 (ATCC® CRL-1619™), U2OS (ATCC® HTB-96™), PANC-1 (ATCC® CRL-1469™) ) and immortalized human epithelial cells (hTERT RPE-1, ATCC® CRL-4000™) were cultured in Dulbecco's modified Eagle's medium (D-MEM, Thermo Fisher Scientific, Waltham, MA, USA) supplemented with 10% fetal bovine serum (FBS, Gibco/Thermo Fisher Scientific) and 4.5 g/l of glucose. Primary human diploid fibroblast BJ (ATCC® CRL-2522™, population doubling 25-85), MRC5 (ATCC® CCL-171™, population doubling 24-61), and human skin fibroblasts (HSF-1; population doubling 20 - 26) were cultured in Dulbecco's modified Eagle's medium (D-MEM, Thermo Fisher Scientific) supplemented with 10% fetal bovine serum (FBS, Gibco/Thermo Fisher Scientific) and 1 g/l of glucose. Both cell culture media were supplemented with penicillin/streptomycin (Sigma-Aldrich). Cells were plated to match the equal cell density of control and senescent cell culture at the time of harvest.

Cells were kept at 37°C under 5% $CO_2$ atmosphere and 95% humidity. To bring cells to replicative senescence, BJ cells were split in ratio 1 : 2 until proliferation exhaustion (population doubling 85). To induce premature senescence, cells were treated either with 100 μM BrdU (BJ, MRC5, HSF-1, RPE, PC3, DU145, U2OS, PANC-1) for 10 days or with 10 μM BrdU (A375) for 7 days, 500 U/ml IFNγ (BJ) for 21 days, or irradiated with a dose of 10 or 20 Gy, as indicated. Oncogenic mutant H-Ras$^{V12}$ expressed in BJ was prepared as described earlier [93, 94]. H-Ras was induced by addition of 2 μg/ml of doxycycline every 48 hours for 16 days.

### Preparation of tet-one p16 and p21 constructs

cDNA sequences for p16 and p21 were synthesized in Genescript. The cDNAs were subcloned to the Lenti-X™ Tet-One™ Inducible Expression System, which was obtained from Clontech (631847).

**Preparation of recombinant lentiviruses, transduction of cells and clonal expansion**

Recombinant lentiviruses were obtained from calcium-phosphate transfected HEK 293T cells using packaging plasmids psPAX2 (Addgene, 12260) and pMD2.G (Addgene, 12259) together with either tet-one empty or tet-one p16 and p21 constructs. The medium containing lentiviral particles was harvested 36 to 48 h post-transfection, and the viral particles were precipitated using PEG-it (System Biosciences). Target cells H28 were transduced with viruses at multiplicity of infection MOI 5-10 and selected for puromycin resistance (2 µg/ml; Invivogen). For clonal expansion of each transduced cell type, single cells were sorted by BD FACSaria and the clones were then selected according to the expression profile of p16 or p21 protein.

**Senescence-associated-β-galactosidase assay**

Cells grown on glass coverslips were fixed with 0.5% glutaraldehyde at room temperature for 15 minutes, washed with PBS supplemented with 1 mM $MgCl_2$, and then incubated with pre-warmed X-gal solution (1 mg/ml X-gal (Sigma-Aldrich), 0.12 mM $K_3Fe[CN]_6$, 0.12 mM $K_4Fe[CN]_6 \times 3\ H_2O$, 1 mM $MgCl_2$ in PBS, pH 6.0) at 37°C and 5% $CO_2$ for 4 to 24 hours (depending on the cell type) according to Dimri et al. [95]. After development of visible blue coloring inside the cells, coverslips were mounted in Mowiol containing 4',6-diamidino-2-phenylindole (DAPI; Sigma-Aldrich) and viewed by fluorescence microscope Leica DMRXA (Leica Microsystems, Germany) equipped with a color camera.

**Live cell immunofluorescence**

Cells grown on glass coverslips were incubated with primary antibodies at room temperature for 15 minutes in PBS supplemented with $Ca^{2+}$ and $Mg^{2+}$ ($PBS^+$). After washing with $PBS^+$, incubation with secondary antibody was performed at room temperature for 15 minutes. After washing with $PBS^+$, cells were fixed with 4% formaldehyde at room temperature for 15 minutes. Coverslips were mounted in Mowiol containing DAPI to counterstain nuclei and viewed by fluorescence microscope Leica DMRXA.

**Indirect immunofluorescence**

Cells grown on glass coverslips were fixed with 4% formaldehyde and permeabilized with 0.1% Triton X-100 in two consecutive steps, each at room temperature for 15 minutes, and blocked with 10% FBS at room temperature for 30 minutes. After washing with PBS, cells were incubated with diluted primary antibodies at room temperature for 1 hour and then extensively washed with PBS/0.1% Tween 20. The incubation with secondary antibodies was performed at room temperature for 1 hour. Coverslips were mounted in Mowiol containing DAPI to counterstain nuclei and viewed by fluorescence microscope Leica DMRXA.

**Cell sorting**

Cells were washed two times with PBS and detached from the cultivation plates by incubation with accutase (Accumax, Merck Millipore, USA) at 37°C and 5% $CO_2$ for 2 to 3 minutes. To stop the protease, cultivation medium was added to the detached cells. Cell suspension was centrifuged at 700 x g for 5 minutes. The pellet was once washed with cultivation medium to get rid of the accutase, and the suspension was again centrifuged. Cell pellets were then stained with L1CAM antibody diluted 1 : 100 in cultivation medium on ice for 20 minutes, centrifuged, washed twice with culture medium and incubated with secondary antibody (diluted 1 : 500 in cultivation medium) on ice for 15 minutes. Cells were then washed twice with culture medium and after the last wash, they were resuspended in cultivation medium without serum and subjected to cell sorting.

**Cell cycle measurement**

Cells were washed with PBS, trypsinized, and subsequently collected into fresh medium. After centrifugation (500 x g at 4°C for 3 min), the cell pellet was resuspended in PBS. For fixation, a suspension drop was let drop into a centrifuge tube with -20°C 100% ethanol while vortexing and kept in -20°C for at least 2 hours. Fixed cells were collected by centrifugation, the cell pellet washed with PBS, resuspended in PBS containing RNase A (final concentration 0.2 mg/ml; Thermo Fisher Scientific, Waltham, MA, USA) and incubated at RT for 30 min. Prior to FACS measurement, propidium iodide (final concentration 12.5 µg/ml)/NP40 (final concentration 0.1%) solution was added to the samples.

**Surface protein purification and mass spectrometry**

BJ cells were labeled with $^{13}C_6$ arginine. The surface proteins were isolated using the biotinylation method (according to manufacturer's protocol, Thermo Fisher Scientific). Briefly, cells growing on a 10 $cm^2$ dish were washed with ice-cold DPBS and incubated with 0.25 mg/ml sulfoNHS-S-S-biotin (Thermo Fisher Scientific) solution in DPBS at 4°C for 15 min. Cells were washed three times and the remaining unreacted NHS ester was quenched with 100 mM glycine in DPBS. After 10 min at 4°C, the unreacted NHS ester was washed away with DPBS. Cells were then lysed on

the dish by adding 500 µl of lysis buffer (0.5% SDS, 500 mM NaCl, 50 mM Tris, pH 7.4). The lysate was denatured at 95°C for 5 min and sonicated. Total protein in light and heavy labeled samples was measured by the BCA method and samples were mixed in a 1 : 1 protein concentration ratio. One hundred µl of pre-equilibrated streptavidin-sepharose (GE Healthcare, USA) was mixed with the lysate and agitated at room temperature for 1 hour. After extensive washing four times with 1 ml of lysis buffer followed by washing four times with 1 ml of 1 M NaCl, 50 mM Tris (pH 7.4) and 2 × 1 ml of distilled water, the bound proteins were eluted three times with 200 µl 0.5% SDS, 50 mM Tris (pH 6.8), 10% glycerol, 50 mM TCEP at 95°C for 5 minutes. The pooled eluate was concentrated on a 10 kDa cut-off Microcon ultrafiltration column (Merck Millipore, USA) and loaded on the SDS-PAGE gel. After electrophoresis, each gel lane was cut into six slices, the protein reduced and alkylated by iodoacetamide, and digested with trypsin.

Digested peptides were desalted and peptide mixtures were measured using LC-MS consisting of a Dionex UltiMate 3000 RSLCnano system (Thermo Fisher Scientific) coupled via an EASY-spray ion source (Thermo Fisher Scientific) to an Orbitrap Elite mass spectrometer (Thermo Fisher Scientific). Purified peptides were separated on 15 cm EASY-Spray column (75 µm ID, PepMap C18, 2 µm particles, 100 Å pore size; Thermo Fisher Scientific). For each LC-MS/MS analysis, about 1 µg peptides were used for 165 min runs. First 5 min, peptides were loaded onto 2 cm trap column (Acclaim PepMap 100, 100 µm ID, C18, 5 µm particles, 100 Å pore size; Thermo Fisher Scientific) in loading buffer (98.9%/ 1%/0.1%, v/v/v, water/ acetonitrile/ formic acid) at a flow rate of 6 µl/min. Thereafter has been switched valve and peptides were loaded in buffer A (0.1% v/v formic acid in water) and eluted from EASY-Spray column with a linear 120 min gradient of 2% - 35% of buffer B (0.1% v/v formic acid in acetonitrile), followed by a 5 min 90% B wash at a flow rate 300 nl/min. EASY-Spray column temperature was kept at 35°C. Mass spectrometry data were acquired with a Top12 data-dependent MS/MS scan method. Target values for the full scan MS spectra were 1 x $10^6$ charges in the 300-1700 m/z range, with a maximum injection time of 35 ms and resolution of 120,000 at m/z 400. A 2 m/z isolation window and a fixed first mass of 110 m/z was used for MS/MS scans. Fragmentation of precursor ions was performed by CID dissociation with normalized collision energy of 35. MS/MS scans were performed in an ion trap with ion target value of 5 x $10^4$ and maximum injection time of 100 ms. Dynamic exclusion was set to 70 s to avoid repeated sequencing of identical peptides.

MS raw files were analysed by MaxQuant software (version 1.4.1.2), and peptide list were searched against the human Uniprot FASTA database and common contaminants database by the Andromeda search engine with cysteine carbamidomethylation as a fixed modification and N-terminal acetylation, methionine oxidations and thioacyl-lysine as variable modification. The false discovery rate was set to 0.01 for both proteins and peptides with a minimum length of six amino acids and was determined by searching a reverse database. Trypsin was set as protease, and a maximum of two missed cleavages were allowed in the database search. Peptide identification was performed with an allowed initial precursor mass deviation up to 7 ppm and an allowed fragment mass deviation of 0.5 Da. Matching between runs was performed. Quantification of SILAC pairs was performed by MaxQuant with standard setting using a minimum ratio count of 2.

Bioinformatics analyses were performed with the Perseus software.

**Quantitative real time reverse transcription polymerase chain reaction (qRT-PCR)**

Total RNA was isolated using RNeasy Mini Kit (Qiagen, MD, USA) according to the manufacturer's protocol. First strand cDNA was synthesized from 200 ng of total RNA with random hexamer primers using TaqMan Reverse Transcription Reagents (Applied Biosystems). qRT-PCR was performed in ABI Prism 7300 (Applied Biosystems) using SYBR Green I Master Mix (Applied Biosystems).

The following sets of primers were used:

L1CAM: forward: 5' –CGGCTACTCTGGAGAGGAC TAC-3', reverse: 5'- CGGCACTTGAGTTGAGGAT-3';
ANT2: forward: 5'-GCCGCCTACTTCGGTATCTAT G-3', reverse: 5'-CAGCAGTGACAGTCTGTGCGAT-3';
GAPDH: forward: 5'-GCCAAAAGGGTCATCATCT C-3', reverse: 5'-CTAAGCAGTTGGTGGTGCAG-3'.

The relative quantity of cDNA was estimated by the ΔΔCt method [96]; data were normalized to GAPDH. Samples were measured in triplicates.

**SDS-PAGE and immunoblotting**

Cells were washed two times with PBS and then harvested into Laemmli SDS sample lysis buffer, sonicated, and centrifuged at 1600 x g for 10 min. Concentration of proteins was estimated by the BCA method (Pierce Biotechnology Inc., Rockford, USA).

Before separation by SDS-PAGE (9% and 14% gels were used), 100 mM DTT and 0.01% bromophenol blue were added to the cell lysates. The same protein amount (40 μg) was loaded into each well. After electrophoresis, proteins were electrotransferred from the gel onto a nitrocellulose membrane using the wet transfer method and detected by specific antibodies combined with horseradish peroxidase-conjugated secondary antibodies (donkey anti-mouse, Bio-Rad, Hercules, CA, USA). Peroxidase activity was detected by ECL (Pierce Biotechnology Inc.). GAPDH or pan-actin were used as a marker of equal loading, as indicated.

**Wound healing assay**

A confluent monolayer was disrupted with 10 μl micropipette tip. To remove floating cells, the culture medium was removed and replaced by fresh medium. Recovery of the disrupted area was monitored with time-lapse Leica Microscope DMI6000 for 32 to 48 hours. Cell migration was quantified by comparing the corrupted area with the recovered area according to formula: % of recovering = [(corrupted area – recovered area) / corrupted area] × 100. The size of the area was measured using ImageJ Software; velocity was analyzed with tracking plug-in.

**3D migration assay**

BJ cells sorted according to the L1CAM surface level were serum-starved for 24 hours and then seeded into collagen-containing Matrigel inserted in the column (μ-Slide Chemotaxis 3D, Ibidi, Munich, Germany) according to the manufacturer's protocol. Migration directed towards serum-containing medium was monitored with time-lapse Leica Microscope DMI6000 for 8 hours. Cell tracking was performed using ImageJ Software. For estimation of velocity and distance of the tracked cells, Chemotaxis and Migration Tool Software (Ibidi) was used. To evaluate random migration, the same procedure was used except that BJ cells were stained with antibody against L1CAM prior to seeding into Matrigel (to discriminate cells according to the L1CAM level based on the intensity of L1CAM surface staining (no fluorescence signal referred to cells with a low L1CAM level; in contrast, high L1CAM cells were those that showed strong fluorescence signal).

**Adhesion assay**

A 96-well cell culture plate was coated with laminin-1 (10 μg/ml in Hank's balanced salt solution), fibronectin (20 μg/ml in H2O), or rat tail collagen 1 (2 μg/ml in H2O) at 37°C at 5% CO2 for 1 hour. After washing with 0.1% BSA dissolved in DMEM (WB), the wells were blocked with blocking buffer (0.5% BSA in DMEM) at 37°C at 5% CO2 for 1 hour. After subsequent washing with WB, the plate was chilled on ice for 5 minutes, cell suspensions were seeded into the wells and left to adhere in a CO2 incubator at 37°C for 30 minutes. Next, the plate was shaken at 200 rpm for 10 to 15 seconds and washed three times with WB. Cells were then fixed with 4% formaldehyde at room temperature for 15 minutes, washed with WB and stained with crystal violet (5 mg/ml in 2% ethanol) for 10 minutes. The plate was subsequently washed several times with H2O to get rid of the remains of crystal violet. After drying up the plates, 2% SDS (in H2O) was added and incubated at room temperature for 30 minutes. Optical density at 550 nm was estimated by a spectrophotometer (Multiskan EX, Thermo Scientific, USA).

**RNA interference**

siRNAs targeting L1CAM (sense: GCAAGAGACAUA UCCACAAtt, antisense: UUGUGGAUAUGUCUCUU GCtg) were introduced into the cells using Lipofectamine™ RNAiMAX (Invitrogen, Carlsbad, CA, USA). Nonsense siRNA sequences (siNT; Ambion, CA, USA) were used as a negative control. shRNAs targeting L1CAM were introduced into the cells using a lentiviral vector. The shRNA vector targeting L1CAM was obtained by insertion of double-stranded oligo: 5'-CGGCAGCAAGAGACATATCCACAACTCGAG TTGTGGATATGTCTCTTGCTGTTTTT-3' into the *Age*I and *Eco*RI sites in the pLKO.1 vector. A non-target shRNA plasmid was obtained from Sigma (cat. No. SHC016). Lentiviral particles were produced by co-transfection with pMD2.G and psPAX2 (a kind gift from Didier Trono) in HEK293T cells as described previously [93]. Stably transduced cells were selected after 7 days by growing in media containing 2.5 μg/ml of puromycin.

**RhoA activity measurement**

RhoA activity was measured using G-LISA Activation Assay (Cytoskeleton, Inc). The procedure was performed according to manufacturer's protocol.

**Determination of cell nuclei polarization**

Confluent cell monolayer was scratched by pipette tip. After 4 hours, cells were stained (live) with the L1CAM antibody, then fixed, permeabilized and stained with antibody against a marker of MTOC, γ-tubulin. For determination of cell polarization, the position of MTOC was measured relatively to perpendicular lines (90°) positioned toward the scratch line [97]. The nuclei with MTOC present within the perpendicular lines were considered as polarized.

## Abbreviations

ADAMTS1: a disintegrin and metalloproteinase with thrombospondin motif 1; ANT2: adenine nucleotide translocase 2; BrdU: 5-bromo-2'-deoxyuridine; DAPI: 4',6-diamidino-2-phenylindole; FACS: fluorescence-activated cell sorting; GAPDH: glyceraldehyde 3-phosphate dehydrogenase; GGT2: gamma-glutamyl-transpeptidase 2; IFNγ: interferon gamma; IL: interleukin; IR: ionizing radiation; MAPK: mitogen-activated protein kinase; MCP-1: monocyte chemotactic protein 1; NFI: nuclear factor I; NFκB: nuclear factor kappa B; PD: population doubling; PVR: poliovirus receptor; SASP: senescence-associated secretory phenotype; SA-β-gal: senescence-associated beta-galactosidase; SC: senescent cells; SMAD: small mothers against decapentaplegic; TGFβ: transforming growth factor beta; TIMP3: tissue inhibitor of metalloproteinase 3.

## AUTHOR CONTRIBUTIONS

BM performed the research, analyzed the data and wrote the paper. RD, TI, LK, PB, PD, DH, MH, ZN, LA, PH, PV and OS performed the research and analyzed the data. JB wrote the paper. ZH designed the study, analyzed and interpreted the data, and wrote the paper.

## ACKNOWLEDGEMENTS

We acknowledge EATRIS-CZ infrastructure for providing open-access to the study. We thank Zdenek Cimburek and Matyas Sima for assistance with cell sorting, Ondrej Horvath for FACS technical support, Martin Capek for helping with cell tracking, Tomas Vomastek and Miloslava Maninova for the help with migration experiments, Gita Novakova for preparation of cell clones with ectopic expression of cdk inhibitors and Marketa Vancurova for technical assistance with cell cultures.

We confirm that the data presented in the manuscript are novel; they have not been published and are not under consideration for publication elsewhere.

## CONFLICTS OF INTEREST

The authors declare they have no conflict of interest.

## FUNDING

This study was supported by the Grant Agency of the Czech Republic (Project 15-03379S), the Institutional Grant (Project RVO 68378050), Diana21 (Smartbrain s.r.o.), the Danish Council for Independent Research and the Swedish Research Council.

## REFERENCES

1. Baker DJ, Childs BG, Durik M, Wijers ME, Sieben CJ, Zhong J, Saltness RA, Jeganathan KB, Verzosa GC, Pezeshki A, Khazaie K, Miller JD, van Deursen JM. Naturally occurring p16(Ink4a)-positive cells shorten healthy lifespan. Nature. 2016; 530:184–89. https://doi.org/10.1038/nature16932

2. Baker DJ, Wijshake T, Tchkonia T, LeBrasseur NK, Childs BG, van de Sluis B, Kirkland JL, van Deursen JM. Clearance of p16Ink4a-positive senescent cells delays ageing-associated disorders. Nature. 2011; 479:232–36. https://doi.org/10.1038/nature10600

3. Muñoz-Espín D, Serrano M. Cellular senescence: from physiology to pathology. Nat Rev Mol Cell Biol. 2014; 15:482–96. https://doi.org/10.1038/nrm3823

4. Jun JI, Lau LF. The matricellular protein CCN1 induces fibroblast senescence and restricts fibrosis in cutaneous wound healing. Nat Cell Biol. 2010; 12:676–85. https://doi.org/10.1038/ncb2070

5. Demaria M, Ohtani N, Youssef SA, Rodier F, Toussaint W, Mitchell JR, Laberge RM, Vijg J, Van Steeg H, Dollé ME, Hoeijmakers JH, de Bruin A, Hara E, Campisi J. An essential role for senescent cells in optimal wound healing through secretion of PDGF-AA. Dev Cell. 2014; 31:722–33. https://doi.org/10.1016/j.devcel.2014.11.012

6. Michaloglou C, Vredeveld LC, Soengas MS, Denoyelle C, Kuilman T, van der Horst CM, Majoor DM, Shay JW, Mooi WJ, Peeper DS. BRAFE600-associated senescence-like cell cycle arrest of human naevi. Nature. 2005; 436:720–24. https://doi.org/10.1038/nature03890

7. Bartkova J, Rezaei N, Liontos M, Karakaidos P, Kletsas D, Issaeva N, Vassiliou LV, Kolettas E, Niforou K, Zoumpourlis VC, Takaoka M, Nakagawa H, Tort F, et al. Oncogene-induced senescence is part of the tumorigenesis barrier imposed by DNA damage checkpoints. Nature. 2006; 444:633–37. https://doi.org/10.1038/nature05268

8. Di Micco R, Fumagalli M, Cicalese A, Piccinin S, Gasparini P, Luise C, Schurra C, Garre' M, Nuciforo PG, Bensimon A, Maestro R, Pelicci PG, d'Adda di Fagagna F. Oncogene-induced senescence is a DNA damage response triggered by DNA hyper-replication. Nature. 2006; 444:638–42. https://doi.org/10.1038/nature05327

9. Chang BD, Broude EV, Dokmanovic M, Zhu H, Ruth A, Xuan Y, Kandel ES, Lausch E, Christov K, Roninson IB.

A senescence-like phenotype distinguishes tumor cells that undergo terminal proliferation arrest after exposure to anticancer agents. Cancer Res. 1999; 59:3761–67.

10. te Poele RH, Okorokov AL, Jardine L, Cummings J, Joel SP. DNA damage is able to induce senescence in tumor cells in vitro and in vivo. Cancer Res. 2002; 62:1876–83.

11. Nelson G, Wordsworth J, Wang C, Jurk D, Lawless C, Martin-Ruiz C, von Zglinicki T. A senescent cell bystander effect: senescence-induced senescence. Aging Cell. 2012; 11:345–49. https://doi.org/10.1111/j.1474-9726.2012.00795.x

12. Orjalo AV, Bhaumik D, Gengler BK, Scott GK, Campisi J. Cell surface-bound IL-1alpha is an upstream regulator of the senescence-associated IL-6/IL-8 cytokine network. Proc Natl Acad Sci USA. 2009; 106:17031–36. https://doi.org/10.1073/pnas.0905299106

13. Schafer MJ, White TA, Iijima K, Haak AJ, Ligresti G, Atkinson EJ, Oberg AL, Birch J, Salmonowicz H, Zhu Y, Mazula DL, Brooks RW, Fuhrmann-Stroissnigg H, et al. Cellular senescence mediates fibrotic pulmonary disease. Nat Commun. 2017; 8:14532. https://doi.org/10.1038/ncomms14532

14. Coppé JP, Patil CK, Rodier F, Sun Y, Muñoz DP, Goldstein J, Nelson PS, Desprez PY, Campisi J. Senescence-associated secretory phenotypes reveal cell-nonautonomous functions of oncogenic RAS and the p53 tumor suppressor. PLoS Biol. 2008; 6:2853–68. https://doi.org/10.1371/journal.pbio.0060301

15. Acosta JC, Banito A, Wuestefeld T, Georgilis A, Janich P, Morton JP, Athineos D, Kang TW, Lasitschka F, Andrulis M, Pascual G, Morris KJ, Khan S, et al. A complex secretory program orchestrated by the inflammasome controls paracrine senescence. Nat Cell Biol. 2013; 15:978–90. https://doi.org/10.1038/ncb2784

16. Hubackova S, Krejcikova K, Bartek J, Hodny Z. IL1- and TGFβ-Nox4 signaling, oxidative stress and DNA damage response are shared features of replicative, oncogene-induced, and drug-induced paracrine 'bystander senescence'. Aging (Albany NY). 2012; 4:932–51. https://doi.org/10.18632/aging.100520

17. Starr ME, Saito M, Evers BM, Saito H. Age-Associated Increase in Cytokine Production During Systemic Inflammation-II: The Role of IL-1β in Age-Dependent IL-6 Upregulation in Adipose Tissue. J Gerontol A Biol Sci Med Sci. 2015; 70:1508–15. https://doi.org/10.1093/gerona/glu197

18. Hoenicke L, Zender L. Immune surveillance of senescent cells--biological significance in cancer- and non-cancer pathologies. Carcinogenesis. 2012; 33:1123–26. https://doi.org/10.1093/carcin/bgs124

19. Cudejko C, Wouters K, Fuentes L, Hannou SA, Paquet C, Bantubungi K, Bouchaert E, Vanhoutte J, Fleury S, Remy P, Tailleux A, Chinetti-Gbaguidi G, Dombrowicz D, et al. p16INK4a deficiency promotes IL-4-induced polarization and inhibits proinflammatory signaling in macrophages. Blood. 2011; 118:2556–66. https://doi.org/10.1182/blood-2010-10-313106

20. Fuentes L, Wouters K, Hannou SA, Cudejko C, Rigamonti E, Mayi TH, Derudas B, Pattou F, Chinetti-Gbaguidi G, Staels B, Paumelle R. Downregulation of the tumour suppressor p16INK4A contributes to the polarisation of human macrophages toward an adipose tissue macrophage (ATM)-like phenotype. Diabetologia. 2011; 54:3150–56. https://doi.org/10.1007/s00125-011-2324-0

21. Bürrig KF. The endothelium of advanced arteriosclerotic plaques in humans. Arterioscler Thromb. 1991; 11:1678–89. https://doi.org/10.1161/01.ATV.11.6.1678

22. Jeon OH, Kim C, Laberge RM, Demaria M, Rathod S, Vasserot AP, Chung JW, Kim DH, Poon Y, David N, Baker DJ, van Deursen JM, Campisi J, Elisseeff JH. Local clearance of senescent cells attenuates the development of post-traumatic osteoarthritis and creates a pro-regenerative environment. Nat Med. 2017; 23:775–81. https://doi.org/10.1038/nm.4324

23. McCulloch K, Litherland GJ, Rai TS. Cellular senescence in osteoarthritis pathology. Aging Cell. 2017; 16:210–18. https://doi.org/10.1111/acel.12562

24. Zhu F, Li Y, Zhang J, Piao C, Liu T, Li HH, Du J. Senescent cardiac fibroblast is critical for cardiac fibrosis after myocardial infarction. PLoS One. 2013; 8:e74535. https://doi.org/10.1371/journal.pone.0074535

25. Kim KH, Chen CC, Monzon RI, Lau LF. Matricellular protein CCN1 promotes regression of liver fibrosis through induction of cellular senescence in hepatic myofibroblasts. Mol Cell Biol. 2013; 33:2078–90. https://doi.org/10.1128/MCB.00049-13

26. Sone H, Kagawa Y. Pancreatic beta cell senescence contributes to the pathogenesis of type 2 diabetes in high-fat diet-induced diabetic mice. Diabetologia. 2005; 48:58–67. https://doi.org/10.1007/s00125-004-1605-2

27. Bhat R, Crowe EP, Bitto A, Moh M, Katsetos CD, Garcia FU, Johnson FB, Trojanowski JQ, Sell C, Torres C. Astrocyte senescence as a component of Alzheimer's disease. PLoS One. 2012; 7:e45069. https://doi.org/10.1371/journal.pone.0045069

28. Chinta SJ, Lieu CA, Demaria M, Laberge RM, Campisi J, Andersen JK. Environmental stress, ageing and glial cell senescence: a novel mechanistic link to Parkinson's disease? J Intern Med. 2013; 273:429–36. https://doi.org/10.1111/joim.12029

29. Demaria M, O'Leary MN, Chang J, Shao L, Liu S, Alimirah F, Koenig K, Le C, Mitin N, Deal AM, Alston S, Academia EC, Kilmarx S, et al. Cellular Senescence Promotes Adverse Effects of Chemotherapy and Cancer Relapse. Cancer Discov. 2017; 7:165–76. https://doi.org/10.1158/2159-8290.CD-16-0241

30. Campisi J, d'Adda di Fagagna F. Cellular senescence: when bad things happen to good cells. Nat Rev Mol Cell Biol. 2007; 8:729–40. https://doi.org/10.1038/nrm2233

31. Li Y, Galileo DS. Soluble L1CAM promotes breast cancer cell adhesion and migration in vitro, but not invasion. Cancer Cell Int. 2010; 10:34. https://doi.org/10.1186/1475-2867-10-34

32. Fogel M, Mechtersheimer S, Huszar M, Smirnov A, Abu-Dahi A, Tilgen W, Reichrath J, Georg T, Altevogt P, Gutwein P. L1 adhesion molecule (CD 171) in development and progression of human malignant melanoma. Cancer Lett. 2003; 189:237–47. https://doi.org/10.1016/S0304-3835(02)00513-X

33. Bondong S, Kiefel H, Hielscher T, Zeimet AG, Zeillinger R, Pils D, Schuster E, Castillo-Tong DC, Cadron I, Vergote I, Braicu I, Sehouli J, Mahner S, et al. Prognostic significance of L1CAM in ovarian cancer and its role in constitutive NF-κB activation. Ann Oncol. 2012; 23:1795–802. https://doi.org/10.1093/annonc/mdr568

34. Chen DL, Zeng ZL, Yang J, Ren C, Wang DS, Wu WJ, Xu RH. L1cam promotes tumor progression and metastasis and is an independent unfavorable prognostic factor in gastric cancer. J Hematol Oncol. 2013; 6:43. https://doi.org/10.1186/1756-8722-6-43

35. Tischler V, Pfeifer M, Hausladen S, Schirmer U, Bonde AK, Kristiansen G, Sos ML, Weder W, Moch H, Altevogt P, Soltermann A. L1CAM protein expression is associated with poor prognosis in non-small cell lung cancer. Mol Cancer. 2011; 10:127. https://doi.org/10.1186/1476-4598-10-127

36. Geismann C, Morscheck M, Koch D, Bergmann F, Ungefroren H, Arlt A, Tsao MS, Bachem MG, Altevogt P, Sipos B, Fölsch UR, Schäfer H, Müerköster SS. Up-regulation of L1CAM in pancreatic duct cells is transforming growth factor beta1- and slug-dependent: role in malignant transformation of pancreatic cancer. Cancer Res. 2009; 69:4517–26. https://doi.org/10.1158/0008-5472.CAN-08-3493

37. Tsutsumi S, Morohashi S, Kudo Y, Akasaka H, Ogasawara H, Ono M, Takasugi K, Ishido K, Hakamada K, Kijima H. L1 Cell adhesion molecule (L1CAM) expression at the cancer invasive front is a novel prognostic marker of pancreatic ductal adenocarcinoma. J Surg Oncol. 2011; 103:669–73. https://doi.org/10.1002/jso.21880

38. Kim YM, Byun HO, Jee BA, Cho H, Seo YH, Kim YS, Park MH, Chung HY, Woo HG, Yoon G. Implications of time-series gene expression profiles of replicative senescence. Aging Cell. 2013; 12:622–34. https://doi.org/10.1111/acel.12087

39. Martin MN, Saladores PH, Lambert E, Hudson AO, Leustek T. Localization of members of the gamma-glutamyl transpeptidase family identifies sites of glutathione and glutathione S-conjugate hydrolysis. Plant Physiol. 2007; 144:1715–32. https://doi.org/10.1104/pp.106.094409

40. Yoon IK, Kim HK, Kim YK, Song IH, Kim W, Kim S, Baek SH, Kim JH, Kim JR. Exploration of replicative senescence-associated genes in human dermal fibroblasts by cDNA microarray technology. Exp Gerontol. 2004; 39:1369–78. https://doi.org/10.1016/j.exger.2004.07.002

41. Smith JR, Hayflick L. Variation in the life-span of clones derived from human diploid cell strains. J Cell Biol. 1974; 62:48–53. https://doi.org/10.1083/jcb.62.1.48

42. Robles SJ, Adami GR. Agents that cause DNA double strand breaks lead to p16INK4a enrichment and the premature senescence of normal fibroblasts. Oncogene. 1998; 16:1113–23. https://doi.org/10.1038/sj.onc.1201862

43. Michishita E, Nakabayashi K, Suzuki T, Kaul SC, Ogino H, Fujii M, Mitsui Y, Ayusawa D. 5-Bromodeoxyuridine induces senescence-like phenomena in mammalian cells regardless of cell type or species. J Biochem. 1999; 126:1052–59. https://doi.org/10.1093/oxfordjournals.jbchem.a022549

44. Kim KS, Kang KW, Seu YB, Baek SH, Kim JR. Interferon-gamma induces cellular senescence through p53-dependent DNA damage signaling in human endothelial cells. Mech Ageing Dev. 2009; 130:179–88. https://doi.org/10.1016/j.mad.2008.11.004

45. Yeo EJ, Hwang YC, Kang CM, Kim IH, Kim DI, Parka JS, Choy HE, Park WY, Park SC. Senescence-like changes induced by hydroxyurea in human diploid fibroblasts. Exp Gerontol. 2000; 35:553–71. https://doi.org/10.1016/S0531-5565(00)00108-X

46. Serrano M, Lin AW, McCurrach ME, Beach D, Lowe SW. Oncogenic ras provokes premature cell senescence associated with accumulation of p53 and

p16INK4a. Cell. 1997; 88:593–602. https://doi.org/10.1016/S0092-8674(00)81902-9

47. Grage-Griebenow E, Jerg E, Gorys A, Wicklein D, Wesch D, Freitag-Wolf S, Goebel L, Vogel I, Becker T, Ebsen M, Röcken C, Altevogt P, Schumacher U, et al. L1CAM promotes enrichment of immunosuppressive T cells in human pancreatic cancer correlating with malignant progression. Mol Oncol. 2014; 8:982–97. https://doi.org/10.1016/j.molonc.2014.03.001

48. Simova J, Sapega O, Imrichova T, Stepanek I, Kyjacova L, Mikyskova R, Indrova M, Bieblova J, Bubenik J, Bartek J, Hodny Z, Reinis M. Tumor growth accelerated by chemotherapy-induced senescent cells is suppressed by treatment with IL-12 producing cellular vaccines. Oncotarget. 2016; 7:54952–64. https://doi.org/10.18632/oncotarget.10712

49. Braumüller H, Wieder T, Brenner E, Aßmann S, Hahn M, Alkhaled M, Schilbach K, Essmann F, Kneilling M, Griessinger C, Ranta F, Ullrich S, Mocikat R, et al. T-helper-1-cell cytokines drive cancer into senescence. Nature. 2013; 494:361–65. https://doi.org/10.1038/nature11824

50. Galanos P, Vougas K, Walter D, Polyzos A, Maya-Mendoza A, Haagensen EJ, Kokkalis A, Roumelioti FM, Gagos S, Tzetis M, Canovas B, Igea A, Ahuja AK, et al. Chronic p53-independent p21 expression causes genomic instability by deregulating replication licensing. Nat Cell Biol. 2016; 18:777–89. https://doi.org/10.1038/ncb3378

51. Leontieva OV, Lenzo F, Demidenko ZN, Blagosklonny MV. Hyper-mitogenic drive coexists with mitotic incompetence in senescent cells. Cell Cycle. 2012; 11:4642–49. https://doi.org/10.4161/cc.22937

52. Schaefer AW, Kamiguchi H, Wong EV, Beach CM, Landreth G, Lemmon V. Activation of the MAPK signal cascade by the neural cell adhesion molecule L1 requires L1 internalization. J Biol Chem. 1999; 274:37965–73. https://doi.org/10.1074/jbc.274.53.37965

53. Silletti S, Yebra M, Perez B, Cirulli V, McMahon M, Montgomery AM. Extracellular signal-regulated kinase (ERK)-dependent gene expression contributes to L1 cell adhesion molecule-dependent motility and invasion. J Biol Chem. 2004; 279:28880–88. https://doi.org/10.1074/jbc.M404075200

54. Yi YS, Baek KS, Cho JY. L1 cell adhesion molecule induces melanoma cell motility by activation of mitogen-activated protein kinase pathways. Pharmazie. 2014; 69:461–67.

55. Zhang H, Wong CC, Wei H, Gilkes DM, Korangath P, Chaturvedi P, Schito L, Chen J, Krishnamachary B, Winnard PT Jr, Raman V, Zhen L, Mitzner WA, et al. HIF-1-dependent expression of angiopoietin-like 4 and L1CAM mediates vascular metastasis of hypoxic breast cancer cells to the lungs. Oncogene. 2012; 31:1757–70. https://doi.org/10.1038/onc.2011.365

56. Li M, Durbin KR, Sweet SM, Tipton JD, Zheng Y, Kelleher NL. Oncogene-induced cellular senescence elicits an anti-Warburg effect. Proteomics. 2013; 13:2585–96. https://doi.org/10.1002/pmic.201200298

57. Gey C, Seeger K. Metabolic changes during cellular senescence investigated by proton NMR-spectroscopy. Mech Ageing Dev. 2013; 134:130–38. https://doi.org/10.1016/j.mad.2013.02.002

58. Maya-Mendoza A, Ostrakova J, Kosar M, Hall A, Duskova P, Mistrik M, Merchut-Maya JM, Hodny Z, Bartkova J, Christensen C, Bartek J. Myc and Ras oncogenes engage different energy metabolism programs and evoke distinct patterns of oxidative and DNA replication stress. Mol Oncol. 2015; 9:601–16. https://doi.org/10.1016/j.molonc.2014.11.001

59. Kretova M, Sabova L, Hodny Z, Bartek J, Kollarovic G, Nelson BD, Hubackova S, Luciakova K. TGF-β/NF1/Smad4-mediated suppression of ANT2 contributes to oxidative stress in cellular senescence. Cell Signal. 2014; 26:2903–11. https://doi.org/10.1016/j.cellsig.2014.08.029

60. Hubackova S, Kucerova A, Michlits G, Kyjacova L, Reinis M, Korolov O, Bartek J, Hodny Z. IFNγ induces oxidative stress, DNA damage and tumor cell senescence via TGFβ/SMAD signaling-dependent induction of Nox4 and suppression of ANT2. Oncogene. 2016; 35:1236–49. https://doi.org/10.1038/onc.2015.162

61. Chevrollier A, Loiseau D, Reynier P, Stepien G. Adenine nucleotide translocase 2 is a key mitochondrial protein in cancer metabolism. Biochim Biophys Acta. 2011; 1807:562–67. https://doi.org/10.1016/j.bbabio.2010.10.008

62. Chevrollier A, Loiseau D, Chabi B, Renier G, Douay O, Malthièry Y, Stepien G. ANT2 isoform required for cancer cell glycolysis. J Bioenerg Biomembr. 2005; 37:307–16. https://doi.org/10.1007/s10863-005-8642-5

63. Giraud S, Bonod-Bidaud C, Wesolowski-Louvel M, Stepien G. Expression of human ANT2 gene in highly proliferative cells: GRBOX, a new transcriptional element, is involved in the regulation of glycolytic ATP import into mitochondria. J Mol Biol. 1998; 281:409–18. https://doi.org/10.1006/jmbi.1998.1955

64. Valiente M, Obenauf AC, Jin X, Chen Q, Zhang XH, Lee DJ, Chaft JE, Kris MG, Huse JT, Brogi E, Massagué J. Serpins promote cancer cell survival and vascular co-

option in brain metastasis. Cell. 2014; 156:1002–16. https://doi.org/10.1016/j.cell.2014.01.040

65. Wang E. Are cross-bridging structures involved in the bundle formation of intermediate filaments and the decrease in locomotion that accompany cell aging? J Cell Biol. 1985; 100:1466–73. https://doi.org/10.1083/jcb.100.5.1466

66. Nishio K, Inoue A. Senescence-associated alterations of cytoskeleton: extraordinary production of vimentin that anchors cytoplasmic p53 in senescent human fibroblasts. Histochem Cell Biol. 2005; 123:263–73. https://doi.org/10.1007/s00418-005-0766-5

67. Evangelou K, Lougiakis N, Rizou SV, Kotsinas A, Kletsas D, Muñoz-Espín D, Kastrinakis NG, Pouli N, Marakos P, Townsend P, Serrano M, Bartek J, Gorgoulis VG. Robust, universal biomarker assay to detect senescent cells in biological specimens. Aging Cell. 2017; 16:192–97. https://doi.org/10.1111/acel.12545

68. Biran A, Zada L, Abou Karam P, Vadai E, Roitman L, Ovadya Y, Porat Z, Krizhanovsky V. Quantitative identification of senescent cells in aging and disease. Aging Cell. 2017; 16:661–71. https://doi.org/10.1111/acel.12592

69. Rathjen FG, Schachner M. Immunocytological and biochemical characterization of a new neuronal cell surface component (L1 antigen) which is involved in cell adhesion. EMBO J. 1984; 3:1–10.

70. Chang S, Rathjen FG, Raper JA. Extension of neurites on axons is impaired by antibodies against specific neural cell surface glycoproteins. J Cell Biol. 1987; 104:355–62. https://doi.org/10.1083/jcb.104.2.355

71. Fischer G, Künemund V, Schachner M. Neurite outgrowth patterns in cerebellar microexplant cultures are affected by antibodies to the cell surface glycoprotein L1. J Neurosci. 1986; 6:605–12.

72. Keilhauer G, Faissner A, Schachner M. Differential inhibition of neurone-neurone, neurone-astrocyte and astrocyte-astrocyte adhesion by L1, L2 and N-CAM antibodies. Nature. 1985; 316:728–30. https://doi.org/10.1038/316728a0

73. Lindner J, Rathjen FG, Schachner M. L1 mono- and polyclonal antibodies modify cell migration in early postnatal mouse cerebellum. Nature. 1983; 305:427–30. https://doi.org/10.1038/305427a0

74. Bapat AA, Hostetter G, Von Hoff DD, Han H. Perineural invasion and associated pain in pancreatic cancer. Nat Rev Cancer. 2011; 11:695–707. https://doi.org/10.1038/nrc3131

75. Geismann C, Arlt A, Bauer I, Pfeifer M, Schirmer U, Altevogt P, Müerköster SS, Schäfer H. Binding of the transcription factor Slug to the L1CAM promoter is essential for transforming growth factor-β1 (TGF-β)-induced L1CAM expression in human pancreatic ductal adenocarcinoma cells. Int J Oncol. 2011; 38:257–66.

76. Cheng L, Wu Q, Huang Z, Guryanova OA, Huang Q, Shou W, Rich JN, Bao S. L1CAM regulates DNA damage checkpoint response of glioblastoma stem cells through NBS1. EMBO J. 2011; 30:800–13. https://doi.org/10.1038/emboj.2011.10

77. Nishimune H, Bernreuther C, Carroll P, Chen S, Schachner M, Henderson CE. Neural adhesion molecules L1 and CHL1 are survival factors for motoneurons. J Neurosci Res. 2005; 80:593–99. https://doi.org/10.1002/jnr.20517

78. Friedli A, Fischer E, Novak-Hofer I, Cohrs S, Ballmer-Hofer K, Schubiger PA, Schibli R, Grünberg J. The soluble form of the cancer-associated L1 cell adhesion molecule is a pro-angiogenic factor. Int J Biochem Cell Biol. 2009; 41:1572–80. https://doi.org/10.1016/j.biocel.2009.01.006

79. Mechtersheimer S, Gutwein P, Agmon-Levin N, Stoeck A, Oleszewski M, Riedle S, Postina R, Fahrenholz F, Fogel M, Lemmon V, Altevogt P. Ectodomain shedding of L1 adhesion molecule promotes cell migration by autocrine binding to integrins. J Cell Biol. 2001; 155:661–73. https://doi.org/10.1083/jcb.200101099

80. Sebens Müerköster S, Werbing V, Sipos B, Debus MA, Witt M, Grossmann M, Leisner D, Kötteritzsch J, Kappes H, Klöppel G, Altevogt P, Fölsch UR, Schäfer H. Drug-induced expression of the cellular adhesion molecule L1CAM confers anti-apoptotic protection and chemoresistance in pancreatic ductal adeno-carcinoma cells. Oncogene. 2007; 26:2759–68. https://doi.org/10.1038/sj.onc.1210076

81. Zhang YE. Non-Smad pathways in TGF-beta signaling. Cell Res. 2009; 19:128–39. https://doi.org/10.1038/cr.2008.328

82. Kretzschmar M, Doody J, Timokhina I, Massagué J. A mechanism of repression of TGFbeta/ Smad signaling by oncogenic Ras. Genes Dev. 1999; 13:804–16. https://doi.org/10.1101/gad.13.7.804

83. Battini R, Ferrari S, Kaczmarek L, Calabretta B, Chen ST, Baserga R. Molecular cloning of a cDNA for a human ADP/ATP carrier which is growth-regulated. J Biol Chem. 1987; 262:4355–59.

84. Luciakova K, Kollarovic G, Kretova M, Sabova L, Nelson BD. TGF-β signals the formation of a unique NF1/Smad4-dependent transcription repressor-complex in human diploid fibroblasts. Biochem Biophys Res Commun. 2011; 411:648–53.

https://doi.org/10.1016/j.bbrc.2011.07.017

85. Schmid RS, Pruitt WM, Maness PF. A MAP kinase-signaling pathway mediates neurite outgrowth on L1 and requires Src-dependent endocytosis. J Neurosci. 2000; 20:4177–88.

86. McRobb LS, McKay MJ, Gamble JR, Grace M, Moutrie V, Santos ED, Lee VS, Zhao Z, Molloy MP, Stoodley MA. Ionizing radiation reduces ADAM10 expression in brain microvascular endothelial cells undergoing stress-induced senescence. Aging (Albany NY). 2017; 9:1248–68. https://doi.org/10.18632/aging.101225

87. Cruickshanks HA, McBryan T, Nelson DM, Vanderkraats ND, Shah PP, van Tuyn J, Singh Rai T, Brock C, Donahue G, Dunican DS, Drotar ME, Meehan RR, Edwards JR, et al. Senescent cells harbour features of the cancer epigenome. Nat Cell Biol. 2013; 15:1495–506. https://doi.org/10.1038/ncb2879

88. Harper KL, Sosa MS, Entenberg D, Hosseini H, Cheung JF, Nobre R, Avivar-Valderas A, Nagi C, Girnius N, Davis RJ, Farias EF, Condeelis J, Klein CA, Aguirre-Ghiso JA. Mechanism of early dissemination and metastasis in Her2$^{+}$mammary cancer. Nature. 2016; 540:588–92. https://doi.org/10.1038/nature20609

89. Hosseini H, Obradović MM, Hoffmann M, Harper KL, Sosa MS, Werner-Klein M, Nanduri LK, Werno C, Ehrl C, Maneck M, Patwary N, Haunschild G, Gužvić M, et al. Early dissemination seeds metastasis in breast cancer. Nature. 2016; 540:552–58. https://doi.org/10.1038/nature20785

90. Bernards R, Weinberg RA. A progression puzzle. Nature. 2002; 418:823. https://doi.org/10.1038/418823a

91. Beauséjour CM, Krtolica A, Galimi F, Narita M, Lowe SW, Yaswen P, Campisi J. Reversal of human cellular senescence: roles of the p53 and p16 pathways. EMBO J. 2003; 22:4212–22. https://doi.org/10.1093/emboj/cdg417

92. Ansieau S, Bastid J, Doreau A, Morel AP, Bouchet BP, Thomas C, Fauvet F, Puisieux I, Doglioni C, Piccinin S, Maestro R, Voeltzel T, Selmi A, et al. Induction of EMT by twist proteins as a collateral effect of tumor-promoting inactivation of premature senescence. Cancer Cell. 2008; 14:79–89. https://doi.org/10.1016/j.ccr.2008.06.005

93. Novakova Z, Hubackova S, Kosar M, Janderova-Rossmeislova L, Dobrovolna J, Vasicova P, Vancurova M, Horejsi Z, Hozak P, Bartek J, Hodny Z. Cytokine expression and signaling in drug-induced cellular senescence. Oncogene. 2010; 29:273–84. https://doi.org/10.1038/onc.2009.318

94. Kosar M, Bartkova J, Hubackova S, Hodny Z, Lukas J, Bartek J. Senescence-associated heterochromatin foci are dispensable for cellular senescence, occur in a cell type- and insult-dependent manner and follow expression of p16(ink4a). Cell Cycle. 2011; 10:457–68. https://doi.org/10.4161/cc.10.3.14707

95. Dimri GP, Lee X, Basile G, Acosta M, Scott G, Roskelley C, Medrano EE, Linskens M, Rubelj I, Pereira-Smith O. A biomarker that identifies senescent human cells in culture and in aging skin in vivo. Proc Natl Acad Sci USA. 1995; 92:9363–67. https://doi.org/10.1073/pnas.92.20.9363

96. Livak KJ, Schmittgen TD. Analysis of relative gene expression data using real-time quantitative PCR and the 2(-Delta Delta C(T)) Method. Methods. 2001; 25:402–08. https://doi.org/10.1006/meth.2001.1262

97. Maninová M, Klímová Z, Parsons JT, Weber MJ, Iwanicki MP, Vomastek T. The reorientation of cell nucleus promotes the establishment of front-rear polarity in migrating fibroblasts. J Mol Biol. 2013; 425:2039–55. https://doi.org/10.1016/j.jmb.2013.02.034

## SUPPLEMENTARY MATERIAL

Please browse the Full Text version to see:

**Supplementary Table 1.** List of proteins with significantly changed expression identified by mass spectrometry.
**Supplementary Video 1.** Wound healing assay of proliferating BJ fibroblasts.
**Supplementary Video 2.** Wound healing assay of replicatively senescent BJ fibroblasts.

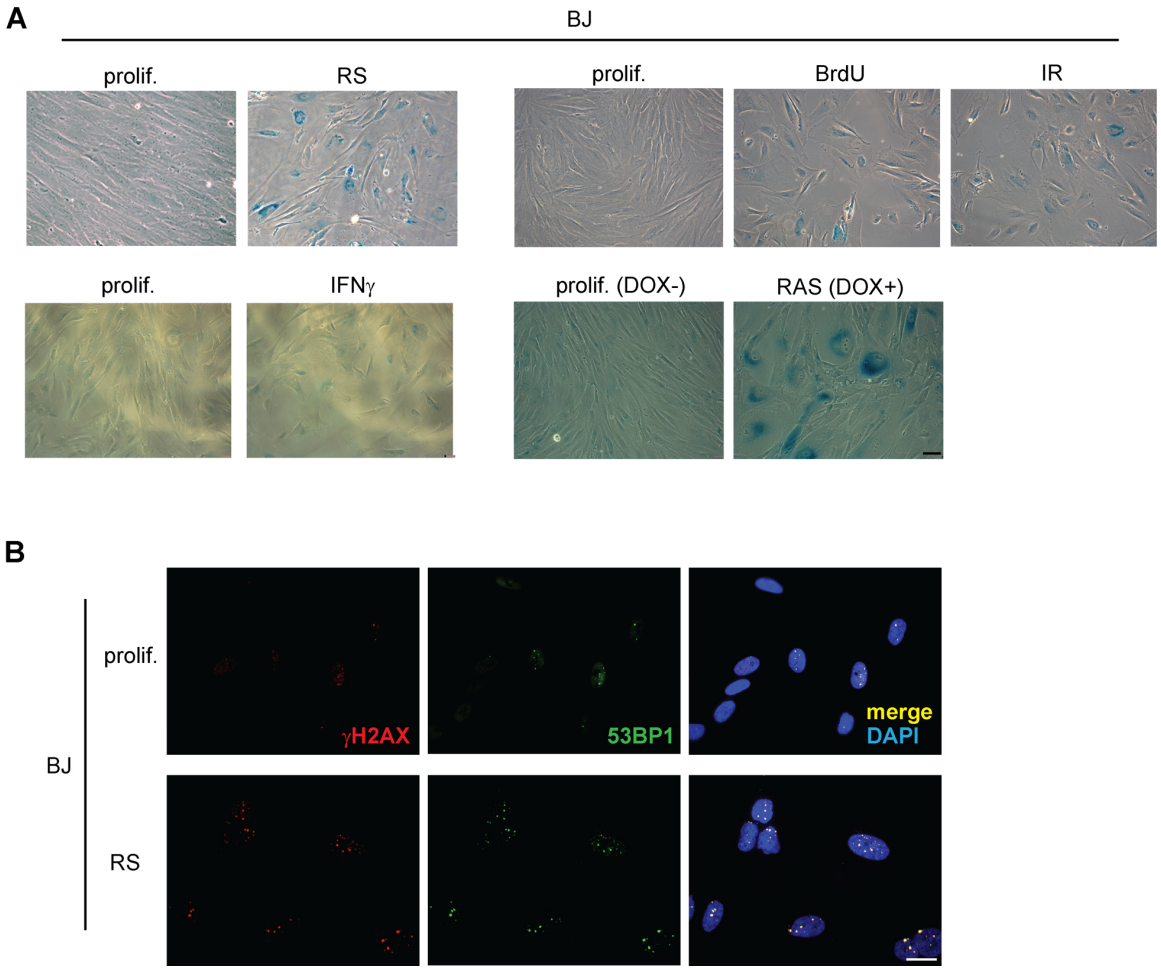


**Supplementary Figure 1**. (**A**) Senescence-associated β-galactosidase staining of BJ fibroblasts brought to senescence by various means: replicatively senescent (by splitting cell culture in ratio 1 : 2 until proliferation exhaustion at PD 85), by treatment of BJ cells (PD 32) with 100 μM BrdU, by irradiation of BJ cells (PD 32; IR, 20 Gy), by exposure of BJ cells (PD 35) to IFNγ (500 U/ml; for 21 days) and by tetracycline-inducible oncogenic H-RAS (see Materials and Methods and reference [94]). (**B**) DNA damage response of proliferating (PD 30) and replicatively senescent (PD 85) BJ fibroblasts detected as DNA damage foci with antibodies against γH2AX and 53BP1. Scale bar, 20 μm.

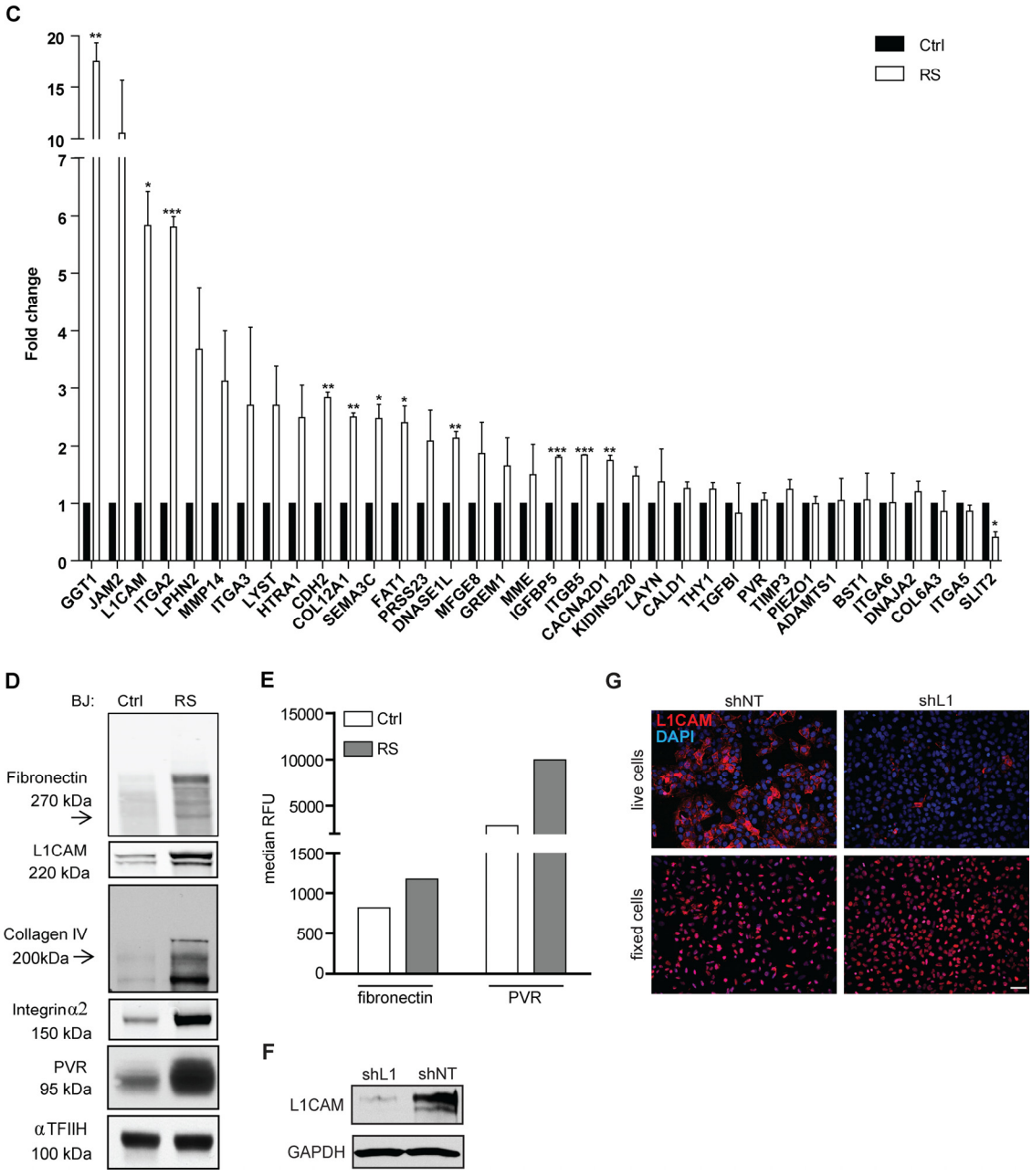


**Supplementary Figure 1**. (**C**) Transcript levels estimated by real time quantitative RT-PCR in subset of most upregulated hits obtained by mass spectrometry analysis in proliferating (Ctrl) and replicatively senescent (RS) BJ fibroblasts. GAPDH was used as a reference gene. Measurements were performed in two independent replicates. $p < 0.05$ (*); $p < 0.01$ (**); $p < 0.001$ (***), (**D**) Immunoblot comparing total protein levels of fibronectin, L1CAM, collagen IV, integrin α2 and PVR in proliferating (Ctrl) and replicatively senescent (RS) BJ fibroblasts. αTFIIH was used as a loading control. (**E**) FACS analysis of surface expression of fibronectin and PVR in proliferating (Ctrl) and replicatively senescent (RS) BJ cells. (**F**) Effectiveness of shRNA-mediated downregulation of L1CAM using lentiviral transduction (shL1) compared to control U2OS cells transduced with non-targeting shRNA (shNT) detected by Western blotting. GAPDH was used as a loading control. (**G**) Immunofluorescence staining of live control (shNT) and shL1CAM-treated U2OS cells (shL1) with L1CAM antibody (upper row) and after cell permeabilization (lower row; note that the signal in permeabilized cells is nonspecific). Scale bars, 50 μm.

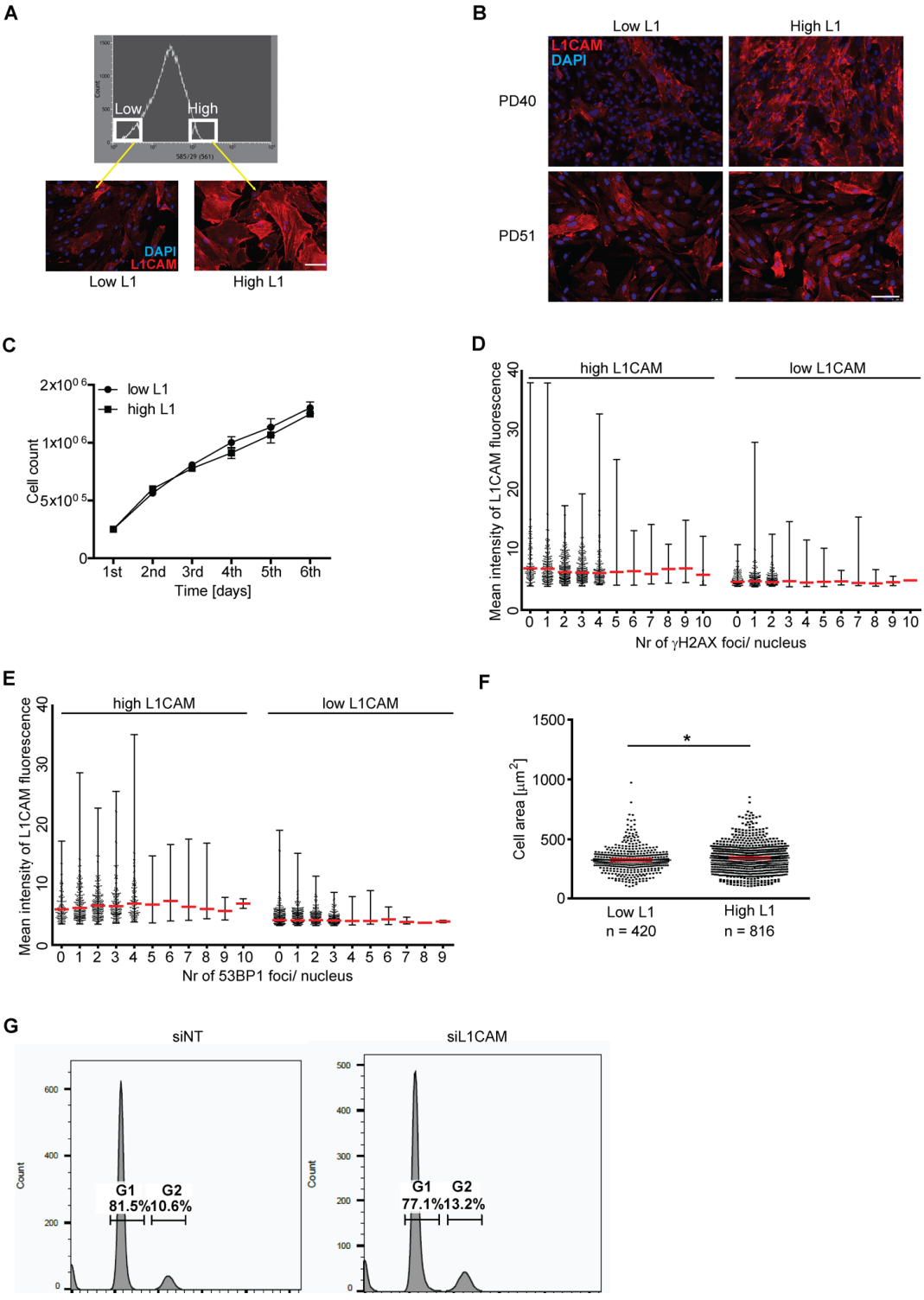


**Supplementary Figure 2.** (**A**) Fluorescence-associated cell sorting of replicatively senescent BJ fibroblasts. Live cells were sorted according to their surface L1CAM level into two subpopulations with low L1CAM and high L1CAM. Scale bar, 50 µm. (**B**) Immunofluorescence staining of surface L1CAM in sorted BJ fibroblasts (PD 40) and after additional 11 population doublings (PD 51). Scale bar, 50 µm. (**C**) Comparison of proliferation of L1CAM 'high' and 'low' BJ cells sorted by FACS. Quantification of number of γH2A.X (**D**) and 53BP1 (**E**) DNA damage foci per cell nucleus plotted relative to the L1CAM surface fluorescent intensity. Replicatively senescent BJ fibroblasts were presorted according to L1CAM surface level by FACS ($L1CAM^{high}$ versus $L1CAM^{low}$). (**F**) Cell area of BJ fibroblasts sorted for L1CAM high and low level. (**G**) FACS analysis of DNA content in replicatively BJ fibroblasts after knockdown of L1CAM (right) using propidium iodide staining. Control cells were transfected with non-specific siRNA (siNT; left).

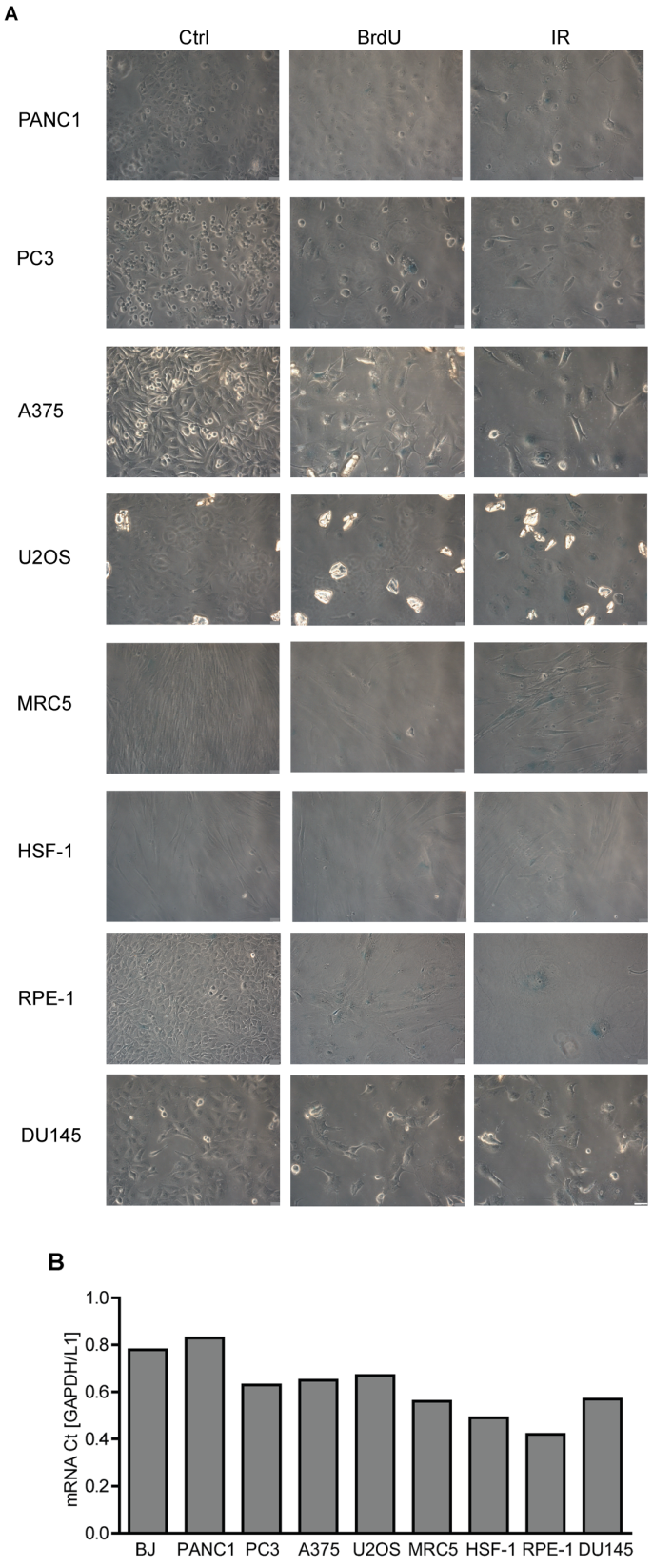


**Supplementary Figure 3**. (**A**) Senescence-associated β-galactosidase staining of PANC-1, PC3, A375, U2OS, MRC5, HSF-1, RPE-1 and DU145 cells brought to premature senescence by BrdU and IR (10 Gy). Scale bar, 50 μm. (**B**) Comparison of basal L1CAM transcript levels in different cell types calculated as an average GAPDH to L1CAM Ct values ratio.

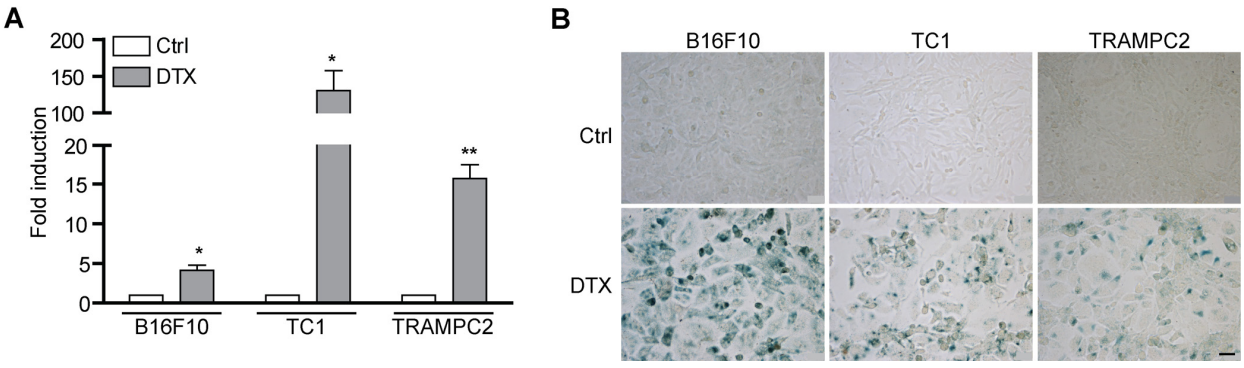


**Supplementary Figure 4**. L1CAM transcript levels (**A**) and senescence-associated β-galactosidase activity (**B**) estimated in mouse cell lines B16F10, TC1, and TRAMPC2 after exposure to docetaxel (0.75 µM, 4 days). Scale bar, 50 µm.

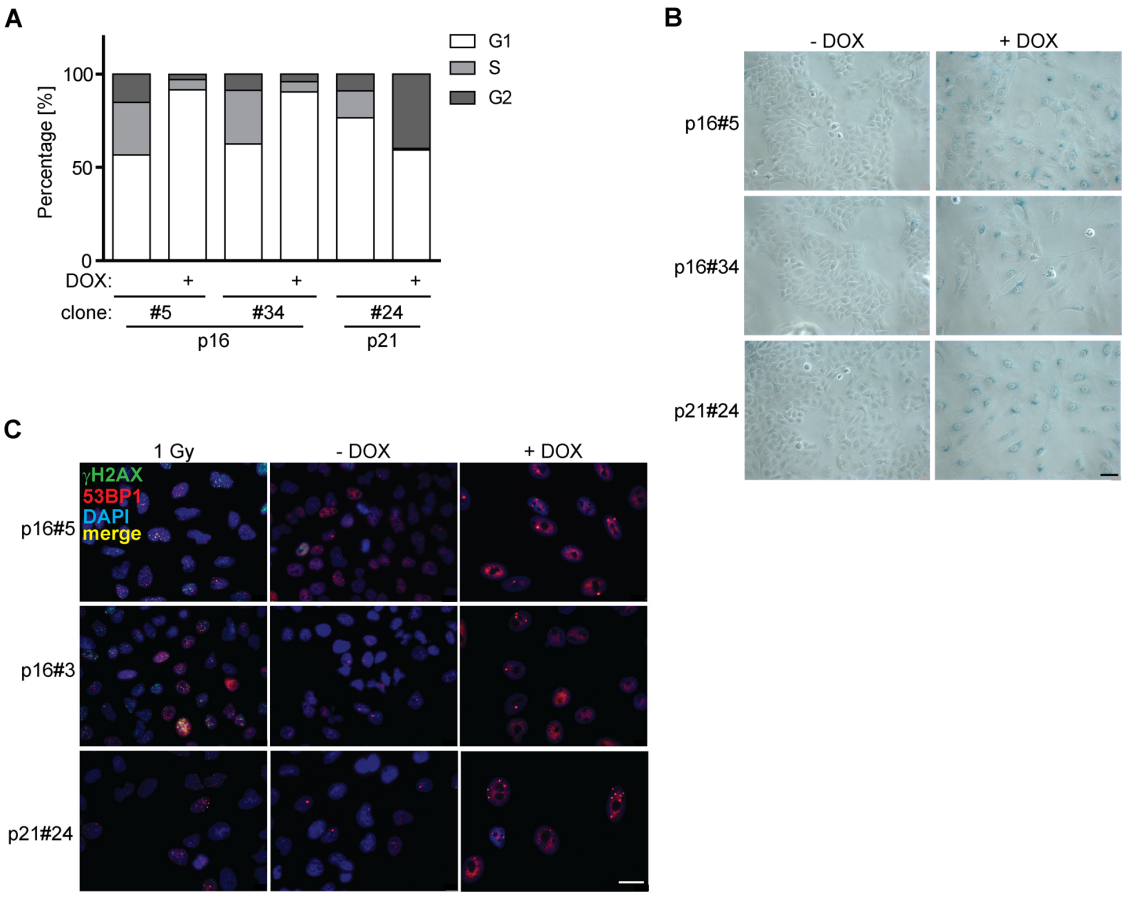


**Supplementary Figure 5**. (**A**) Cell cycle arrest after overexpression of cyclin-dependent kinase inhibitors p16 and p21 (induction with doxycycline, DOX+). (**B**) Senescence-associated β-galactosidase staining of H28 clones after cell cycle arrest (DOX+). (**C**) DNA damage markers (γH2AX and 53BP1) staining. Cells irradiated with dose of 1Gy were used as a staining control (40 minutes after irradiation). Scale bars, 20 µm.

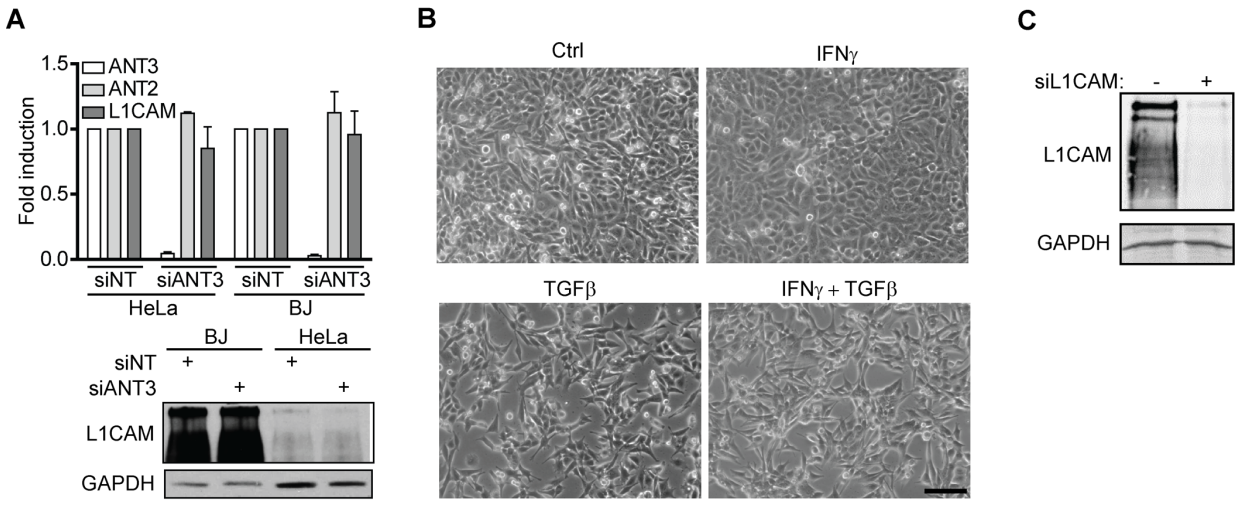


**Supplementary Figure 6**. (**A**) mRNA of ANT3, ANT2, and L1CAM after downregulation of ANT3 using RNA interference in HeLa and BJ cells (upper chart) and total L1CAM protein in Hela and BJ cells after downregulation of ANT3 using RNA interference (lower panel). GAPDH was used as a loading control. (**B**) Phase contrast microscopic images of A375 cells after exposure to 500 U/ml IFNγ, 10 ng/ml TGFβ, or their combination for 4 days. (**C**) Effectiveness of L1CAM downregulation by L1CAM siRNA in replicatively senescent BJ fibroblasts detected by Western blotting (siNT, control; L1CAM). GAPDH was used as a loading control. Scale bar, 100 μm.

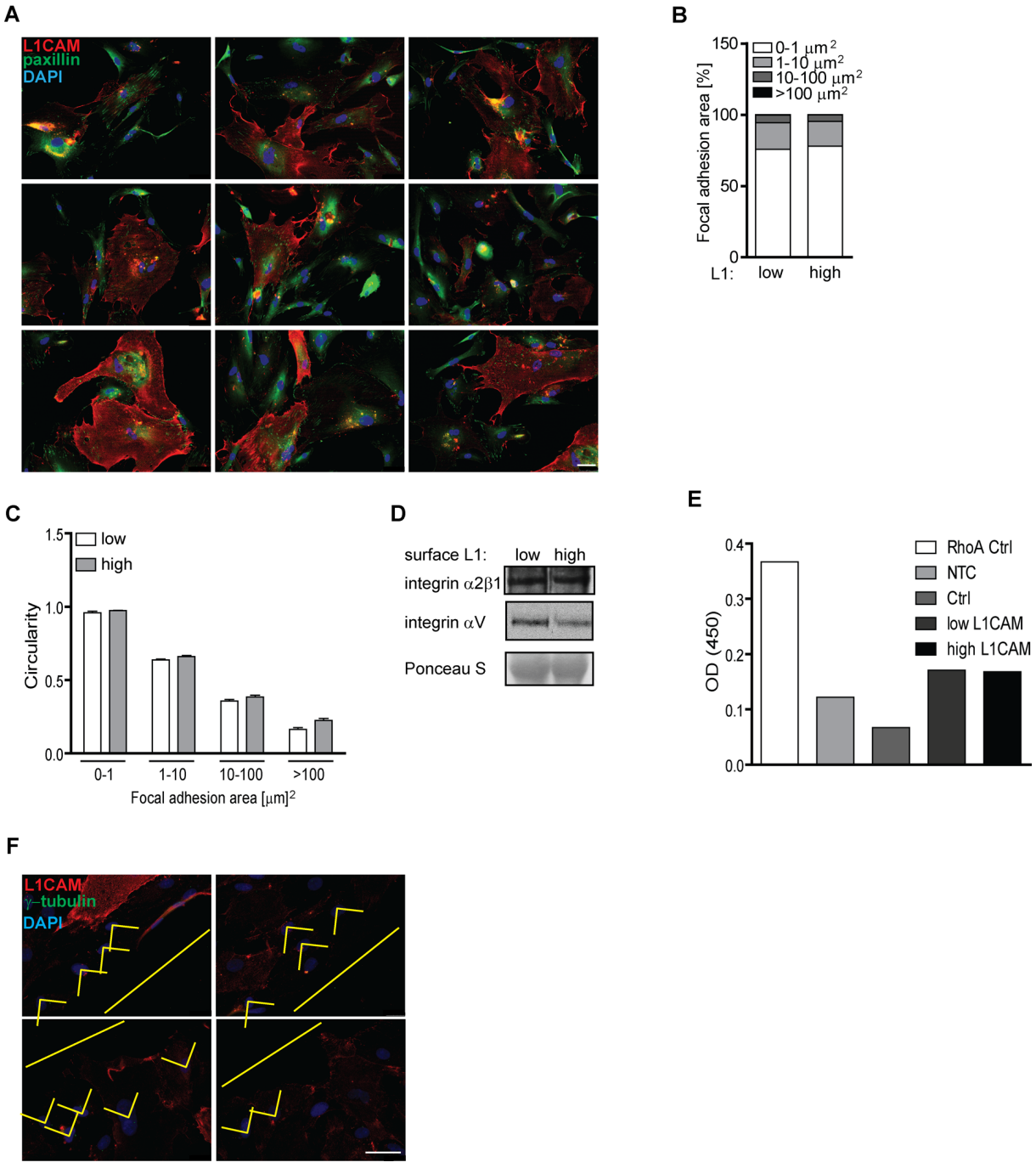


**Supplementary Figure 7.** (**A**) Fluorescence staining of L1CAM (surface labeling) and paxillin (after permeabilization) in non-sorted replicatively senescent BJ fibroblasts. (**B**) The ratio of adhesion (paxillin) numbers and area in low L1CAM and high L1CAM BJ replicatively senescent cells. (**C**) Circularity of adhesions in individual area categories. (**D**) Western blot detecting integrins in low and high L1CAM cells (BJ replicatively senescent fibroblasts). β–actin was used as a loading control. (**E**) RhoA activity in low and high L1CAM cells. "RhoA control" was part of the kit compounds; as negative control (NTC) were used cells with overnight serum starvation and control cells (Ctrl) were cells treated with 2 μM lysophosphatidic acid. (**F**) Polarization of nuclei after wound healing. Yellow line represents the direction of scratch ("wound) in cells monolayer. "v"-shaped perpendicular yellow lines for determination of nuclei polarization. Scale bar, 50 μm. All experiments were performed in three independent replicates. For statistics, two-tailed Student's t-test was used.

Research Paper

# Dynamic PML protein nucleolar associations with persistent DNA damage lesions in response to nucleolar stress and senescence-inducing stimuli

**Terezie Imrichova[1], Sona Hubackova[1,4], Alena Kucerova[1], Jan Kosla[1], Jiri Bartek[1,2,3], Zdenek Hodny[1], Pavla Vasicova[1]**

[1]Department of Genome Integrity, Institute of Molecular Genetics of the Czech Academy of Sciences, Prague, Czech Republic
[2]Genome Integrity Unit, Danish Cancer Society Research Center, Copenhagen, Denmark
[3]Division of Genome Biology, Department of Medical Biochemistry and Biophysics, Karolinska Institute, Stockholm, Sweden
[4]Present address: Institute of Biotechnology, Czech Academy of Sciences, Prague-West, Czech Republic

**Correspondence to:** Pavla Vasicova, Zdenek Hodny, Jiri Bartek; **email:** vasicova@img.cas.cz, hodny@img.cas.cz, jb@cancer.dk
**Keywords:** rDNA loci, super-resolution microscopy, time-lapse imaging, nucleolar segregation, DNA damage
**Received:** July 19, 2019 **Accepted:** August 22, 2019 **Published:**



## ABSTRACT

**Diverse stress insults trigger interactions of PML with nucleolus, however, the function of these PML nucleolar associations (PNAs) remains unclear. Here we show that during induction of DNA damage-induced senescence in human non-cancerous cells, PML accumulates at the nucleolar periphery simultaneously with inactivation of RNA polymerase I (RNAP I) and nucleolar segregation. Using time-lapse and high-resolution microscopy, we followed the genesis, structural transitions and destiny of PNAs to show that: 1) the dynamic structural changes of the PML-nucleolar interaction are tightly associated with inactivation and reactivation of RNAP I-mediated transcription, respectively; 2) the PML-nucleolar compartment develops sequentially under stress and, upon stress termination, it culminates in either of two fates: disappearance or persistence; 3) all PNAs stages can associate with DNA damage markers; 4) the persistent, commonly long-lasting PML multi-protein nucleolar structures (PML-NDS) associate with markers of DNA damage, indicating a role of PNAs in persistent DNA damage response characteristic for senescent cells. Given the emerging evidence implicating PML in homologous recombination-directed DNA repair, we propose that PNAs contribute to sequestration and faithful repair of the highly unstable ribosomal DNA repeats, a fundamental process to maintain a precise balance between DNA repair mechanisms, with implications for genomic integrity and aging.**

## INTRODUCTION

One of the biological processes contributing to aging and age-related diseases is cellular senescence – a cell response to various stresses, characterized by protracted halt of cell cycle due to supra-threshold elevation of inhibitors of cyclin-dependent kinases (iCdk). Cellular senescence participates in aging by two main mechanisms: cell cycle arrest of progenitor cells, preventing tissue renewal; and secretion of pro-inflammatory molecules, leading to chronic inflammation and tissue deterioration (reviewed in refs. [1, 2]). Accordingly, elimination of senescent cells in mice has a positive effect on their health and lifespan [3, 4]. The upstream insults leading to senescence *via* iCdk of Kip and INK4 families are diverse, encompassing oncogene activation, oxidative or genotoxic stress, often involving cytokine signaling, phenomena commonly leading to

DNA damage and persistent DNA damage response (DDR; reviewed in ref. [5]). The persistent DDR due to irreparable or perpetual DNA damage is thought to be the main mechanism behind most forms of cellular senescence. The nature of this senescence-associated DNA damage seems to be complex and multifactorial though irreparability of telomeres is the factor most frequently cited [6, 7]. A decade ago, it has been proposed that rDNA instability is the major determinant of life-span in budding yeast [8, 9]. Recently, the direct evidence that damage of ribosomal DNA (rDNA) loci can also cause senescence has been reported [10, 11].

Nucleolus is a membrane-less organelle formed around the active rDNA repeats through a biophysical phenomenon known as liquid-liquid phase separation [12]. The main function of this compartment is ribosome biogenesis; however, in recent years, the role of nucleolus in cellular stress responses has been increasingly recognized. In short, various stress stimuli deregulate ribosome biogenesis, which results in activation of multiple nucleolus-associated molecular pathways that cause p53-dependent and -independent cell cycle arrest (reviewed in refs. [13–16]). Dependent on cellular context, this cell-cycle arrest may ultimately lead to, or reinforce, senescence [17, 18].

The PML is a structural component of specific nuclear compartment termed PML nuclear bodies (PML NBs; [19]) that is comprised of hundreds of proteins and involved in multitude of cellular functions such as transcription, posttranslational modifications, protein sequestration and degradation, antiviral response, DNA repair, cellular senescence and apoptosis (reviewed in ref. [20]). PML NBs co-associate with late (irreparable) DNA damage foci [21–24] characteristic for senescent cells [25–27]. The exact function of PML and PML NBs in DNA repair is still under investigation, however, emerging evidence indicates their involvement in DNA repair by homologous recombination [25, 28].

Replicative senescence of human mesenchymal stem cells is associated with interaction of PML with the surface of the nucleolus [29]. The association of PML with nucleolus was also observed after treatment of various cell types with several senescence-inducing stimuli, for instance mouse and human embryonic fibroblasts with doxorubicin and γ-irradiation (IR) and human mesenchymal stem cells (hMSC) with actinomycin D (AMD; [29–32]). Strikingly, the association of PML with nucleoli of most cancer cell lines is rather low [29]. Two general structural types of PML association with the nucleolus were described after AMD treatment of hMSC [29]. The first type is characterized by association of PML with the border of a segregated nucleolus during functional inactivation of DNA-dependent RNA polymerase I (RNAP I). The second type termed PML nucleolus-derived structure (PML-NDS; [29]) is localized tightly to reactivated/active nucleolus as a structure of sub-nucleolar size accumulating some nucleolar proteins and appearing in increasing frequency with time after AMD removal during pre-rRNA transcription recovery. Based on indirect evidence, it was proposed that these two structures resemble two developmental stages of the same process triggered by nucleolar stress, however, no direct proof for such concept has been provided.

In this study we employed a long-term live-cell time-lapse imaging with 3-D image reconstruction and super-resolution microscopy to provide evidence that the PML nucleolar compartment is dynamic, including several structural transition states that are associated with inactivation and reactivation of nucleolar transcription during nucleolar stress, respectively. All forms of PML nucleolar associations including the late forms of PNAs, the PML-NDS, colocalized with DNA damage markers indicating a role of PML in DNA repair of nucleoli-associated rDNA loci. PML-NDS may last for very long periods of time despite some of them can eventually lose the DNA damage signal. The persistence of PML-NDS associated with DNA damage suggests that irreparable damage of rDNA loci might contribute to the pool of damaged DNA responsible for maintenance of the cellular senescent phenotype.

## RESULTS

### Senescence-inducing doses of doxorubicin provoke structurally variable association of PML with nucleoli

Several classes of compounds including topoisomerase and RNAP I inhibitors can induce the association of PML with nucleolus in human non-cancerous cells ([29–32] and our unpublished data). For the purpose of this study, we selected the topoisomerase II inhibitor doxorubicin used clinically as a chemotherapeutic agent for treatment of several human malignancies as a DNA damaging agent, and the human telomerase-immortalized retinal pigment epithelial cell line RPE-1$^{hTERT}$ as an easily manipulatable non-transformed model. At first, we determined the senescence-inducing dose of doxorubicin (0.75 μM) in RPE-1$^{hTERT}$ as the treatment with the highest ratio of the extent and variability of PNAs to cell death (Supplementary Figure 1A). After two weeks, RPE-1$^{hTERT}$ cells treated with this dose of doxorubicin developed cellular senescence as shown by loss of proliferation, presence of DNA damage detected as γH2A.X foci, characteristic morphological changes, and positivity for senescence-associated β-galactosidase staining (Supplementary Figure 1B–1E). Senescent cells survived at least for four weeks without regaining cell proliferation

(data not shown). The formation of diverse PML nucleolar associations was followed by wide field microscopy of formaldehyde-fixed cells harvested at several time points after doxorubicin addition (12, 24 and 48 hours) and after doxorubicin washout (24 and 96 hours; see scheme in Figure 1A). The relative presence of specific forms of PNAs resembling caps, forks, circles and PML-NDS (termed according to their 2-D appearance) clearly changed during the time of doxorubicin treatment and washout (Figure 1B, 1C). The proportion of PML 'cap-like' nucleolar structures dominated in the 12-hour sample and coincided with the stress-induced elevation of the PML protein levels (note, unperturbed RPE-1$^{hTERT}$ cells showed a very low level of PML and number of PML NBs). The appearance of PML 'fork-like' and 'circle-like' nucleolar structures followed the PML caps as could be detected in the 48-hour samples and these structures persisted even after doxorubicin removal. PML-NDS were almost undetected until 48 hours after doxorubicin addition, however, their presence strongly increased after doxorubicin washout and was associated with the decrease of other PNAs forms as can be observed at 96 hours after doxorubicin removal. All forms of PNAs were positive for other constituents of PML NBs such as Sp100, Daxx and SUMO1 (Figure 1D). Note, not all cell nucleoli contained PNAs at the same time and some cells contained nucleoli with different forms of PNAs simultaneously, indicating asynchronous changes in functional states of individual nucleoli (Supplementary Figure 2A, 2B). The formation of PNAs was not restricted to doxorubicin-treated RPE-1$^{hTERT}$ cells, as human mesenchymal stem cells (hMSC) or normal diploid BJ fibroblasts showed similar extents and patterns of PNAs formation (Supplementary Figure 2C).

Altogether, this data shows that PML protein can associate with nucleoli during senescence-inducing stress to form structurally variable accumulations at nucleolar periphery. This newly formed PML nucleolar compartment was relatively stable, however, not all nucleoli of a given cell were affected at the same time indicating their asynchronous response to the stress.

**Structural transitions of PML nucleolar associations follow the activity state of the nucleolus**

Doxorubicin inhibits rDNA transcription resulting in nucleolar segregation [33], a well-established nucleolar restructuring process ensuing inhibition of RNAP I activity [34]. To link specific types of PNAs to the RNAP I activity, the distribution of RNAP I subunit PAF49 was followed after the exposure of cells to doxorubicin by indirect immunofluorescence. As shown in Figure 2A, the presence of PML caps, forks and circles was always linked to the PAF49 segregated to nucleolar periphery pointing to their association with the RNAP I inhibition. In fact, the PML cap-like structures tightly co-associated with the PAF49 segregated into a structure termed nucleolar cap [34]. This association was even more apparent in the PML fork-like PNAs where PAF49 localized directly in between the fork arms (Figure 2A).

The PML-NDS were usually present next to the active nucleolus, indicating their association with a recovery of pre-rRNA transcription. Indeed, the gradual onset of RNAP I activity after doxorubicin washout was verified by 5-fluorouridine (5-FUrd) incorporation (see Supplementary Figure 3A, 3B) when a fraction of 5-FUrd-positive nucleoli was detected already 3 hours after doxorubicin washout. 24 hours after drug removal, most of the nucleoli were 5-FUrd-positive indicating almost complete restoration of rDNA transcription. Notably, PML-NDS accumulating B23 and DHX9 were present in the cells even 17 days after doxorubicin washout (Figure 2B) indicating their strong association with long-term cell-cycle arrest and senescent state [29].

The characteristic feature of the PML-NDS, distinguishing them from the large PML NBs, is an accumulation of nucleophosmin (B23), and DNA helicase II (DHX9) (Figure 2B, 2C; [29]). Sequestration of these proteins into PML-NDS is most likely a selective process, as several other nucleolar proteins, such as fibrillarin, Nopp140, PAF49 and UBF, localized into PML-NDS only partly or not at all (Supplementary Figure 4). To test whether the genesis of these accumulations requires PML, we utilized the RPE-1$^{hTERT}$ cells in which *PML* had been completely ablated by gene knock-out (PML-KO; [25]). The PML wild-type (PML-WT) and PML-KO cells were stained for DHX9 and subjected to quantitative analysis by Olympus ScanR at 96 hours after doxorubicin washout, i.e. at a time-point when PML-NDS were readily detectable in PML-WT cells. As shown in Figure 2D, a five times higher number of PML-WT cells with DHX9 spots – compared to PML-KO cells – was detected, indicating a functional role of PML in the formation of PML-NDS. It should be emphasized that the DHX9 accumulations identified in PML-KO cells were overall less intense and of irregular shape (Supplementary Figure 5A), suggesting they reflected rather random spots of higher DHX9 signal accumulation, unlikely representing the proper PML-derived DHX9 accumulations. To elucidate whether DHX9 might be primed for degradation in PML-NDS, we measured the total protein level of DHX9 in PML-WT and PML-KO cells at several time-points after doxorubicin addition and found that even though DHX9 was gradually degraded after doxorubicin treatment, the degradation was not dependent on PML, as there was no significant difference in DHX9 level between PML-WT and PML-KO cells (Supplementary Figure 5B).

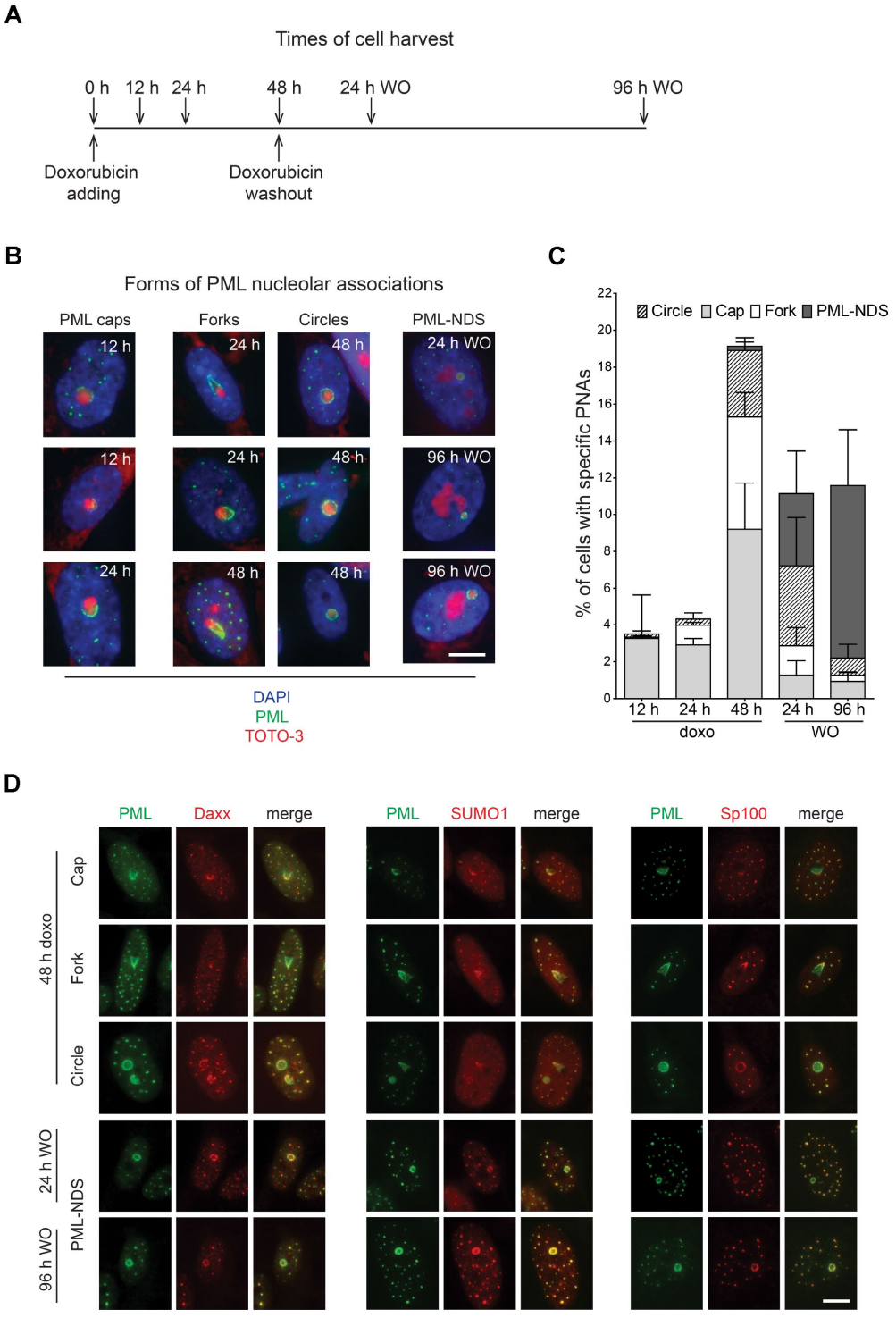


**Figure 1. Time-dependent differences in structural forms of PML nucleolar associations induced by doxorubicin.** As schematically depicted (**A**), RPE-1$^{hTERT}$ were treated with 0.75 μM doxorubicin and diverse types of PNAs were quantified by analysis of microscopic images in several time-points as indicated in the scheme. (**B**) Representative images of structural categories of PNAs obtained by wide-field indirect immunofluorescence microscopy of nuclei immunostained for PML (green). Nuclear and nucleolar compartments were visualized with DAPI (blue) and TOTO-3 (red), respectively. The images were captured with 63×/1.4 objective. Bar, 10 μm. (**C**) The percentage of cells containing specific structural subtypes of PNAs categorized as 'circles', 'caps', 'forks' and 'PML nucleoli-derived structures' (PML-NDS) was estimated. Over 200 cells in three biological replicates were evaluated for each time-point. Results are presented as a mean ± s.d. (**D**) Indirect immunofluorescence showing the colocalization of PNAs with proteins of PML nuclear bodies (PML-NBs). PML (green) and PML-NBs proteins (red) are visualized with respective antibodies, the nucleus was stained with DAPI (blue) and the nucleolus with TOTO-3 (cyan). The images were captured with 63×/1.4 objective. Bar, 10 μm.

Altogether, these findings indicate that the structural changes of PML nucleolar compartment reflect the state of rDNA transcription inhibited by the topoisomerase inhibitor doxorubicin, when PML can associate with either of the two distinct nucleolar states: inactive (segregated) or reactivated nucleolus. The latter is represented as small relatively long-lived nucleolar accessory structures (PML-NDS) with PML-dependent accumulation of specific proteins such as DHX9 and localization juxtaposed to the reactivated nucleolus.

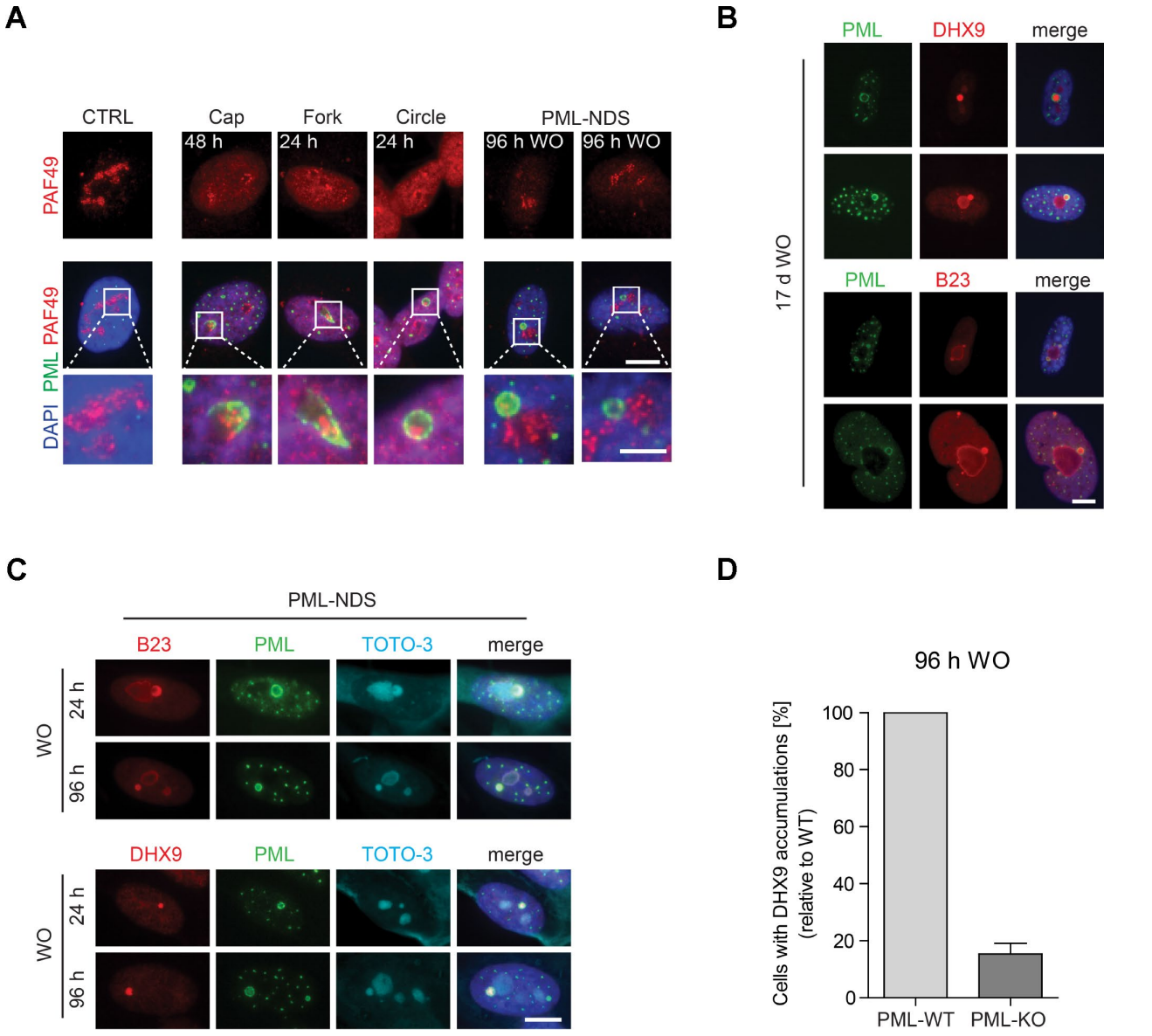


**Figure 2. The association of specific subtypes of PNAs with different functional states of nucleoli.** (**A**) The activity of RNAP I, evaluated as relocalization (segregation) of RNAP I subunit PAF49 and the presence of specific forms of PNAs were visualized by wide-field immunofluorescence microscopy of PAF49 (red) and PML (green) in RPE-1$^{hTERT}$ during different time-points of doxorubicin-treatment (0.75 μM) and its removal (WO). The insets show selected nucleoli with different states of RNAP I. Bars, 10 μm for whole cells and 4 μm for insets. (**B**) Long-term persistence (17 days after doxorubicin removal) of PML-NDS marked by PML (green) with accumulations of nucleolar proteins DHX9 and B23 (both in red). Bar, 10 μm. (**C**) Accumulation of B23 and DHX9 inside PML-NDS was visualized by immunostaining with respective antibodies (accumulated proteins – red, PML – green). Nuclei (**A**–**C**) and nucleoli (**C**) were visualized by DAPI (blue) and TOTO-3 (cyan), respectively. The images were captured with 63×/1.4 objective. Bar, 10 μm. (**D**) RPE-1$^{hTERT}$ PML-WT and PML-KO cells were treated with 0.75 μM doxorubicin for 48 hours; after that doxorubicin was removed and the cells were further cultured. 96 hours after doxorubicin washout the cells were fixed, stained with antibodies against DHX9 and PML and imaged with the Olympus ScanR microscope. The occurrence of cells with DHX9 accumulations were analyzed by the ScanR analysis software. The relative occurrence of cells with accumulations of DHX9 is shown. Two biological replicates were evaluated. Results are presented as a mean ± s.d.

### High-resolution 3-D structures of individual PNAs

To obtain detailed information about a 3-D structure of PNAs, we performed live-cell imaging analysis of RPE-$1^{hTERT}$ cells stably expressing EGFP-PML IV, a PML isoform with the highest capacity to form PNAs after doxorubicin [31], using structured illumination microscopy (SIM) after doxorubicin treatment. We noted that in 3 dimensions, the structures represented in 2-D as caps, circles and forks were in fact bowls and hollow balloons and funnels, respectively (Figure 3A–3C and Supplementary Videos 1–3). Importantly, we could clearly differentiate the two distinct shapes, balloons and funnels, confirming that the formerly observed circles and forks are not the same type of PNA seen from different angles but rather two structurally separate types of PNAs.

To unambiguously dissect the position of the PNAs relative to nucleoli, we employed SIM on doxorubicin-treated live cells expressing ectopic EGFP-PML IV, and RFP-B23 as a nucleolar marker. In this setting, we could observe that both the balloons and the funnels undeniably enclose the nucleolus (Supplementary Figure 6A, 6B). Furthermore, we confirmed that also PML-NDS contain nucleolar material. The RFP-B23 signal inside PML-NDS was very dense without observable small pores; whereas the RFP-B23 signal in adjacent nucleoli was less intense with numerous pores and holes, resembling the nucleoli of untreated cells (Figure 3D). On the other

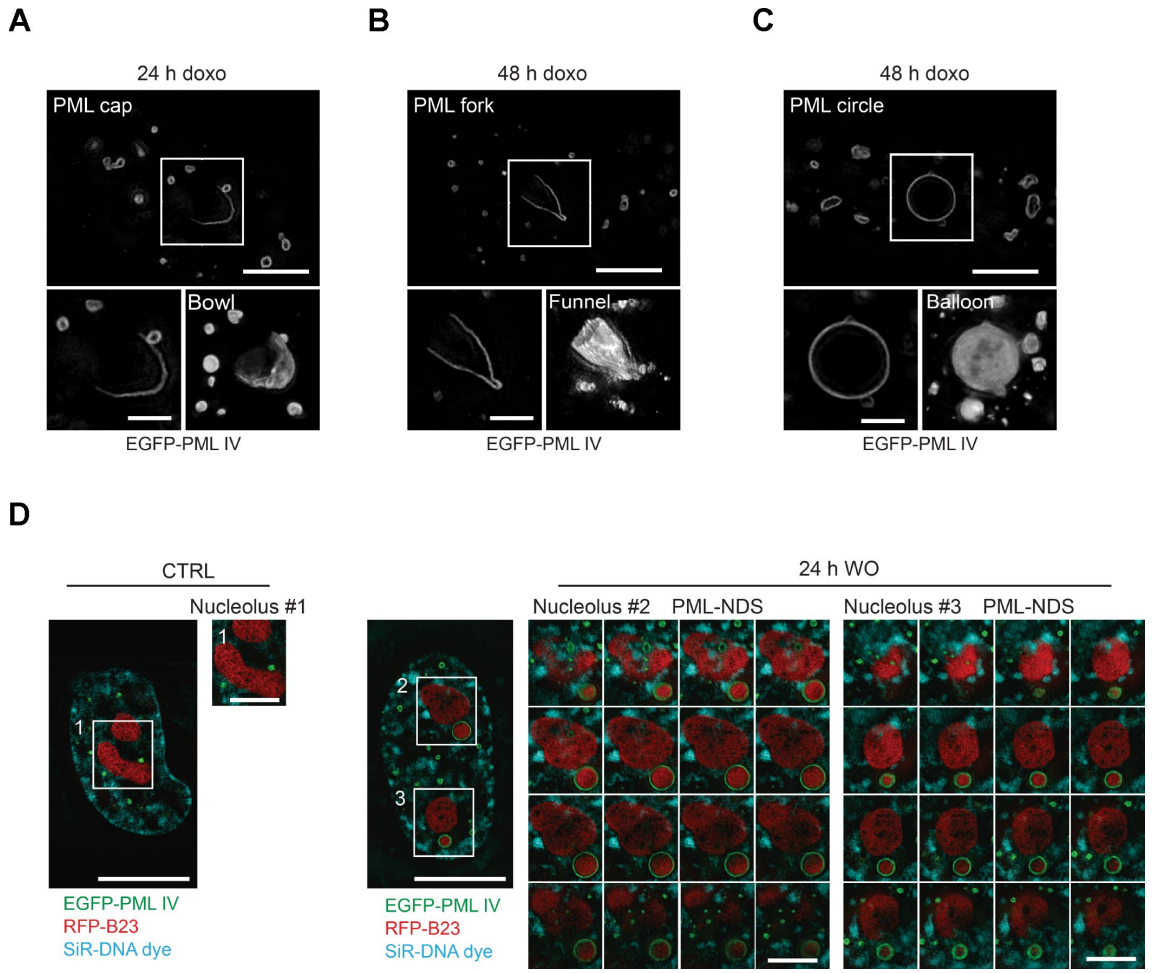


**Figure 3. Three-dimensional reconstruction of structural subtypes of PNAs.** High resolution live-cell structured illumination microscopy of the cap- (**A**), fork- (**B**) and circle-like (**C**) PNAs of RPE-$1^{hTERT}$ cells stably expressing the EGFP-PML IV isoform harvested 24 and 48 hours after doxorubicin-treatment. Central layer of the whole cell (upper images; bar, 5 µm) and central layer of respective type of PNAs (lower-left images; bar, 2 µm) are shown together with reconstructed 3-D images (lower-right images) from 28 (cap), 30 (fork) and 54 (circle) layers using ImageJ 3D viewer plugin. (**D**) High resolution live-cell SIM images of RPE-$1^{hTERT}$ stably expressing EGFP-PML IV and RFP-B23. A control untreated cell (left) and a cell containing PML-NDS, imaged 24 hours after doxorubicin washout (right). The central layer of whole cells (bar, 10 µm) are shown together with three insets of nucleoli (1 layer for the nucleolus of control cell and 16 layers for the nucleoli with adjacent PML-NDS; bar, 4 µm). DNA was labeled with SiR-DNA dye.

and balloon-like PNAs indicating their similar metabolic state (Supplementary Figure 6A, 6B). To exclude artifacts that could result from the use of ectopically expressed fluorescently tagged PML protein, we hand, the density and structure of RFP-B23 in the PML-NDS was comparable with RFP-B23 enclosed in funnel-employed stimulated emission depletion (STED) super-resolution microscopy of fixed cells with endogenous PML and B23 stained by indirect immunofluorescence. Although the sample preparation caused reduction of cell volume and compromised the continuity of the PML shell, we could still detect the PML signal around the whole nucleolus, confirming our SIM data (Supplementary Figure 6C, 6D).

Overall, using two super-resolution techniques, we confirmed that the PML can form several structurally variable interactions with the nucleolar periphery.

**Evolution and fate of 'early' PNAs**

To track the genesis of the PNAs formation and to assess whether there is a direct temporal relation/ continuum among their individual subtypes we followed the development of the PNAs in RPE-1$^{hTERT}$ cells stably expressing the EGFP-PML IV by live-cell imaging after doxorubicin exposure (0.75 μM). In concert with the results showed above in Figure 1C, the cap-like accumulations of otherwise diffuse PML at the nucleolar periphery at 4.5 hours after doxorubicin addition, were the first type of PNAs that appeared (see Figure 4A and complementary Supplementary Videos 4–7). It should be emphasized that new caps emerged in cells continuously during the whole monitoring time (60 hours) after doxorubicin addition, indicating that the signal for the formation of PNAs is not limited to the specific time but present for a long time period. The percentage of cells with the new cap peaked around 28 hours after doxorubicin addition suggesting the period of the highest manifestation of the signal for PNAs formation (Figure 4B).

The caps then gradually evolved into either the fork-like structures or the circles but a reversion between the forks and circles was observed as well (see Figure 4C and complementary Supplementary Videos 8–11). Figure 4D shows quantification of a proportion of individual PNAs during the entire monitored period of 72 hours divided into three intervals: 1–24, 24–48 and 48–72 hours. The total extent of PNAs formation was highest in the 24–48-hour interval consistently with the non-continuous, time-course end-point observations of the PNAs formed by endogenous PML (Figure 1C). The stability and frequency of transitions among specific PNAs during 72 hours of doxorubicin exposure is shown in Figure 4E. The most frequent PNAs transitions observed were cap-to-fork, the less frequent cap-to-circle, fork-to-circle and circle-to-fork. Based on quantitative evaluations it was also evident that most forks and circles were stable over 5 hours.

Altogether, the time-lapse analysis revealed that the formation of PNAs started by the accumulation of the initially diffuse PML on the pole of the nucleolus and the signal for such association persisted over several days after stress initiation. This data also clearly demonstrates that structurally different PNAs are actually temporally distinct, dynamic developmental stages of newly formed PML nucleolar compartments.

**Genesis, stability and fate of late PNAs: PML-NDS**

As shown above, PML-NDS represent the specific type of PML nucleolar associations that developed as the final structural subtype after stress initiation, in connection with stress release (drug removal) and rDNA transcription re-initiation. To trace unambiguously the evolution and fate of such PML-NDS structures, the RPE-1$^{hTERT}$ cells expressing EGFP-PML IV together with B23-RFP as a nucleoli-specific marker were exposed to doxorubicin for 48 hours and followed by time-lapse imaging divided into two capture sessions of 2–15 and 24–34 hours after the drug removal. As shown in Figure 5A and Supplementary Video 12, PML-NDS originated predominantly from forks by stripping and enclosing a part of nucleolar material from originally segregated nucleolus immediately after the drug removal. The first PML-NDS were detected 3 hours after the drug removal and they continued to appear during the next 12 hours, indicating that the signal for fork transformation into the PML-NDS lasted during the early period of drug washout (Supplementary Figure 7A) concurrently with the recovery of RNAP I activity (Supplementary Figure 3). As documented in Supplementary Figure 7B, the lifetime of PML-NDS was variable, from 0.8 to 13 hours. Note the exact estimation of PML-NDS lifetime was partly limited due to escape of some cells from the visual field or emergence of some PML-NDS close to the end of the capture interval. However, we can conclude that the maximal lifetime of single PML-NDS was at least 13 hours. The destiny of PML-NDS was variable (see Figure 5B for quantitative cumulative data and Supplementary Figure 7B for the fate of individual PML-NDS). Thus, whereas most PML-NDS were quite stable (74 and 61% in 2–15- and 24–34-hour interval, respectively; Figure 5C and Supplementary Video 13), another three, less frequent modes of their fate were recorded: 1) fusion with the nucleolus with simultaneous reduction of PNAs into the residual regular PML nuclear body (6 and 21% in 2–15- and 24–34-hour interval, respectively; Figure 5D and Supplementary Video 14),

2) stripping of PML into PML NBs with persistence of B23 (14% in both intervals; Figure 5E and Supplementary Video 15), and 3) fusion with the fork-like PNAs (6 and 4% in 2–15- and 24–34-hour interval, respectively; Figure 5F and Supplementary Video 16).

Hence, the PML-NDS appeared apparently as the final stage of the transition sequence of cap/fork/PML-NDS (see Figure 5G for scheme). Note, however, that we also detected *de novo* initiation of this complete sequence during the doxorubicin removal phase (Supplementary Figure 7C and Supplementary Video 17). The PNAs transition sequence from the cap to the PML-NDS after doxorubicin removal lasted between 2–6.5 hours; nevertheless, an incomplete PNAs transition sequence could be observed as well.

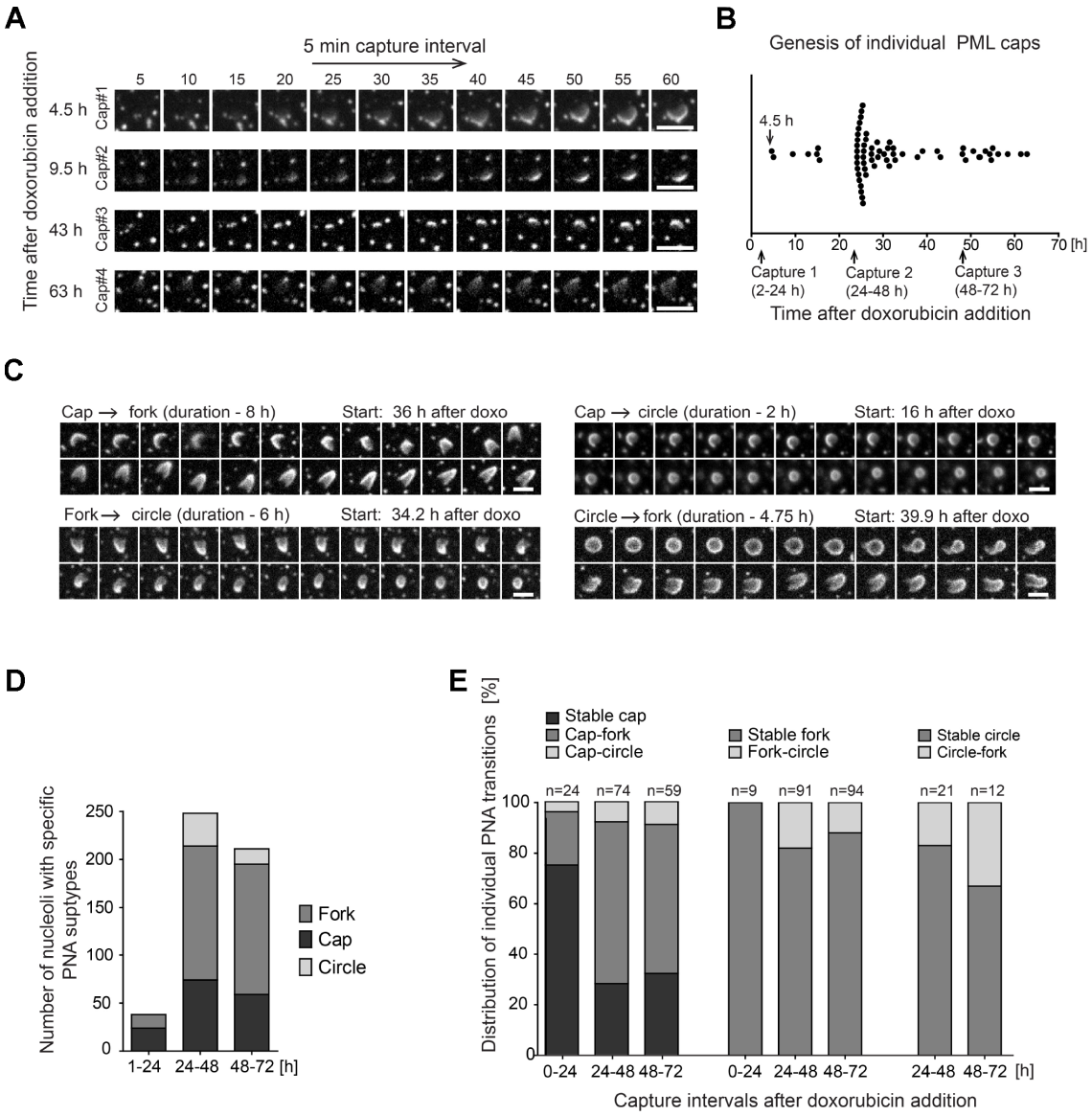


**Figure 4. Structural transitions of PNAs subtypes.** RPE-1$^{hTERT}$ stably expressing EGFP-PML IV were analyzed by live-cell imaging in three consecutive capturing sessions spanning 2–24, 24–48 and 48–72 hours after doxorubicin treatment (0.75 μM). (**A**) Series of sequential images of four individual cap formations (cap#1–4) that initiated 4.5, 9.5, 43 and 63 hours after doxorubicin addition. (**B**) Plot of all genesis of PML-caps recorded during three capturing intervals. Dots represent *de novo* formation of individual PML-caps. (**C**) Time-dependent evolution and transition of subtypes of PNAs. The four characteristic transitions – 'cap-to-fork', 'cap-to-circle', 'fork-to-circle' and 'circle-to-fork' – are represented by series of sequential images. The initiation of capturing and the length of recorded time (in parentheses) are given for each type of transition. (**D**) The quantitative distribution of specific subtypes of PNAs in three capturing sessions (see Figure 1B for comparison). (**E**) The quantitative distribution of specific PNAs subtype transitions in three capturing sessions. The PNAs that did not change for over 5 hours were considered as stable. Bars, 4 μm.

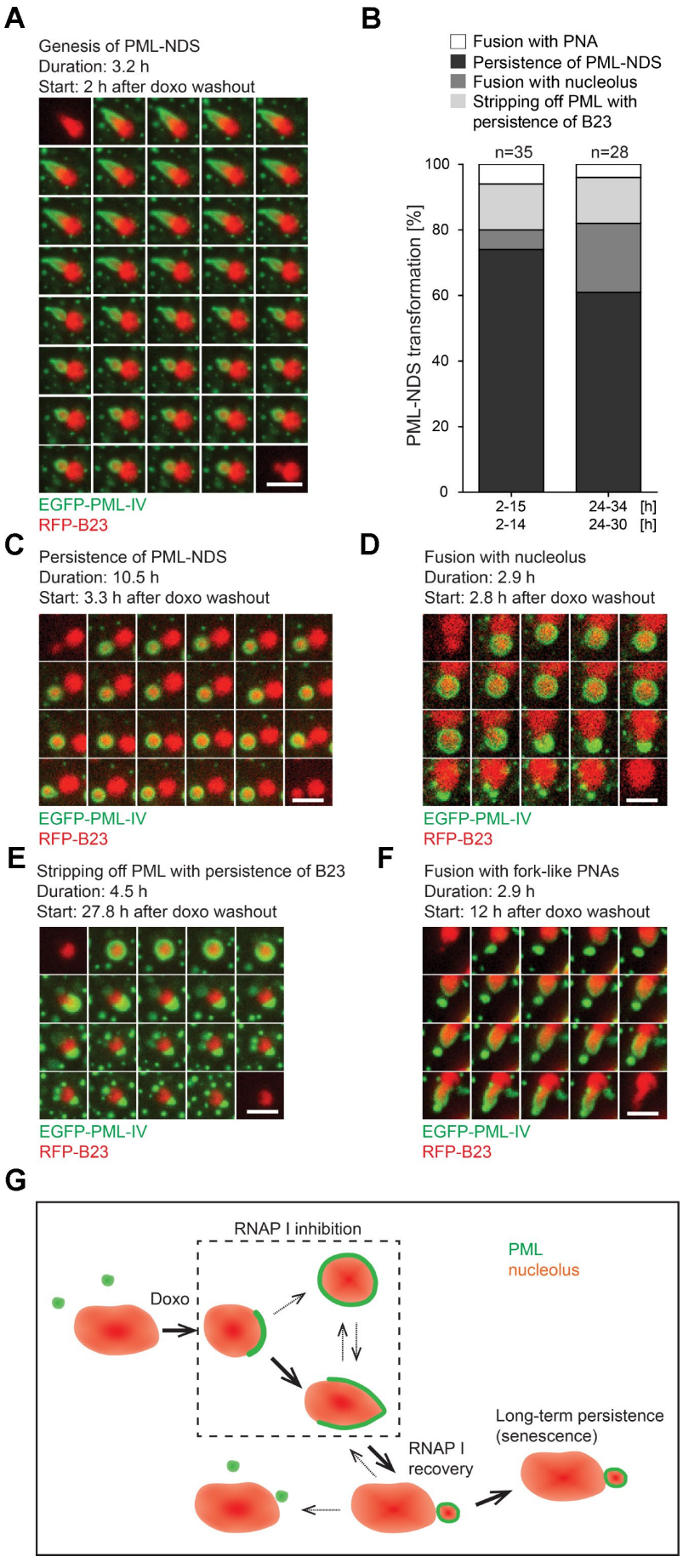
A
Genesis of PML-NDS
Duration: 3.2 h
Start: 2 h after doxo washout
EGFP-PML-IV
RFP-B23
B
Fusion with PNA
Persistence of PML-NDS
Fusion with nucleolus
Stripping off PML with persistence of B23
n=35
n=28
PML-NDS transformation [%]
100
80
60
40
20
0
2-15
2-14
24-34
24-30
[h]
[h]
C
Persistence of PML-NDS
Duration: 10.5 h
Start: 3.3 h after doxo washout
EGFP-PML-IV
RFP-B23
D
Fusion with nucleolus
Duration: 2.9 h
Start: 2.8 h after doxo washout
EGFP-PML-IV
RFP-B23
E
Stripping off PML with persistence of B23
Duration: 4.5 h
Start: 27.8 h after doxo washout
EGFP-PML-IV
RFP-B23
F
Fusion with fork-like PNAs
Duration: 2.9 h
Start: 12 h after doxo washout
EGFP-PML-IV
RFP-B23
G
RNAP I inhibition
PML
nucleolus
Doxo
Long-term persistence
(senescence)
RNAP I
recovery

**Figure 5. The genesis, stability and fate of PML-NDS.** RPE-1$^{hTERT}$ stably expressing EGFP-PML IV (green) and RFP-B23 (red) were treated with 0.75 μM doxorubicin for 48 hours and analyzed by live-cell imaging after doxorubicin washout (up to 34 hours) for the presence of PML-NDS. (**A**) Series of sequential images mapping the genesis of PML-NDS. (**B**) Comparison of proportional representation of PML-NDS fates between two time-lapse capturing sessions (experiment I: 2–15 and 24–34 hours; experiment II: 2–14 and 24–30 hours) after drug removal. Four different fates of PML-NDS were monitored: persistence (no change) (**C**), fusion with nucleolus (**D**), stripping of PML with B23 persistence (**E**), and fusion with fork-like PNAs (**F**). EGFP-PML IV, green; RFP-B23, red; bars, 4 μm. The initiation of capturing and the length of recorded time are given for each type of transition. (**G**) Schematic representation of PNAs transmutations recorded by time-lapse microscopy. The bold arrows show the main transition pathways observed.

It should be stressed that PML-NDS were the only PNAs structures present when very low doses of doxorubicin (0.075 and 0.375 μM) were applied (see Supplementary Figure 1A), suggesting that a low-level nucleolar stress may induce them directly, without the preceding stages of the PML nucleolar associations (caps, forks, circles), i.e. in a transient period of inhibition of RNAP I activity and nucleolar segregation. Whether these two forms of PML-NDS are functionally equivalent or not needs to be further elucidated.

To conclude, the formation of PML-NDS was linked to restoration of nucleolar activity by transition from early PML nucleolar associations in a process comprising a separation of a part of nucleolar and nucleoplasmic content into a detached body. This structure can either fuse with nucleolus or persist for a long time, the latter pattern indicating a block or irreversibility of a normal PNAs transition sequence.

### PNAs co-associate with DNA damage foci

As PML nuclear bodies associate with irreparable DNA damage foci [21–24] characteristic for senescent cells [25, 26] and doxorubicin induces DNA damage and DNA damage response (DDR), we analyzed next whether there is an association of the PNAs with a DNA damage marker, histone H2A.X phosphorylated on serine 139 (γH2AX; [35]). Using confocal fluorescence microscopy, we found that 48 hours after doxorubicin addition all types of PNAs (caps, forks, circles and PML-NDS) associated with γH2AX signal (Figure 6A). Furthermore, to examine whether all the PML-NDS stay in contact with the DNA lesions we compared the cells 48 hours after addition of doxorubicin with those 24 and 96 hours after doxorubicin washout. We found out that all PML-NDS captured before doxorubicin washout (i.e. 48 hours after doxorubicin addition) associated with γH2AX, which was very similar to the sample obtained 24 hours after doxorubicin washout (the γH2AX signal was not detected only in one PML-NDS from 13 captured). However, 96 hours after doxorubicin washout only 60% of analyzed PML-NDS (n = 14) contained detectable γH2AX signal (Figure 6B).

The association of early PNAs with γH2AX was further assessed by super-resolution microscopy. Using the STED microscopy, a clear co-association of the PML with γH2AX on the nucleolar border was detected (Figure 6C). Intensity profiling of STED images of cap-, fork-, circle-like and PML-NDS forms of PNAs (Supplementary Figure 8) showed both overlapping and flanking patterns of both signals, the latter indicating similar juxtaposition of the PML to the DNA damage foci as described for the nuclear PML NBs/DNA damage lesions [25].

To conclude, the PNAs formed and localized closely with the DNA damage lesions at the nucleolar periphery in cells exposed to doxorubicin. These findings indicate that PML can be involved in the repair of lesions formed either in rDNA or DNA in the close proximity to rDNA arrays. The persistence of DNA damage response close to nucleoli suggests that the damage of nucleolus-associated DNA can contribute to the pool of irreparable DNA lesions responsible for senescence induction.

## DISCUSSION

Cellular senescence emerges as an important factor contributing to aging and aging-associated diseases (for a review, see ref. [2]). Mechanistically, cellular senescence is a long-lasting cell cycle arrest due to prolonged activity of cell cycle checkpoints. DNA damage is considered as a key upstream activator of checkpoint response of senescent cells, however, the nature of the DNA "irreparability" or DDR signaling persistency has not been fully resolved yet. The elucidation of the causal mechanisms of cellular senescence might facilitate a discovery of new approaches to control aging.

The interaction of PML with nucleolar components was reported as a characteristic feature of replicative senescence of human mesenchymal stem cells [29]. In our present study, as a basic prerequisite for understanding the role of the PML-nucleolar subcompartment in development of cellular senescence, we analyzed the genesis and dynamics of PML-nucleolar structures in the context of premature senescence induced by the chemotherapeutic drug doxorubicin. Employing live-cell imaging time-lapse

and high-resolution microscopy, we have found that 1) the dynamic changes of PML-nucleolar associations are intimately linked to inactivation and reactivation of RNAP I transcription, respectively; 2) the PML-nucleolar compartment develops dynamically in a sequence of events that includes structurally distinct, yet temporally linked PNAs, eventually leading to either their resolution or persistence; 3) all the PNA subtypes associate with the markers of DNA damage; 4) the long-lasting PML nucleolar structures (PML-NDS) also commonly associate with markers of DNA damage, thereby implicating the PNAs in persistent DDR typical of senescent cells; and 5) the formation of such PNAs depends on intact PML.

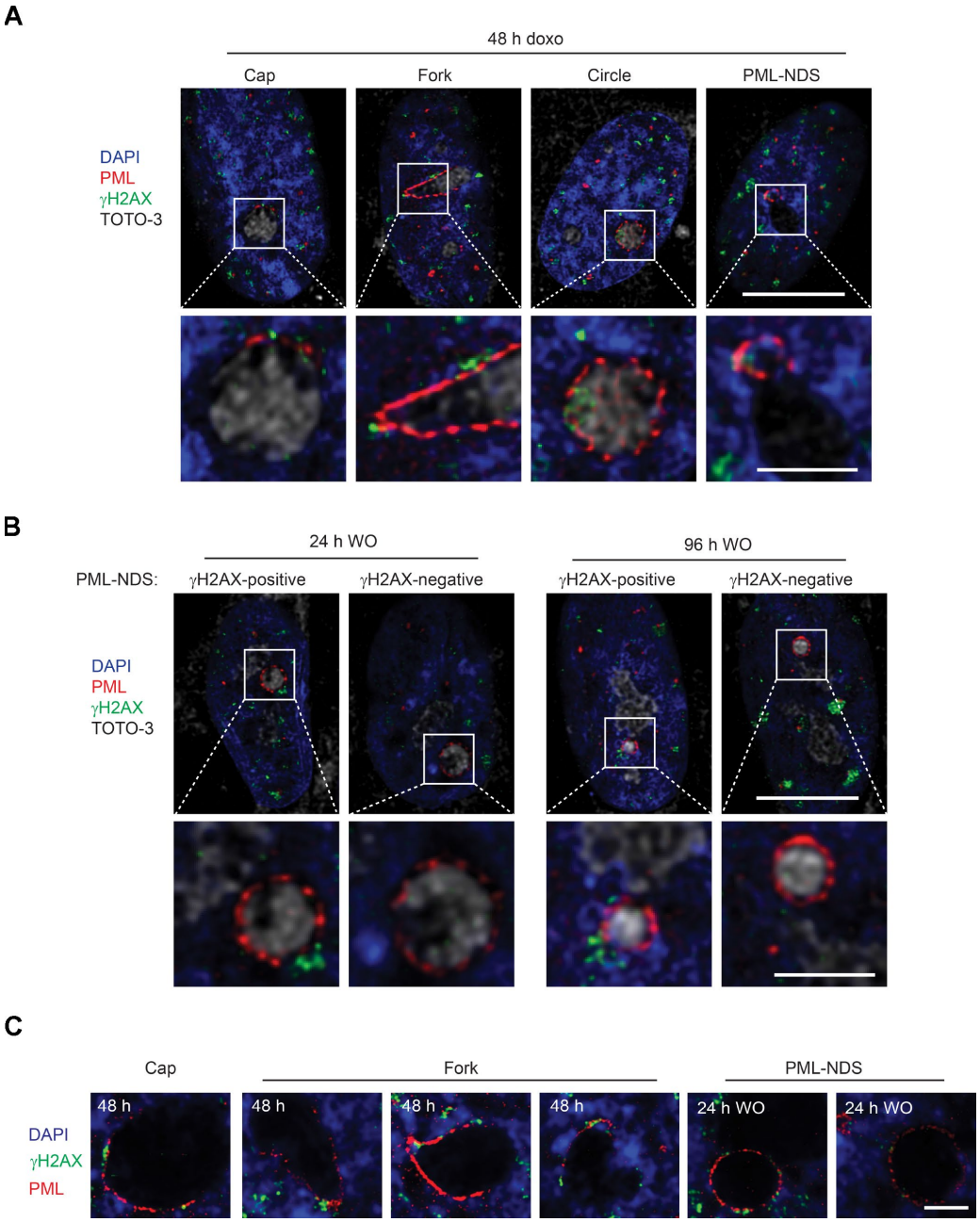


**Figure 6. PNAs colocalize with persistent DNA damage foci.** Co-association of DNA damage foci and PNAs detected by γH2AX (green) and PML (red) immunostaining, respectively, in RPE-1$^{hTERT}$ treated with 0.75 μM doxorubicin for 48 hours (**A**) and 24 and 96 hours after drug removal (**B**). Higher magnifications of confocal microscopic images of PML/γH2AX co-associations (insets) are shown in the lower rows. Bars, 10 μM for the whole cells and 3 μM for the insets. (**C**) High resolution STED microscopic images of PNAs/γH2AX co-associations in RPE-1$^{hTERT}$ treated with 0.75 μM doxorubicin for 48 hours and followed for PML-NDS appearance 24 hours after drug removal (WO). Nuclei are stained with DAPI (blue). Bars, 4 μM.

We provide evidence that the PML nucleolar compartment undergoes continuous structural reorganizations associated with the repression of RNA polymerase I activity. It was reported that after RNAP I inhibition by actinomycin D or after rDNA damage, several proteins including subunits of RNAP I and also rDNA relocate from nucleolar interior to the nucleolar periphery forming the so-called nucleolar cap [34, 36, 37]. Importantly, we revealed an intimate relationship between the 'cap' and 'fork' subtypes of PNAs with the canonical nucleolar caps (i.e. those formed by segregated PAF49), where the PNAs form structural shields/covers juxtaposed to nucleolar caps, a scenario suggesting that the cap-specific factors could interact with the PML. Nevertheless, despite all nucleoli were segregated at the specified time, only fraction of them formed the PNAs. This indicates that individual nucleoli could be in different functional states, and that the nucleolar segregation itself is not sufficient to provide the signal for accumulation of PML at the nucleolar surface, a process that seems to require an additional factor(s).

The dynamic nature of the structural reorganization of PNAs reported here raises a question about forces governing the process. The PML nuclear bodies and nucleoli are membrane-less compartments and it is postulated that the chemico-physical nature of formation of these structures is a liquid-liquid phase separation ([12], for reviews, see refs. [38, 39]). It should be emphasized that the PML interacts with the nucleolus only under specific stress conditions. Ectopic (over)expression of the PML isoforms was insufficient to establish PML interaction with the nucleoli (our unpublished data) indicating that this interaction was not a result of a saturation of the PML NB compartment. Moreover, the formation of asymmetric funnel-like shape PNAs can be hardly accounted for by liquid-liquid phase separation as a sole mechanism of its genesis. Although the forces behind the transition sequence of PNAs are unknown, several mechanisms including the asymmetric flux of ribosome biogenesis components linked to the asymmetry of segregated nucleolus, perinucleolar chromatin movement or an involvement of mechanical forces of nucleolar motors during the DNA damage response and repair (see further) can be assumed.

Arguably the most intriguing feature of the PNAs was their intimate and long-term co-association with markers of the DNA damage. Even the early-stage PNAs were positive for phosphorylated histone H2AX. From the dynamics of PNAs and the presence of DNA damage foci in a fraction of the persistent PML-NDS we assume that during the cap/fork/PML-NDS transition sequence the PML concentrates the damaged DNA originally spread on nucleolar surface to one pole of the nucleolus, the tip of the funnel-like structure, which is then further detached from the functionally restored nucleoli into a separated structure, PML-NDS. Such sequestration of damaged DNA could serve as a mechanism protecting the interference of ongoing DNA repair with reestablished nucleolar transcription. Notably, recent evidence indicates that β-actin and nuclear myosin I are the factors necessary for repositioning of RNAP I and rDNA back into nucleolar interior after successful completion of rDNA repair [40]. Whether also the structural transitions of PNAs are the results of similar mechanical forces should be explored.

The last stage of PNAs, the PML-NDS, emerges almost exclusively from the tip of the funnel-shaped PNAs during stress release (here drug removal). The presence of highly concentrated proteins such as DHX9 and B23 in these structures indicates ongoing active sequestration of nucleolar factors into this structure. The force behind the genesis of PML-NDS might be a tendency of PML to form a balloon-like structure with the lowest energy state like in the PML NBs. Alternatively, the transmutation of funnel-like PNAs into PML-NDS may be a consequence of the transition of segregated nucleolus into the active one. Reactivation of nucleoli is accompanied by volume growth and reorganization of the nucleolar interior that may cause an alteration of nucleolar surface weakening the interactions essential for maintenance of the PNAs. However, the external (mechanical) forces cannot be excluded either.

The further fate of the DNA segregated in PML-NDS may be multiple, including its degradation or repair, consistent with the notion we present here, namely that only a fraction of PML-NDS remains positive for phosphorylated histone H2AX at later time-points after doxorubicin washout.

We observed that a significant subset of PML-NDS decays by three distinct mechanisms which, however, could be functionally equivalent. We propose that a loss of phosphorylated histone H2AX from the PML-NDS or a disappearance of the whole PML-NDS reflect a successful DNA repair event, whereas those PML-NDS remaining persistently positive for phosphorylated histone H2AX likely highlight persistence of unrepaired rDNA lesions.

Notably, some PML-NDS can persist for very long time periods (at least 17 days after doxorubicin washout). This is further underscored by the presence of PML-NDS in senescent cells [29], the co-association of PML NBs with persistent DNA lesions [26], and the recent evidence that an introduction of DNA double strand breaks into rDNA loci results in premature senescence [10], all indicating that nucleoli-associated chromatin is, besides telomeric loci [6, 7, 41], another type of DNA locus sensitive to specific senescence-inducing genomic damage.

The exact function of PML in the DNA repair is still under investigation. Recent evidence points to the involvement of PML and PML nuclear bodies in homologous recombination-directed DNA repair (HDR; [25, 28]). Boichuk et al. showed that knockdown of PML affected HDR efficiency, possibly reflecting an inability to accumulate several HDR proteins (Rad51, Mre11 and BRCA1) in DNA lesions [28]. Recently, Vancurova et al. reported that PML knockout cells revealed higher sensitivity to treatments causing DNA lesions requiring repair by HDR [25]. Both findings indicate that PML may modulate the HDR and thus the cell fate under genotoxic stress. As shown recently, proteins of both pathways (NHEJ and HR) colocalized with DSB presented in rDNA [36, 37, 42]. Warmerdam et al. implied that HR-directed repair can block the repair of rDNA breaks inserted by I-PpoI or CRISPR/Cas9 and when HR is involved in repair of such rDNA breaks the rDNA copy number is significantly reduced [42]. In general, HDR is considered less erroneous compared to NHEJ [43], however, in case of rDNA, there is a substantial risk of recombination event occurring between two rDNA repeats in *trans* or *cis*, resulting in extensive translocations and deletions, both leading to genomic instability [42]. Nevertheless, the several variants of HDR pathways were described [44, 45] and some of them may specifically participate in rDNA maintenance by proper repair of rDNA, as was proposed recently [46, 47]. One of the regulators of HDR is BLM helicase [48–51], depletion of which destabilized rDNA [52]. Notably, our results indicate that BLM accumulated in PNAs (see Supplementary Figure 9) implying that PNAs may modulate the local concentration of proteins involved in DDR and thus contribute to regulation of HDR. Altogether, it can be proposed that the PNAs are involved in a specific form of DNA repair, likely of difficult-to-repair DNA breaks in damaged rDNA repeats. Although a direct evidence that PML associates with damaged rDNA loci was not provided, the findings that the damage of ribosomal DNA is linked to relocation of rDNA to nucleolar caps [36, 37, 53] underscores such notion.

In conclusion, the interaction of PML with the nucleolus is a dynamic process linked to inactivation of RNA polymerase I, with the ensuing nucleolar segregation in response to stress. The association of PML nucleolar compartment with the rDNA damage lesions implicates the dynamic PNA structures reported here in DNA repair and separation of unrepaired DNA from nucleoli especially during the period of subsiding stress and reconstitution of nucleolar function. Whether senescence-inducing insults other than those examined here, such as oncogene-induced stresses that are associated with enhanced PML bodies accumulation [54] and DNA breakage [55] also lead to formation of PML-NDS reminiscent of those we describe in this study, remains to be elucidated.

## MATERIALS AND METHODS

### Chemicals and antibodies

4′,6-diamidino-2-phenylindole (D9542), doxorubicin hydrochloride (D1515), 5-fluorouridine (F5130), G418 disulfate salt (G5013) and puromycin dihydrochloride (P7255) were obtained from Sigma-Aldrich/Merck (Darmstadt, Germany); Click-iT EdU Alexa Fluor 488 Imaging Kit (C10337) and TOTO-3 (T-3604) were obtained from Thermo Fisher Scientific (Waltham, MA, USA); SiR-DNA dye (SC007) was purchased from Spirochrome (Stein am Rhein, Switzerland); Antifade Pro-long Gold Mounting Media (AF-400-H) was obtained from Immunological Sciences, Rome, Italy). Specification of primary and secondary antibodies used throughout the study is listed in Supplementary Table 1.

### Cell culture

Immortalized human retinal pigment epithelial cells (RPE-1$^{hTERT}$, ATCC), RPE-1$^{hTERT}$ PML knockout cells [25], RPE-1$^{hTERT}$ cells stably expressing EGFP-PML IV or EGFP-PML IV together with RFP-B23, and primary human diploid fibroblasts (BJ, ATCC), all checked for absence of mycoplasma infection, were cultured in Dulbecco's modified Eagle's medium (Gibco/Thermo Fisher Scientific, Waltham, MA, USA) containing 1.5 g/L (BJ) or 4.5 g/L (RPE-1) glucose and supplemented with 10% fetal bovine serum (Gibco/Thermo Fisher Scientific, Waltham, MA, USA) and antibiotics (100 U/mL penicillin and 100 µg/mL streptomycin sulfate, Sigma, St. Louis, MO, USA). Primary human mesenchymal stem cells (hMSC, ATCC) were grown in mesenchymal stem cells growth medium (composed of medium PT 3238 and supplements PT 4105, Lonza, Basel, Switzerland). The cells were cultivated in normal atmospheric air containing 5% $CO_2$ in a standard humidified incubator at 37°C, on a tissue culture dish (TPP Techno Plastic Products AG, Trasadingen, Switzerland). Doxorubicin was used at final concentrations 0.75, 0.375 or 0.075 µM

### Plasmid construction and lentiviral transduction

For stable expression of PML isoform IV tagged with EGFP at N-terminus, lentiviral vector pCDH-EGFP-PML IV was prepared as follows: PCR-amplified PML IV cDNA was inserted into *Hinc*II-digested pGEM4z plasmid (P2161, Promega, Madison, WI, USA) and PML IV was subsequently excised and inserted into pEGFP-C3 plasmid (6082-1, Clontech/TaKaRa, Kusatsu, Shiga, Japan) via the *Hind*III/*BamH*I sites.

Finally, EGFP-PML IV was excised and inserted into the *Bmt*I/*BamH*I sites of pCDH-CMV-MCS-EF1-Puro vector (CD510B-1, System Biosciences, Palo Alto, CA, USA). For stable expression of B23 tagged with RFP at N-terminus, lentiviral vector pCDH-RFP-B23 was prepared as follows: RFP-B23 was excised by *BamH*I/*Nhe*I from the mRFP-C2-B23 plasmid that was kindly provided by A. Holoubek [56]. The fragment was inserted into pCDH-CMV-MCS-EF1-Neo vector (CD514B-1, System Biosciences, Palo Alto, CA, USA), digested by the same restriction enzymes. The stable RPE-1$^{hTERT}$ cell lines expressing EGFP-PML IV and RFP-B23 were generated by lentiviral infection using the respective pCDH-CMV-MCS-EF1 vectors and subsequent selection with puromycin (15 μg/mL) and neomycin (1.12 mg/mL). Afterwards, the cells were sorted for low expression of the fluorescence markers using a cell sorter (BD Influx Cell Sorter, BD Biosciences, San Jose, CA, USA).

**Indirect immunofluorescence, confocal microscopy, ScanR microscopy and stimulated emission depletion (STED) microscopy**

Cells grown on glass coverslips were fixed with 4% formaldehyde in PBS for 15 min, permeabilized in 0.2% Triton X-100 in PBS for 10 min, blocked in 10% FBS in PBS for 30 min, and incubated with primary antibodies for 1 hour, all in RT. In case of BLM staining, pre-extraction with a specific pre-extraction buffer (0.5% Triton X-100, 20 mM HEPES pH 7.4, 50 mM NaCl, 3 mM MgCl2, 1 mM PMSF, 10 mM β-glycerol phosphate) for 10 min was done before cell fixation. After that, cells were washed three times 5 min in PBS, and secondary antibodies (Alexa Fluor 555 used specifically for STED) were applied in RT for 1 hour. For some experiments, TOTO-3 was applied together with secondary antibodies. Subsequently, cells were counterstained with 1 μg/mL DAPI for 2 min, washed 3 times with PBS for 5 min, let dry and mounted with Antifade Pro-long Gold Mounting Media. The wide-field images were subsequently acquired on the Leica DM6000 fluorescent microscope using the HCX PL APO 63×/1.40 OIL PH3 CS and HCX PL APO 40×/0.75 DRY PH2 objectives and monochromatic CCD camera Leica DFC 350FX (Leica Microsystems GmbH, Wetzlar, Germany); the confocal images were acquired on microscope DMI6000 with laser scanning confocal head Leica TCS SP5 AOBS Tandem, using the HC PL APO 63×/1.40 OIL CS2 objective (Leica Microsystems GmbH, Wetzlar, Germany). High-content image acquisition was done on the Olympus IX81 microscope (Olympus Corporation, Tokyo, Japan) equipped with ScanR module using the UPLFN 40×/1.3 OIL objective and sCMOS camera Hamamatsu ORCA-Flash4.0 V2 (Hamamatsu Photonics, Shizuoka, Japan). The data were analyzed in ScanR Analysis software (Olympus Corporation, Tokyo, Japan). The DHX9 accumulations and γH2AX foci were detected by the Spot detector function. The percentage of cells containing 3–15 γH2AX foci was counted from EdU-negative cells only, since untreated S-phase cells often exhibit high γH2AX signal and would therefore perturb the analysis. For super-resolution STED microscopy, the cells were mounted with glycine/N-propyl gallate and imaged on the microscope DMi8 with laser scanning confocal head Leica TCS SP8 and STED 3X module using the HC PL APO100×/1.40 OIL STED WHITE CS2l objective. Image deconvolution of confocal and STED images was done using Huygens Professional software (Scientific Volume Imaging B.V., Hilversum, The Netherlands).

**Live-cell structured illumination microscopy (SIM) and time-lapse microscopy**

RPE-1$^{hTERT}$ cells stably expressing EGFP-PML IV or EGFP-PML IV and RFP-B23 were seeded on glass-bottom plastic dishes (HBST-3522, WillCo Wells, Amsterdam, The Netherlands) and cultivated in FluoroBrite™ DMEM (A1896701, Gibco/Thermo Fisher Scientific, Waltham, MA, USA) supplemented with 10% FBS. This medium was also used instead of classical DMEM for all indicated doxorubicin treatments and removals. For super-resolution SIM microscopy, 1 μM SiR-DNA dye was added to the cells at least 1 hour before capturing and the live cells were then imaged on the DeltaVision OMX™ V4 imaging system with the Blaze SIM Module (Applied Precision/GE Healthcare, Chicago, IL, USA), using the PLAN APO N 60×/1.42 OIL objective (Olympus Corporation, Tokyo, Japan) and pco.edge 5.5 sCMOS cameras (PCO AG, Kelheim, Germany). Image reconstruction and registration was done in softWoRx software (Applied Precision/GE Healthcare, Chicago, IL, USA). For time-lapse microscopy, the live cells were imaged on the inverted fluorescence Olympus microscope version IX-71 (Olympus Corporation, Tokyo, Japan) coupled with the Delta Vision Core system (GE Healthcare, Chicago, IL, USA), using the U APO/340 40×/1.35-0.65 CORR OIL objective (Olympus Corporation, Tokyo, Japan) and CoolSANP HQ CCD camera (Teledyne Photometrics, Tucson, AZ, USA). All live-cell imaging was done at 37°C in normal atmospheric air containing 5% $CO_2$. Tracking of selected cells was done post-imaging in ImageJ, using the Resolve3D plugin.

**5-Fluorouridine incorporation assay**

Cells were incubated with 1 mM 5-fluorouridine (5-FUrd) for 30 min, at indicated time-points after doxorubicin treatment and removal. After that, cells were fixed with

4% formaldehyde at RT for 15 min and the 5-FUrd incorporation was visualized using anti-BrdU antibody cross-reacting with 5-FUrd. The standard protocol for immunofluorescence described above was used.

**Cell proliferation assay**

Cells were incubated with 10 μM 5-ethynyl-2′-deoxyuridine (EdU) for 6 hours and fixed with 4% formaldehyde at RT for 15 min at indicated time-points. To visualize EdU incorporation, click chemistry was performed with Click-iT EdU Alexa Fluor 488 Imaging Kit according to manufacturer's instructions.

**Senescence-associated beta-galactosidase assay**

Cells were fixed with 0.5% glutaraldehyde at RT for 15 min at indicated time-points. After that, cells were washed twice with 1 mM $MgCl_2$/PBS and incubated with X-Gal staining solution for 3 h at 37 °C. The staining was terminated by three consecutive washes with $ddH_2O$. Finally, the cells were let dry, mounted with Antifade Prolong Gold Mounting Media and imaged on the Leica DM6000 fluorescent microscope using the HC PLAN APO 20×/0.70 DRY PH2 objective and color CCD camera Leica DFC490 (Leica Microsystems GmbH, Wetzlar, Germany).

**SDS-PAGE and immunoblotting**

Cells were harvested into Laemmli SDS sample lysis buffer (62.5 mM Tris-HCl, pH 6.8, 2% SDS, 10% glycerol), boiled at 95°C for 5 min, sonicated and centrifuged at 18,000 × g for 10 min. Concentration of proteins was estimated by the BCA method (Pierce Biotechnology Inc., Rockford, USA). Equal amounts of total protein were mixed with DTT and bromphenol blue to final concentration 100 mM and 0.01%, respectively, and separated by SDS-PAGE (8% or 12% polyacrylamide gels were used). The proteins were electrotransferred to a nitrocellulose membrane using wet transfer. Immunostaining followed by ECL detection was performed. The intensity of DHX9 bands was measured in ImageJ Gel Analyzer plugin. The DHX9 level was calculated as the intensity of DHX9 bands related to the intensity of loading control, while the relative intensity of untreated PML-WT cells was set as one.

## Abbreviations

5-FUrd: 5-fluorouridine; AMD: actinomycin D; B23: nucleophosmin; DAPI: 4',6-diamidino-2-phenylindole; DDR: DNA damage response; DHX9: DExH-box helicase 9/nuclear DNA helicase II; doxo: doxorubicin hydrochloride; EdU: 5-ethynyl-2′-deoxyuridin; EGFP: enhanced green fluorescent protein; γH2AX: histone H2AX phosphorylated on serine 139; hMSC: human mesenchymal stem cells; HR: homologous recombination; iCdk: inhibitors of cyclin-dependent kinases; INK4: inhibitors of CDK4; IR: ionizing radiation; Kip: kinase inhibitory protein; NHEJ: non-homologous end joining: PAF49: RNA polymerase I-associated factor 49; PBS: phosphate buffered saline; PML: promyelocytic leukemia; PML NBs: PML nuclear bodies; PML-KO: PML knock-out; PML-NDS: PML nucleolus-derived structure; PML-WT: PML wild-type; PNAs: PML nucleolar associations; rDNA: ribosomal DNA; RFP: red fluorescent protein; RNAP I: RNA polymerase I; RPE-1$^{hTERT}$: retinal pigment epithelial cells immortalized with human telomerase reverse transcriptase; SIM: structured illumination microscopy; SiR-DNA: silicon rhodamine DNA dye; STED: stimulated emission depletion; WO: doxorubicin washout.

## AUTHOR CONTRIBUTIONS

Study design: PV, ZH, JB, TI; Funding: JB; Data collection: TI, PV, AK, SH, JK; Data analysis: TI, PV; Data interpretation: PV, TI, ZH, JB; Manuscript preparation: PV, JB, TI, ZH; Critical revision of the manuscript: all authors.

## ACKNOWLEDGMENTS

We would like to thank Marketa Vancurova, Ivan Novotny, Anna Malinova, Michaela Efenberkova and Magdalena Opravilova for their excellent technical support. We acknowledge the Light Microscopy Core Facility, IMG ASCR, Prague, Czech Republic, supported by MEYS (LM2015062, CZ.02.1.01/0.0/0.0/16_013/0001775), OPPK (CZ.2.16/3.1.00/21547) and MEYS (LO1419), for their support with the wide-field, confocal, Olympus ScanR, super-resolution and time-lapse imaging, and image analysis presented herein.

## CONFLICTS OF INTEREST

The authors declare they have no conflicts of interest.

## FUNDING

This study was supported by Grant Agency of the Czech Republic (Project 17-14743S), Institutional Grant (Project RVO 68378050). T.I. was supported in part by the Faculty of Science, Charles University, Prague. J.B. was supported in part by the Danish Cancer Society and the Swedish Research Council.

## REFERENCES

1. Childs BG, Durik M, Baker DJ, van Deursen JM. Cellular senescence in aging and age-related disease:

from mechanisms to therapy. Nat Med. 2015; 21:1424–35.
https://doi.org/10.1038/nm.4000 PMID:26646499

2. McHugh D, Gil J. Senescence and aging: Causes, consequences, and therapeutic avenues. J Cell Biol. 2018; 217:65–77.
https://doi.org/10.1083/jcb.201708092
PMID:29114066

3. Baker DJ, Childs BG, Durik M, Wijers ME, Sieben CJ, Zhong J, Saltness RA, Jeganathan KB, Verzosa GC, Pezeshki A, Khazaie K, Miller JD, van Deursen JM. Naturally occurring p16(Ink4a)-positive cells shorten healthy lifespan. Nature. 2016; 530:184–89.
https://doi.org/10.1038/nature16932
PMID:26840489

4. Baker DJ, Wijshake T, Tchkonia T, LeBrasseur NK, Childs BG, van de Sluis B, Kirkland JL, van Deursen JM. Clearance of p16Ink4a-positive senescent cells delays ageing-associated disorders. Nature. 2011; 479:232–36.
https://doi.org/10.1038/nature10600
PMID:22048312

5. Muñoz-Espín D, Serrano M. Cellular senescence: from physiology to pathology. Nat Rev Mol Cell Biol. 2014; 15:482–96.
https://doi.org/10.1038/nrm3823 PMID:24954210

6. d'Adda di Fagagna F, Reaper PM, Clay-Farrace L, Fiegler H, Carr P, Von Zglinicki T, Saretzki G, Carter NP, Jackson SP. A DNA damage checkpoint response in telomere-initiated senescence. Nature. 2003; 426:194–98.
https://doi.org/10.1038/nature02118
PMID:14608368

7. Hewitt G, Jurk D, Marques FD, Correia-Melo C, Hardy T, Gackowska A, Anderson R, Taschuk M, Mann J, Passos JF. Telomeres are favoured targets of a persistent DNA damage response in ageing and stress-induced senescence. Nat Commun. 2012; 3:708.
https://doi.org/10.1038/ncomms1708
PMID:22426229

8. Kobayashi T. A new role of the rDNA and nucleolus in the nucleus—rDNA instability maintains genome integrity. BioEssays. 2008; 30:267–72.
https://doi.org/10.1002/bies.20723
PMID:18293366

9. Ganley AR, Ide S, Saka K, Kobayashi T. The effect of replication initiation on gene amplification in the rDNA and its relationship to aging. Mol Cell. 2009; 35:683–93.
https://doi.org/10.1016/j.molcel.2009.07.012
PMID:19748361

10. Paredes S, Angulo-Ibanez M, Tasselli L, Carlson SM, Zheng W, Li TM, Chua KF. The epigenetic regulator SIRT7 guards against mammalian cellular senescence induced by ribosomal DNA instability. J Biol Chem. 2018; 293:11242–50.
https://doi.org/10.1074/jbc.AC118.003325
PMID:29728458

11. Ganley AR, Kobayashi T. Ribosomal DNA and cellular senescence: new evidence supporting the connection between rDNA and aging. FEMS Yeast Res. 2014; 14:49–59.
https://doi.org/10.1111/1567-1364.12133
PMID:24373458

12. Feric M, Vaidya N, Harmon TS, Mitrea DM, Zhu L, Richardson TM, Kriwacki RW, Pappu RV, Brangwynne CP. Coexisting Liquid Phases Underlie Nucleolar Subcompartments. Cell. 2016; 165:1686–97.
https://doi.org/10.1016/j.cell.2016.04.047
PMID:27212236

13. Boisvert FM, van Koningsbruggen S, Navascués J, Lamond AI. The multifunctional nucleolus. Nat Rev Mol Cell Biol. 2007; 8:574–85.
https://doi.org/10.1038/nrm2184 PMID:17519961

14. Boulon S, Westman BJ, Hutten S, Boisvert FM, Lamond AI. The nucleolus under stress. Mol Cell. 2010; 40:216–27.
https://doi.org/10.1016/j.molcel.2010.09.024
PMID:20965417

15. Golomb L, Volarevic S, Oren M. p53 and ribosome biogenesis stress: the essentials. FEBS Lett. 2014; 588:2571–79.
https://doi.org/10.1016/j.febslet.2014.04.014
PMID:24747423

16. Lindström MS, Jurada D, Bursac S, Orsolic I, Bartek J, Volarevic S. Nucleolus as an emerging hub in maintenance of genome stability and cancer pathogenesis. Oncogene. 2018; 37:2351–66.
https://doi.org/10.1038/s41388-017-0121-z
PMID:29429989

17. Nishimura K, Kumazawa T, Kuroda T, Katagiri N, Tsuchiya M, Goto N, Furumai R, Murayama A, Yanagisawa J, Kimura K. Perturbation of ribosome biogenesis drives cells into senescence through 5S RNP-mediated p53 activation. Cell Rep. 2015; 10:1310–23.
https://doi.org/10.1016/j.celrep.2015.01.055
PMID:25732822

18. Lessard F, Igelmann S, Trahan C, Huot G, Saint-Germain E, Mignacca L, Del Toro N, Lopes-Paciencia S, Le Calvé B, Montero M, Deschênes-Simard X, Bury M, Moiseeva O, et al. Senescence-associated ribosome biogenesis defects contributes to cell cycle arrest through the Rb

pathway. Nat Cell Biol. 2018; 20:789–99. https://doi.org/10.1038/s41556-018-0127-y PMID:29941930

19. Ishov AM, Sotnikov AG, Negorev D, Vladimirova OV, Neff N, Kamitani T, Yeh ET, Strauss JF 3rd, Maul GG. PML is critical for ND10 formation and recruits the PML-interacting protein daxx to this nuclear structure when modified by SUMO-1. J Cell Biol. 1999; 147:221–34. https://doi.org/10.1083/jcb.147.2.221 PMID:10525530

20. Guan D, Kao HY. The function, regulation and therapeutic implications of the tumor suppressor protein, PML. Cell Biosci. 2015; 5:60. https://doi.org/10.1186/s13578-015-0051-9 PMID:26539288

21. Seker H, Rubbi C, Linke SP, Bowman ED, Garfield S, Hansen L, Borden KL, Milner J, Harris CC. UV-C-induced DNA damage leads to p53-dependent nuclear trafficking of PML. Oncogene. 2003; 22:1620–28. https://doi.org/10.1038/sj.onc.1206140 PMID:12642865

22. Carbone R, Pearson M, Minucci S, Pelicci PG. PML NBs associate with the hMre11 complex and p53 at sites of irradiation induced DNA damage. Oncogene. 2002; 21:1633–40. https://doi.org/10.1038/sj.onc.1205227 PMID:11896594

23. Dellaire G, Ching RW, Ahmed K, Jalali F, Tse KC, Bristow RG, Bazett-Jones DP. Promyelocytic leukemia nuclear bodies behave as DNA damage sensors whose response to DNA double-strand breaks is regulated by NBS1 and the kinases ATM, Chk2, and ATR. J Cell Biol. 2006; 175:55–66. https://doi.org/10.1083/jcb.200604009 PMID:17030982

24. Bøe SO, Haave M, Jul-Larsen A, Grudic A, Bjerkvig R, Lønning PE. Promyelocytic leukemia nuclear bodies are predetermined processing sites for damaged DNA. J Cell Sci. 2006; 119:3284–95. https://doi.org/10.1242/jcs.03068 PMID:16868026

25. Vancurova M, Hanzlikova H, Knoblochova L, Kosla J, Majera D, Mistrik M, Burdova K, Hodny Z, Bartek J. PML nuclear bodies are recruited to persistent DNA damage lesions in an RNF168-53BP1 dependent manner and contribute to DNA repair. DNA Repair (Amst). 2019; 78:114–27. https://doi.org/10.1016/j.dnarep.2019.04.001 PMID:31009828

26. Rodier F, Muñoz DP, Teachenor R, Chu V, Le O, Bhaumik D, Coppé JP, Campeau E, Beauséjour CM, Kim SH, Davalos AR, Campisi J. DNA-SCARS: distinct nuclear structures that sustain damage-induced senescence growth arrest and inflammatory cytokine secretion. J Cell Sci. 2011; 124:68–81. https://doi.org/10.1242/jcs.071340 PMID:21118958

27. Hubackova S, Novakova Z, Krejcikova K, Kosar M, Dobrovolna J, Duskova P, Hanzlikova H, Vancurova M, Barath P, Bartek J, Hodny Z. Regulation of the PML tumor suppressor in drug-induced senescence of human normal and cancer cells by JAK/STAT-mediated signaling. Cell Cycle. 2010; 9:3085–99. https://doi.org/10.4161/cc.9.15.12521 PMID:20699642

28. Boichuk S, Hu L, Makielski K, Pandolfi PP, Gjoerup OV. Functional connection between Rad51 and PML in homology-directed repair. PLoS One. 2011; 6:e25814. https://doi.org/10.1371/journal.pone.0025814 PMID:21998700

29. Janderová-Rossmeislová L, Nováková Z, Vlasáková J, Philimonenko V, Hozák P, Hodný Z. PML protein association with specific nucleolar structures differs in normal, tumor and senescent human cells. J Struct Biol. 2007; 159:56–70. https://doi.org/10.1016/j.jsb.2007.02.008 PMID:17428679

30. Jiang WQ, Ringertz N. Altered distribution of the promyelocytic leukemia-associated protein is associated with cellular senescence. Cell Growth Differ. 1997; 8:513–22. PMID:9213441

31. Condemine W, Takahashi Y, Le Bras M, de Thé H. A nucleolar targeting signal in PML-I addresses PML to nucleolar caps in stressed or senescent cells. J Cell Sci. 2007; 120:3219–27. https://doi.org/10.1242/jcs.007492 PMID:17878236

32. Bernardi R, Scaglioni PP, Bergmann S, Horn HF, Vousden KH, Pandolfi PP. PML regulates p53 stability by sequestering Mdm2 to the nucleolus. Nat Cell Biol. 2004; 6:665–72. https://doi.org/10.1038/ncb1147 PMID:15195100

33. Burger K, Mühl B, Harasim T, Rohrmoser M, Malamoussi A, Orban M, Kellner M, Gruber-Eber A, Kremmer E, Hölzel M, Eick D. Chemotherapeutic drugs inhibit ribosome biogenesis at various levels. J Biol Chem. 2010; 285:12416–25. https://doi.org/10.1074/jbc.M109.074211 PMID:20159984

34. Shav-Tal Y, Blechman J, Darzacq X, Montagna C, Dye BT, Patton JG, Singer RH, Zipori D. Dynamic sorting of nuclear components into distinct nucleolar caps during transcriptional inhibition. Mol Biol Cell. 2005; 16:2395–413.

https://doi.org/10.1091/mbc.e04-11-0992
PMID:15758027

35. Rogakou EP, Pilch DR, Orr AH, Ivanova VS, Bonner WM. DNA double-stranded breaks induce histone H2AX phosphorylation on serine 139. J Biol Chem. 1998; 273:5858–68.
https://doi.org/10.1074/jbc.273.10.5858
PMID:9488723

36. Harding SM, Boiarsky JA, Greenberg RA. ATM Dependent Silencing Links Nucleolar Chromatin Reorganization to DNA Damage Recognition. Cell Rep. 2015; 13:251–59.
https://doi.org/10.1016/j.celrep.2015.08.085
PMID:26440899

37. van Sluis M, McStay B. A localized nucleolar DNA damage response facilitates recruitment of the homology-directed repair machinery independent of cell cycle stage. Genes Dev. 2015; 29:1151–63.
https://doi.org/10.1101/gad.260703.115
PMID:26019174

38. Ditlev JA, Case LB, Rosen MK. Who's In and Who's Out-Compositional Control of Biomolecular Condensates. J Mol Biol. 2018; 430:4666–84.
https://doi.org/10.1016/j.jmb.2018.08.003
PMID:30099028

39. Sawyer IA, Bartek J, Dundr M. Phase separated microenvironments inside the cell nucleus are linked to disease and regulate epigenetic state, transcription and RNA processing. Semin Cell Dev Biol. 2019; 90:94–103.
https://doi.org/10.1016/j.semcdb.2018.07.001
PMID:30017905

40. Cerutti E, Daniel L, Donnio LM, Neuillet D, Magnani C, Mari PO, Giglia-Mari G. β-Actin and Nuclear Myosin I are responsible for nucleolar reorganization during DNA Repair. bioRxiv. 2019.
https://doi.org/10.1101/646471

41. Fumagalli M, Rossiello F, Clerici M, Barozzi S, Cittaro D, Kaplunov JM, Bucci G, Dobreva M, Matti V, Beausejour CM, Herbig U, Longhese MP, d'Adda di Fagagna F. Telomeric DNA damage is irreparable and causes persistent DNA-damage-response activation. Nat Cell Biol. 2012; 14:355–65.
https://doi.org/10.1038/ncb2466 PMID:22426077

42. Warmerdam DO, van den Berg J, Medema RH. Breaks in the 45S rDNA Lead to Recombination-Mediated Loss of Repeats. Cell Rep. 2016; 14:2519–27.
https://doi.org/10.1016/j.celrep.2016.02.048
PMID:26972008

43. Chapman JR, Taylor MR, Boulton SJ. Playing the end game: DNA double-strand break repair pathway choice. Mol Cell. 2012; 47:497–510.
https://doi.org/10.1016/j.molcel.2012.07.029
PMID:22920291

44. Morrical SW. DNA-pairing and annealing processes in homologous recombination and homology-directed repair. Cold Spring Harb Perspect Biol. 2015; 7:a016444.
https://doi.org/10.1101/cshperspect.a016444
PMID:25646379

45. Renkawitz J, Lademann CA, Jentsch S. Mechanisms and principles of homology search during recombination. Nat Rev Mol Cell Biol. 2014; 15:369–83.
https://doi.org/10.1038/nrm3805
PMID:24824069

46. van Sluis M, McStay B. Nucleolar DNA Double-Strand Break Responses Underpinning rDNA Genomic Stability. Trends Genet. 2019. [Epub ahead of print].
https://doi.org/10.1016/j.tig.2019.07.001
PMID:31353047

47. Warmerdam DO, Wolthuis RM. Keeping ribosomal DNA intact: a repeating challenge. Chromosome Res. 2019; 27:57–72.
https://doi.org/10.1007/s10577-018-9594-z
PMID:30556094

48. Wu L, Hickson ID. The Bloom's syndrome helicase suppresses crossing over during homologous recombination. Nature. 2003; 426:870–74.
https://doi.org/10.1038/nature02253
PMID:14685245

49. Bugreev DV, Yu X, Egelman EH, Mazin AV. Novel pro- and anti-recombination activities of the Bloom's syndrome helicase. Genes Dev. 2007; 21:3085–94.
https://doi.org/10.1101/gad.1609007
PMID:18003860

50. Karow JK, Constantinou A, Li JL, West SC, Hickson ID. The Bloom's syndrome gene product promotes branch migration of holliday junctions. Proc Natl Acad Sci USA. 2000; 97:6504–08.
https://doi.org/10.1073/pnas.100448097
PMID:10823897

51. van Brabant AJ, Ye T, Sanz M, German IJ, Ellis NA, Holloman WK. Binding and melting of D-loops by the Bloom syndrome helicase. Biochemistry. 2000; 39:14617–25.
https://doi.org/10.1021/bi0018640 PMID:11087418

52. Killen MW, Stults DM, Adachi N, Hanakahi L, Pierce AJ. Loss of Bloom syndrome protein destabilizes human gene cluster architecture. Hum Mol Genet. 2009; 18:3417–28.
https://doi.org/10.1093/hmg/ddp282
PMID:19542097

53. Korsholm LM, Gal Z, Lin L, Quevedo O, Ahmad DA, Dulina E, Luo Y, Bartek J, Larsen DH. Double-strand

breaks in ribosomal RNA genes activate a distinct signaling and chromatin response to facilitate nucleolar restructuring and repair. Nucleic Acids Res. 2019. [Epub ahead of print]. https://doi.org/10.1093/nar/gkz518 PMID:31184714

54. Liontos M, Koutsami M, Sideridou M, Evangelou K, Kletsas D, Levy B, Kotsinas A, Nahum O, Zoumpourlis V, Kouloukoussa M, Lygerou Z, Taraviras S, Kittas C, et al. Deregulated overexpression of hCdt1 and hCdc6 promotes malignant behavior. Cancer Res. 2007; 67:10899–909. https://doi.org/10.1158/0008-5472.can-07-2837 PMID:18006835

55. Halazonetis TD, Gorgoulis VG, Bartek J. An oncogene-induced DNA damage model for cancer development. Science. 2008; 319:1352–5. https://doi.org/10.1126/science.1140735 PMID:18323444

56. Brodska B, Holoubek A, Otevrelova P, Kuzelova K. Low-Dose Actinomycin-D Induces Redistribution of Wild-Type and Mutated Nucleophosmin Followed by Cell Death in Leukemic Cells. J Cell Biochem. 2016; 117:1319–29. https://doi.org/10.1002/jcb.25420 PMID:26505272

# SUPPLEMENTARY MATERIALS

## Supplementary Figures

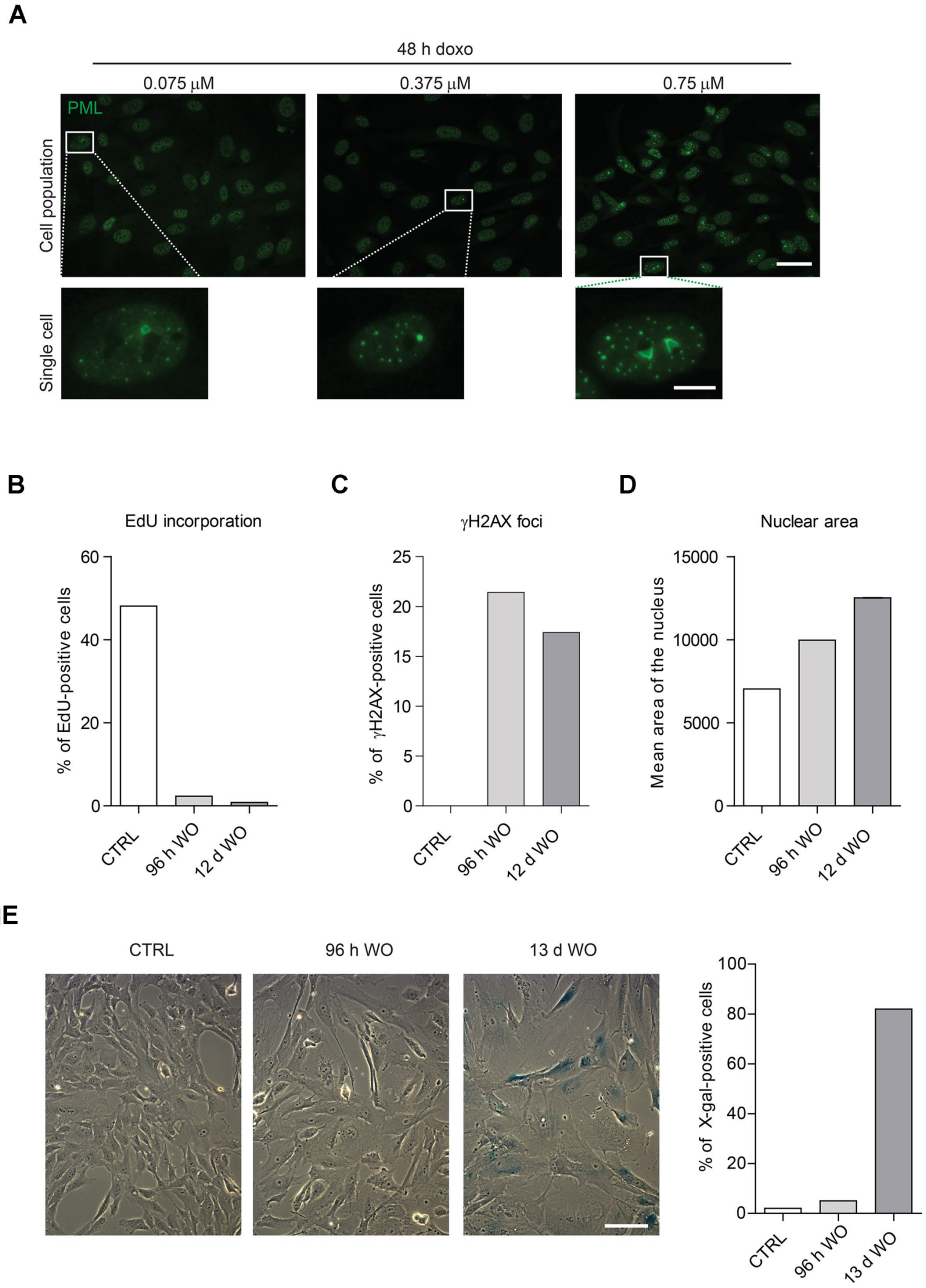


**Supplementary Figure 1. The dose-dependent formation of PML nucleolar associations (PNAs) and doxorubicin-induced senescence.** (**A**) RPE-1$^{hTERT}$ were treated with 0.075 μM, 0.375 μM and 0.75 μM doxorubicin for 48 hours and PNAs were detected by PML indirect immunofluorescence. Wide-field immunofluorescence images of cell populations (upper row; bar, 50 μm) and individual cells (lower row; bar, 10 μm) are shown. The images were captured with 40×/0.75 objective. (**B**–**D**) RPE-1$^{hTERT}$ were treated with 0.75 μM doxorubicin for 48 hours, after that the drug was removed and the cells were further cultured. At two time-points after drug removal (96 h WO, 12 d WO), the cells were incubated with EdU for 6 hours and stained for γH2AX foci. ScanR microscopic images were analyzed for percentage of EdU-positive cells (**B**), percentage of cells with 3–15 γH2AX foci (**C**), and the mean area of the nucleus (**D**). (**E**) RPE-1$^{hTERT}$ were treated as in (**B**–**D**). Senescence-associated β-galactosidase activity was estimated in untreated and doxorubicin-treated cells at two time-points after drug removal (96 h WO, 13 d WO) and the cells were imaged with 20×/0.70 objective and color CCD camera; bar, 100 μm. To estimate the percentage of β-galactosidase-positive cells, 178, 128 and 92 cells were counted for control, 96 h WO and 13 d WO samples, respectively. (**B**–**E**) The charts present the data from one experiment.

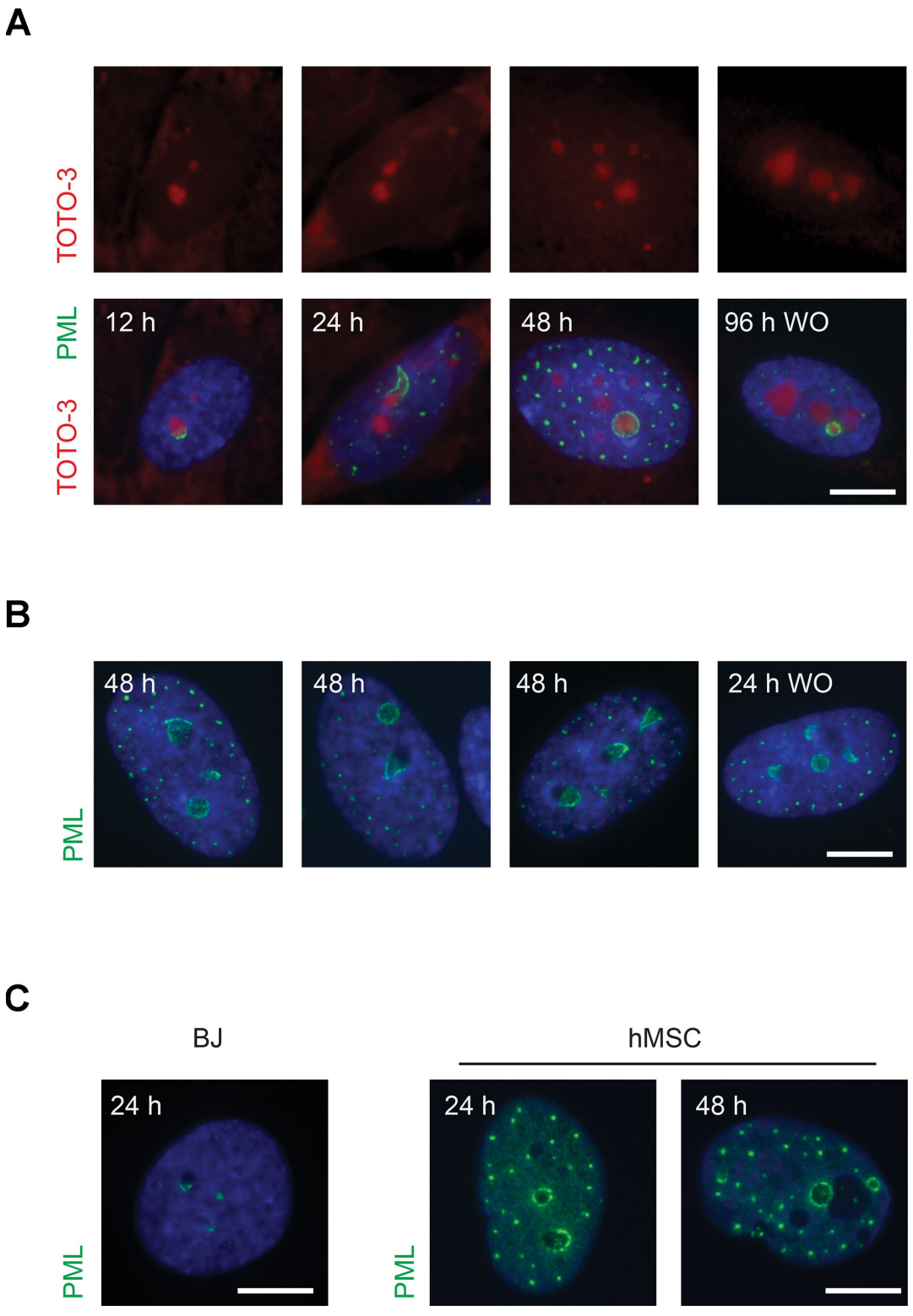


**Supplementary Figure 2. The diversity of PML nucleolar associations (PNAs) and their occurrence in different cell types.** PNAs detection by PML immunostaining (green) in RPE-1$^{hTERT}$ treated with 0.75 μM doxorubicin for 48 hours and after drug removal (up to 96 hours). Wide-field immunofluorescence images show representative cells, in which nucleoli with and without PNAs (**A**) or with different types of PNAs (**B**) occur at the same time. (**C**) The immunofluorescence detection of PNAs by PML immunostaining in human BJ fibroblasts and mesenchymal stem cells (hMSC) exposed to 0.75 μM doxorubicin. Nuclei and nucleoli were stained with DAPI (blue) and TOTO-3 (red), respectively. The images were captured with 63×/1.4 objective. Bar, 10 μm.

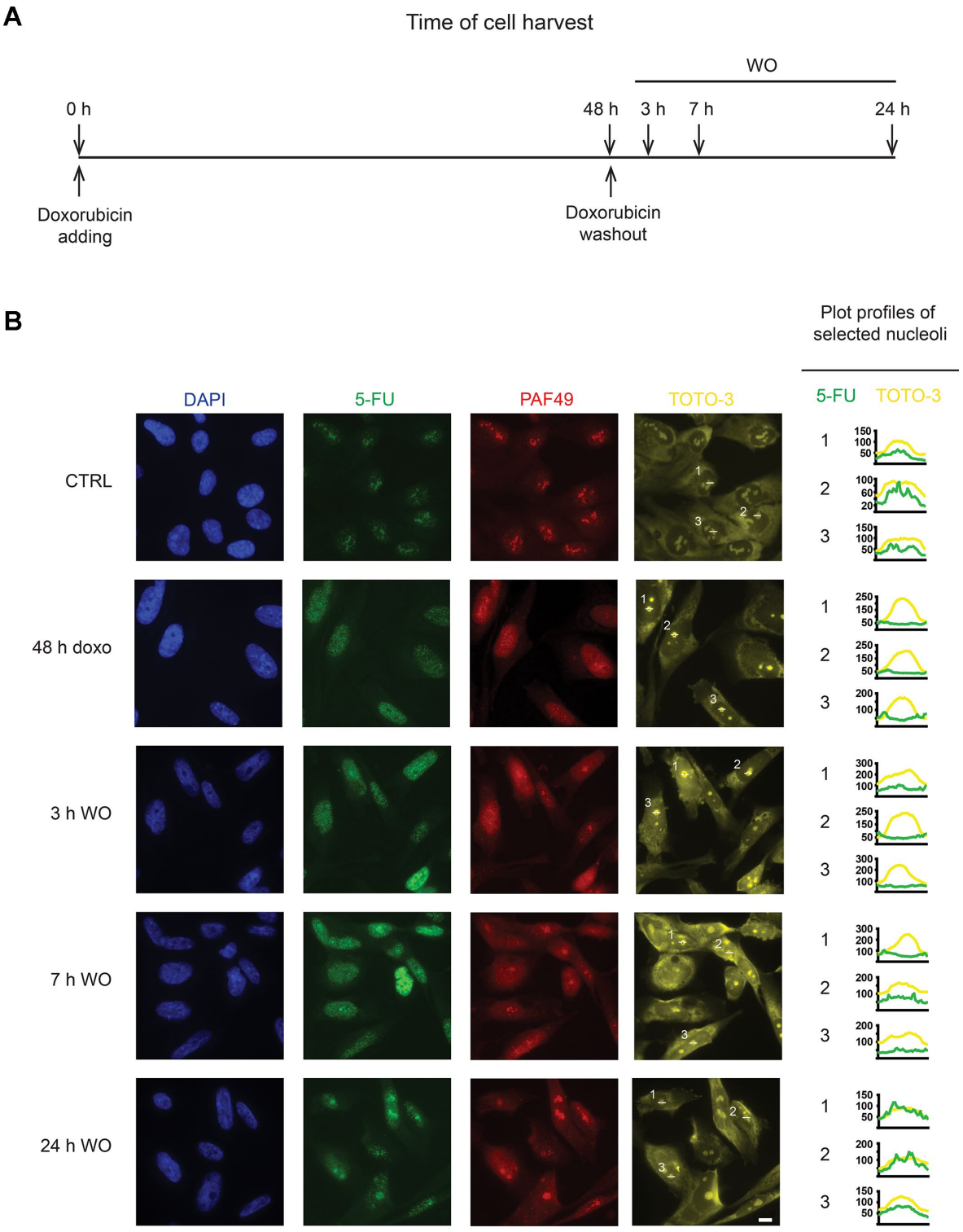


**Supplementary Figure 3. RNAP I transcription in the nucleolus is gradually restored during 24 hours after doxorubicin removal.** As shown in the scheme of the experiment (**A**), RPE-1$^{hTERT}$ were treated with 0.75 μM doxorubicin for 48 hours; after that doxorubicin was removed and cells were further cultured. Transcription in the nucleolus was estimated by incorporation of 5-fluorouridine (5-FUrd) at indicated time-points. (**B**) The immunofluorescence detection of 5-FUrd (green), representing newly synthesized nucleolar RNA, and localization/segregation of RNAPI subunit PAF49 (red) was performed. The nuclei and nucleoli were stained with DAPI (blue) and TOTO-3 (yellow), respectively. The images were captured with 40·/0.75 objective. Bar, 10 μm. For selected nucleoli, plot profiles of TOTO-3 and 5-FUrd signal were generated, to clearly demonstrate the absence of 5-FUrd signal in inactive nucleoli.

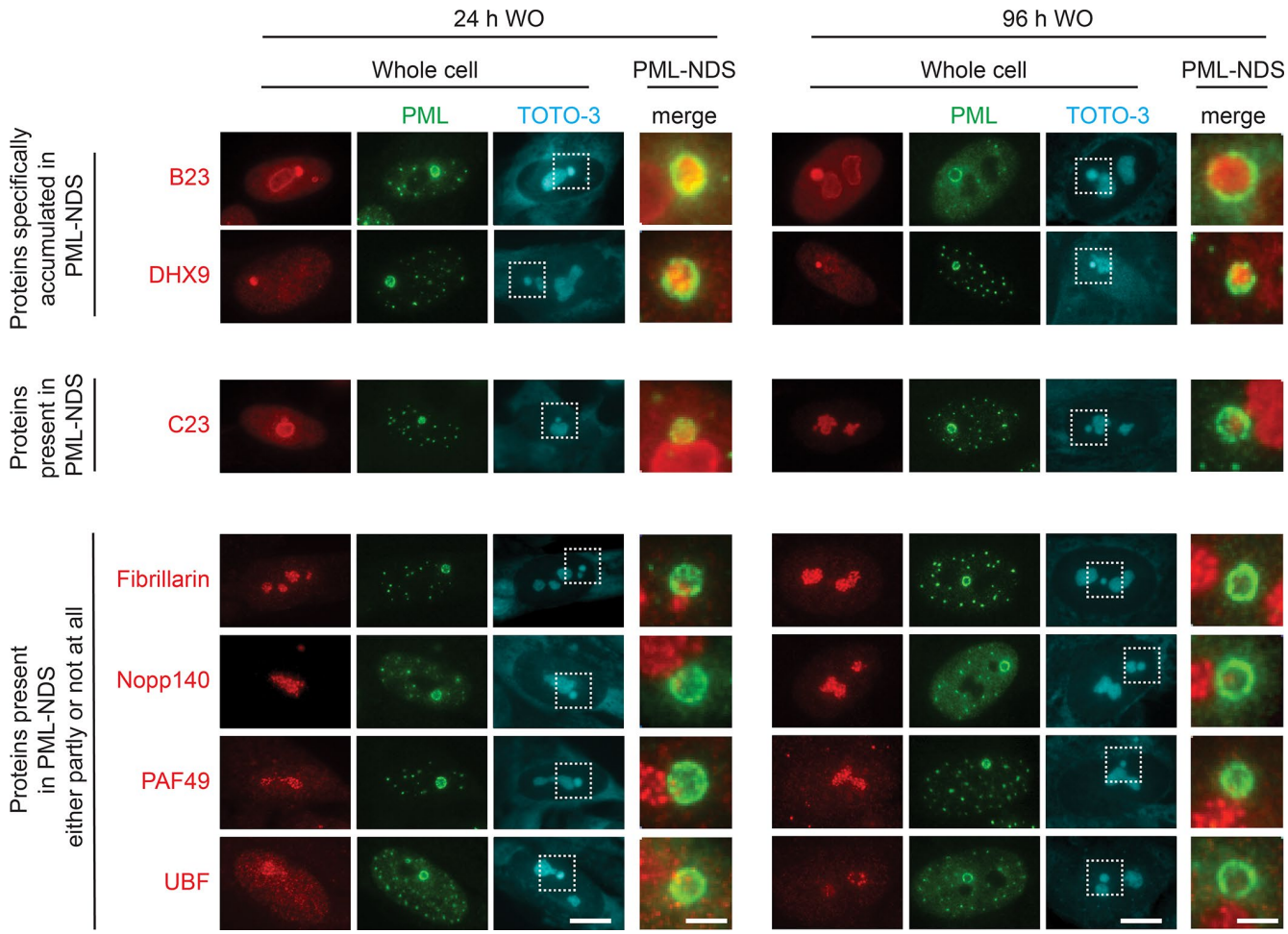


**Supplementary Figure 4. Accumulation of proteins into PML-NDS is a selective process.** RPE-1$^{hTERT}$ were treated with 0.75 μM doxorubicin for 48 hours; after that doxorubicin was removed and cells were further cultured for 24 or 96 hours. Accumulation of selected nucleolar proteins within PML-NDS was examined by immunostaining with specific antibodies (the proteins of interest – red, PML – green). The nucleoli were visualized by TOTO-3 (cyan). The images were captured with 63·/1.4 objective. Bars, 10 μm (whole cells), 3 μm (insets).

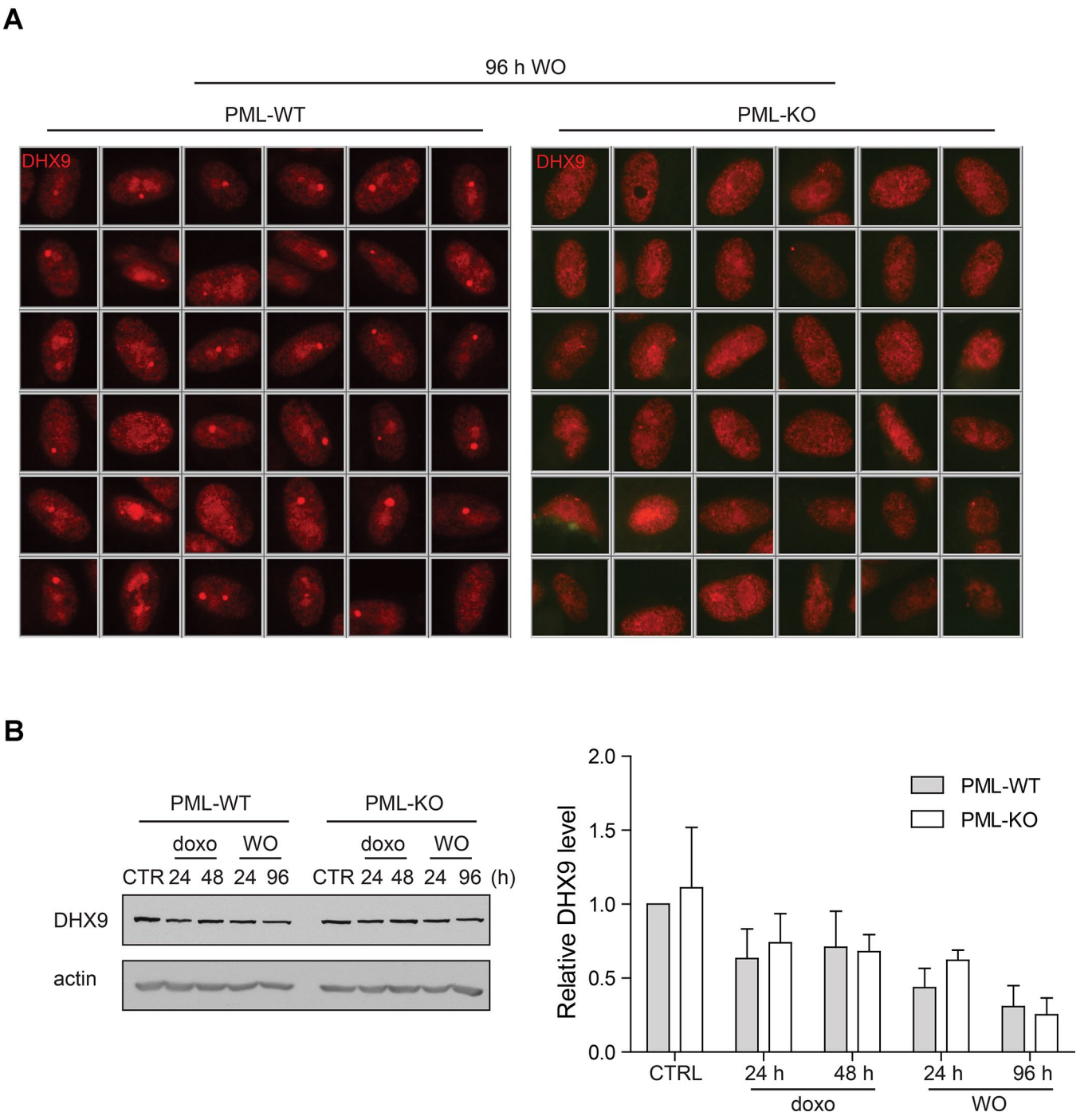


**Supplementary Figure 5. Cells identified as positive for DHX9 accumulations and total levels of DHX9 after doxorubicin.** RPE-1$^{hTERT}$ PML-WT and PML-KO cells were treated with 0.75 μM doxorubicin for 48 hours; after that doxorubicin was removed and cells were further cultured. (**A**) 96 hours after doxorubicin washout the cells were fixed, stained with antibodies against DHX9 (red) and PML (not shown) and imaged with the ScanR microscope. The galleries of cells identified as positive for DHX9 accumulations were generated as part of the ScanR analysis. Here, thirty-six cells from each gallery are shown. (**B**) At selected time-points during doxorubicin treatment and washout, cell lysates were harvested for SDS-PAGE and immunoblotting (left panel). The DHX9 level was then calculated as the intensity of DHX9 bands related to the intensity of a loading control, while the relative intensity of untreated PML-WT cells was set as one (right panel). Mean values and standard errors of means from three independent experiments are given.

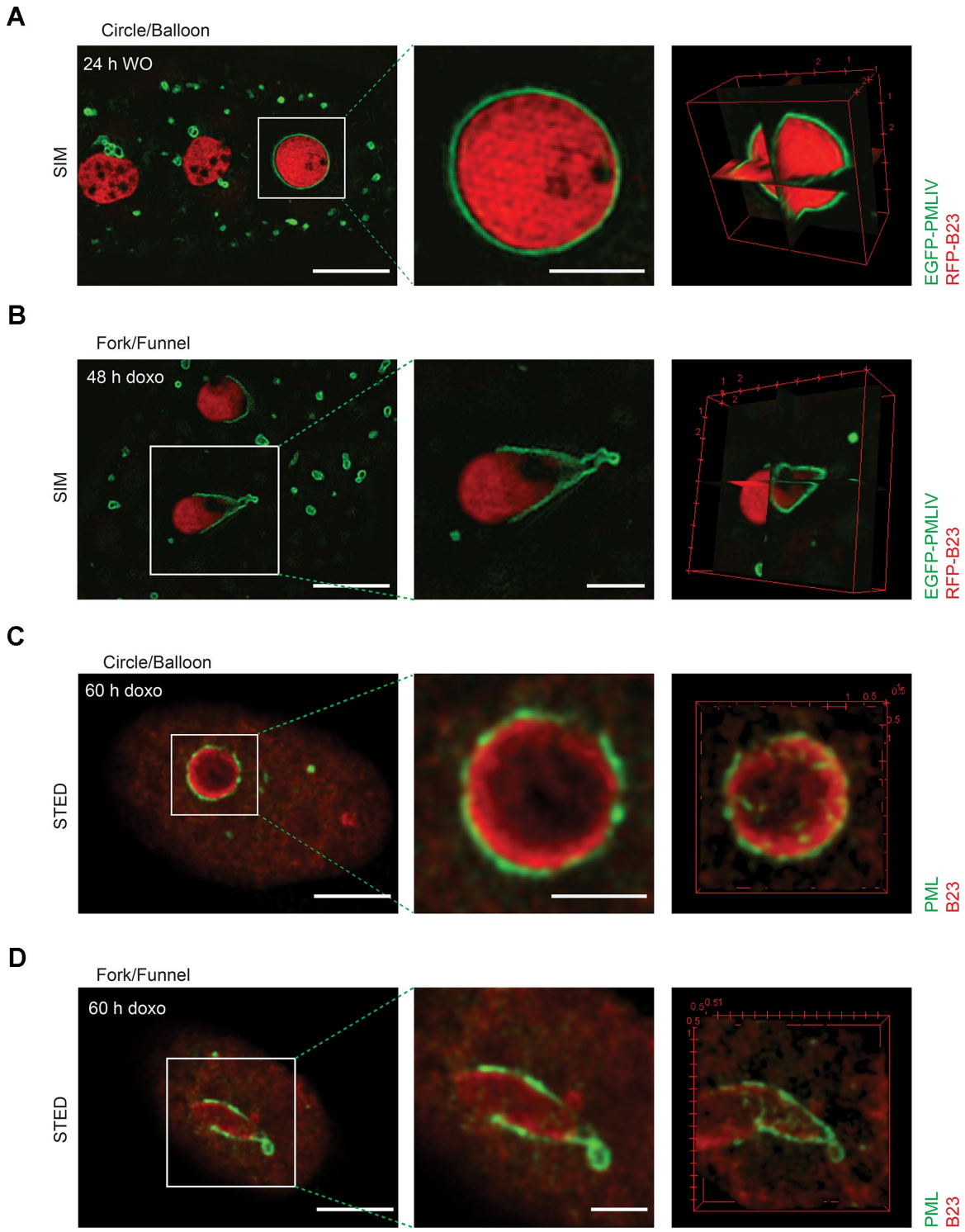


**Supplementary Figure 6. PNAs are hollow shells enclosing nucleolar material.** PML circles and forks were imaged with two different high resolution microscopy techniques: structured illumination microscopy (SIM) of live doxorubicin-treated RPE-1$^{hTERT}$ cells stably expressing EGFP-PML IV and RFP-B23 (**A**, **B**); and stimulated emission depletion (STED) of fixed doxorubicin-treated RPE-1$^{hTERT}$ cells with endogenous PML and B23 stained by antibodies (**C**, **D**). Central layers of whole cells (left images; bar, 5 μm) and respective PNAs (middle images; bar, 2 μm) are displayed together with 3-D-reconstructed PNAs (right images, for SIM displayed as ortho-views, for STED displayed as whole surfaces). The 3-D reconstruction was done from 22 (**A**), 24 (**B**), 15 (**C**) and 21 (**D**) layers in ImageJ program, using the ImageJ 3D viewer plugin. The distance between two layers is 0.125 μm for SIM and 0.05 μm for STED images; i.e. the depths of the stacks are, namely: 2.75 μm (**A**), 3 μm (**B**), 0.75 μm (**C**) and 1.05 μm (**A**).

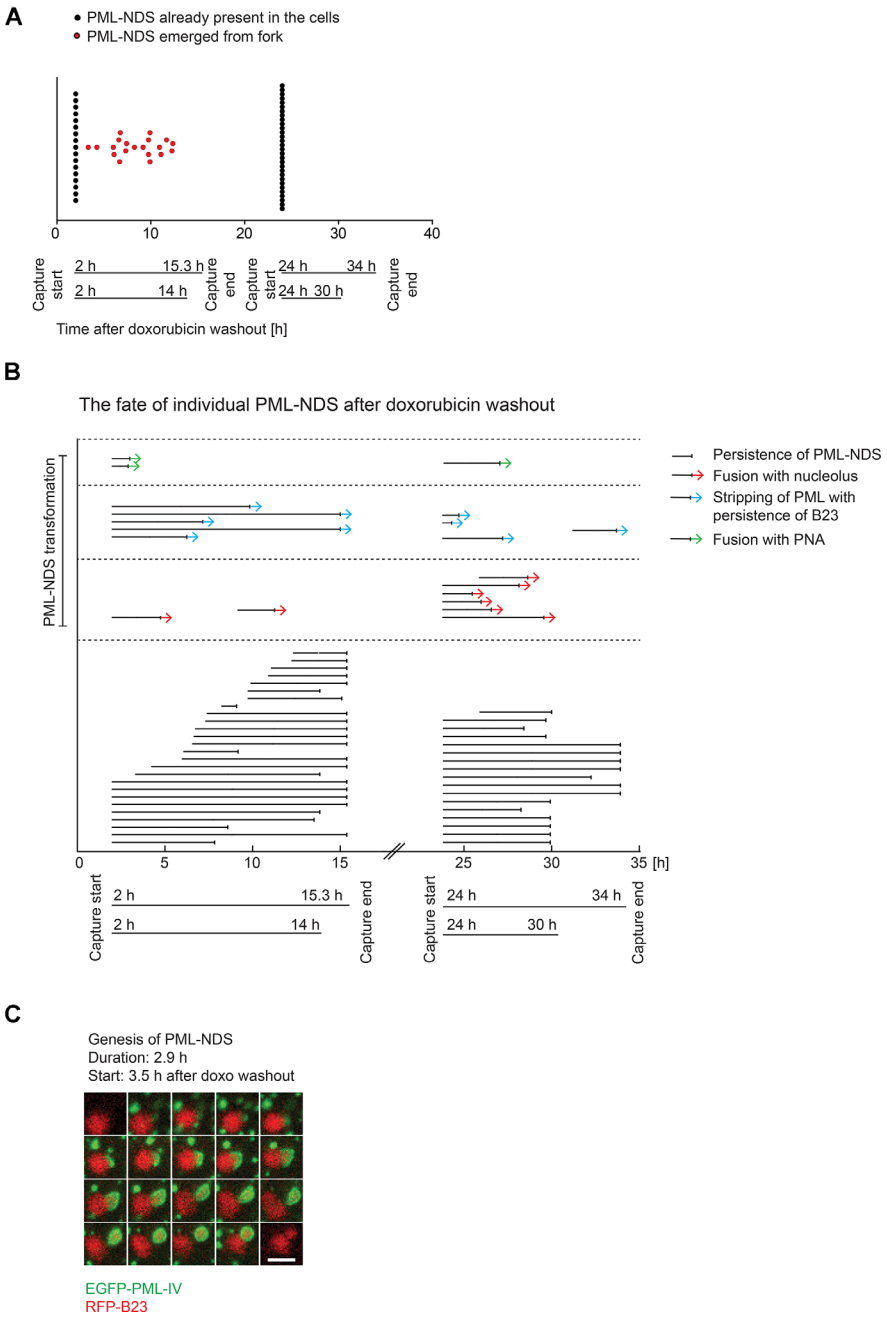


**Supplementary Figure 7. PML-NDS originate preferentially from PML-nucleolar forks in early time-points after doxorubicin removal.** (**A**) Quantitative analysis of the genesis of PML-NDS in RPE-1$^{hTERT}$ stably expressing EGFP-PML IV and RFP-B23 after the treatment with 0.75 μM doxorubicin and the drug removal. The appearance of PML-NDS was followed by time-lapse microscopy in two sequential sessions from two independent experiments after the drug removal (experiment I: 2–15 and 24–34 hours; experiment II: 2–14 and 24–30 hours). PML-NDS that were already present in the beginning of the observation are marked by black dots; PML-NDS that emerged from forks during the observation time are marked by red dots and placed on the time scale according to the time when they emerged. (**B**) The genesis, stability and destiny of individual PML-NDS was followed in two sequential sessions from two independent experiments after the drug removal (experiment I: 2–15 and 24–34 hours; experiment II: 2–14 and 24–30 hours). The life-time of individual PML NDS is represented by solid lines with different endings marking the fates of PML-NDS: black line segment mark, end of capture session or cell escape from the view field; green arrow, fusion of PML-NDS with fork/cap; blue arrow, loss of PML but with persistence of B23; and red arrow, fusion of PML-NDS with nucleolus. (**C**) Time-lapse microscopy of the nucleolus illustrating the formation of PML-NDS. Note on the right side of the nucleolus, the whole transmutation cycle of PNAs was captured, i.e. the genesis of PML-cap on the border of the nucleolus, its transition into PML-fork, and finally into PML-NDS. EGFP-PML IV is shown in green, RFP-B23 in red. The initiation of capturing and the length of recorded time are given for each type of transition. Bar, 4 μm.

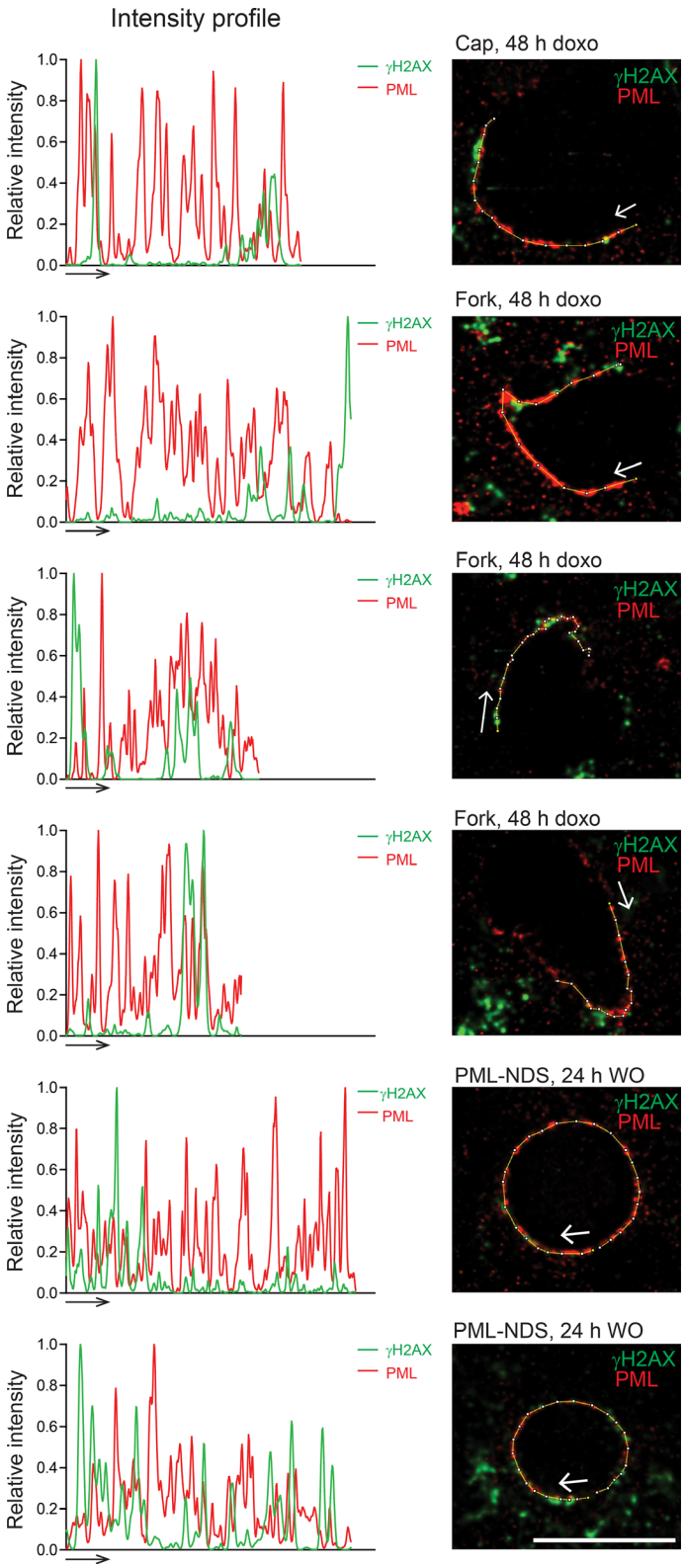


**Supplementary Figure 8. PNAs associate with γH2AX.** RPE-1$^{hTERT}$ were treated with 0.75 μM doxorubicin for 2 days; after that doxorubicin was removed and cells were further cultivated. Super-resolution STED microscopy images of cells at different time-points are shown, and intensity profiles of γH2AX signal (green) and PML signal (red) at the border of each PNA are presented. The white and black arrows show the direction of intensity profile. Bar, 4 μm.

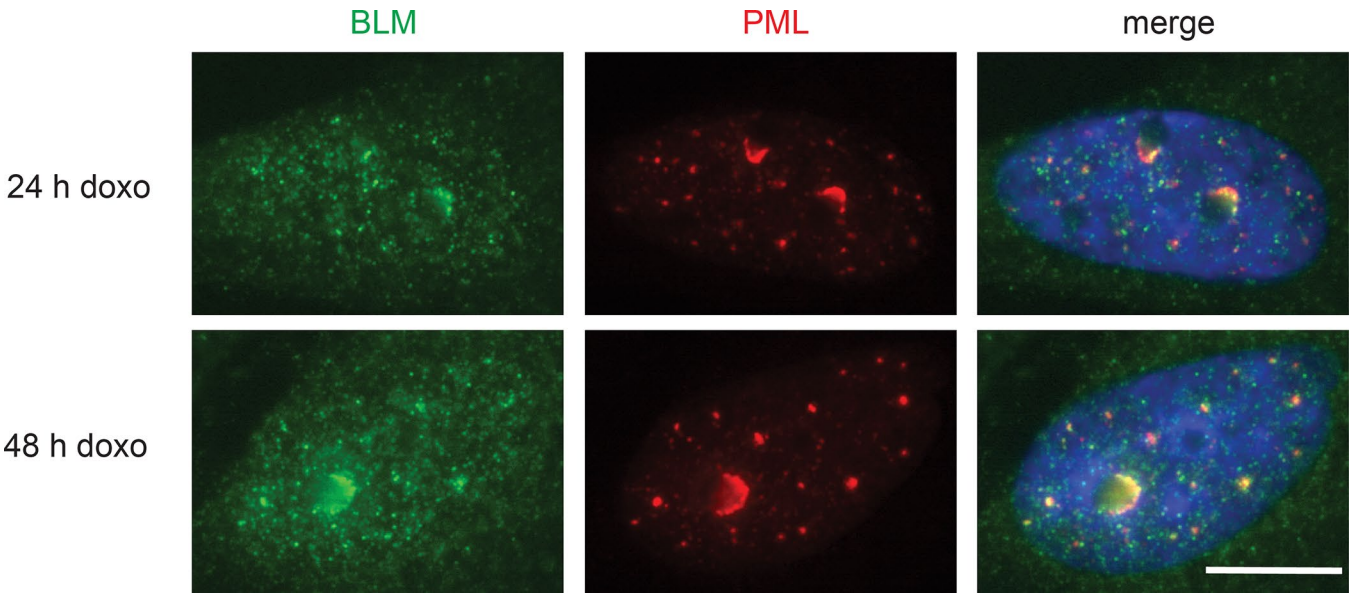


**Supplementary Figure 9. BLM localizes to PNAs.** RPE-1$^{hTERT}$ were treated with 0.75 μM doxorubicin, harvested after 1 and 2 days and stained for PML (green) and BLM (red). The nuclei were counterstained with DAPI. The images were captured with 63×/1.4 objective. Bar, 10 μM.

## Supplementary Videos

Please browse Full Text version to see the data of Supplementary Videos 1–17

**Supplementary Video 1. 3-D structure of cap shown in Figure 3A.** RPE-1$^{hTERT}$ expressing EGFP-PML IV were treated for 24 hours with doxorubicin and analyzed by live-cell SIM. "Volume" 3-D model was prepared from 28 layers using ImageJ 3D viewer plugin.

**Supplementary Video 2. 3-D structure of fork shown in Figure 3B.** RPE-1$^{hTERT}$ expressing EGFP-PML IV were treated for 24 hours with doxorubicin and analyzed by live-cell SIM. "Volume" 3-D model was prepared from 30 layers using ImageJ 3D viewer plugin.

**Supplementary Video 3. 3-D structure of circle shown in Figure 3C.** RPE-1$^{hTERT}$ expressing EGFP-PML IV were treated with doxorubicin for 24 hours and analyzed by live-cell SIM. "Volume" (left position) and "orthoslice" (right position) 3-D model was prepared from 54 layers using ImageJ 3D viewer plugin.

**Supplementary Video 4. Genesis of EGFP-PML IV cap#1 as shown in Figure 4A captured between 4.5 and 5.5 hours after doxorubicin addition.**

**Supplementary Video 5. Genesis of EGFP-PML IV cap#2 as shown in Figure 4A captured between 9.5 and 10.5 hours after doxorubicin addition.**

**Supplementary Video 6. Genesis of EGFP-PML IV cap#3 as shown in Figure 4A captured between 43 and 44 hours after doxorubicin addition.**

**Supplementary Video 7. Genesis of EGFP-PML IV cap#4 as shown in Figure 4A captured between 63 and 64 hours after doxorubicin addition.**

**Supplementary Video 8. Transition EGFP-PML IV "cap to fork" presented in Figure 4C captured between 36 and 44 hours after doxorubicin addition.**

**Supplementary Video 9. Transition EGFP-PML IV "cap to circle" presented in Figure 4C captured between 16 and 18 hours after doxorubicin addition.**

**Supplementary Video 10. Transition EGFP-PML IV "fork to circle" presented in Figure 4C captured between 34 and 40 hours after doxorubicin addition.**

**Supplementary Video 11. Transition EGFP-PML IV "circle to fork" presented in Figure 4C captured between 40 and 45 hours after doxorubicin addition.**

**Supplementary Video 12. Genesis of PML-NDS from fork presented in Figure 5A captured between 2 and 5.2 hours after doxorubicin washout.** EGFP-PML IV (green) and RFP-B23 (red).

**Supplementary Video 13. Persistence of PML-NDS presented in Figure 5C captured between 3.3 and 13.8 hours after doxorubicin washout.** EGFP-PML IV (green) and RFP-B23 (red).

**Supplementary Video 14. Fusion of PML-NDS with nucleolus presented in Figure 5D captured between 2.8 and 5.7 hours after doxorubicin washout.** EGFP-PML IV (green) and RFP-B23 (red).

**Supplementary Video 15. Stripping of PML from PML-NDS with persistence of B23 presented in Figure 5E captured between 27.8 and 32.3 hours after doxorubicin washout.** EGFP-PML IV (green) and RFP-B23 (red).

**Supplementary Video 16. Fusion of PML-NDS with fork-like PNA presented in Figure 5F captured between 12 and 14.6 hours after doxorubicin washout.** EGFP-PML IV (green) and RFP-B23 (red).

**Supplementary Video 17. Whole sequence of genesis of PML-NDS (cap – fork – PML-NDS) presented in Supplementary Figure 7C captured between 3.5 and 6.4 hours after doxorubicin washout.** EGFP-PML IV (green) and RFP-B23 (red).

# Casein kinase 2 regulates SUMO-mediated interaction of PML with nucleolus during topoisomerase and RNA polymerase I inhibition

Terezie Imrichova[1], Sona Hubackova[1], Alena Kucerova[1], Jan Kosla[1], Jiri Bartek[1,2*], Zdenek Hodny[1*] and Pavla Vasicova[1*]

[1]Department of Genome Integrity, Institute of Molecular Genetics of the Czech Academy of Sciences, Prague, Czech Republic

[2]Genome Integrity Unit, Danish Cancer Society Research Center, Copenhagen, Denmark, Copenhagen DK-2100, Denmark

[*]Correspondence to: Pavla Vasicova, PhD; Department of Genome Integrity,
Institute of Molecular Genetics ASCR, v.v.i., Videnska 1083, CZ 142 20 Prague 4,
Czech Republic; Tel: (420)-24106 3151, Fax: (420)-24106 2289; E-mail: vasicova@img.cas.cz Zdenek Hodny, MD, PhD E-mail: hodny@img.cas.cz and Jiri Bartek, MD, PhD; E-mail: jb@cancer.dk

**Introduction**

One of the factors that are recognized as the cause of aging and age-related diseases is cellular senescence [1, 2]. It is defined as an irreversible cell cycle arrest, induced by inhibitors of cyclin-dependent kinases that are activated upon persistent or perpetual DNA damage signaling. This kind of damage often evolves at telomeres, and telomeric loci are therefore commonly put into connection with an onset of senescence [3, 4]. However, recent evidence suggests that also ribosomal DNA (rDNA), given its repetitive nature, is difficult to repair and might serve as a source of long-term DNA damage that leads to development of senescence [5, 6].

The promyelocytic leukemia protein (PML) is a multifunctional protein that is known, above all, for its ability to form non-membrane nuclear compartments, called PML nuclear bodies (PML NBs) [7]. The function of PML NBs spans from anti-viral response and DNA damage repair, through tumor suppression, cell cycle inhibition and senescence, to transcription regulation and post-translational modifications of proteins. From post-translational modifications, SUMOylation is especially important and characteristic for this compartment, as it seems that most constituent proteins of PML bodies, including PML itself, contain either residues that can be SUMOylated or SUMO-interacting motif (SIM) and the SUMO-SIM based interactions are the force that holds PML bodies together [8-10].

Importantly, PML comprises seven splicing variants, resulting from alternative splicing of the PML gene. The PML gene contains nine exons, however, only four of them coding N-terminal part are present in all seven isoforms. The C-terminus varies among the isoforms and is therefore responsible for the isoform-specific PML properties and functions [11, 12]. The isoforms I and IV, most examined by us in this study, share seven whole exons and part of the exon 8. In PML I, these exons are followed by exon 9, while in PML IV, only short exon 8b follows. Exon 8b seems to be functionally important, as it confers PML IV many specific functions, including interaction with selected proteins, recruitment and activation of p53 in PML NBs, enhancement of apoptosis and senescence following various stimuli, destabilization of c-Myc or protection against several viral infections (reviewed in [11]).

Another important exon of PML is the exon 7a. It is present in PML isoforms I - V and it contains two important domains – the SUMO-interacting motif [8] and a target sequence for casein kinase 2 (CK2) (CK2 phospho-motif;[13]). The SIM is important for non-covalent binding of PML to SUMOylated partner proteins and phosphorylation of the adjacent CK2 phospho-motif facilitates this process [14-16]. Interestingly, SIM is dispensable for PML NBs formation [8, 17], however, it is necessary for attraction of partner proteins to PML NBs [8]. Another role of SIM and CK2 phospho-motif is in the process of PML degradation, as it has been shown that PML variant lacking SIM is resistant to $A_2O_3$-activated degradation [14, 16] and CK2-mediated phosphorylation promotes PML degradation after osmotic shock, anisomycin, or UV radiation [18].

Actively transcribed rDNA genes are the core of a non-membrane compartment, the nucleolus. The nucleolus is not only the site of rDNA transcription and ribosome biogenesis but also an important hub of cellular stress response. More specifically, various stress stimuli are able to perturb ribosome biogenesis, which is followed by activation of multiple nucleolus-associated pathways that halt the cell cycle in a p53-dependent or -independent way [19-22]. A direct damage of rDNA is one of those stimuli. rDNA is prone to DSBs, given its high transcription rate and

resulting propensity to frequent collisions with other DNA-related processes [23, 24]. As torsional stress is inevitable side effect of the transcription process, the proper function of topoisomerases is vital for error-less transcription, even when a collision with other DNA-binding machineries does not occur (reviewed in [25]). In case of DSB, there are two main pathways for DSB repair, non-homologous end joining (NHEJ) and homologous recombination (HR). It has been shown that proteins of both pathways are localized to the nucleolar caps that form on the nucleolar border following rDNA damage and contain segregated rDNA [26-28], so probably both pathways can participate on rDNA repair upon certain conditions. Regarding the role of SUMO in the rDNA integrity, it has been found that several proteins that maintain rDNA, including topo I, topo II, condensins and cohesins ar SUMOylated in yeast [29, 30] and also many proteins of HR pathway are subject to SUMOylation, including RPA [31], ATRIP [32] or BRCA1 [33].

In this context, it is intriguing that PML associates with nucleolar compartment, forming structures termed PML nucleolar associations (PNAs; [74]). PNAs have been documented in replicatively senescent human mesenchymal stem cells (hMSC) [34] and human fibroblasts [35, 36], in doxorubicin-treated human and mouse fibroblasts [37] and in actinomycin D (AMD)-treated hMSC and human fibroblasts [34]. Apart from that, PML has been shown to translocate into the nucleolus after AMD treatment in HeLa cells [38]; upon proteasome inhibition in MCF-7, HeLa and IB-4 cells [39]; and after doxorubicin, gamma-radiation or proteasome inhibition when ectopically expressed in MEFs [35].

Doxorubicin is a DNA intercalator [40, 41] and an inhibitor of topoisomerase 2 [42], it is involved in generation of reactive oxygen species [43] and causes histone eviction [44], all of which leads to DNA damage. Furthermore, it induces nucleolar stress and inhibits RNA polymerase I (RNAP I) transcription [45]. AMD is a DNA intercalator as well that binds preferentially GC-rich DNA segments and thus, in low concentrations, specifically inhibits RNAP I transcription from GC-rich rDNA arrays. By inhibiting rDNA transcription, AMD effectively induces ribosomal stress and activates p53 [45, 46], while, surprisingly, also several players of the DNA damage checkpoint pathway are involved in the AMD-mediated p53 activation, suggesting that the pathways are somehow intertwined [20, 47].

Recently, live time lapse cell imaging and super-resolution microscopy revealed that PNAs that were induced by doxorubicin treatment are formed by several subsequent transitions reflecting the activity of RNAP I [74]. The last stage of PNAs, termed PML nucleoli-derived structures (PML-NDS), are formed during the recovery of RNAP I activity. These structures are usually placed next to nucleolus and accumulate some nuclear and nucleolar proteins [74]. Even these PNAs transmutations in their early phase co-localize with markers of DNA damage. The exact function of these structures is not known, however, considering that PML and PML NBs have been implicated in DNA repair by HR [48, 49] and that DNA damage within rDNA locus has been associated with cellular senescence, it is not unlikely that PML might be involved in HR-based repair of complicated or complex rDNA damage.

In present work, we managed to show that the inhibition of RNAP I together with the inhibition or downregulation of topoisomerases are necessary for PNAs formation, while the process is independent of p53. Furthermore, we identified two PML domains – exon 8b and the phospho-SIM domain of exon 7a – as being responsible for the interaction. Finally, we showed that SUMOylated rDNA is present in all stages of PNAs and might therefore be the signal that guides PML to the nucleolus. Together with the former notion that the late stages of PNAs persist for

long time periods in senescent cells, this further supports our previous suggestion that unresolved issues on rDNA could be intimately linked to senescence induction and maintenance.

## Results

### *Simultaneous inhibition of RNAP I and topoisomerases triggers an association of PML with nucleolus*

To reveal a nature of a signal activating the association of PML with nucleolus, we exposed human telomerase-immortalized retinal pigment epithelial cells (RPE-1$^{hTERT}$) to various classes of compounds and treatments listed in Table 1 including inductors of DNA damage or ribosomal and replicative stress, topoisomerase (Topo) and RNAP I inhibitors, DNA crosslinkers and DNA G-quadruplex stabilizers. 48 hours after treatments, we followed a segregation of PAF49 subunit of RNAP I as an indicator of RNAP I inhibition together with quantitative assessment of the PNAs ([74]; see Figure 1A for their classification) using indirect fluorescence microscopy. On top of that, the level of p53 protein and DNA damage marker serine 139 phosphorylated histone H2AX (γH2A.X; [50]) was followed to control an activation of DNA damage response (DDR) for each treatment (Supplementary Figure 1 and 2A). As shown in Figure 1B, this analysis uncovered that both Topo and RNAP I inhibitors are the strongest inducers of PNAs formation, whereas DNA damaging agents and replicative stressors such as ionizing radiation (IR; 10 Gy), 5-bromo-2'-deoxyuridine (BrdU), aphidicolin and 5-fluorouracil (5-FU) induced PNAs substantially weekly in less than 1% of cells. The rest of compounds, i.e. proteasome inhibitor MG-132, cyclin-dependent kinase inhibitor roscovitine, ribonucleotide reductase inhibitor hydroxyurea (HU), quadruplex stabilizer pyridostatin, and DNA damaging cytokine IFNγ did not induce PNAs at all. Altogether, these results indicate that the association of PML with nucleolus resulted predominantly from processes related to the inhibition of topoisomerases or RNAP I. DNA damage induced by IR, inhibition of pre-rRNA processing, replicative stress, stabilization of DNA G-quadruplexes or induction of PML expression by IFNγ were no or weak signals to induce PNAs. Further analysis of the data revealed that the propensity for PNAs formation by compounds referred to inhibit Topo correlated in parallel with their ability to inhibit RNAP I (Figure 1B and 1C). Note, the application of topoisomerase inhibitors camptothecin, doxorubicin, topotecan and aclarubicin resulted in simultaneous RNAP I inhibition (PAF49 segregation) nearly in each nucleolus and the proportion of cells with presence of PNAs was the highest observed (27%, 22%, 13% and 12%, respectively). On the other hand, etoposide, despite its effect on Top2a protein degradation and DNA damaging activity (Supplementary Figure 1 and 2B), did induce formation of PNAs only in 2% cells. This weak effect of etoposide on PNAs formation can be accounted for by low inhibition of RNAP I (note, like in untreated cells, the PAF49 was equally distributed in most nucleoli of cells without marks of segregation), the findings underscoring the role of RNAP I inhibition in formation of the PNAs. It should be emphasized that RNAP I inhibition either by AMD or RNAP I inhibitor CX-5461 was accompanied also by a decline of Top2a protein levels (Figure 1B and Supplementary Figure 2B).

The requirement for simultaneous inhibition of both RNAP I and topoisomerase activity to reach the high formation of PNAs was further underscored by treatment with oxaliplatin. This compound, primarily designated as a DNA cross-linker, showed a combined effect on the RNAP I inhibition and Top2a decline and, indeed, high number of PNAs (> 10%) after oxaliplatin treatment was detected. Collectively, these findings indicate that simultaneous defects in Topo and RNAP I activities potentiate the signal for formation of PNAs.

Next, to exclude well-known non-specific pleiotropic effects of topoisomerase inhibitors and to test whether the signal for association of the PML with nucleolus is directly linked to abrogation of topoisomerase function we downregulated Top1, Top2a and Top2b using RNA interference (RNAi). Downregulation of Top1 and Top2a but not Top2b induced the formation of PNAs (Figure 2A) indicating the formation of PNAs is related to a loss of specific topoisomerase function. Three days after knockdown of Top1 and Top2a about 31% and 12% of cells with the PNAs were identified, respectively. Importantly, knockdown of both Top1 and Top2a topoisomerases resulted in gradual inhibition of RNAP I activity. Six days after Top1 downregulation, the RNAP I in many nucleoli was segregated, and at this time-point the number of PNAs was much higher than earlier when the RNAP I was still active. These results underscored again that topoisomerase deficiency is causal for formation of PNAs and that long term inhibition of Topo results also in the inhibition of RNAP I, and combination of these two conditions induced PNAs most effectively.

Several of the treatments that caused high number of PNAs are known to interfere with RNAP I transcription. Therefore, we explored next whether the interference with running rDNA transcription, and resulting topological problems, might be the reason for generation of PNAs. For this purpose, we inhibited RNAP I by AMD or CX-5461 prior to the addition of doxorubicin or the knock-down of Top1. The effectiveness of RNAP I inhibition at the time of doxorubicin addition was estimated by 5-FU incorporation (Supplementary Figure 3). Notably, the cessation of pre-rRNA transcription before the inhibition or downregulation of Topo caused the appearance of higher number of cells with the PNAs when compared to doxorubicin or esiTop1 treatment alone (Figure 3A-C). These findings indicated that the ongoing pre-rRNA transcription was not necessary for the induction of PNAs by the Topo inhibitor doxorubicin or esiTop1. Furthermore, these observations pointed to the notion that Topo can be involved in some process(es) occurring after RNAP I inhibition.

Altogether, our data indicate that the defect in topoisomerase activity after the inhibition of RNAP I formed the signal for association of PML with nucleolus.

*Genesis of PNAs is independent of p53-mediated ribosomal stress response*

As expected, the formation of the PNAs induced by inhibition of the RNAP I and topoisomerases was associated with stabilization of p53 (Supplementary Figure 2A). To test, whether the genesis of the PNAs depends on p53 function, we employed RPE1$^{hTERT}$ cells with complete CRISPR-CAS9-mediated knock-out of p53 (p53$^{-/-}$ RPE-1$^{hTERT}$) and compared the formation of the PNAs to p53 wild type cells after the depletion of Top1 or after the exposure to doxorubicin. Note, to reestablish doxorubicin-induced expression of the PML, which we revealed to be p53-dependent in RPE-1$^{hTERT}$ cells [51], a pretreatment of cells with IFNγ to substitute p53-driven PML expression

was utilized [52]. As doxorubicin induced the formation of PNAs even in IFNγ-treated p53-deficient cells we could conclude that functional p53 is necessary only for doxorubicin-induced PML transcription but not for the genesis of PML nucleolar associations (Supplementary Figure 4 A, B).

*Cooperative effect of PML exon 8b and phospho-SIM domain (exon 7a) in PML interaction with nucleolus*

To identify domains responsible for association of PML with nucleolus induced by doxorubicin we followed at first the localization of fluorescently tagged PML isoforms PML I-GFP, PML IV-GFP, PML V-GFP and PML VI-GFP in RPE-1$^{hTERT}$ cells carrying complete CRISPR-CAS9-mediated knock-out of PML (PML$^{-/-}$ RPE-1$^{hTERT}$; [48]) after their exposure to doxorubicin. PML isoforms differ from each other by C-terminal part. Only PML IV and PML I isoforms were capable to associate with nucleolus when expressed individually, mapping the putative interacting motifs to the C-terminus comprising of exon 8a, 8b and 9 of the PML I and the PML IV (Figure 4A). Hence, we prepared a set of PML IV-GFP deletion constructs and analysed their localization in the PML-/- RPE-1$^{hTERT}$ cells treated with doxorubicin (Figure 4B). This analysis revealed two regions of the PML IV which were involved in the doxorubicin-induced association of the PML with the nucleolus. The first one spanning the amino acids 560 – 570 is a part of exon 7a and can be phosphorylated with CK2 on serines 560, 561, 562 and 565 ('CK2 target'; [13]). After deletion of this region the number of cells with the PNAs dropped by 70% relatively to the PML IV wild type cells. The second region spanning the amino acids 621 to 633 of exon 8b is present only in the PML IV isoform. After deletion of this motif 80% decrease of cells with the PNAs was identified. As soon as both domains were deleted simultaneously (PML IV Δ560 – 633 and PML IV Δ560 – 570 plus Δ621 – 633), no cells with the PNAs were detected (Figure 4B). The role of both PML IV domains in formation of the PNAs was further confirmed by the deletion of exon 8a comprising amino acids 571 to 619 (PML IV Δ571 – 619) linking both domains, i.e. only exon 8b and the 'CK2 target' were present and the interlinking sequence of exon 8a was deleted. The ability of the PML IV Δ571 – 619 cells to form the PNAs was mostly retained as the number of cells with the PNAs was only slightly lower (70%) compared to the WT form indicating the exon 8a is dispensable for the formation of PNAs.
The role of the CK2 target domain of the PML I isoform for formation of the PNAs was also confirmed (Figure 4C). Deletion of this motif in the PML I caused that only 2% of cells relatively to the PML IV WT (and 8% relatively to the PML I) contained the PNAs pointing to a major contribution of this domain to the formation of the PNAs by the PML I isoform. However, the residual activity indicated a presence of weak additional nucleolus-interacting motif in the PML I isoform. A comparison of the PML I and PML IV ability to form the PNAs revealed that the PML IV formed the PNAs with four times higher efficiency underscoring the dominant role of the exon 8b in this process.
Altogether, the PML CK2 target domain (the part of exon 7a) and the exon 8b are the main determinants responsible for stress-induced interaction of the PML with the nucleolus.

*The role of CK2 activity and SUMO interaction motif in the PML nucleolar interaction*

Exon 7a of the PML comprises SUMO interaction motif (SIM) and the CK2 target domain (Figure 4A). Given the phosphorylation status of the CK2 target domain regulates an interaction of neighbouring SIM with SUMO-modified proteins, we investigated whether the phosphorylation of the CK2 target domain and intact SIM could be involved in control of PML interaction with the nucleolus. For this purpose we prepared a set of phosphomimetic and unphosphorable mutants of the CK2 target domain and mutants of the SIM.

As is shown in Figure 4D, unphosphorable mutant of the CK2 target domain formed low number of cells with the PNAs comparable to the CK2 target deletion indicating the phosphorylation of the CK2 target domain facilitates the interaction of the PML with the nucleolus. Moreover, the mutation or deletion of the SIM caused a reduction in the PNAs formation in similar extent as the unphosphorable mutant of CK2 implying that the SUMO-SIM interaction is involved in the PNAs formation and that the phosphorylation of the neighbouring CK2 target domain positively regulates this process.

To test whether the CK2 kinase regulates the formation of the PNAs we utilized a chemical or RNAi-mediated inhibition of the CK2 activity. As shown in Figure 4E and F, both the inhibition of the CK2 by a CK2 inhibitor CX-4945 and RNAi-downregulation of a regulatory subunit CK2β (see Supplementary Figure 5A and B for potency of CK2 inactivation evaluated as global changes in phosphorylation of CK2 substrate and Supplementary Figure 5C for the effectiveness of the CK2 knock-down) resulted in the significant reduction of the PNAs formation. Note, the knock-down of catalytic subunit of CK2 (CK2α) did not have a significant effect on a global phosphorylation pattern of the CK2 substrate and the occurrence of the PNAs even though the level of CK2α protein was significantly reduced (Supplementary Figure 5B and C).

Collectively, these findings indicate that the PML CK2 target domain/SIM (exon 7a) is functionally involved in the regulation of the PML nuclear interaction. Our data also suggests that the phosphorylation of exon7a by the CK2 controls the interaction of the SIM with SUMOylated interacting partners of the PML at nucleolar interface. Coordinated activity of exon 7a and exon 8b of the PML IV is responsible for high frequency of interaction of this PML isoform with the nucleolus under specific stress conditions.

Altogether, our data indicate that the interaction of PML with the nucleolus is mediated by exon 8b being present only in PML IV and SIM that is positively regulated with phosphorylation of CK2 target. We can also suppose that protein that guide PML towards the nucleolus is SUMOylated.

*p14ARF is not necessary for PML nucleolar interaction*

Given that PML region coded by exon 8b can interact with p14ARF [53] and this interaction can be responsible for interaction of the PML with the nucleolus, we analysed next the ARF expression in control and doxorubicin-treated RPE-1$^{hTERT}$ cells. However, no p14ARF transcript and protein levels were detected both in control and doxorubicin-treated cells (Supplementary Figure 6A and B) indicating that the relocalization of the PML to the surface of nucleolus in RPE-1$^{hTERT}$ is not dependent on the presence of the p14ARF.

*PML associates with rDNA on the nucleolar surface*

As the segregation of the nucleoli is linked to the PML localisation onto the nucleolar border, we asked next whether a segregated rDNA is in close contact with the PNAs employing stimulated depletion microscopy (STED) of RPE-1$^{hTERT}$ treated with doxorubicin. The co-localization of the PML and rDNA was followed using immunofluorescence-in situ hybridisation (immuno-FISH) 24 and 48 hours of doxorubicin treatment and 6 hours after drug removal. As is shown in Figure 5, we found that at least small portion of the rDNA co-localized with the PML in most analysed nucleoli, indicating that some rDNA loci tend to accumulate in the close proximity of the PNAs. The mean size of contact between the rDNA and PML was lower in the PML-capped nucleoli but increased in later stage represented by fork-shaped PNAs, suggesting that rDNA is gradually enclosed by the PML moiety. In the newly formed PML-NDS (6 hours after drug washout), the co-localization of rDNA with PML-NDs shell decreased (Figure 5A), but was localized inside the structure instead. Importantly, concerning the fork-like structures (Figure 5C), the fraction of total rDNA accumulated in the tip of all analysed PML forks, the site where the PML-NDS were originating, i.e. during the pre-rRNA transcription recovery [74]. Moreover, we observed that there was a border formed by the DNA (DAPI positive region; Figure 5D) that separated the PML-NDS compartment and the original nucleolus. This border was probably formed in later stages of fork, as we detected this separation from the nucleolus also in several forks (Figure 5D).
Our findings indicate the dynamic relationship between PNAs and rDNA after doxorubicin-induced stress. Part of rDNA relocalized to specific type of PNAs containing rDNA-processing proteins, indicating that the PNAs are involved in sequestration and processing of specific rDNA loci.

*The SUMO-1 signal is present on rDNA following doxorubicin treatment*

As our results pointed to the involvement of the SIM domain of PML in nucleolar interaction, we wanted to estimate whether rDNA or rDNA-binding proteins might be SUMOylated after treatment that leads to PNAs formation. RPE-1 $^{hTERT}$ PML$^{+/+}$ cells were treated with doxorubicin and immuno-FISH with the rDNA probe and an anti-SUMO-1 antibody was performed in early time-points after treatment, when the presence of PML localization signal on the nucleolus is expected. The cells were imaged with a confocal microscope and analysed for the rate of co-localization between rDNA and the SUMO-1 signal. We saw an increase in SUMO-1-rDNA co-localization in RPE-1$^{hTERT}$ PML$^{+/+}$ cells after doxorubicin treatment (Figure 6). However, as majority of PML is SUMOylated, it is not clear whether the detected SUMO-1 signal comes from the SUMO bound to rDNA/nucleolar proteins or from the SUMO bound to nucleolar PML. Therefore, we performed the same analysis in RPE-1$^{hTERT}$ PML$^{-/-}$ cells, assuming that the rDNA-based processes would progress in the same way in PML$^{+/+}$ and in PML$^{-/-}$ cells. And indeed, we observed slight increase in SUMO-1 signal on rDNA also in PML$^{-/-}$ cells (Figure 6), suggesting that rDNA is SUMOylated in response to doxorubicin and this modification might be at least partly responsible for PML nucleolar targeting.

**Discussion**

In our previous article, we identified dynamics and 3D structure of PML nucleolar associations (PNAs) that form after doxorubicin treatment. As PNAs co-localized with DNA damage markers, we implied that these structures may be involved in repair or sorting of damaged rDNA [74]. To better understand these associations, we present here 1) detailed analysis of nature of PNAs induction; 2) analysis of PML domains that are involved in PNAs formation; and 3) discussion of possible role of rDNA in PNAs genesis and function.
We found that the highest probability for PNAs formation was after treatments that cause simultaneous inhibition of RNAP I and an inhibition and downregulation of topoisomerases. Moreover, our results indicate that the signal for PML association with nucleolus is amplified when the inhibition of RNAP I preceds the inhibition/downregulation of topoisomerases, excluding the hypothesis that deficiency of topoisomerases during the pre-rRNA transcription may be the source of damage/signal for PNAs genesis. We found that an exon 8b and the SUMO-interacting motif of PML are involved in the association with the nucleolus. We proved that a portion of rDNA always co-localizes with PNAs.

As we showed previously, the doxorubicin-induced PNAs co-localize with γH2A.X, an early marker of DNA damage (DNA double-strand breaks) and we proposed that PNAs may be involved in repair of damaged rDNA or in sorting of damaged/irreparable rDNA/DNA out of the nucleolus. In this study, we show that there is no clear correlation between the presence of γH2A.X and PNAs occurrence: some treatments (e.g., etoposide and IR) induced γH2A.X foci and at the same time did not lead to formation of high number of PNAs, whereas other treatments (e.g. oxaliplatin and AMD) caused formation of higher number of PNAs compared to etoposide and IR, though they induced no or only a few γH2A.X foci. Provided the assumption that formation of PNAs is dependent on the presence of damage in rDNA region that is buried inside the nucleolus, we could suppose that rDNA has different sensitivity to applied treatments. E.g., both IR and doxorubicin are inducing robust DNA damage but only doxorubicin is able to cause the damage of rDNA. Alternatively, both treatments are able to damage rDNA but after doxorubicin treatment the specific rDNA damage is hardly reparable or irreparable at all. Notably, we were not able to detect γH2A.X in all PNAs formed after AMD treatment (data not shown). We consider a possibility that after some forms of DNA damage the γH2A.X signal is too transient or too weak to be detected. For example, it is known that the classical γH2A.X foci are in fact clusters of several nano-foci. However, not all nano-foci form clusters and then they are undetectable by conventional microscopy methods [54]. Also, it has to be taken into account that the DNA damage signalling inside the nucleolus utilizes different histone marks and signalling cascades than in the rest of the nucleus [55, 56]. In case of CRISPR/Cas9-mediated DSBs, γH2A.X mark is imposed on rDNA as soon as it forms nucleolar cap [56] but the process is much less described for other types and sources of nucleolar DNA damage. Finally, it is possible that some other type(s) of DNA damage, different from double strand break but marked by γH2A.X (or absence of DNA damage), may all be present in subsets of PNAs. In such case, we assume that other DNA-related processes could be responsible for PNAs formation, while only in specific cases (including doxorubicin treatment) they are accompanied by DNA double strand breaks and γH2A.X foci formation. As our

results point to the fact that the highest propensity for PNAs formation is after those treatments when the inhibition of RNAP I precedes the deficiency or inhibition of topoisomerases, we can speculate that the damage or other unidentified defects of rDNA are caused by deficiency of topoisomerases during the formation of nucleolar cap when the rDNA is pulled out from interior of the nucleolus towards its surface.

One of the processes that are related to the nucleolus after various treatments, and might but do not have to involve DNA damage [46], is nucleolar stress. Importantly, both chemicals that have been previously referred to PNAs formation, i.e. doxorubicin and AMD [34, 37], are also known to cause nucleolar stress. Multiple chemicals have been reported to induce nucleolar stress by disrupting individual steps of ribosome biogenesis [45]. We tested several of them, namely oxaliplatin, AMD and doxorubicin that inhibit rDNA transcription; camptothecin and roscovitin that inhibit early rRNA processing; and 5-FU and etoposide that inhibit late rRNA processing. However, the response ranged from very high (camptothecin, > 25%) to no (roscovitine, MG132, both 0%) number of PNAs, so we concluded that nucleolar stress in general is not responsible for PNAs formation but only its specific form, the inhibition of RNAP I is able to trigger the association of PML with nucleolus.

Our results indicate that most of the tested inhibitors of topoisomerases and even the downregulation of Top1 and Top2a are able to induce a high amount of PNAs. One would incline to interpret these results in a way that the sole inhibition of topoisomerases causes defects that are the main signal for PNAs evolving. Nevertheless, when etoposide, the Top2a inhibitor was applied, only about 2% of cells contained PML-NDS, a subtype of PNAs that is associated with non-segregated nucleolus (Figure 1A; [34][74]). As is shown in Supplementary Figure 1A, these cells were γH2A.X-positive and Top2a was degraded, which all proves the presence of topological stress, resulting in DNA damage and cell cycle arrest. The only difference between etoposide and the other used topoisomerase inhibitors (doxorubicin, camptothecin and topotecan) was that the applied concentration of etoposide was unable to inhibit RNAP I. The preserved activity of RNAP I upon application of low concentration of topoisomerase inhibitors was observed when various concentrations of Top1 inhibitors, camptothecin and topotecan (data not shown), and Top2 inhibitor doxorubicin [74] were tested. Notably, low concentrations were able to induce DNA damage and cell cycle arrest, but the long-term inhibition of RNAP I and higher presence of PNAs were not observed. These data indicate that the mere inhibition of topoisomerases without simultaneous inhibition of RNAP I is not sufficient to induce PNAs. Thus, the application of higher concentrations of Topo inhibitors might cause some other forms of DNA damage. For instance, doxorubicin interferes with Top2 cleavage complex by inhibiting DNA re-ligation, but in higher concentration it is also able to intercalate the DNA [42], so the DNA damage may be caused not only by inhibition of Top2 but also by its intercalation. In addition, the intercalation into rDNA region might induce the inhibition of RNAP I. Similarly, camptothecin and topotecan are referred as S-phase-specific anticancer drugs [57, 58] but it was described that at higher concentrations they might be toxic also for non-dividing cells by interfering with transcription [59, 60]. Importantly, the rDNA damage induced by high dose of camptothecin was reported [61]. Thus, only the drug concentration that is able to inhibit not only the Topo activity but also the pre-rRNA transcription, is the prerequisite for PNAs formation.

The connection between the topological stress, RNAP I activity and the probability of PNAs formation, was visible after the knockdown of Top1. In the first days after siRNA-mediated Top1 downregulation, RNAP I was not segregated and the variability and number of PNAs was relatively low; whereas it increased remarkably in the next days after Top1 downregulation, when RNAP I become segregated (Figure 2C). Hence, RNAP I segregation seems to be the key determinant of PNAs genesis in the presence of topological stress; however, it is obviously not an exclusive stimulus, as treatment with a specific RNAP I inhibitor, CX-5461 and actinomycin D induced much lower number of PNAs than those Topo inhibitors that simultaneously inhibited RNAP I.

One of the most unexpected results was the observation that the probability for PNAs formation significantly increased when the inhibition of RNAP I preceded the inhibition or downregulation of topoisomerases. rDNA, as a region that is extensively transcribed, requires a high activity of topoisomerases [62, 63]. One would expect that the lack of Topo functions upon strong pre-rRNA transcription could cause topological problems that lead to RNAP I inhibition and rDNA damage followed by PNAs formation. Oppositely, when the transcription of pre-rRNA is silenced, the defect in Topo activity would not cause such a robust rDNA damage. During testing of this hypothesis, we inhibited RNAP I by AMD or CX-5461 before the treatment with Top2 inhibitor doxorubicin, or downregulation of Top1. Surprisingly, the number of PNAs in this scenario did not decrease but actually increased, implying that ongoing transcription is not required for PNAs formation and, furthermore, that RNAP I segregation is not only a consequence of topological stress but also one of the prerequisites for PNAs formation. This is further supported by the fact that the pre-treatment with RNAP I inhibitor CX-5461 increased the amount of PNAs in cells treated with 0.375 μM doxorubicin, i.e. the concentration that itself does not lead to segregation of RNAP I; in contrast to cells treated with 0.75 μM doxorubicin, as this concentration already inhibits RNAP I and thus the CX-5461 has no additional effect (Figure 3B). Interestingly, not only the number but also the type of PNAs changed after the pre-treatment with RNAP I inhibitors, supporting our previous notion that the type of PNAs is linked to the activity state of the nucleolus [74]. From our observations we concluded that the main signal for PNAs evolution is primarily generated when RNAP I inhibition occurs before Topo deficiency or inhibition.

These results may be explained in two ways.

First, our observations may indicate a possible role of topoisomerases during formation of segregated nucleolus, when the transcribed genes of rDNA are pulled from the interior of the nucleolus towards the surface. The mechanism of this rDNA movement is still unresolved. How the topoisomerases can be involved in this process and what form of rDNA damage may their deficiency cause must be elucidated as well.

The second explanation may comprise following observations: On the example of Top2a inhibition with etoposide it has been shown recently that there are two ways how to resolve the trapped complexes of Topo and DNA that form after Topo poisons. Either topoisomerase is removed from DNA and the remaining DNA break is quickly repaired by NHEJ; or the enzyme cannot be removed, in which case the more complicated HR takes place. Importantly, the decision between the two pathways largely relies on the ongoing transcription, as the transcribed loci more frequently proceed into DSBs, followed by NHEJ [64]. PML is known to participate in DNA repair by HR [48, 49], therefore, it is possible that it is involved in the decision process or directly in the HR. This would be in agreement

with our observation that RNAP I stalling contributes to PNAs genesis, as the absence of transcription would shift the balance between the repair pathways more towards HR and hence towards PML involvement. Moreover, the transcription in general is needed for an error-free NHEJ [65], therefore, RNAP I inhibition could theoretically favour HR before NHEJ even without Topo-DNA complex formation. Furthermore, HR at rDNA loci is known to occur at the outer part of the nucleolus [66]; and indeed, we see the formation of nucleolar cap and so rDNA segregation and translocation to the nucleolar periphery during the treatments that cause high number of PNAs (Figure 1C). Finally, γH2A.X signalling is not necessary for HR (reviewed in [67]), which makes this hypothesis even more plausible.

We identified two domains necessary for PML interaction with nucleolus after doxorubicin treatment: exon 8b and phospho-SIM domain, coded by exon 7a. The exon 8b of PML has been described to interact with p14ARF and this interaction was essential for the induction of cellular senescence [53]. As most of the treatments inducing the PNAs are also inductors of senescence, we tested the role of p14ARF in the interaction of PML with the nucleolus. Surprisingly, no p14ARF transcript or protein was detectable in RPE-1$^{hTERT}$ cells, with or without doxorubicin treatment. Obviously, p14ARF is not necessary for PML nucleolar localization. Similar observation was made in p14ARF$^{-/-}$ MEF cells [37]. Therefore, another protein probably interacts with exon 8b at the nucleolar periphery and we have been currently employing several methods to find this PML binding partner.

Another domain, identified by us as necessary for PML nucleolar localization, is exon 7a, more specifically its SIM and neighbouring CK2-phosphorylated motif, the phosphorylation status of which regulates the interaction of SIM with SUMOylated proteins [15]. Importantly, the deletion of the SIM domain did not impair its localization to PML nuclear bodies ([8], our observation), indicating that it is mainly required for the interaction of PML with other proteins and not for the PML multimerization. As phosphorylation of the CK2 motif regulates its SIM-mediated PML interactions [15], we next examined the role of CK2 in PNAs formation. Indeed, CK2 inhibition or downregulation lead to substantial decrease of PNAs, while it had no effect on PML levels, even though CK2-dependent PML degradation has been reported previously [13, 68]. This discrepancy might be accounted for by the fact that, in contrast to the previous studies, we performed our experiments in a non-cancerous cell line, while a clear difference between tumour and non-tumour cell lines in terms of CK2 regulation [69] and PNAs formation [34] has been described previously. Furthermore, serine 565 of PML has been identified as the most important residue for CK2-mediated PML degradation [13], while in our analysis, serines 560 – 562 showed to be more important for PML nucleolar interaction. Notably, our results differ from previously published observations by Condemine et al. [35], as according that work the association with nucleolus is dependent mainly on exon 9 of PML I isoform but our results did not confirm this observation (Figure 3C). Notably, the SIM domain is presented by the authors as inhibitiory for the PNAs formation, but our results point to the opposite function. This contradictory results can be explained by the use of GFP-fused fragments of human PML that do not necessarily have to reflect the behaviour of the full-length isoforms (e.g., the fragments localized to the nucleolus without additional treatment, which normally does not happen with the full-length isoforms).

Previously, we have described the dynamics of PNAs formation, when the last stage are so called PML-NDS that accumulate proteins involved in DNA metabolism (DHX9 and B23) and they co-localize with γH2A.X at least at time of their formation [74]. Hence, we inferred that these PML-NDS are a compartment where rDNA is segregated and processed. However, only now did we provide a direct evidence that rDNA is really present in PML-NDS. What is more, rDNA was observed in all newly formed PML-NDS, while it could be detected only in part of the PML-NDS in later time-points (data not shown). This is in agreement with the data we obtained earlier with γH2A.X and it supports our hypothesis that problematic rDNA is segregated into PML-NDS where it can be either repaired or degraded and so it remains intact only in part of the PML-NDS. To our knowledge, this is the first proof that rDNA can be sequestered within small structures containing proteins important in rDNA metabolism and positive for γH2A.X. What is more, as has been shown previously [74], formation of these structures is fully dependent on PML.

The SIM domain of PML showed to be important for PML nucleolar translocation, indicating that the interaction partner of PML could be SUMOylated. In addition, as we suppose that the signal for PNAs formation is the damage of rDNA, we assume that protein(s) binding such rDNA might be marked by post-translational modification with SUMO. Interestingly, we observed an increase in SUMO-1/rDNA co-localization in RPE-1$^{hTERT}$ PML$^{+/+}$ cells after doxorubicin treatment. However, as majority of PML is SUMOylated, it is not clear whether SUMO signal on rDNA comes from the SUMO bound to rDNA/nucleolar proteins or from the SUMO bound to nucleolar PML. Therefore, we performed the same analysis in RPE-1$^{hTERT}$ PML$^{-/-}$ cells, assuming that the rDNA-based processes would progress in the same way in PML$^{+/+}$ and in PML$^{-/-}$ cells. And indeed, we observed slight increase of SUMO-1 signal on rDNA also in PML$^{-/-}$ cells, suggesting that rDNA is SUMOylated in response to doxorubicin and this modification might be at least partly responsible for PML nucleolar targeting. Interestingly, SUMOylation of several proteins, including Top1, Top2, condensins and cohesins, is important for maintenance of rDNA integrity in yeast [29, 30], suggesting similar role of this modification in mammalian cells. Intriguingly, many proteins of HR pathway are subject to SUMOylation, including RPA [31], ATRIP [32], and BRCA1 [33]; and SUMOylation also promotes enrichment of tyrosyl-DNA phosphodiesterase 1 (TDP1), the enzyme that is important for removal of Topo-DNA adducts on a DNA [70]. This together forms another presumable link between rDNA damage, choice of the repair pathway, SUMOylation and PML nucleolar association.

## Material and Methods

### Chemicals and antibodies

4',6-diamidino-2-phenylindole (D9542), aphidicolin (A0781), actinomycinD (50-76-0), 5-bromo-2´-deoxyuridine (B5002), camptothecin (C9911), CX-5461 (1138549-36-6), daunorubicin (30450), doxorubicine hydrochloride (D1515), doxycycline hydrochloride (D-9891), etoposide (E1383 ), 5-fluorouracil (F6627 ), 5-fluorouridine (F5130), hydroxyurea (H8627), MG-132 (C2211 ), oxaliplatin (O9512), roscovitine (R7772) and topotecan hydrochloride (T2705) were all purchased from Sigma-Aldrich/Merck (Darmstadt, Germany), aclarubicin (A2601) was from APExBIO (Houston, TX, USA), CX-4945 (HY-50855 ) was from MedChemExpress (Monmouth

Junction, NJ, USA), pyridostatin (4763) from TOCRIS (Bristol, United Kingdom), the IFNgamma recombinant protein (300-02) was from Peprotech (Rocky Hill, NJ, USA), RNAse A (EN0531), TOTO-3 (T-3604) and Lipofectamine RNAiMAX Reagent (13778075) were obtained from Thermo Fisher Scientific (Waltham, MA, USA), Antifade Pro-long Gold Mounting Media (AF-400-H) was from Immunological Sciences, Rome, Italy) and the rDNA probe (LPE NOR) was from Cytocell (Cambridge, UK).

Specification of primary and secondary antibodies used in the study is listed in Supplementary Table 1.

**Cell culture**

Immortalized human retinal pigment epithelial cells (RPE-1$^{hTERT}$, ATCC) or RPE-1$^{hTERT}$ PML knockout cells [48], RPE-1$^{hTERT}$ p53 knockout cells (kind gift from Libor Macurek), HeLa cells and H1299 cells (both from ATCC), checked for absence of mycoplasma infection, were cultured in Dulbecco's modified Eagle's medium (Gibco/Thermo Fisher Scientific, Waltham, MA, USA) containing 4.5 g/L glucose and supplemented with 10% fetal bovine serum (Gibco/Thermo Fisher Scientific, Waltham, MA, USA) and antibiotics (100 U/mL penicillin and 100 µg/mL streptomycin sulfate, Sigma, St. Louis, MO, USA). The cells were cultivated in normal atmospheric air containing 5% CO2 in a standard humidified incubator at 37°C, on a tissue culture dish (TPP Techno Plastic Products AG, Trasadingen, Switzerland). For most of the treatments the compounds were used in following concentration: doxorubicin - 0.75 µM, camptothecin - 50 µM, topotecan - 50 µM, aclarubicin - 0.05 µM, etoposide - 5 µM, actinomycin D - 10 nM, CX-5461 - 5 µM, 5-fluorouracil – 200 µM; MG-132 – 10 µM, roscovitine- 20 µM, aphidicoline - 0.4 µM, hydroxyurea - 100 µM, oxaliplatin – 10 µM, BrdU – 100 µM, pyridostatin – 5 µM; IFNγ - 100 U, CX-4945 – 10 µM. When a different concentration was applied it is mentioned in a corresponding Figure or its legend. The cells were irradiated with orthovoltage X-ray instrument T-200 (Wolf-Medizintechnik) using 10 Gy.

**Plasmid constructions**

All plasmids used in this study are listed in Supplementary Table 2. Primers used in the construction of plasmids are listed in Supplementary Table 3. pEGFP-N1-PML IV and pEGFP-N3-PML I were used as template for deletion and site-directed mutagenesis. Both isoforms fused to EGFP were prepared by PCR-amplification of cDNA and by insertion of coding region into HincII-digested pGEM4z plasmid. From this plasmid was the fragment coding PML I or PML IV transferred into pEGFP-N3 and pEGFP-N1 plasmids, respectively via HindIII and SmaI sites. Deletion mutagenesis was done by one-step PCR-based method for fragment deletion [71], briefly the pEGFP-N1-PML IV and pEGFP-N3-PML I were amplified using Phusion High-Fidelity DNA Polymerase (M0530L) and corresponding primers for insertion of desired deletion. Site-directed mutagenesis was done according the QuikChange manual and the PfuUltra II Fusion HS DNA polymerase (Agilent #600670) for plasmid amplification was used. The primers for side directed mutagenesis were designed in Primer Design Program (http://www.genomics.agilent.com/primerDesignProgram).

**Transient transfection with plasmids bearing wild-type and mutated variants of PML IV and PML I-EGFP**

The RPE-1$^{hTERT}$ PML knockout cells were seeded on coverslips in concentration 27,000 cells/cm2. One day after seeding, the cells were transfected with desired plasmid using FuGENE HD transfection reagent (Promega; E2311) in DNA: FuGENE ratio 1:3. 24 hours after transfection were these cells treated with doxorubicin (0.75 μM) for another 48 hours. After treatment the cells were fixed, stained with B23 and DAPI and analyzed by wide field fluorescent microscopy.

**Indirect immunofluorescence, confocal microscopy, and stimulated emission depletion (STED) microscopy**

Cells grown on glass coverslips were fixed with 4% formaldehyde in PBS for 15 min, permeabilized in 0.2% Triton X-100 in PBS for 10 min, blocked in 10% FBS in PBS for 30 min, and incubated with primary antibodies for 1 hour, all in RT. After that, cells were washed three times 5 min in PBS, and secondary antibodies (Abberior STAR 635P used specifically for STED) were applied in RT for 1 hour. For some experiments, TOTO-3 was applied together with secondary antibodies. Subsequently, cells were counterstained with 1 μg/mL DAPI for 2 min, washed 3 times with PBS for 5 min and let dry. For wide-field and confocal microscopy, the glasses were mounted with Antifade Pro-long Gold Mounting Media. The wide-field images were subsequently acquired on the Leica DM6000 fluorescent microscope using the HCX PL APO 63×/1.40 OIL PH3 CS and HCX PL APO 40×/0.75 DRY PH2 objectives and monochromatic CCD camera Leica DFC 350FX (Leica Microsystems GmbH, Wetzlar, Germany); the confocal images were acquired on microscope DMI6000 with laser scanning confocal head Leica TCS SP5 AOBS Tandem, using the HC PL APO 63×/1.40 OIL CS2 objective (Leica Microsystems GmbH, Wetzlar, Germany). For super-resolution STED microscopy, the cells were mounted with glycine/N-propyl gallate and imaged on the microscope DMi8 with laser scanning confocal head Leica TCS SP8 and STED 3X module using the HC PL APO100×OIL STED WHITE CS2l objective. Image deconvolution of confocal and STED images was done using Huygens Professional software (Scientific Volume Imaging B.V., Hilversum, The Netherlands).The segmentation analysis and co-localization was done with plugin for ImageJ: Mosaic/Segmentation/Squassh [72].

**5-FUrd incorporation assay**

For 5-FUrd incorporation assay, cells were incubated with 1 mM 5-FUrd for 30 min, at indicated time-points after doxorubicin treatment and removal. After that, cells were fixed with 4% formaldehyde at RT for 15 min and the 5-FUrd incorporation was visualized using anti-BrdU antibody cross-reacting with 5-FUrd. The standard protocol for immunofluorescence described above was used.

**rDNA immuno-FISH**

For immuno-FISH, the cells were grown on cover glasses, washed with PBS, fixed in 3:1 methanol/acetic acid solution in -20°C for 1 hour and washed 3× with PBS. After that, the cells were incubated 90 min at 37°C with 10 mg/mL RNase A, washed 2× in 2×SSC, pH 7, and dehydrated in 70%, 85% and 100% ethanol, respectively, 2 min each. Afterwards, the rDNA probe was administered onto the cells, the DNA was denatured by heating on a hotplate at 76°C for 5 min and incubated with the probe in a wet chamber overnight. The following day, the cells were

washed in 0.4×SSC, pH 7, 72ºC for 2 min and in 2×SSC/0.05% Tween-20, pH 7, at RT for 30 s. Afterwards, the cells were permeabilized, blocked, stained and imaged as described for STED microscopy.

**si-RNA-mediated silencing**

The cells were plated on 6-well plates one day before esi/si RNA transfection. esiRNAs targeting topoisomerase 1 (EHU101551) and topoisomerase 2α (EHU073241, Sigma) were purchased at Sigma-Aldrich/Merck (Darmstadt, Germany) and transfected into cells in a final amount of 300 ng. siRNAs targeting HEATR1 (mix of siRNAs, #1: s30230, 5′-CCACUUUCCAUUUGCGAUATT-3′; #2: s30231, 5′-GAUGUUGUUUUGUCGGCUATT-3′; #3: s30232, 5′-CACUUUCCAUUUGCGAUAATT-3′), topoisomerase 3α (s14311, 5′-CAGGUUAAAGUUAAAGUUUTT-3′), ribosomal protein RPS6 (s12270, 5′-CCUUAAAUAAAGAAGGUAATT-3′) and non-targeting siRNA (Silencer® Select Negative Control No. 1, 4390843) were purchased at Ambion/Thermo Fisher Scientific (Waltham, MA, USA). siRNAs targeting casein kinase 2 subunit α (5′-GAUCCACGUUUCAAUGAUATT-3′) and casein kinase 2 subunit β (5′- AGAGUGACCUGAUUGAGCATT-3′) were purchased at Santa Cruz Biotechnology (Dallas, TX, USA). All si RNAs were transfected into cells at a final amount of 30 pM. The transfections were performed using Lipofectamine™ RNAiMAX, according to the manufacturer's instructions.

**SDS-PAGE and immunoblotting**

Cells were harvested into Laemmli SDS sample lysis buffer (62.5 mM Tris-HCl, pH 6.8, 2% SDS, 10% glycerol), boiled at 95°C for 5 min, sonicated and centrifuged at 18,000×g for 10 min. Concentration of proteins was estimated by the BCA method (Pierce Biotechnology Inc., Rockford, USA). Equal amounts of total protein were mixed with DTT and bromphenol blue to final concentration 100 mM and 0.01%, respectively, and separated by SDS-PAGE (8% or 12% polyacrylamide gels were used). The proteins were electrotransferred to a nitrocellulose membrane using wet transfer. Immunostaining followed by ECL detection was performed. The intensity of the bands was measured in ImageJ Gel Analyzer plugin; and the protein levels were calculated as the band intensities of the proteins of interest, related to the band intensities of loading control, while the relative intensity of untreated cells (or cells treated with a dissolvent – acetic acid or DMSO) was set as one.

**Quantitative real time RT-PCR (qRT-PCR)**

Total RNA samples were isolated using RNeasy Mini Kit (Qiagen, MD, USA) according to the manufacturer's protocol. First strand cDNA was synthesized from 200 ng of total RNA with random hexamer primers using TaqMan Reverse Transcription Reagents (N8080234, Applied Biosystems/Thermo Fisher Scientific, Waltham, MA, USA). qRT-PCR was performed in ABI Prism 7300, using SYBR Green I Master Mix (4364344, Applied Biosystems/Thermo Fisher Scientific, Waltham, MA, USA). Following set of primers were used:
ARF: 5'- CGAGTGAGGGTTTTCGTGGTT-3', 5'- CCATCATCATGACCTGGTCTTCTAG-3';
GAPDH: 5'- GTCGGAGTCAACGGATTTGG-3', 5'-AAAAGCAGCCCTGGTGACC-3'.

The relative quantity of cDNA was estimated by ΔΔCt [73]; data were normalized to GAPDH. Samples were measured in triplicates.

**References**


1. Childs, B.G., et al., *Cellular senescence in aging and age-related disease: from mechanisms to therapy.* Nat Med, 2015. **21**(12): p. 1424-35.
2. McHugh, D. and J. Gil, *Senescence and aging: Causes, consequences, and therapeutic avenues.* J Cell Biol, 2018. **217**(1): p. 65-77.
3. d'Adda di Fagagna, F., et al., *A DNA damage checkpoint response in telomere-initiated senescence.* Nature, 2003. **426**(6963): p. 194-8.
4. Hewitt, G., et al., *Telomeres are favoured targets of a persistent DNA damage response in ageing and stress-induced senescence.* Nat Commun, 2012. **3**: p. 708.
5. Paredes, S., et al., *The epigenetic regulator SIRT7 guards against mammalian cellular senescence induced by ribosomal DNA instability.* J Biol Chem, 2018. **293**(28): p. 11242-11250.
6. Ganley, A.R. and T. Kobayashi, *Ribosomal DNA and cellular senescence: new evidence supporting the connection between rDNA and aging.* FEMS Yeast Res, 2014. **14**(1): p. 49-59.
7. Lallemand-Breitenbach, V. and H. de The, *PML nuclear bodies.* Cold Spring Harb Perspect Biol, 2010. **2**(5): p. a000661.
8. Shen, T.H., et al., *The mechanisms of PML-nuclear body formation.* Mol Cell, 2006. **24**(3): p. 331-9.
9. Sahin, U., H. de The, and V. Lallemand-Breitenbach, *PML nuclear bodies: assembly and oxidative stress-sensitive sumoylation.* Nucleus, 2014. **5**(6): p. 499-507.
10. Sahin, U., et al., *Oxidative stress-induced assembly of PML nuclear bodies controls sumoylation of partner proteins.* J Cell Biol, 2014. **204**(6): p. 931-45.
11. Nisole, S., et al., *Differential Roles of PML Isoforms.* Front Oncol, 2013. **3**: p. 125.
12. Jensen, K., C. Shiels, and P.S. Freemont, *PML protein isoforms and the RBCC/TRIM motif.* Oncogene, 2001. **20**(49): p. 7223-33.
13. Scaglioni, P.P., et al., *A CK2-Dependent Mechanism for Degradation of the PML Tumor Suppressor.* Cell, 2006. **126**(2): p. 269-283.
14. Percherancier, Y., et al., *Role of SUMO in RNF4-mediated PML degradation: PML sumoylation and phospho-switch control of its SUMO binding domain dissected in living cells".* J Biol Chem, 2009. **284**(24): p. 16595-608.
15. Stehmeier, P. and S. Muller, *Phospho-regulated SUMO interaction modules connect the SUMO system to CK2 signaling.* Mol Cell, 2009. **33**(3): p. 400-9.
16. Maroui, M.A., et al., *Requirement of PML SUMO interacting motif for RNF4- or arsenic trioxide-induced degradation of nuclear PML isoforms.* PLoS One, 2012. **7**(9): p. e44949.
17. Brand, P., T. Lenser, and P. Hemmerich, *Assembly dynamics of PML nuclear bodies in living cells.* PMC Biophys, 2010. **3**(1): p. 3.
18. Scaglioni, P.P., et al., *CK2 mediates phosphorylation and ubiquitin-mediated degradation of the PML tumor suppressor.* Mol Cell Biochem, 2008. **316**(1-2): p. 149-54.
19. Golomb, L., S. Volarevic, and M. Oren, *p53 and ribosome biogenesis stress: the essentials.* FEBS Lett, 2014. **588**(16): p. 2571-9.
20. Lindstrom, M.S., et al., *Nucleolus as an emerging hub in maintenance of genome stability and cancer pathogenesis.* Oncogene, 2018. **37**(18): p. 2351–2366.
21. Boulon, S., et al., *The nucleolus under stress.* Mol Cell, 2010. **40**(2): p. 216-27.
22. Boisvert, F.M., et al., *The multifunctional nucleolus.* Nat Rev Mol Cell Biol, 2007. **8**(7): p. 574-85.
23. Gaillard, H. and A. Aguilera, *Transcription as a Threat to Genome Integrity.* Annu Rev Biochem, 2016. **85**: p. 291-317.
24. Tchurikov, N.A., et al., *Hot spots of DNA double-strand breaks in human rDNA units are produced in vivo.* Sci Rep, 2016. **6**: p. 25866.
25. Pommier, Y., et al., *Roles of eukaryotic topoisomerases in transcription, replication and genomic stability.* Nat Rev Mol Cell Biol, 2016. **17**(11): p. 703-721.
26. Harding, S.M., J.A. Boiarsky, and R.A. Greenberg, *ATM Dependent Silencing Links Nucleolar Chromatin Reorganization to DNA Damage Recognition.* Cell Rep, 2015. **13**(2): p. 251-9.

27. van Sluis, M. and B. McStay, *A localized nucleolar DNA damage response facilitates recruitment of the homology-directed repair machinery independent of cell cycle stage.* Genes Dev, 2015. **29**(11): p. 1151-63.
28. Warmerdam, D.O., J. van den Berg, and R.H. Medema, *Breaks in the 45S rDNA Lead to Recombination-Mediated Loss of Repeats.* Cell Rep, 2016. **14**(11): p. 2519-27.
29. Takahashi, Y., et al., *Cooperation of sumoylated chromosomal proteins in rDNA maintenance.* PLoS Genet, 2008. **4**(10): p. e1000215.
30. Liang, J., et al., *Recruitment of a SUMO isopeptidase to rDNA stabilizes silencing complexes by opposing SUMO targeted ubiquitin ligase activity.* Genes Dev, 2017. **31**(8): p. 802-815.
31. Dou, H., et al., *Regulation of DNA repair through deSUMOylation and SUMOylation of replication protein A complex.* Mol Cell, 2010. **39**(3): p. 333-45.
32. Wu, C.S., et al., *SUMOylation of ATRIP potentiates DNA damage signaling by boosting multiple protein interactions in the ATR pathway.* Genes Dev, 2014. **28**(13): p. 1472-84.
33. Morris, J.R., et al., *The SUMO modification pathway is involved in the BRCA1 response to genotoxic stress.* Nature, 2009. **462**(7275): p. 886-90.
34. Janderova-Rossmeislova, L., et al., *PML protein association with specific nucleolar structures differs in normal, tumor and senescent human cells.* J Struct Biol, 2007. **159**(1): p. 56-70.
35. Condemine, W., et al., *A nucleolar targeting signal in PML-I addresses PML to nucleolar caps in stressed or senescent cells.* J Cell Sci, 2007. **120**(Pt 18): p. 3219-27.
36. Cao, J., et al., *Homoharringtonine combined with aclarubicin and cytarabine synergistically induces apoptosis in t(8;21) leukemia cells and triggers caspase-3-mediated cleavage of the AML1-ETO oncoprotein.* Cancer Med, 2016. **5**(11): p. 3205-3213.
37. Bernardi, R., et al., *PML regulates p53 stability by sequestering Mdm2 to the nucleolus.* Nat Cell Biol, 2004. **6**(7): p. 665-72.
38. Shav-Tal, Y., et al., *Dynamic Sorting of Nuclear Components into Distinct Nucleolar Caps during Transcriptional Inhibition.* Mol Biol Cell, 2005. **16**(5): p. 2395-413.
39. Mattsson, K., et al., *Proteins associated with the promyelocytic leukemia gene product (PML)-containing nuclear body move to the nucleolus upon inhibition of proteasome-dependent protein degradation.* Proc Natl Acad Sci U S A, 2001. **98**(3): p. 1012-7.
40. Mukaida, N., Y. Mahe, and K. Matsushima, *Cooperative interaction of nuclear factor-kappa B- and cis-regulatory enhancer binding protein-like factor binding elements in activating the interleukin-8 gene by pro-inflammatory cytokines.* J Biol Chem, 1990. **265**(34): p. 21128-33.
41. Cutts, S.M., et al., *Sequence specificity of adriamycin-DNA adducts in human tumor cells.* Mol Cancer Ther, 2003. **2**(7): p. 661-70.
42. Tewey, K.M., et al., *Adriamycin-induced DNA damage mediated by mammalian DNA topoisomerase II.* Science, 1984. **226**(4673): p. 466-8.
43. Feinstein, E., E. Canaani, and L.M. Weiner, *Dependence of nucleic acid degradation on in situ free-radical production by adriamycin.* Biochemistry, 1993. **32**(48): p. 13156-61.
44. Pang, B., et al., *Drug-induced histone eviction from open chromatin contributes to the chemotherapeutic effects of doxorubicin.* Nat Commun, 2013. **4**: p. 1908.
45. Burger, K., et al., *Chemotherapeutic drugs inhibit ribosome biogenesis at various levels.* J Biol Chem, 2010. **285**(16): p. 12416-25.
46. Rubbi, C.P. and J. Milner, *Disruption of the nucleolus mediates stabilization of p53 in response to DNA damage and other stresses.* Embo J, 2003. **22**(22): p. 6068-77.
47. Ma, H. and T. Pederson, *The nucleolus stress response is coupled to an ATR-Chk1-mediated G2 arrest.* Mol Biol Cell, 2013. **24**(9): p. 1334-42.
48. Vancurova, M., et al., *PML nuclear bodies are recruited to persistent DNA damage lesions in an RNF168-53BP1 dependent manner and contribute to DNA repair.* DNA Repair (Amst), 2019. **78**: p. 114-127.
49. Boichuk, S., et al., *Functional connection between Rad51 and PML in homology-directed repair.* PLoS ONE, 2011. **6**(10): p. e25814.
50. Rogakou, E.P., et al., *DNA double-stranded breaks induce histone H2AX phosphorylation on serine 139.* J Biol Chem, 1998. **273**(10): p. 5858-68.
51. de Stanchina, E., et al., *PML is a direct p53 target that modulates p53 effector functions.* Mol Cell, 2004. **13**(4): p. 523-35.
52. Chelbi-Alix, M.K., et al., *Induction of the PML protein by interferons in normal and APL cells.* Leukemia, 1995. **9**(12): p. 2027-33.

53. Ivanschitz, L., et al., *PML IV/ARF interaction enhances p53 SUMO-1 conjugation, activation, and senescence.* Proc Natl Acad Sci U S A, 2015. **112**(46): p. 14278-83.
54. Natale, F., et al., *Identification of the elementary structural units of the DNA damage response.* Nat Commun, 2017. **8**: p. 15760.
55. Pefani, D.E., et al., *MST2 kinase suppresses rDNA transcription in response to DNA damage by phosphorylating nucleolar histone H2B.* Embo j, 2018. **37**(15).
56. Korsholm, L.M., et al., *Double-strand breaks in ribosomal RNA genes activate a distinct signaling and chromatin response to facilitate nucleolar restructuring and repair.* Nucleic Acids Res, 2019. **47**(15): p. 8019–8035.
57. Holm, C., et al., *Differential requirement of DNA replication for the cytotoxicity of DNA topoisomerase I and II inhibitors in Chinese hamster DC3F cells.* Cancer Res, 1989. **49**(22): p. 6365-8.
58. D'Arpa, P., C. Beardmore, and L.F. Liu, *Involvement of nucleic acid synthesis in cell killing mechanisms of topoisomerase poisons.* Cancer Res, 1990. **50**(21): p. 6919-24.
59. Morris, E.J. and H.M. Geller, *Induction of neuronal apoptosis by camptothecin, an inhibitor of DNA topoisomerase-I: evidence for cell cycle-independent toxicity.* J Cell Biol, 1996. **134**(3): p. 757-70.
60. Liu, L.F., et al., *Mechanism of action of camptothecin.* Ann N Y Acad Sci, 1996. **803**: p. 44-9.
61. Zhang, H., J.C. Wang, and L.F. Liu, *Involvement of DNA topoisomerase I in transcription of human ribosomal RNA genes.* Proc Natl Acad Sci U S A, 1988. **85**(4): p. 1060-4.
62. El Hage, A., et al., *Loss of Topoisomerase I leads to R-loop-mediated transcriptional blocks during ribosomal RNA synthesis.* Genes Dev, 2010. **24**(14): p. 1546-58.
63. Ray, S., et al., *Topoisomerase IIalpha promotes activation of RNA polymerase I transcription by facilitating pre-initiation complex formation.* Nat Commun, 2013. **4**: p. 1598.
64. Canela, A., et al., *Topoisomerase II-Induced Chromosome Breakage and Translocation Is Determined by Chromosome Architecture and Transcriptional Activity.* Mol Cell, 2019. **75**(2): p. 252-266.e8.
65. Chakraborty, A., et al., *Classical non-homologous end-joining pathway utilizes nascent RNA for error-free double-strand break repair of transcribed genes.* Nat Commun, 2016. **7**: p. 13049.
66. van Sluis, M. and B. McStay, *Nucleolar reorganization in response to rDNA damage.* Curr Opin Cell Biol, 2017. **46**: p. 81-86.
67. Yuan, J., R. Adamski, and J. Chen, *Focus on histone variant H2AX: to be or not to be.* FEBS Lett, 2010. **584**(17): p. 3717-24.
68. Chatterjee, A., U. Chatterjee, and M.K. Ghosh, *Activation of protein kinase CK2 attenuates FOXO3a functioning in a PML-dependent manner: implications in human prostate cancer.* Cell Death Dis, 2013. **4**: p. e543.
69. Trembley, J.H., et al., *Protein kinase CK2 in health and disease: CK2: a key player in cancer biology.* Cell Mol Life Sci, 2009. **66**(11-12): p. 1858-67.
70. Hudson, J.J., et al., *SUMO modification of the neuroprotective protein TDP1 facilitates chromosomal single-strand break repair.* Nat Commun, 2012. **3**: p. 733.
71. Qi, D. and K.B. Scholthof, *A one-step PCR-based method for rapid and efficient site-directed fragment deletion, insertion, and substitution mutagenesis.* J Virol Methods, 2008. **149**(1): p. 85-90.
72. Rizk, A., et al., *Segmentation and quantification of subcellular structures in fluorescence microscopy images using Squassh.* Nat Protoc, 2014. **9**(3): p. 586-96.
73. Livak, K.J. and T.D. Schmittgen, *Analysis of relative gene expression data using real-time quantitative PCR and the 2(-Delta Delta C(T)) Method.* Methods, 2001. **25**(4): p. 402-8.
74. Imrichova T., et al., *Dynamic PML protein nucleolar associations with persistent DNA damage lesions in response to nucleolar stress and senescence-inducing stimuli.* Aging (Albany NY), 2019. (*in press*)

**Figure legends**

**Figure 1: PNAs are formed after simultaneous inhibition of topoisomerasies and RNA polymerase I.** RPE-1$^{hTERT}$ cells were treated with different compounds for 48 hours (only exception 6 hours long treatment with MG-132) and the formation of PNAs and other parameters were evaluated. (**A**) Examples of PML nucleolar associations (PNAs) occurring in RPE-1$^{hTERT}$ cells after treatment with 0.75 μM doxorubicin. The PML cap, fork, circle and PML nucleolus-derived structure (PML-NDS) are visualized by indirect immunofluorescence. PML (green) and TOTO-3 (red, visualizes the nucleoli) and DAPI (blue). (**B**) A chart, showing the percentage of RPE-1$^{hTERT}$ cells containing PNAs after treatment with different stress-inducing stimuli. The stressors were divided into five categories according to their main mechanism of action: blue - inhibitors of topoisomerases, red - inhibitors of RNAP I, violet - inhibitors of pre-RNA processing, orange - inductors of replication stress, black - other stressors. In the table below the chart, p53 stabilization, γH2A.X foci formation, PAF49 segregation and Top1 or Top2a decline is shown. (**C**) The wide-field immunofluorescence microscopy of RNAP I subunit PAF49 (red; the distribution reflect the activity of RNAP I) and the PML (green) in RPE-1$^{hTERT}$ cells, 48 hours after selected treatments. Bar, 10 μm.

**Figure 2: Downregulation of Top1 and Top2a induces PNAs formation.** (**A**) The pattern of PML (green) and B23 (red) in RPE-1$^{hTERT}$ cells, visualized by indirect immunofluorescence, after transfection with esiRNAs targeting topoisomerases 1 and 2a, with siRNA targeting topoisomerase 2b, or with nonsense siRNA, respectively. The percentage of cells containing PNAs after downregulation of respective topoisomerase is written below each image. Bar, 10 μm. (**B**) Immunoblots with lysates extracted from cells after transfection either with nonsense siRNA or with esiRNA/siRNA targeting individual topoisomerases. The membranes were probed with indicated anti-Top antibodies to prove their efficient downregulation. GAPDH was used as a loading control. (**C**) Illustrative images of RPE-1$^{hTERT}$ cells in which Top1 was downregulated by esiRNA transfection show time-dependent changes in the pattern of PML (green) and PAF49 (red; subunit of RNAP I, distribution reflect the activity). The number of days after transfection is written below each image. Bar, 10 μm.

**Figure 3: The RNAP I inhibition prior to topoisomerase inhibition/downregulation increase the amount of PNAs.** (**A**) RPE-1$^{hTERT}$ cells were pre-treated with 10 nM AMD for 5 hours to inhibit RNAP I and then treated with 0.375 μM doxorubicin for another 48 hours. The chart shows the percentage of cells containing either PML-NDSs or PNCs (forks and circles). Three independent experiments are shown. (**B**) RPE-1$^{hTERT}$ cells were pre-treated with 5 μM CX-5461 for 2 hours to inhibit RNAP I and then treated with 0.375 μM or 0.75 μM doxorubicin for another 48 hours. The chart shows the percentage of cells containing either PML-NDSs or PNCs (forks and circles) for both concentrations, within a single replicate. (**C**) RPE-1$^{hTERT}$ cells were pre-treated with 10 nM AMD for 5 hours to inhibit RNAP I and then transfected with esiRNA targeting Top1. The chart shows the percentage of cells containing either PML-NDSs or PNCs (forks and circles), 48 hours after transfection. Three biological replicates were evaluated. Results are presented as a mean ± s.d.

**Figure 4: The presence exon 8b and the SUMO interactive motif that is regulated by CK2-mediated phosphorylation are important for PML localization to the nucleolus.** (**A**) The amino-acid sequences of the C-termini of PML I, IV, V and VI isoform are shown. In the left column the ability to form PNAs is indicated. (B, C and D) RPE-1$^{hTERT}$ PML$^{-/-}$ cells were transfected with PML IV (**B**) and PML I (**C**) deletion mutants and PML IV deletion, phosphomimetic and unphosphorylable mutants (**D**) and their ability to associate with nucleolus was assessed 48 hours after treatment with 0.75 μM doxorubicin. The bars to the right of scheme of the mutations represent the percentage of transfected cells containing PNAs, relative to the cells transfected with the wild-type PML IV isoform. In each experiment over 60 cells with physiological expression of PML was evaluated. Three biological replicates were evaluated. Results are presented as a mean ± s.d. (**E**) RPE-1$^{hTERT}$ cells were treated with 0.75 μM doxorubicin in the presence or absence of CK2 inhibitor CX-4945 and the percentage of cells containing PNAs was assessed after 48 hours. The percentage of PNAs-positive cells in the sample without CX-4945 was set as

100%. Three biological replicates were evaluated. Results are presented as a mean ± s.d. (**F**) RPE-1$^{hTERT}$ cells were transfected with siRNAs targeting CK2 subunit α, β or their combination. Nonsense siRNA was used as a negative control. 0.75 μM doxorubicin was added to the cells 3 days after transfection and the percentage of cells containing PNAs was assessed 48 hours later. The percentage of PNAs-positive cells in the cells transfected with nonsense siRNA was set as 100%. Three biological replicates were evaluated. Results are presented as a mean ± s.d.

**Figure 5: rDNA is localizes in PNAs.** RPE-1$^{hTERT}$ cells were treated with 0.75 μM doxorubicin for 24 and 48 hours to obtain PML caps, forks and 6 hours after doxorubicin washout (WO) to initiate PML-NDS. At selected time-points, immuno-FISH with rDNA probe and anti-PML antibody was performed and the cells were imaged on the super-resolution STED microscope. (**A**) The chart represents the size of the rDNA-PML co-localization, which was calculated for different PNAs using plugin Mosaic/segmentation/SQUASSH in Image J. (**B, C**) Illustrations of selected caps (**B**) or forks (**C**) with low (1, 2, 5, 6) or high (3, 4, 7, 8) co-localization size. rDNA – green, PML – red. The right columns show the images of PNAs after deconvolution, while the left columns show how the images are processed during segmentation analysis. (**D**) Selected images documenting the presence of rDNA within the tip of PML forks and inside PML-NDS 6 hours after doxorubicin washout. rDNA – green, PML – red, DAPI – blue.

**Figure 6: rDNA co-localizes with SUMO-1 after doxorubicin treatment.** RPE-1$^{hTERT}$ PML$^{-/-}$ and PML$^{+/+}$ cells were treated with 0.75 μM doxorubicin for 0, 6, 12 or 24 hours. Then, immuno-FISH with rDNA probe and anti-SUMO-1 antibody was performed and the cells were imaged on the confocal microscope. The chart in the left part represents the size of the rDNA and SUMO-1 co-localization, which was calculated for different time-points of doxorubicin treatment in RPE-1$^{hTERT}$ PML$^{-/-}$ and PML$^{+/+}$ cells using plugin Mosaic/Segmentation/Squassh in Image J. In the right part the images (24 hours after doxorubicin addition) obtained by this analysis are presented. In the upper raw are nucleoli with the highest size (0.5 – 1), in the central raw with medium size (0.2 – 0.5) and in the bottom raw with low size (0 – 0.1) of rDNA (red) and SUMO-1 (green) co-localization.

**Supplementary Figure 1: DNA damage after different treatments.** RPE-1$^{hTERT}$ cells were treated with different stimuli and the DNA damage, demonstrated as phosphorylation of histone H2AX (γH2AX), was visualized after 48 h by indirect immunofluorescence, using the anti-γH2AX antibody. Bars, 20 μm.

**Supplementary Figure 2: The levels of p53, Top1 and Top2a after various treatments.** RPE-1$^{hTERT}$ cells were treated with different stimuli and the levels of p53 (**A**), Top2a (**B**) and Top1 (**C**) were detected by western blot. The same membrane was used for all three proteins, therefore the same loading control (GAPDH) could be used for all of them. The chart on the right shows relative levels of p53, Top2a and Top1, respectively, related to the loading control. The protein levels of untreated cells, or cells treated with drug solvents (acetic acid, DMSO) were set as one. The two-row tables below the charts show the percentage of cells containing PNAs and the status of PAF49 after each of the treatments.

**Supplementary Figure 3: RNAP I inhibition at different times after AMD or CX-5461 treatments.** RPE-1$^{hTERT}$ cells were treated with actinomycin D (10 nM) or CX-5461 (5 μM) for indicated time-points. At each time-point, the cell were incubated for 30 min with 5-FUrd. The immunofluorescence detection of 5-FUrd (green), representing newly synthesized nucleolar RNA, and localization/segregation of RNAPI subunit PAF49 (red) was performed. The nuclei and nucleoli were stained with DAPI (blue) and TOTO-3 (yellow), respectively. Bars, 10 μm.

**Supplementary Figure 4: PNAs form in absence of p53.** (**A**) RPE-1$^{hTERT}$ p53$^{-/-}$ and p53$^{+/+}$ cells were pre-treated with IFNγ, to induce PML expression in p53$^{-/-}$ cells that normally lack PML, and subsequently treated with doxorubicin. The presence of PNAs was estimated by indirect immunofluorescence of PML (green) after 2 days, the nuclei were stained by DAPI (blue). (**B**) esiRNA-mediated downregulation of Top1 was performed in RPE-1$^{hTERT}$ p53$^{-/-}$ and p53$^{+/+}$ cells. The presence of PNAs was estimated by indirect immunofluorescence of PML (green) after 3

days, the nucleoli were visualized by B23 (red). Bars, 15 μm. (**C**) The immunoblot of RPE-1$^{hTERT}$ p53$^{-/-}$ and p53$^{+/+}$ cells, non-transfected, or transfected by esiRNA targeting Top1, 3 days after transfection. The levels of Top1 and p53 are shown, GAPDH is used as a loading control.

**Supplementary Figure 5: Reduction of CK2 activity after inhibition and downregulation.** (**A**) RPE-1$^{hTERT}$ cells were treated with the CK2 inhibitor CX-4945 and the lysate was harvested after 2 days. The activity of CK2 was assessed on immunoblot, using the antibody against phosphorylated CK2 motif. PonceauS is shown as a loading control. (**B, C**) RPE-1$^{hTERT}$ cells were transfected with siRNAs targeting CK2 subunit α, β or their combination. Nonsense siRNA was used as a negative control. 0.75 μM doxorubicin was added to the cells 3 days after transfection. The lysates were harvested at the time of doxorubicin treatment and 2 days after doxorubicin adding. Immunoblot was performed with an antibody against phosphorylated CK2 motif, to detect the activity of CK2 (**B**) and with an antibody against CK2α to show its efficient downregulation (**C**). PonceauS is shown as a loading control.

**Supplementary Figure 6: p14/ARF is undetectable in RPE-1$^{hTERT}$ cells.** RPE-1$^{hTERT}$ cells were treated with 0.75 μM doxorubicin for 1, 2, 3 or 6 days and the lysates were harvested together with untreated RPE-1$^{hTERT}$ , HeLa and H1299 cells. Immunoblot was performed with antibodies against p14/ARF and GAPDH as a loading control. PonceauS is shown as another loading control. (**B**) Total RNA was isolated from RPE-1$^{hTERT}$ cells treated for 1 day with 0.75 μM doxorubicin, as well as from untreated RPE-1$^{hTERT}$ , HeLa and H1299 cells; and RT-qPCR was performed with primers recognizing p14/ARF and actin B. The level of p14/ARF mRNA was normalized to the level of actin B mRNA and the highest value (detected in H1299) was set as one. The samples were measured in a triplicate.

Figure 1

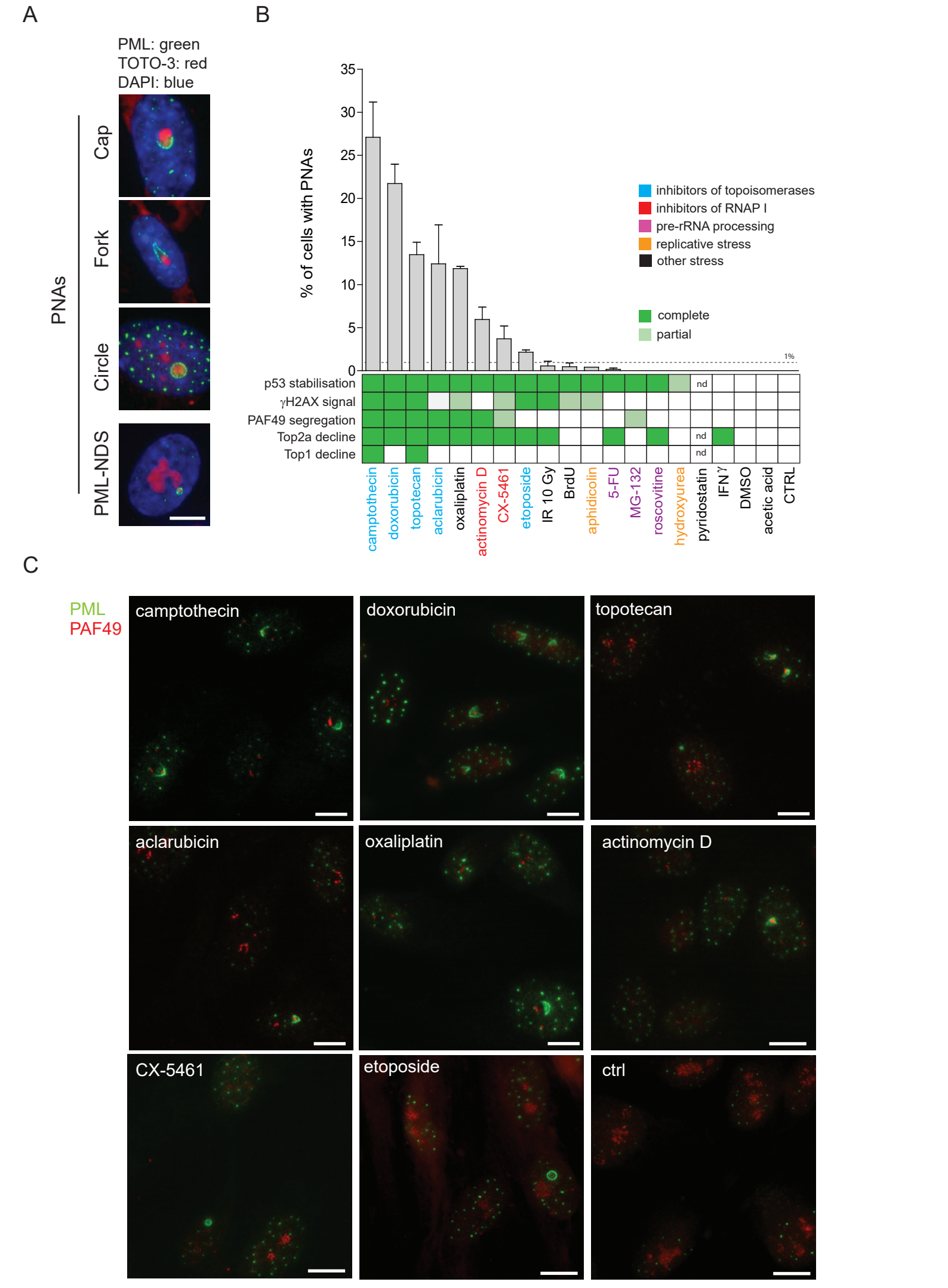
A
PML: green
TOTO-3: red
DAPI: blue
PNAs
Cap
Fork
Circle
PML-NDS
B
% of cells with PNAs
35
30
25
20
15
10
5
0
1%
inhibitors of topoisomerases
inhibitors of RNAP I
pre-rRNA processing
replicative stress
other stress
complete
partial
p53 stabilisation
γH2AX signal
PAF49 segregation
Top2a decline
Top1 decline
nd
camptothecin
doxorubicin
topotecan
aclarubicin
oxaliplatin
actinomycin D
CX-5461
etoposide
IR 10 Gy
BrdU
aphidicolin
5-FU
MG-132
roscovitine
hydroxyurea
pyridostatin
IFN γ
DMSO
acetic acid
CTRL
C
PML
PAF49
camptothecin
doxorubicin
topotecan
aclarubicin
oxaliplatin
actinomycin D
CX-5461
etoposide
ctrl

Figure 2

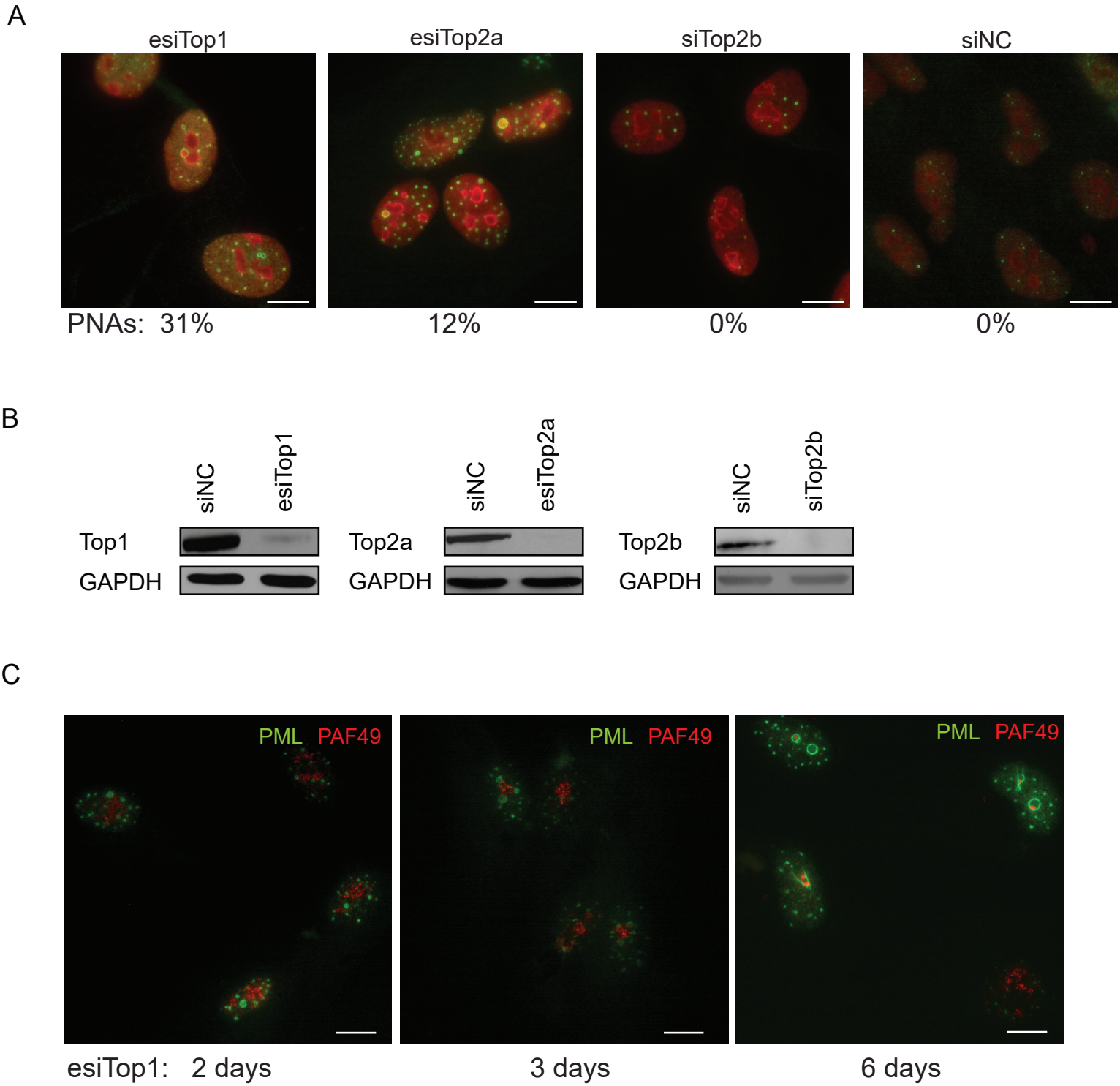
A
esiTop1
esiTop2a
siTop2b
siNC
PNAs: 31%
12%
0%
0%
B
siNC
esiTop1
siNC
esiTop2a
siNC
siTop2b
Top1
GAPDH
Top2a
GAPDH
Top2b
GAPDH
C
PML PAF49
PML PAF49
PML PAF49
esiTop1: 2 days
3 days
6 days

Figure 3

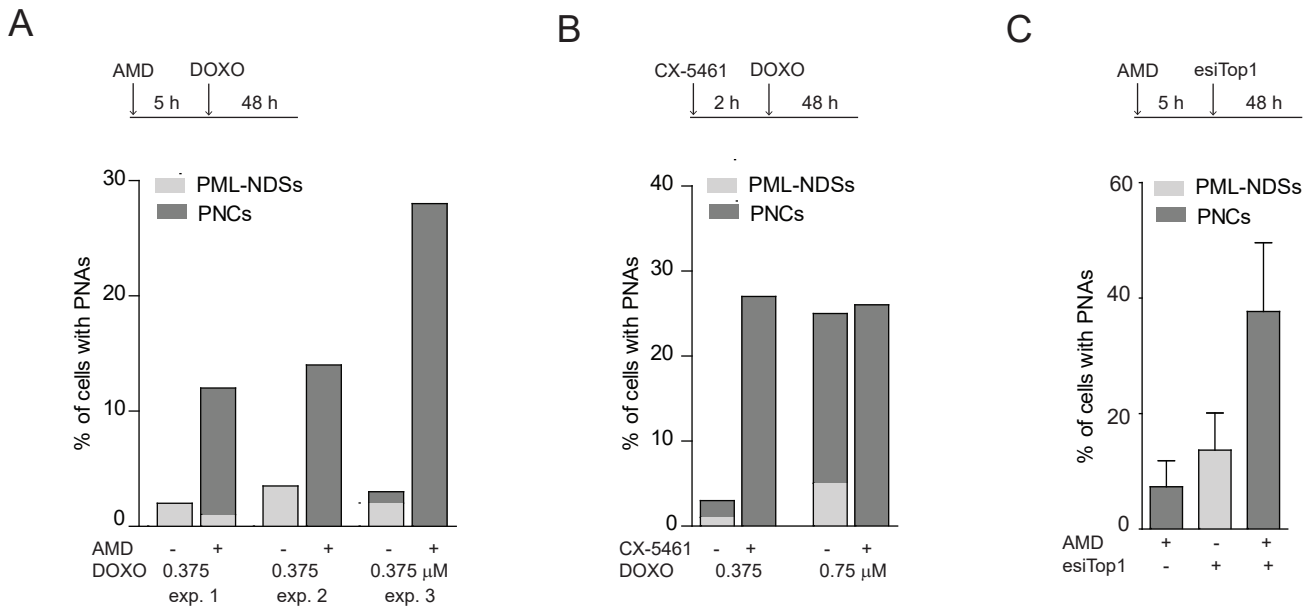
A
AMD
DOXO
5 h
48 h
PML-NDSs
PNCs
% of cells with PNAs
30
20
10
0
AMD - + - + - +
DOXO 0.375 0.375 0.375 μM
exp. 1
exp. 2
exp. 3
B
CX-5461
DOXO
2 h
48 h
PML-NDSs
PNCs
% of cells with PNAs
40
30
20
10
0
CX-5461 - + - +
DOXO 0.375 0.75 μM
C
AMD
esiTop1
5 h
48 h
PML-NDSs
PNCs
% of cells with PNAs
60
40
20
0
AMD + - +
esiTop1 - + +

Figure 4

A

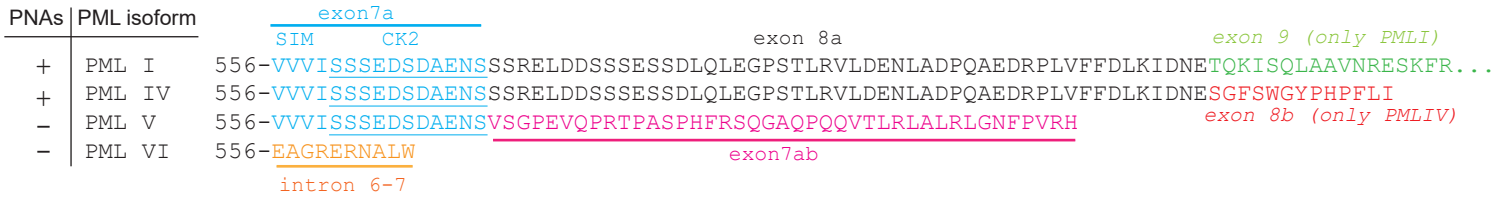


B

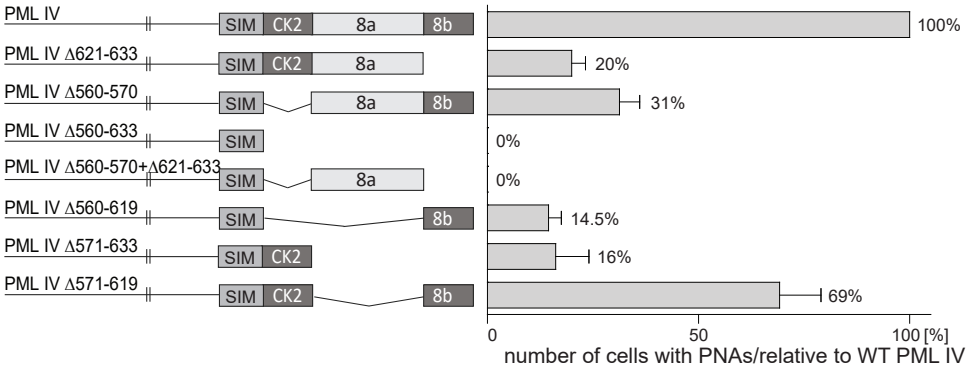


C

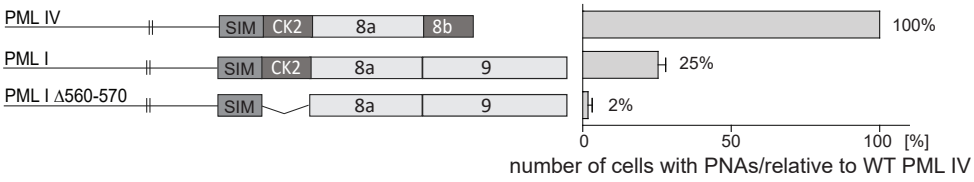


D

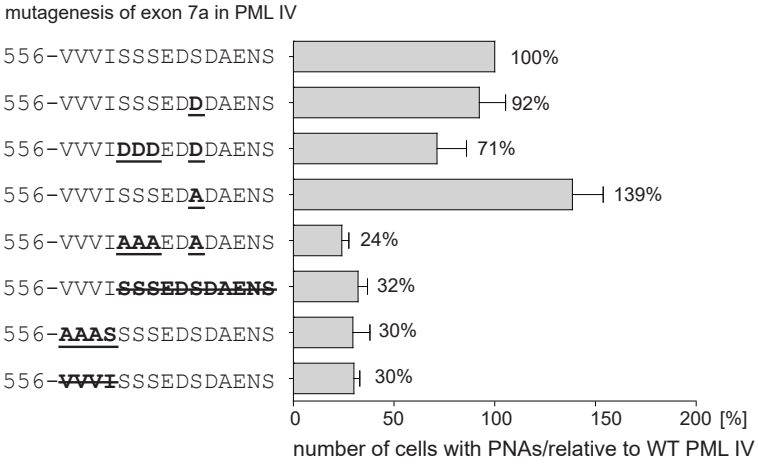


E

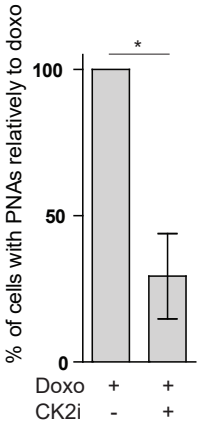


F

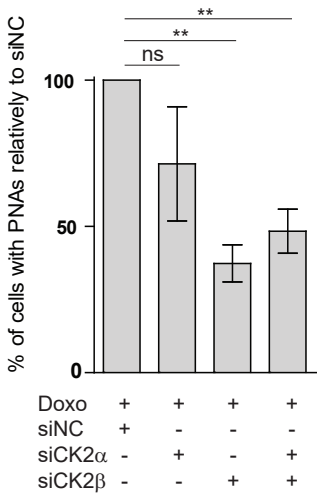

Figure 5

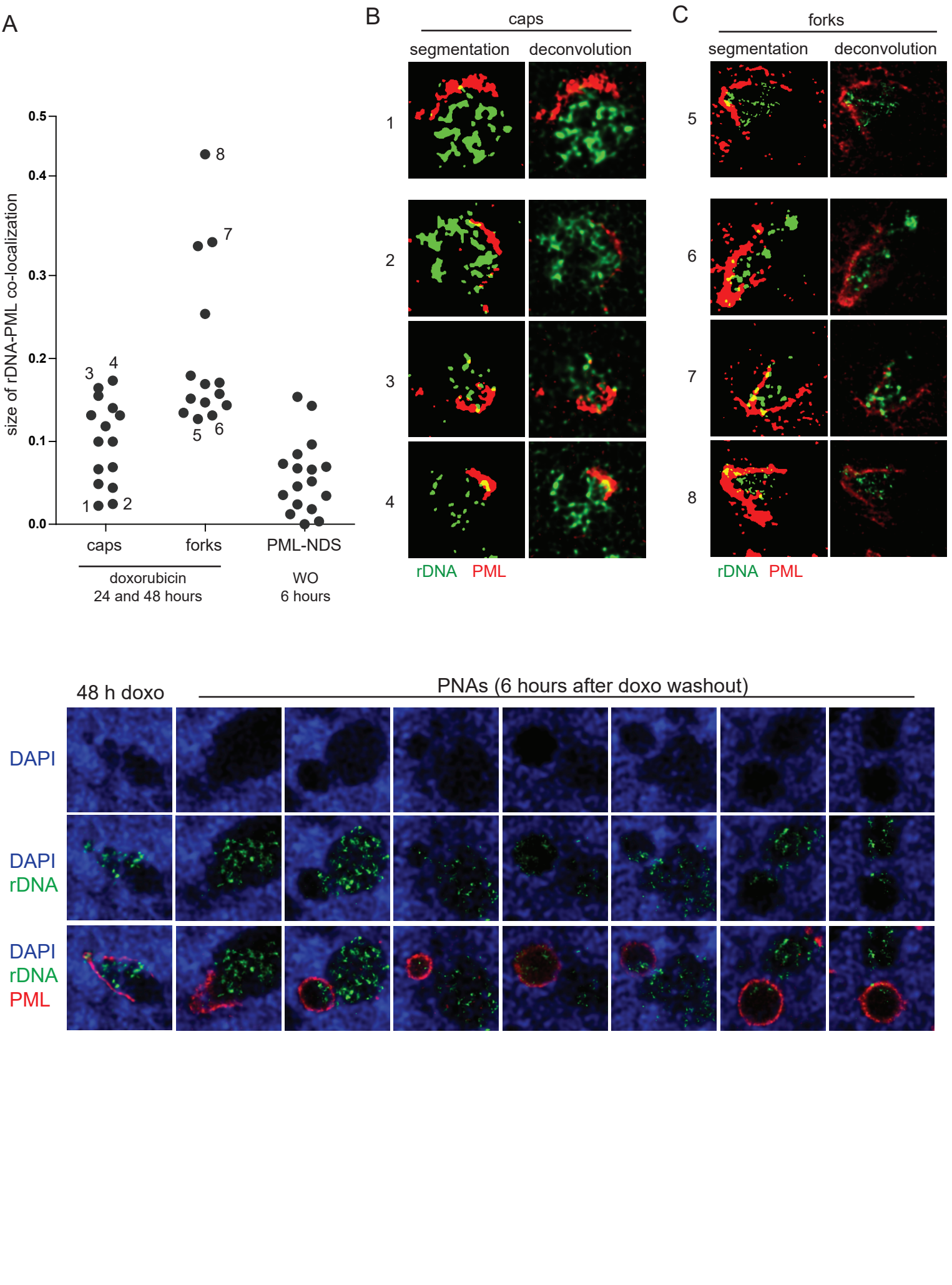
A
size of rDNA-PML co-localization
0.5
0.4
0.3
0.2
0.1
0.0
1
2
3
4
5
6
7
8
caps
forks
PML-NDS
doxorubicin
24 and 48 hours
WO
6 hours
B
caps
segmentation
deconvolution
C
forks
segmentation
deconvolution
rDNA PML
rDNA PML
D
48 h doxo
PNAs (6 hours after doxo washout)
DAPI
DAPI
rDNA
DAPI
rDNA
PML

Figure 6

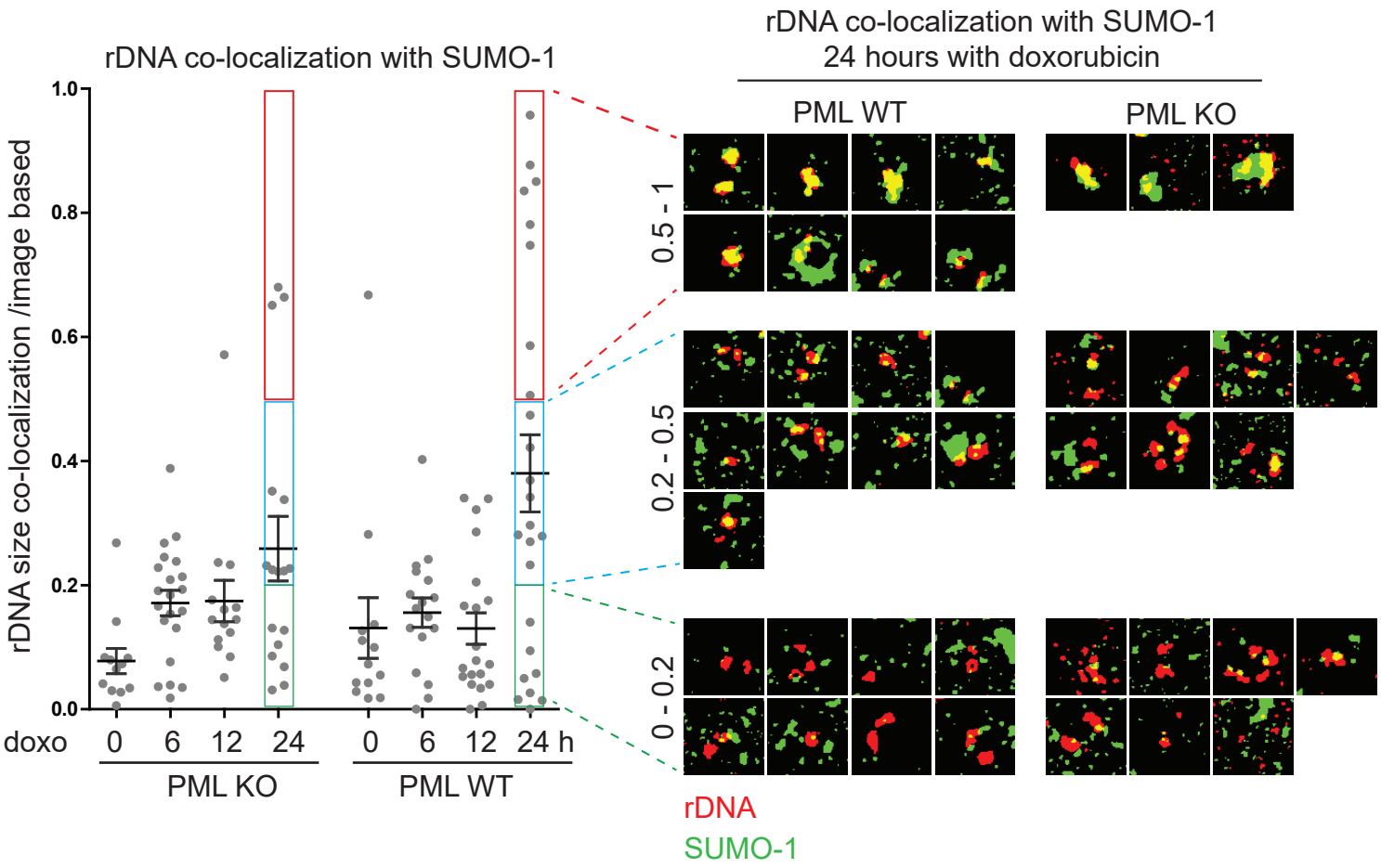
rDNA co-localization with SUMO-1
rDNA size co-localization /image based
1.0
0.8
0.6
0.4
0.2
0.0
doxo
0
6
12
24
0
6
12
24 h
PML KO
PML WT
rDNA co-localization with SUMO-1
24 hours with doxorubicin
PML WT
PML KO
0.5 - 1
0.2 - 0.5
0 - 0.2
rDNA
SUMO-1

**Table 1. List of treatments**

| Class | Compound | Specification |
|---|---|---|
| Topoisomerase inhibitors | camptothecin | Top1 poison |
| | topotecan | Top1 poison |
| | doxorubicin | Top2 poison (< 1 uM), inhibitor of Top2 binding to DNA (> 10 uM), histone eviction |
| | aclarubicin | inhibitor of Top2 binding to DNA, histone eviction |
| | etoposide | Top2 poison |
| RNAP I inhibitors | actinomycin D | intercalates to DNA, preferentially to GC-rich sequences |
| | CX-5461 | inhibits the formation of RNAP I pre-initiation complex |
| Inhibitors of rRNA processing | 5-FU | antimetabolite |
| | MG-132 | proteasome inhibitor |
| | roscovitine | kinase inhibitor |
| Replicative stress inducers | aphidicolin | DNA polymerase A, D inhibitor |
| | HU | antimetabolite |
| Others | oxaliplatin | alkylating agent, inhibits RNAP I |
| | BrdU | nucleotide analogue |
| | IR | DNA-damaging treatment |
| | pyridostatin | G-quadruplex stabilizer |
| | IFNγ | JAK-STAT pathway activator |

Supplementary Figure 1

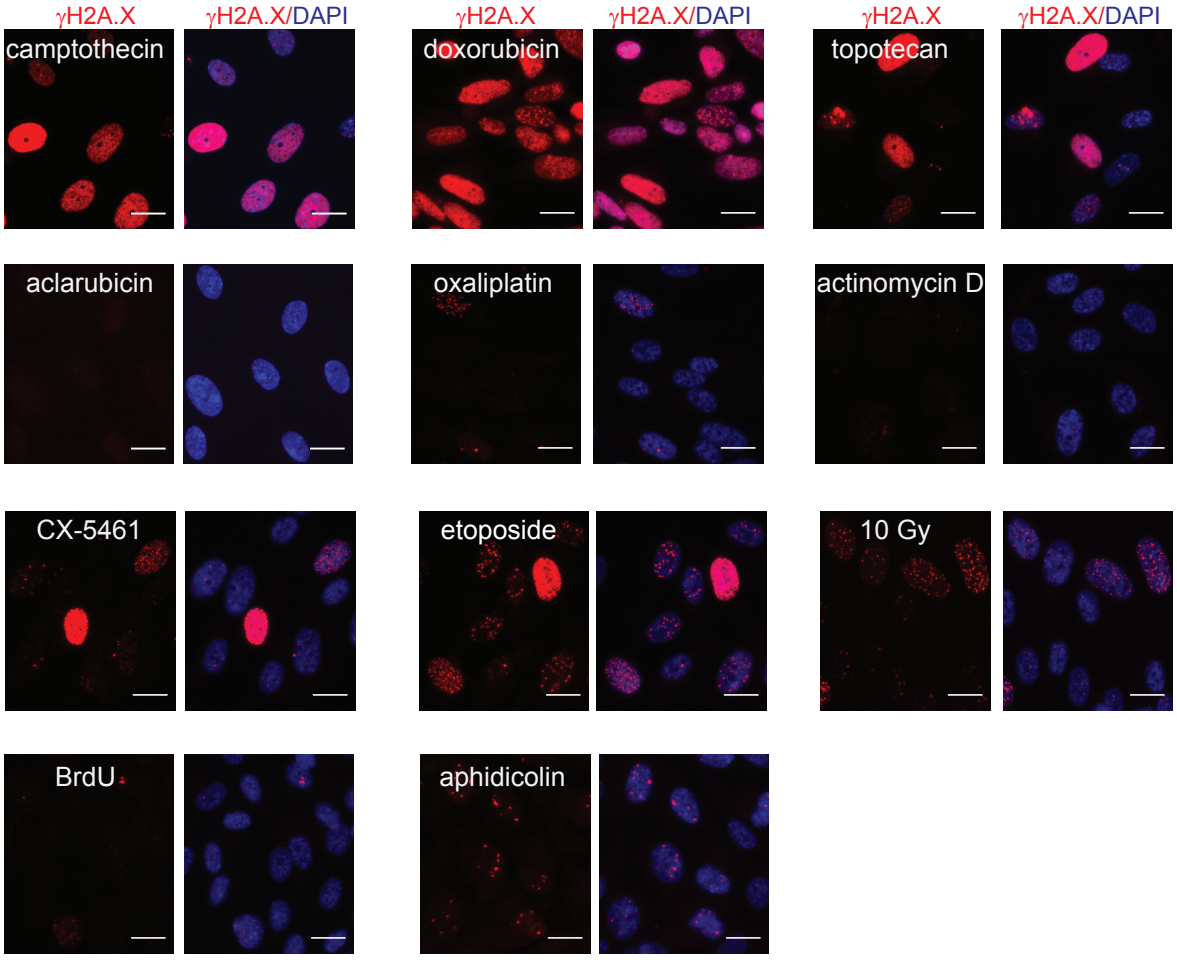

# Supplementary Figure 2

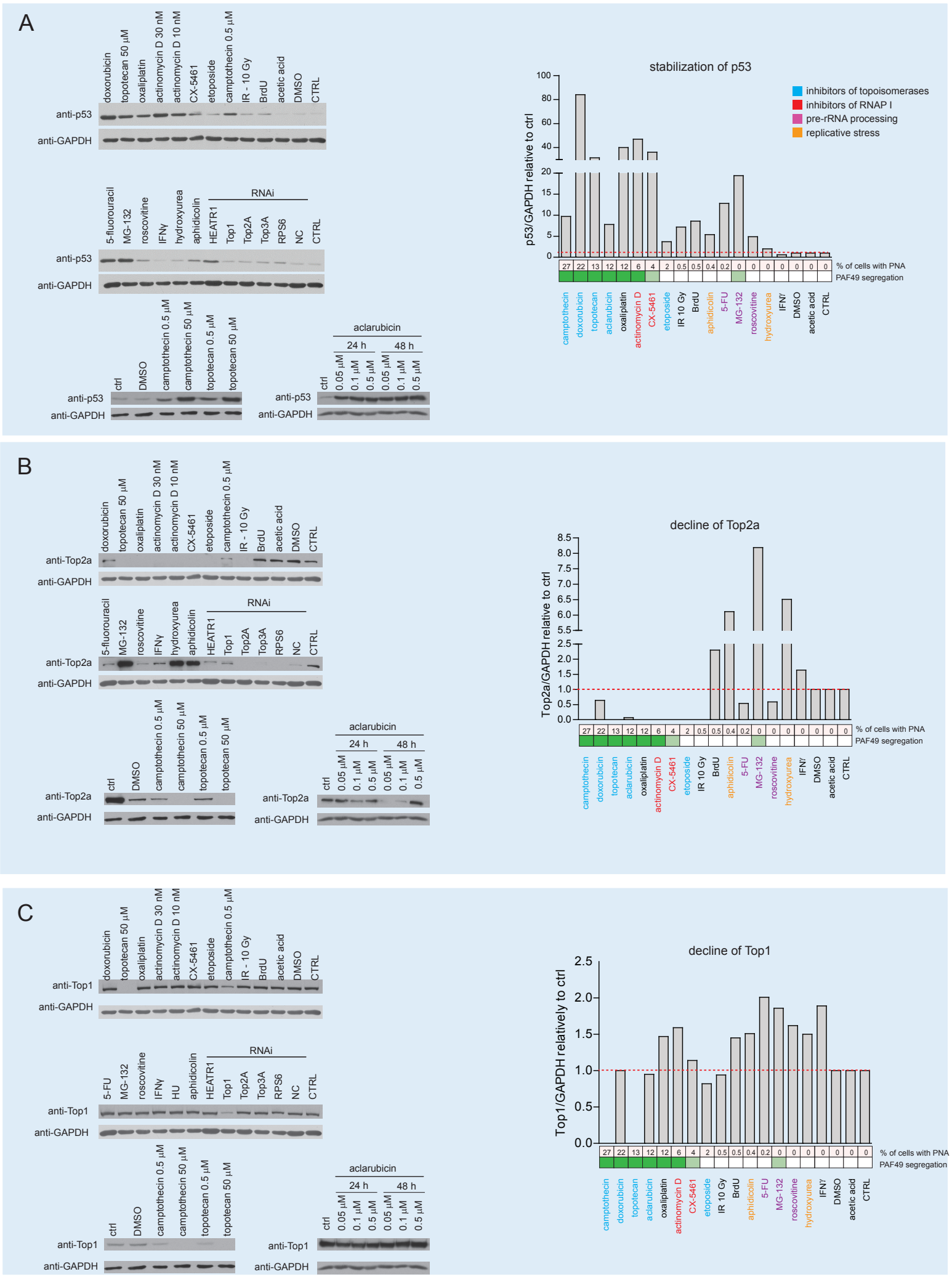

Supplementary Figure 3

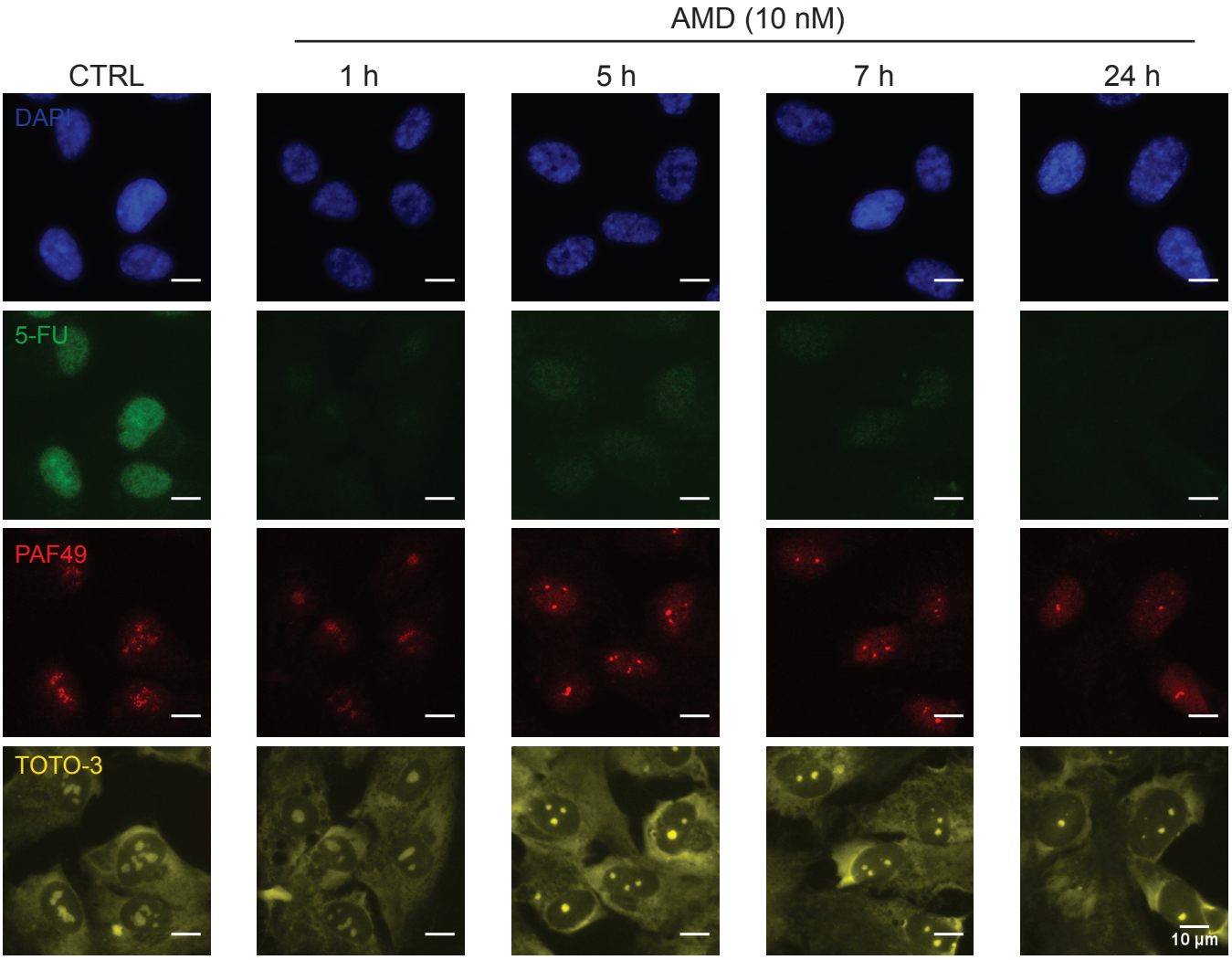


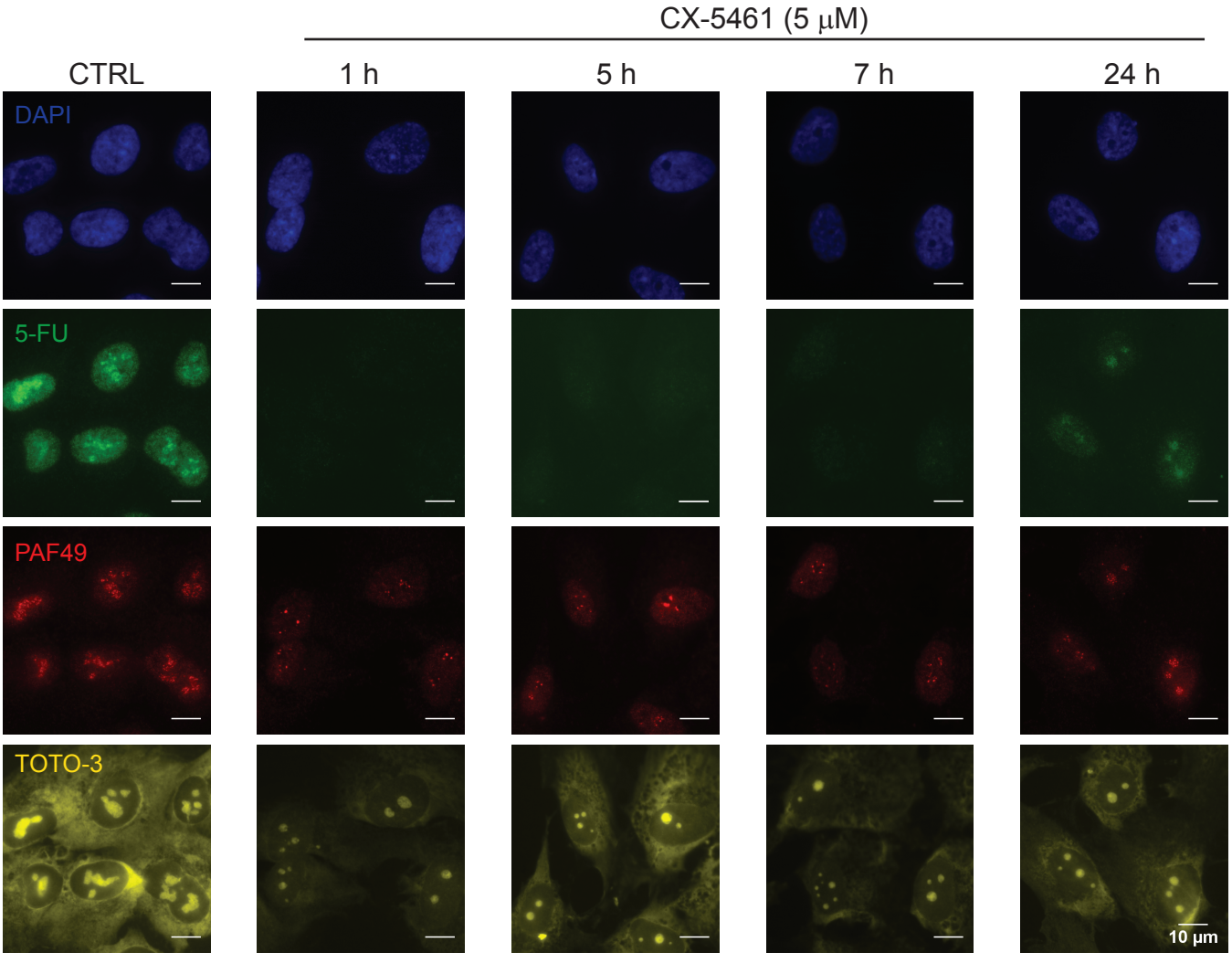

Supplementary Figure 4

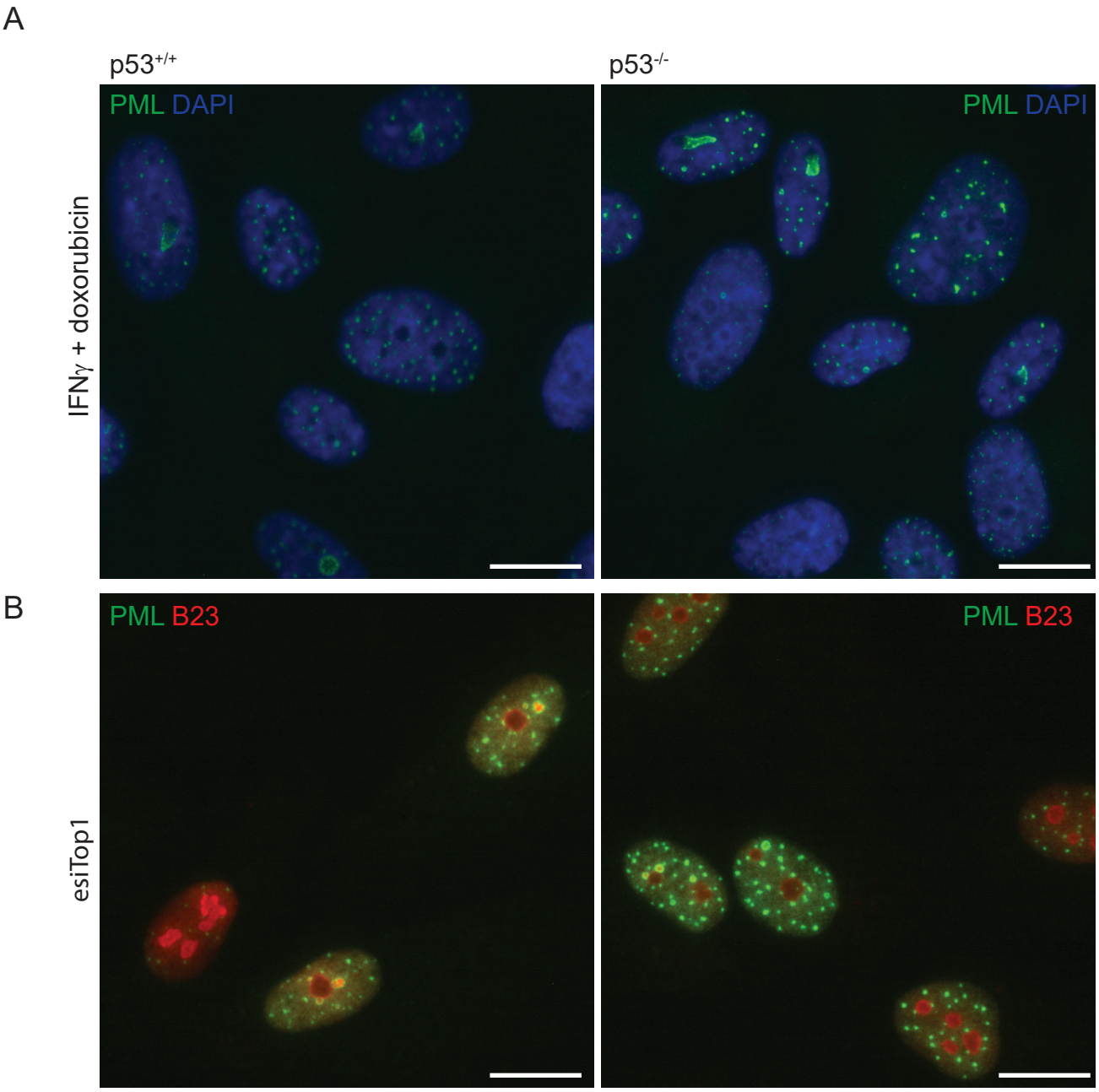

Supplementary Figure 5

A

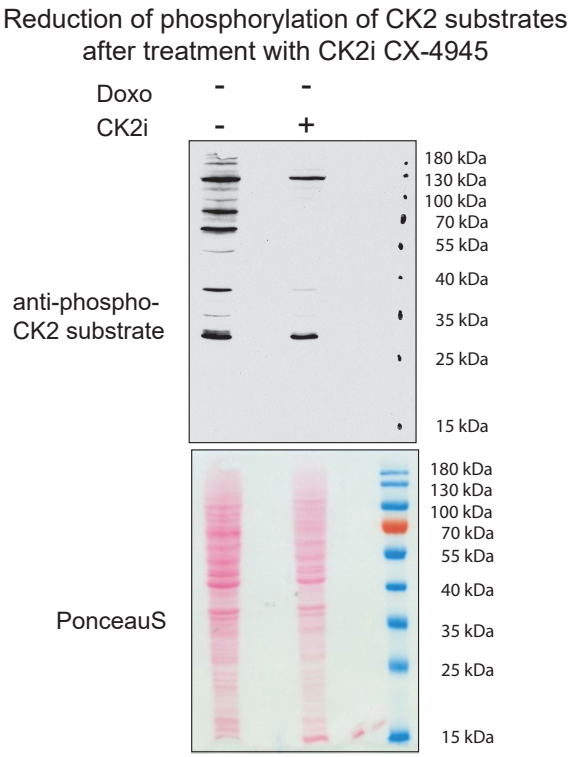


B

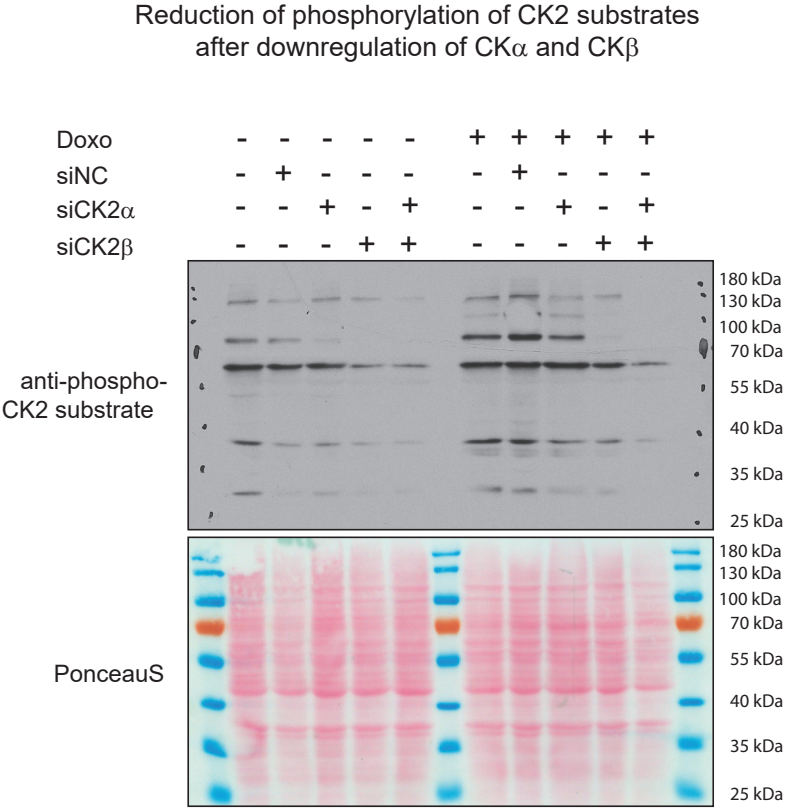


C

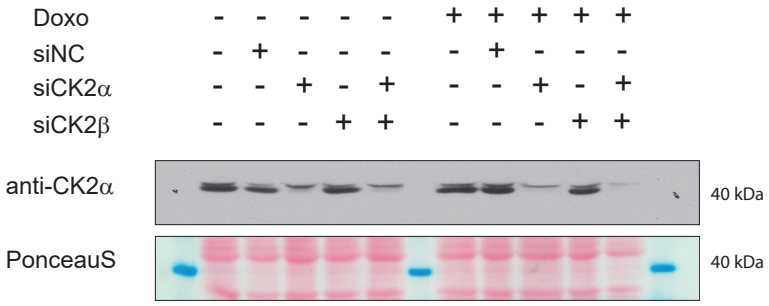

Supplementary Figure 6

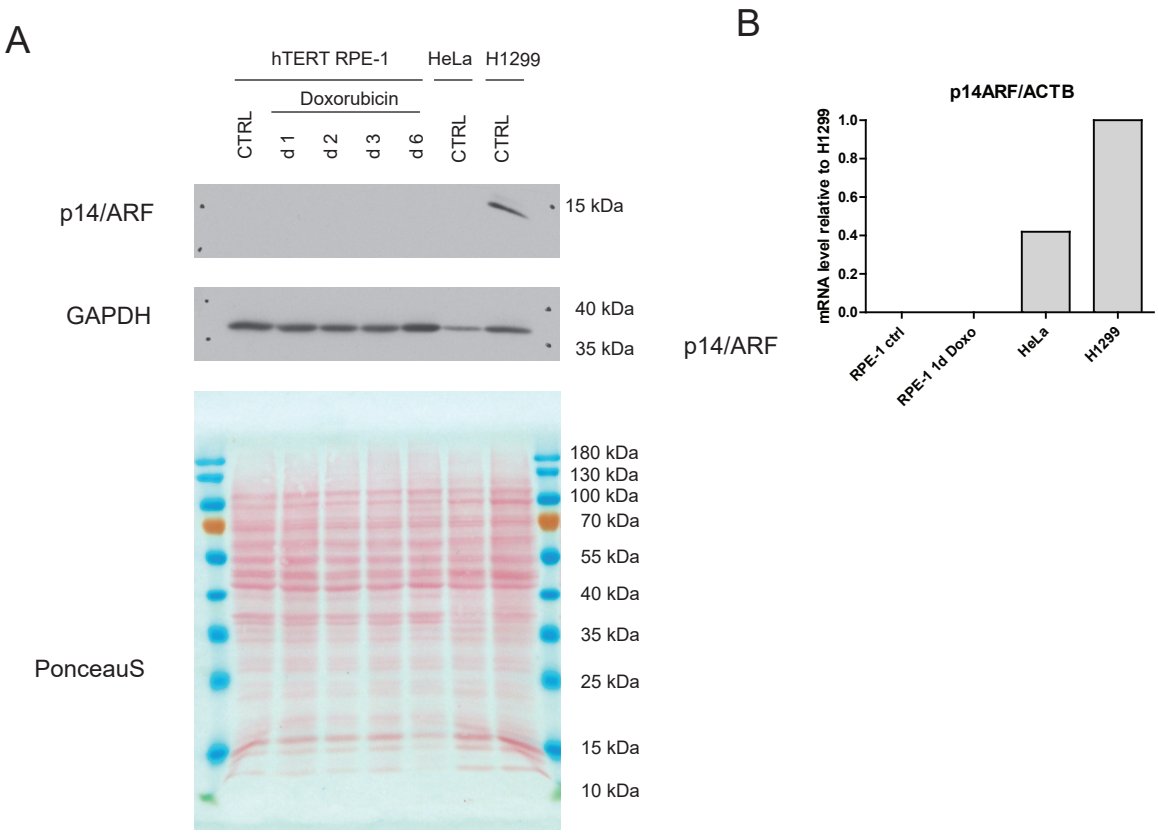

**Supplementary Table 1. Specification of antibodies**

| | | | | |
|---|---|---|---|---|
| Antibodies used for immunofluorescence | | | | |
| anti-BrdU | mouse, monoclonal | B8434 | Sigma-Aldrich/Merck (Darmstadt, Germany) | 1:500 |
| anti-PML | mouse, monoclonal | sc-966 | Santa Cruz Biotechnology (Dallas, TX, USA) | 1:200 |
| anti-PML | rabbit, polyclonal | sc-5621 | Santa Cruz Biotechnology (Dallas, TX, USA) | 1:200 |
| anti-phosphoserine 139 of histone H2AX | mouse, monoclonal | 05-636 | Millipore/Merck (Darmstadt, Germany ) | 1:500 |
| anti-nucleophosmin/B23 | mouse, monoclonal | 32-5200 | Invitrogen/Thermo Fisher Scientific (Waltham, MA, USA) | 1:200 |
| anti-PAF49 | rabbit, polyclonal | ab92428 | Abcam (Cambridge, UK) | 1:250 |
| anti-SUMO1 | rabbit, polyclonal | ab32058 | Abcam (Cambridge, UK) | 1:300 |
| Alexa Fluor 488 goat anti-mouse | goat anti-mouse | A-11029 | Invitrogene/Thermo Fisher Scientific (Waltham, MA, USA) | 1:1000 |
| Alexa Fluor 568 goat anti-mouse | goat anti-mouse | A-11031 | Invitrogene/Thermo Fisher Scientific (Waltham, MA, USA) | 1:1000 |
| Alexa Fluor 488 goat anti-rabbit | goat anti-rabbit | A-11034 | Invitrogene/Thermo Fisher Scientific (Waltham, MA, USA) | 1:1000 |
| Alexa Fluor 568 goat anti-rabbit | goat anti-rabbit | A-11036 | Invitrogene/Thermo Fisher Scientific (Waltham, MA, USA) | 1:1000 |
| Abberior STAR 635 P goat anti-rabbit | goat anti-rabbit | ST635P | Abberior GmbH (Göttingen, Germany) | 1:100 |
| Antibodies used for immunoblotting | | | | |
| anti-ARF | mouse, monoclonal | sc-53639 | Santa Cruz Biotechnology (Dallas, TX, USA) | 1:1 000 |
| anti-GAPDH | mouse, monoclonal | GTX30666 | GeneTEX (Irvine, CA, USA) | 1:10 000 |
| anti-phospho-CK2 substrate | rabbit, polyclonal | #8738 | Cell Signaling (Danver, MA, USA) | 1:1 000 |
| anti-CK2 α | mouse, monoclonal | sc-373894 | Santa Cruz Biotechnology (Dallas, TX, USA) | 1:500 |
| anti-p53 | mouse, monoclonal | sc-126 | Santa Cruz Biotechnology (Dallas, TX, USA) | 1:500 |
| anti-topoisomerase I | rabbit, polyclonal | HPA019039 | Sigma-Aldrich/Merck (Darmstadt, Germany) | 1:1 000 |
| anti-topoisomerase II α | mouse, monoclonal | sc-365916 | Santa Cruz Biotechnology (Dallas, TX, USA) | 1:1 000 |
| anti-topoisomerase II β | rabbit, polyclonal | sc-13059 | Santa Cruz Biotechnology (Dallas, TX, USA) | 1:1 000 |
| IgG-HRP goat anti-rabbit | goat anti-rabbit | 170-6515 | Bio-Rad (Hercules, CA, USA) | 1:10 000 |
| IgG-HRP goat anti-mouse | goat anti-mouse | 170-6516 | Bio-Rad (Hercules, CA, USA) | 1:10 000 |

**Supplementary Table 2: List of plasmids**

| Plasmid | Construction/origin |
|---|---|
| pGEM-4z | Promega (P2161) |
| pEGFP-N1 | Clontech (6085-1) |
| pEGFP-N3 | Clontech (6080-1) |
| pEGFP-N1-PML IV | This work |
| pEGFP-N3-PML I | This work |
| pEGFP-N1-PML IV Δaa556-559 | This work |
| pEGFP-N1-PML IV Δaa560-570 | This work |
| pEGFP-N1-PML IV Δaa560-619 | This work |
| pEGFP-N1-PML IV Δaa560-633 | This work |
| pEGFP-N1-PML IV Δaa571-619 | This work |
| pEGFP-N1-PML IV Δaa571-633 | This work |
| pEGFP-N1-PML IV Δaa621-633 | This work |
| pEGFP-N1-PML IV Δaa560-570+Δaa621-633 | This work |
| pEGFP-N3-PML I Δaa560-570 | This work |
| pEGFP-N1-PML IV S565D | This work |
| pEGFP-N1-PML IV S565A | This work |
| pEGFP-N1-PML IV SSSEDS560-565DDDEDD | This work |
| pEGFP-N1-PML IV SSSEDS560-565AAAEDA | This work |
| pEGFP-N1-PML IV VVVI556-559AAAS | This work |

**Supplementary Table 3: List of primers**

| Primers | sequence | Used for |
|---|---|---|
| PML556-560_F | GAGGAACGCAGCAGCTCGGAAGACTCAGATGCC | Deletion aa556-560 in PML IV |
| PML556-560_R | CGAGCTGCTGCGTTCCTCTGCCTCCCCGGCG | |
| PML4del560-570_F | GTGGTGATCTCCTCCCGAGAGCTGGATGACAG | Deletion aa560-570 in PML I and PML IV |
| PML4del560-570_R | TCGGGAGGAGATCACCACAACGCGTTCCTCTGCC | |
| PML4del560-619_F | *GTGGTGATC*GAAAGTGGGTTCTCCTGGGGCTACC | Deletion aa560-619 in PML IV |
| PML4del560-619_R | *CCCACTTTC*GATCACCACAACGCGTTCCTCTGCC | |
| PML4del560-633_F | GTGGTGATCTGGGATCCACCGGTCGCCAC | Deletion aa560-633 in PML IV |
| PML4del560-633_R | TGGATCCCAGATCACCACAACGCGTTCCTCTGCC | |
| PML4del571-619_F | *GAAAACTCG*GAAAGTGGGTTCTCCTGGGGCTACC | Deletion aa571-619 in PML IV |
| PML4del571-619_R | *CCCACTTTC*CGAGTTTTCGGCATCTGAGTCTTCC | |
| PML4del571-633_F | GAAAACTCGTGGGATCCACCGGTCGCCAC | Deletion aa571-633 in PML IV |
| PML4del571-633_R | TGGATCCCACGAGTTTTCGGCATCTGAGTCTTCC | |
| PML4del621-633_F | GACAATGAATGGGATCCACCGGTCGCCAC | Deletion aa621-633 in PML IV |
| PML4del621-633_R | TGGATCCCATTCATTGTCAATCTTGAGGTCAAAG | |
| PML-S565A_F | CAGCAGCTCGGAAGACGCAGATGCCGAAAACTC | Mutagenesis S565A in PML IV |
| PML-S565A_R | GAGTTTTCGGCATCTGCGTCTTCCGAGCTGCTG | |
| PML-S565D_F | GATCAGCAGCTCGGAAGACGATGATGCCGAAAACTCGTCCT | Mutagenesis S565D in PML IV |
| PML-S565D_R | AGGACGAGTTTTCGGCATCATCGTCTTCCGAGCTGCTGATC | |
| PMLSSS560AAA_F | GAACGCGTTGTGGTGATCGCCGCCGCGGAAGACGCAGATGCCG | Mutagenesis SSS560-562AAA in PML IV-S565A |
| PMLSSS560AAA_R | CGGCATCTGCGTCTTCCGCGGCGGCGATCACCACAACGCGTTC | |
| PML DDSEDD_F | GGAACGCGTTGTGGTGATCGACGACTCGGAAGACGATGATGCC | Mutagenesis SS560-561DD in PML IV-S565D |
| PML DDSEDD_R | GGCATCATCGTCTTCCGAGTCGTCGATCACCACAACGCGTTCC | |
| PML DDDEDD_F | GCGTTGTGGTGATCGACGACGATGAAGACGATGATGCCGAAAA | Mutagenesis S562D in PML IV- SSSEDS560-565 DDSEDD |
| PML DDDEDD_R | TTTTCGGCATCATCGTCTTCATCGTCGTCGATCACCACAACGC | |
| PML-AAVI-F | GGCAGAGGAACGCGCTGCGGTGATCAGCAGCT | Mutagenesis VV556-557AA in PML IV |
| PML-AAVI-R | AGCTGCTGATCACCGCAGCGCGTTCCTCTGCC | |
| PML-AAAS-F | GAACGCGCTGCGGCGAGCAGCAGCTCGGAA | Mutagenesis VI558-559AS in PML IV VV556-557AA |
| PML-AAAS-R | TTCCGAGCTGCTGCTCGCCGCAGCGCGTTC | |